A Molecular Characterization of Biogenic Secondary Organic Aerosol by High-Resolution Time-of-Flight Mass Spectrometry: Composition and Volatility.

Felipe Daniel Lopez-Hilfiker

A dissertation

submitted in partial fulfillment of the

requirements for the degree of

Doctor of Philosophy

University of Washington

2015

Reading Committee:

Joel A. Thornton, Chair

Becky Alexander

Daniel Cziczo

Program Authorized to Offer Degree:

Department of Atmospheric Sciences

University of Washington

Abstract

A Molecular Characterization of Biogenic Secondary Organic Aerosol by High-Resolution Time-of-Flight Mass Spectrometry: Composition and Volatility.

Felipe D Lopez-Hilfiker

Chair of the Supervisory Committee:
Prof. Joel A. Thornton
Atmospheric Sciences

The guiding question to this research is: *To what extent and by what mechanisms do biogenic volatile organic compounds contribute to atmospheric aerosol mass?* To address this question we need to understand the chemistry that produces condensable vapors which when in the presence of particles may partition onto the aerosol surface depending on their chemical and physical properties. I developed an *insitu* gas and aerosol sampling system, the FIGAERO (Filter Inlet for Gases and AEROsol) to speciate gas and particle phase organics derived from photochemical reactions with biogenic volatile organic compounds under both field and laboratory conditions. By coupling the FIGAERO to a High-Resolution Time-of-Flight Chemical Ionization Mass Spectrometer (HR-TOF-CIMS) I am able to elucidate chemical pathways by

identifying elemental compositions and in some cases functional groups present in the detected molecular ions. The coupling of the FIGAERO to the HR-TOF-CIMS also allows the estimation of effective vapor pressures of the aerosol components and this information can be used to improve vapor pressure models and test associated partitioning theories and parameterizations. The approach also provides hundreds of speciated chemical tracers that can be correlated with traditional environmental and chemical measurements (e.g AMS, NO_x, SO_2, SMPS, VOC) to help derive sources and sinks and to constrain the mechanisms responsible for the formation and growth of organic aerosol. Measurements obtained across a wide range of conditions and locations allowing connections and contrasts between different chemical systems, providing insights into generally controlling factors of secondary organic aerosol (SOA) and its properties.

TABLE OF CONTENTS

LIST OF FIGURES

LIST OF TABLES

ACKNOWLEDGEMENTS

First I would like to thank my advisor, Joel Thornton, who quite literally taught me everything I know about atmospheric chemistry. His door has always been open, and he always somehow found time to talk about everything from our semi-regular "life chats" to the details of developing instruments or understanding measurements. He has been an excellent guide through a significant portion of my life, and for that I will always be grateful.

I am also grateful to the other members of the Thornton group: Glenn Wolfe, Reddy Yatavelli, Sara Harrold, Beth Friedman, Julia Wargo, Claudia Mohr, Cassandra Gaston, Ben Lee, Jim Kercher, Tim Bertram, Emma D'Ambro, Lauren Whybrew, Lexie Goldberger, Sigi Schobesberger, and Theran Riedel all who I had the pleasure of working with during my time in the group. I will always remember our time together fondly, whether it was with our hands stuffed inside an electronics box, numerous field outings, or just enjoying lunch in the sun. I am particularly thankful for the time that Glenn spent teaching me how to use a mass spectrometer, and maybe more importantly: to never ask a graduate student how much longer they have left. Claudia has also been a great mentor and friend both in and out of the lab, without her patience and expertise much of this work would not have been possible, or have been nearly as much fun to do. I have truly enjoyed working with all of you and will always value the time we spent together.

Finally, I must thank my family and all my wonderful friends, you have been an incredibly important to keeping things in perspective – and making my time in Seattle so enjoyable, whether on one of our weekend excursions or just out for an evening sail on the lake. To Katie, thank you for being so patient and understanding during all the field campaigns, conferences, and long nights in the lab – you have always been there for me – and for that I am forever in your debt. To my parents and brother, your support and love throughout my life has been unwavering – this accomplishment would not have been possible without you and all that I have learned from you over the years.

Chapter 1. INTRODUCTION

Aerosol particles scatter and absorb radiation, influence cloud formation processes and properties, provide surfaces to facilitate multiphase reactions, and provide an absorptive medium for semi-volatile gases. As a result, aerosol particles have a significant effect on the radiative balance of the atmosphere and thus on earth's climate (Hallquist et al., 2009). Atmospheric particles also have harmful effects on human health, impacting respiratory and cardiovascular systems (Davidson et al., 2005; Hallquist et al., 2009; Pope and Dockery, 2006). Particles have a variety of sources in the atmosphere; they may be directly emitted from natural sources such as tree emissions, bubble bursting, forest fires, volcanic eruptions, blowing dust or from anthropogenic sources including vehicles, agriculture, industry, power generation and other combustion processes. Aerosol from these types of sources are termed primary aerosol as particles are directly emitted. Aerosol that is derived from the oxidation of volatile trace vapors in the atmosphere can lead to lower volatility products that subsequently undergo gas-particle conversion and are termed secondary particle sources. The extent that primary and secondary aerosol sources determine the particle mass loading and size distribution depends on a variety of factors: the proximity to primary particle and vapor sources, meteorological conditions, and relative level of atmospheric oxidants.

Of specific importance to both air quality and climate are particles smaller than ~ 1 μm in diameter, a significant fraction of which is secondary organic aerosol (SOA) (Hallquist et al., 2009; Jimenez et al., 2009). The sources, oxidation pathways and chemical properties of SOA still remain highly uncertain, and these uncertainties can lead to large errors between modeled and measured aerosol loadings (Heald et al., 2010; Volkamer et al., 2006). These uncertainties limit our ability to confidently predict future changes in aerosol properties under a warming climate (Hallquist et al., 2009). To develop adequate model parameterizations of organic aerosol formation, growth, and loss, there remains a need to improve and evaluate chemical mechanisms that involve conversion and partitioning of organic compounds between gas and condensed phases. These needs can be addressed by a more detailed understanding of molecular composition in both phases at higher time resolution. Recently, measurement methods have been

developed which are able to address the volatility distribution and molecular composition of organic aerosol on hourly or better timescales. These advances allow for the evaluation of thermodynamic models which often utilize partitioning theory (Pankow, 2007), and for tests of mechanisms used to describe the evolution of volatility and solubility of organic aerosol as a result of oxidative processing (Kroll et al., 2011).

The chemical conversion of major inorganic atmospheric gases such as sulfur dioxide, nitrogen dioxide and ammonia into particulate phase inorganic components is, for the most part, well understood as it involves only a handful of oxidation products that are readily measured by standard techniques. However, there remains a significant amount of uncertainty over secondary aerosol formed when atmospheric oxidation produces products of volatile organic compounds (VOCs) that undergo gas-particle partitioning leading to production (Hallquist et al., 2009; Ziemann and Atkinson, 2012). Measurements of bulk submicron aerosol mass concentrations across the northern hemisphere have shown that total non-refractory submicron aerosol, and specifically that produced from secondary sources is to a large degree of organic origin and explains the majority of total submicron aerosol (Jimenez et al., 2009). Therefore, there remains a need to understand the evolution of organic aerosol, and specifically secondary organic aerosol in the atmosphere.

While organic aerosol, and specifically SOA, has been found to be ubiquitous in the lower atmosphere, our understanding of the functional groups that contribute to organic aerosol mass, and the types of compounds which participate in nucleation and growth of freshly formed particles is still lacking. Identifying the functional groups of the organic molecules contributing to particle growth remains a difficult analytical challenge, given that the vapors which contribute are likely extremely low volatility present at parts per trillion mixing ratios (or lower), or are transformed into compounds with extremely low vapor pressures by condensed phase chemistry within the growing particles (Ehn et al., 2014; Riipinen et al., 2012; Russell et al., 2011; Ziemann, 2002).

The atmosphere is an incredibly complex chemical reactor; it is estimated that the oxidation of organic molecules in the atmosphere leads to the formation of 10,000-100,000 different chemical

species (Goldstein). These species, depending on their volatility can partition between the gas and particle phase in a dynamic equilibrium with temperature, particle liquid water, organic aerosol mass, particle acidity, etc. further complicating the chemical system and its sensitivity to atmospheric changes. An additional degree of complexity to understanding organic aerosol evolution is that the types of compounds that are likely responsible for new particle formation (i.e. nucleation) are not necessarily the same compounds which are responsible for particle mass growth. However, to constrain the aerosol lifecycle both these processes must be adequately understood and distilled into controlling processes, which can be implemented into global chemical models.

1.1 Atmospheric Oxidation of VOC

The gas-phase oxidation of volatile organic compounds in the atmosphere proceeds by reaction with radicals (e.g. OH, Cl, NO_3) or by reaction with other atmospheric oxidants such as ozone. Additional oxidation pathways involving photolysis, which is major source of atmospheric radicals, is also active. The relative importance of these oxidants is a function of time of day, and the VOC of interest – as different VOC have different reactivity with each oxidant. Some oxidants are only present during the daytime (OH, Cl), nighttime (NO_3) or both (O_3) leading to continuously changing reaction pathways on top of diurnally changing emissions of precursor VOCs. A schematic of atmospheric oxidation involving a generic VOC is shown in Figure 1.1. Depending on the relative concentrations of HO_2, RO_2, and NO_x the oxidation of VOCs leads to the formation of polar oxygenated groups, such as aldehyde (–C(=O)H), ketone (–C(=O)–), alcohol (–OH), nitrate (–ONO2), peroxyacyl nitrate (–C(=O)OONO2), carboxylic acid (–C(=O)OH), hydroperoxide (–OOH) and percarboxylic acid (–C(=O)OOH) groups, which make the oxidation products less volatile (Hallquist et al., 2009). For example, the addition of a single alcohol group during oxidation leads to a vapor pressure reduction of more than 100x, while the addition of a single carboxylic acid group leads to a reduction of more than 1000x (Capouet and Müller, 2006; Ziemann and Atkinson, 2012).

The degree to which atmospheric oxidation leads to the addition of functional groups (functionalization) to a precursor VOC increases its ability to be partitioned to the particle phase

based on a reduction in its vapor pressure. In competition with functionalization is fragmentation, which leads to carbon-carbon bond scission, resulting in smaller molecules, which are less likely to partition to the particle phase, as they are more volatile. A schematic of atmospheric oxidation as a function of vapor pressure is show in Figure 1.2. However, the vapor pressure of gas phase oxidation products is not the only factor in determining the propensity of a compound to contribute to organic aerosol mass. Semi-volatile compounds of specific chemical structures have been shown to participate to multiphase chemistry resulting in further oxidation or oligomerization reactions (e.g. Gao et al., 2004). These processes can rapidly increase the effective molecular weight of individual compounds present in the aerosol, leading to a sharp decrease in volatility despite the initially small size (and high volatility) of the precursor molecules. Reactive uptake mechanisms involving epoxide rings have also been shown to be an efficient means to generate SOA mass. Reactive uptake involves a relatively high volatility gas phase molecule, which is transferred to the particle phase by reaction with condensed phase species (Surratt et al., 2010). Therefore compounds, which were initially thought not participate in SOA formation, have now been reconsidered as potentially abundant SOA sources (Claeys et al., 2004; Surratt et al., 2010).

The identity of the dominant classes (e.g. acids, peroxides, alcohols, etc.) formed as a result of oxidative ageing in the atmosphere has been the subject of intense research over the last decade. Carboxylic acids are thought to be an important component of SOA (Heald et al., 2010; Russell et al., 2011), in part because the acid functionality represents an approximate end point in carbon oxidation state and the incorporation of an acid group leads to a significant reduction (~1000-fold) in vapor pressure relative to the parent compound. Carboxylic acids have also been suggested to participate in the nucleation and growth of new particles via acid-base reactions analogous to the ternary nucleation of NH_3-H_2SO_4-H_2O (Riipinen et al., 2012; Smith et al., 2010). Thus, understanding the gas-phase abundance and sources of such compounds is necessary to evaluating theories of nucleation and growth, a process which has significant implications for sources of cloud condensation nuclei and thus aerosol indirect effects. Russell et. al. (2011) made measurements of filter samples using Fourier Transform Infrared Spectroscopy (FTIR) and identified a large fraction of organic aerosol contained carboxylic acids and alcohol functional groups. Online measurements using an Aerosol Mass Spectrometer (AMS

Aerodyne Inc. Billerica, Massachusetts, USA) have utilized O:C and H:C ratios (Van Krevelen diagram) which have identified atmospheric and chamber derived aerosol to generally fall along a slope between -.5 and -1. This slope suggests that atmospheric ageing involves the production of carboxylic acid groups or approximately equal contributions of carbonyl and alcohol groups (Heald et al., 2010).

1.2 Biogenic Volatile Organic Compounds

Biogenic volatile organic compounds (BVOC) play a dominant role in the chemical production of SOA globally, releasing approximately 1150 TgC/yr (Guenther et al., 1995). The species emitted into the pool of BVOC include isoprene (C_5), monoterpenes(C_{10}), sesquiterpenes (C_{15}) as well as other oxygenated hydrocarbons. The dominant single components of BVOC emissions are isoprene (C_5H_8 ~ 500 TgC/yr), and monoterpenes ($C_{10}H_x$ ~ 130 TgC/yr) (Guenther et al., 1995). These BVOC are mostly unsaturated and therefore are highly reactive towards the dominant atmospheric oxidants (e.g. OH, NO_3, O_3). BVOC lifetimes in the atmosphere depend on oxidant conditions but range from minutes to a few hours and are rapidly oxidized to lower volatility products (Guenther et al., 1995). BVOC are of particular interest as their source is controlled by temperature and in some cases light and water availability; therefore in the future as a result of a changing climate emissions are likely to change, and likely increase as global temperatures rise.

Isoprene is the single largest non-methane VOC emitted and therefore has potential to be a large source of organic aerosol mass in temperate and tropical regions. However, not until recently was isoprene thought to contribute significantly to SOA. This was due primarily to its small carbon chain length, which was thought to limit its ability to produce oxidation products of sufficiently low vapor pressure to partition efficiently to the particle phase. Recently reactive uptake of isoprene-derived epoxydiols on acidic aerosol has been shown to be an efficient mechanism for generating organic aerosol mass with yields approaching 30% (Surratt et al., 2010). However, while isoprene can be an efficient source of particle mass, isoprene oxidation appears to suppress new particle formation (Kiendler-Scharr et al., 2012). In particular, a chemical pathway proposed to be important source of particle mass from isoprene is the

formation of second-generation isoprene epoxydiols (IEPOX) (Lin et al., 2012; Surratt et al., 2010). Subsequent reactive uptake of IEPOX from the gas phase to aerosol surfaces has been shown to be an efficient means of generating secondary organic aerosol and is catalyzed by the presence of acidic particles (e.g. sulfate) (Surratt et al., 2010). Aerosol growth by IEPOX reactive uptake is facilitated by acid catalyzed ring-opening reactions in the condensed phase leading to the addition of sulfate, alcohol and nitrate groups, significantly lowering the vapor pressure of the precursor molecule. The further addition of other monomer units to compounds already present in the aerosol can result in the formation of dimers or other low volatility accretion products, however do to their inherent low volatility quantifying their concentration remains an analytical challenge. Recently, gas phase formation of multifunctional organic peroxides has been shown to be an efficient means to generate organic aerosol under pristine conditions where high HO_2 concentrations are found. This presents a new, efficient pathway to aerosol formation other than the aforementioned IEPOX pathway.

The single largest monoterpene emitted is a-pinene, which alone explains nearly 50% of global monoterpene emissions or 10-15% of total non-methane organic carbon. Therefore monoterpene emissions are of similar magnitude to total non-methane anthropogenic organic carbon emissions. Monoterpenes are dominant in boreal forest regions and are known to be a significant source of secondary organic aerosol by leading to the formation of low volatility oxidations products (Ehn et al., 2014; Lopez-Hilfiker et al., 2015).

The reaction between OH and α-pinene, which is dominant during the daytime, proceeds by either hydrogen abstraction or OH addition across the a-pinene double bond, forming alkyl radicals. The alkyl radicals rapidly react with oxygen produce peroxy radicals (RO_2). These peroxy radicals may subsequently react with NO, HO_2 or RO_2 radicals, generating a suite of stable products including organic nitrates, alcohols, acids, and peroxides. The peroxy radicals may also react with alkoxy radicals (RO), which typically dissociate or isomerize to produce stable products or/and alkyl radicals. These radicals subsequently react with oxygen continuing the oxidation process by regenerating peroxy radicals. In the case of a-pinene ozonolysis, ozone adds across the double bond leading to the formation of a primary ozonide, which can isomerize

to yield reactive Criegee intermediates, which undergo further reaction or fragment (Mauldin et al., 2012).

Recently, the auto-oxidation of reactive intermediates from the oxidation of a-pinene by ozone and OH was shown to be an efficient source of aerosol mass with vapor pressures low enough to participate in new particle formation (Ehn et al., 2014). This recent work highlights the ability of gas phase oxidation of a-pinene to produce extremely low volatility products that rapidly condense to form SOA. While the primary impact of low volatility monoterpene oxidation products on SOA mass is the condensation of vapors on existing particles, that vapors of extremely low vapor pressure are efficiently produced from monoterpene oxidation could explain the discrepancy between observed particle growth rates and that explained by the condensation of sulfuric acid during new particle formation events. In Figure 1.3 a new particle formation event from Hyytiälä is shown along with a schematic of the relative importance between sulfuric acid, the formation of organic salts produced via acid base reactions and the condensation of extremely low volatility organic molecules. Organics are thought to play a critical role in new particle formation events and subsequent particle growth – but to date no online measurements have been able to link highly oxidized organic molecules to quantitatively explain particle growth during a nucleation event.

1.3 Chemical Modeling of SOA

Climate change, and with it gradual warming of the planet will lead to changes in BVOC emissions, and therefore a change in the mass flux of SOA to the atmosphere. If emissions increase purely due to increases in global average temperatures BVOC could act as a negative feedback stabilizing temperatures over forested regions. However if heat and water stress instead lead to reduced BVOC emissions the decreased production of SOA could represent a positive feedback. Chemical models are one way which we can estimate these types of effects but require detailed knowledge by which (1) plants and trees respond to temperature changes, water stress, etc. and (2) the dominant mechanisms by which VOC oxidation leads to SOA mass. Chemical models of SOA formation therefore need to represent the gas phase oxidation of precursor VOC through many generations of oxidation as well as shift compounds between the gas and

condensed phase as a function of atmospheric ageing. In the condensed phase multiphase reactions that may lead to fragmentation, further functionalization or oligomerization also must be explicitly tracked or parameterized.

The modeling of SOA requires dynamic movement of organic mass between the gas and condensed phase. Few models explicitly treat particle phase multiphase chemistry therefore most compounds are produced in the gas phase and then may partition to the particle phase via two dominant mechanisms, water based partitioning governed by solubility (Henry's Law) or partitioning into an organic medium based on Raoult's Law. Pankow 1994 introduced a formulation of partitioning in which organics prefer to be in an organic solution (i.e. "like dissolves like"). Therefore the partitioning of an organic when gas-particle partitioning is dominated by absorptive partitioning should be governed by the following equation:

$$K_p = \frac{F_{i,om} / TSP}{A_i} = \frac{f_{om}\, 760\, RT}{M 10^6 \zeta P} \qquad \text{(Eq. 1.1)}$$

Where K_p is the partitioning constant, TSP is the total suspended particulate matter, $F_{i,om}$ is the concentration of compound *i* as associated with the organic matter of the suspended particles and A_i is the gas phase concentration. This formula can be rearranged to derive the fraction of a given compound present in the particle phase.

$$F_p = \frac{Particle}{Gas + Particle} \qquad \text{(Eq. 1.2)}$$

$$F_p = \left(1 + \frac{\frac{M 10^6 \zeta P}{760 RT}}{C_{OA}}\right)^{-1} \qquad \text{(Eq. 1.3)}$$

In Equation the above equations, C_{OA} (μg m^{-3}) is the organic aerosol mass concentration, M (g mol^{-1}) is the molar mass of the compound of interest, ζ is the activity coefficient, P (torr) is the vapor pressure of a compound the over the pure component, R (8.2 x 10^{-5} m^3 atm K^{-1} mol^{-1}) is the gas constant, T (K) is the environmental temperature and 760 (torr atm^{-1}) and 10^6 (μg g^{-1}) are unit conversion factors. It is evident from Equation 1.3 that partitioning is a strong function of

vapor pressure, which varies with molecular composition and degree of oxidation. Therefore volatility (vapor pressure) is a key physical parameter required for the accurate modeling of organic aerosol, yet even for well-characterized compounds, vapor pressures often differ by orders of magnitude (Hallquist et al., 2009).

Atmospheric oxidation, partitioning and multiphase chemistry are all coupled and in dynamic equilibrium as discussed above, therefore modeling SOA is an inherently challenging task. Explicit models like the Master Chemical Mechanism (MCM) (Jenkin et al., 2015) or the Generator of Explicit Chemistry and Kinetics of Organics in the Atmosphere (GECKO-A) (Aumont et al., 2005) track gas phase chemistry and use gas-particle partitioning theory to shift mass between the gas and condensed phases as described above (Pankow, 1994). These models are currently too complex (and computationally expensive) to be implemented into global scale models and therefore parameterizations based on chamber data are often implemented instead of explicit mechanisms. It is therefore not surprising that global models differ from observations by as much as an order of magnitude across a wide range of conditions(Heald et al., 2011; Volkamer et al., 2006). Even the most complex models suffer (e.g. GECKO-A , MCM), in part, due to a limited understanding of the key chemical and physical properties of organic aerosol (e.g. volatility, yields, composition). Therefore, there remains a need to further develop mechanistic insights through improved measurement techniques and experimental capabilities, which can quantitatively and comprehensively provide insights into the controlling properties of organic aerosol needed to improve models.

1.4 Online Measurement Techniques for SOA

To a large degree our understanding of the chemical and physical properties required to accurately model SOA has been limited by the lack of adequate measurement technologies measure many compounds in a wide range of volatiles at fast enough timescales to be relevant in the atmosphere. Mass spectrometry is one commonly used analytical tool that allows fast, sensitive, and reproducible measurements of chemical species. Much of the work to date has utilized the AMS (DeCarlo et al., 2006) one of the first commercial mass spectrometers for aerosol research. While this tool is useful for providing total bulk organic loading in a fast and

quantitative way it looses much of its chemical information buy using electron impact ionization. This type of ionization is well known to lead to the nearly complete fragmentation of organic molecules thereby masking their composition and functionalities.

In Chapter 2 we describe the development of a new type of mass spectrometer designed for the specific application to the atmosphere for both aircraft and ground based measurements. This instrument utilizes chemical ionization a soft and selective means to ionize neutral molecules. Chemical ionization as implemented in our instrument preserves the molecular identity of the compounds present in the atmosphere in a systematic and quantitative way. As part of my research I led the development and deployed two time-of-flight chemical ionization mass spectrometers optimized for the detection of atmospheric organic and inorganic molecules utilizing iodide and acetate ion chemistry (Lee et al., 2014; Veres et al., 2008). These instruments were deployed to a variety of locations around the world both on ground based towers, research aircraft, and atmospheric simulation chambers. Our chemical ionization mass spectrometer (CIMS) has a number of advantages compared to previous techniques. Our TOF mass spectrometers are (1) Fast, acquiring 22,222 unique mass spectra per second spanning 15-525 Th, (2) Accurate, allowing for the assignment of a molecular formula of detected ions by accurate mass determinations, (3) sensitive, allowing detection of concentrations well below 1 pptv, (4) high-resolution which allows separation of isobaric compounds, and (5) field deployable weighing only 300 lbs and drawing ~750 W. The combination of rapid acquisition of full mass spectra and the ability to derive molecular compositions allows new mechanistic insights into the controlling properties of atmospheric oxidation which until now was primarily limited to offline analysis or laboratory chambers.

This newly developed instrument is particularly powerful when coupled with a Filter Inlet for Gases and AEROsol (FIGAERO) (Lopez-Hilfiker et al., 2014), which adds the ability to measure in both the gas and particle phase as well as constrain the effective volatility of the collected organics in the particle phase on a semi-continuous basis. This instrument and its coupling to the FIGAERO is described in detail in Chapter 3. The instrument was designed to compliment exiting measurement techniques while filling critical gaps in our measurement technology. The FIGAERO inlet when coupled to a CIMS allows molecular analysis of the dynamic equilibrium

between gas and particle phase organics largely free of ionization-induced fragmentation. The inlet utilizes thermal desorption as a means to evaporate condensed organics found in the particles. By using a slow heating we are able to determine the effective volatilities of the condensed organics providing important constraints for gas-particle partitioning models. By coupling the volatility distribution determined with the FIGAERO with molecular composition afforded by the TOF-MS we are also able to provide a quantitative measurement of oligomeric material, its effective vapor pressure and the relevant monomer building blocks.

The research described hereafter addresses some of the current limitations in our understanding of the evolution of organic aerosol, specifically that derived from BVOC oxidation by application of the new measurement technologies I helped develop. The subsequent chapters describe the new insights into SOA formation that were afforded by the development, characterization and deployment of this instrument. We first apply a prototype of the instrument to an environmental simulation chamber in Jülich, Germany where we focused on monoterpene oxidation. We highlight the formation low volatility organics derived from a-pinene oxidation in Chapter 4.

In Chapter 5 we investigate the role of isoprene and the effective volatility distribution in a polluted region of the southeast United States as part of a large-scale field project (Southern Atmosphere Study). In this region both monoterpenes and isoprene are present, therefore allowing us to compare the effective volatility and composition between the two dominant chemical systems in the atmosphere. In Chapter 6 we utilize measurements from the top of a tall tower in a boreal forest site in Hyytiälä, Finland where nucleation events are routinely observed. We provide molecular constraints and volatility measurements as part of the first online measurements of highly oxidized organic molecules in particles during nucleation.

The measurements presented herein, all utilizing the same ion chemistry on both chambers and in the atmosphere allow us to draw general conclusions about the controlling chemical and physical properties of organic aerosol and the most important oxidative pathways and products relevant to particle growth and new particle formation processes.

Aumont, B., Szopa, S. and Madronich, S.: Modelling the evolution of organic carbon during its gas-phase tropospheric oxidation: development of an explicit model based on a self generating approach, Atmos. Chem. Phys., 5(9), 2497–2517, doi:10.5194/acp-5-2497-2005, 2005.

Capouet, M. and Müller, J. F.: A group contribution method for estimating the vapour pressures of α-pinene oxidation products, Atmos. Chem. Phys., 6(6), 1455–1467, doi:10.5194/acp-6-1455-2006, 2006.

Claeys, M., Wang, W., Ion, A. C. and Kourtchev, I.: Formation of secondary organic aerosols from isoprene and its gas-phase oxidation products through reaction with hydrogen peroxide, Atmospheric …, 2004.

Davidson, C. I., Phalen, R. F. and Solomon, P. A.: Airborne Particulate Matter and Human Health: A Review, Aerosol Science and Technology, 39(8), 737–749, doi:10.1080/02786820500191348, 2005.

DeCarlo, P. F., Kimmel, J. R., Trimborn, A., Northway, M. J., Jayne, J. T., Aiken, A. C., Gonin, M., Fuhrer, K., Horvath, T., Docherty, K. S., Worsnop, D. R. and Jimenez, J. L.: Field-Deployable, High-Resolution, Time-of-Flight Aerosol Mass Spectrometer, Anal. Chem., 78(24), 8281–8289, doi:10.1021/ac061249n, 2006.

Ehn, M., Thornton, J. A., Kleist, E., Sipilä, M., Junninen, H., Pullinen, I., Springer, M., Rubach, F., Tillmann, R., Lee, B., Lopez-Hilfiker, F., Andres, S., Acir, I.-H., Rissanen, M., Jokinen, T., Schobesberger, S., Kangasluoma, J., Kontkanen, J., Nieminen, T., Kurtén, T., Nielsen, L. B., Jørgensen, S., Kjaergaard, H. G., Canagaratna, M., Maso, M. D., Berndt, T., Petäjä, T., Wahner, A., Kerminen, V.-M., Kulmala, M., Worsnop, D. R., Wildt, J. and Mentel, T. F.: A large source of low-volatility secondary organic aerosol, Nature, 506(7489), 476–479, doi:10.1038/nature13032, 2014.

Gao, S., Keywood, M., Ng, N. L., Surratt, J., Varutbangkul, V., Bahreini, R., Flagan, R. C. and Seinfeld, J. H.: Low-Molecular-Weight and Oligomeric Components in Secondary Organic Aerosol from the Ozonolysis of Cycloalkenes and α-Pinene, The Journal of Physical Chemistry A, 108(46), 10147–10164, doi:10.1021/jp047466e, 2004.

Guenther, A., Hewitt, C. N. and Erickson, D.: A global model of natural volatile organic compound emissions, Journal of …, 1995.

Hallquist, M., Wenger, J. C., Baltensperger, U., Rudich, Y., Simpson, D., Claeys, M., Dommen, J., Donahue, N. M., George, C., Goldstein, A. H., Hamilton, J. F., Herrmann, H., Hoffmann, T., Iinuma, Y., Jang, M., Jenkin, M. E., Jimenez, J. L., Kiendler-Scharr, A., Maenhaut, W., McFiggans, G., Mentel, T. F., Monod, A., Prevot, A. S. H., Seinfeld, J. H., Surratt, J. D., Szmigielski, R. and Wildt, J.: The formation, properties and impact of secondary organic aerosol: current and emerging issues, Atmos. Chem. Phys., 9(14), 5155–5236, doi:10.5194/acp-9-5155-2009, 2009.

Heald, C. L., Coe, H., Jimenez, J. L., Weber, R. J., Bahreini, R., Middlebrook, A. M., Russell, L. M., Jolleys, M., Fu, T. M., Allan, J. D., Bower, K. N., Capes, G., Crosier, J., Morgan, W. T., Robinson, N. H., Williams, P. I., Cubison, M. J., DeCarlo, P. F. and Dunlea, E. J.: Exploring the

vertical profile of atmospheric organic aerosol: comparing 17 aircraft field campaigns with a global model, Atmos. Chem. Phys., 11(24), 12673–12696, doi:10.5194/acp-11-12673-2011-supplement, 2011.

Heald, C. L., Kroll, J. H., Jimenez, J. L., Docherty, K. S., DeCarlo, P. F., Aiken, A. C., Chen, Q., Martin, S. T., Farmer, D. K. and Artaxo, P.: A simplified description of the evolution of organic aerosol composition in the atmosphere, Geophys. Res. Lett., 37(8), L08803, doi:10.1029/2010GL042737, 2010.

Jenkin, M. E., Young, J. C. and Rickard, A. R.: The MCM v3.3 degradation scheme for isoprene, Atmos. Chem. Phys. Discuss., 15(6), 9709–9766, doi:10.5194/acpd-15-9709-2015-supplement, 2015.

Jimenez, J. L., Canagaratna, M. R., Donahue, N. M., Prevot, A. S. H., Zhang, Q., Kroll, J. H., DeCarlo, P. F., Allan, J. D., Coe, H., Ng, N. L., Aiken, A. C., Docherty, K. S., Ulbrich, I. M., Grieshop, A. P., Robinson, A. L., Duplissy, J., Smith, J. D., Wilson, K. R., Lanz, V. A., Hueglin, C., Sun, Y. L., Tian, J., Laaksonen, A., Raatikainen, T., Rautiainen, J., Vaattovaara, P., Ehn, M., Kulmala, M., Tomlinson, J. M., Collins, D. R., Cubison, M. J., E., Dunlea, J., Huffman, J. A., Onasch, T. B., Alfarra, M. R., Williams, P. I., Bower, K., Kondo, Y., Schneider, J., Drewnick, F., Borrmann, S., Weimer, S., Demerjian, K., Salcedo, D., Cottrell, L., Griffin, R., Takami, A., Miyoshi, T., Hatakeyama, S., Shimono, A., Sun, J. Y., Zhang, Y. M., Dzepina, K., Kimmel, J. R., Sueper, D., Jayne, J. T., Herndon, S. C., Trimborn, A. M., Williams, L. R., Wood, E. C., Middlebrook, A. M., Kolb, C. E., Baltensperger, U. and Worsnop, D. R.: Evolution of Organic Aerosols in the Atmosphere, Science, 326(5959), 1525–1529, doi:10.1126/science.1180353, 2009.

Kiendler-Scharr, A., Andres, S., Bachner, M., Behnke, K., Broch, S., Hofzumahaus, A., Holland, F., Kleist, E., Mentel, T. F., Rubach, F., Springer, M., Steitz, B., Tillmann, R., Wahner, A., Schnitzler, J. P. and Wildt, J.: Isoprene in poplar emissions: effects on new particle formation and OH concentrations, Atmos. Chem. Phys., 12(2), 1021–1030, doi:10.5194/acp-12-1021-2012, 2012.

Kroll, J. H., Donahue, N. M., Jimenez, J. L., Kessler, S. H., Canagaratna, M. R., Wilson, K. R., Altieri, K. E., Mazzoleni, L. R., Wozniak, A. S., Bluhm, H., Mysak, E. R., Smith, J. D., Kolb, C. E. and Worsnop, D. R.: Carbon oxidation state as a metric for describing the chemistry of atmospheric organic aerosol, Nature Chemistry, 3(2), 133–139, doi:10.1038/nchem.948, 2011.

Lee, B. H., Lopez-Hilfiker, F. D., Mohr, C., Kurtén, T., Worsnop, D. R. and Thornton, J. A.: An Iodide-Adduct High-Resolution Time-of-Flight Chemical-Ionization Mass Spectrometer: Application to Atmospheric Inorganic and Organic Compounds, Environ. Sci. Technol., 48(11), 6309–6317, doi:10.1021/es500362a, 2014.

Lin, Y.-H., Zhang, Z., Docherty, K. S., Zhang, H., Budisulistiorini, S. H., Rubitschun, C. L., Shaw, S. L., Knipping, E. M., Edgerton, E. S., Kleindienst, T. E., Gold, A. and Surratt, J. D.: Isoprene Epoxydiols as Precursors to Secondary Organic Aerosol Formation: Acid-Catalyzed Reactive Uptake Studies with Authentic Compounds, Environ. Sci. Technol., 46(1), 250–258, doi:10.1021/es202554c, 2012.

Lopez-Hilfiker, F. D., Mohr, C., Ehn, M., Rubach, F., Kleist, E., Wildt, J., Mentel, T. F., Lutz, A., Hallquist, M., Worsnop, D. and Thornton, J. A.: A novel method for online analysis of gas and particle composition: description and evaluation of a Filter Inlet for Gases and AEROsols (FIGAERO), Atmos. Meas. Tech., 7(4), 983–1001, doi:10.5194/amt-7-983-2014, 2014.

Lopez-Hilfiker, F., Mohr, C., Ehn, M., Rubach, F., Kleist, E., Wildt, J., Mentel, T. F., Carrasquillo, A., Daumit, K., Hunter, J.others: Phase partitioning and volatility of secondary organic aerosol components formed from α-pinene ozonolysis and OH oxidation: the importance of accretion products and other low volatility compounds, Atmos. Chem. Phys. Discuss., 15(4), 4463–4494, 2015.

Mauldin, R. L., III, Berndt, T., Sipilä, M., Paasonen, P., Petäjä, T., Kim, S., Kurtén, T., Stratmann, F., Kerminen, V. M. and Kulmala, M.: A new atmospherically relevant oxidant of sulphur dioxide, Nature, 488(7410), 193–196, doi:doi:10.1038/nature11278, 2012.

Pankow, J. F.: An absorption model of gas/particle partitioning of organic compounds in the atmosphere, Atmospheric Environment, 28(2), 185–188, doi:10.1016/1352-2310(94)90093-0, 1994.

Pankow, J. F.: An absorption model of the gas/aerosol partitioning involved in the formation of secondary organic aerosol, Atmospheric Environment, 41, 75–79, doi:10.1016/j.atmosenv.2007.10.060, 2007.

Pope, C. A., III and Dockery, D. W.: Health Effects of Fine Particulate Air Pollution: Lines that Connect, Journal of the Air & Waste Management Association, 56(6), 709–742, doi:10.1080/10473289.2006.10464485, 2006.

Riipinen, I., Yli-Juuti, T., Pierce, J. R., Petäjä, T., Worsnop, D. R., Kulmala, M. and Donahue, N. M.: The contribution of organics to atmospheric nanoparticle growth, Nature Geosci, 5(7), 453–458, doi:10.1038/ngeo1499, 2012.

Russell, L. M., Bahadur, R. and Ziemann, P. J.: Identifying organic aerosol sources by comparing functional group composition in chamber and atmospheric particles, Proceedings of the National Academy of Sciences, 108(9), 3516–3521, doi:10.1073/pnas.1006461108, 2011.

Smith, J. N., Barsanti, K. C., Friedli, H. R., Ehn, M., Kulmala, M., Collins, D. R., Scheckman, J. H., Williams, B. J. and McMurry, P. H.: Observations of aminium salts in atmospheric nanoparticles and possible climatic implications, Proceedings of the National Academy of Sciences, 107(15), 6634–6639, doi:10.1073/pnas.0912127107, 2010.

Surratt, J. D., Chan, A. W. H., Eddingsaas, N. C., Chan, M., Loza, C. L., Kwan, A. J., Hersey, S. P., Flagan, R. C., Wennberg, P. O. and Seinfeld, J. H.: Reactive intermediates revealed in secondary organic aerosol formation from isoprene, Proceedings of the National Academy of Sciences, 107(15), 6640–6645, doi:10.1073/pnas.0911114107, 2010.

Veres, P., Roberts, J. M., Warneke, C., Welsh-Bon, D., Zahniser, M., Herndon, S., Fall, R. and de Gouw, J.: Development of negative-ion proton-transfer chemical-ionization mass spectrometry (NI-PT-CIMS) for the measurement of gas-phase organic acids in the atmosphere,

International Journal of Mass Spectrometry, 274(1-3), 48–55, doi:10.1016/j.ijms.2008.04.032, 2008.

Volkamer, R., Jimenez, J. L., San Martini, F., Dzepina, K., Zhang, Q., Salcedo, D., Molina, L. T., Worsnop, D. R. and Molina, M. J.: Secondary organic aerosol formation from anthropogenic air pollution: Rapid and higher than expected, Geophys. Res. Lett., 33(17), L17811, doi:10.1029/2006GL026899, 2006.

Ziemann, P. J.: Evidence for Low-Volatility Diacyl Peroxides as a Nucleating Agent and Major Component of Aerosol Formed from Reactions of O 3with Cyclohexene and Homologous Compounds, The Journal of Physical Chemistry A, 106(17), 4390–4402, doi:10.1021/jp012925m, 2002.

Ziemann, P. J. and Atkinson, R.: Kinetics, products, and mechanisms of secondary organic aerosol formation, Chem. Soc. Rev., 41(19), 6582, doi:10.1039/c2cs35122f, 2012.

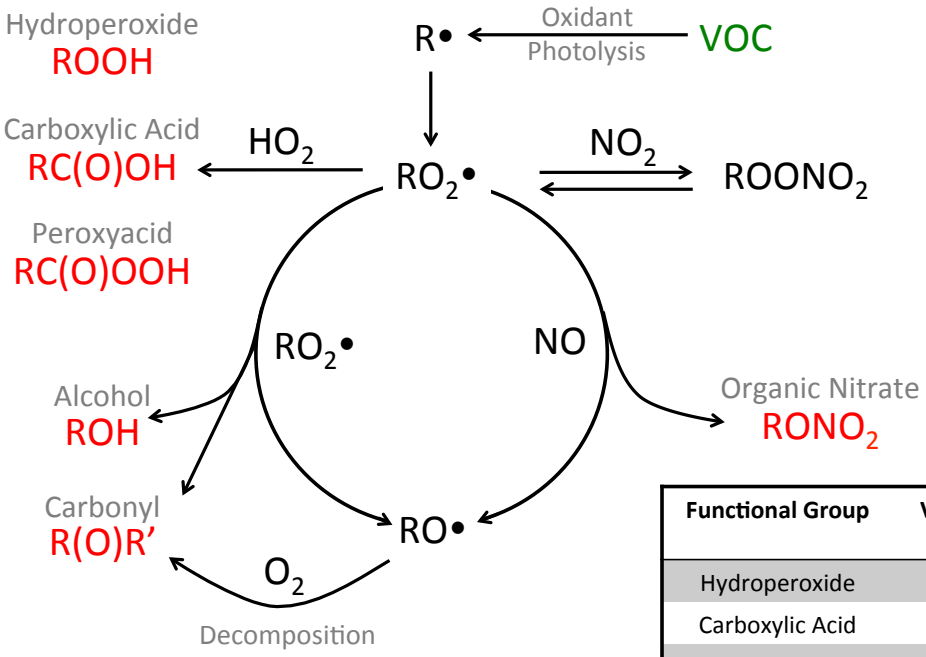

Functional Group	Vapor Pres. Reduction
Hydroperoxide	300x
Carboxylic Acid	3800x
Peroxyacid	300x
Alcohol	170x
Carbonyl	10x
Nitrate	170x

Figure 1.1. Schematic of generic VOC oxidation in the atmosphere.

Oxidation processes lead to the formation of oxidized functional groups which lower the precursor VOC vapor pressures by approximately the factors listed in the inset table (Ziemann and Atkinson, 2012).

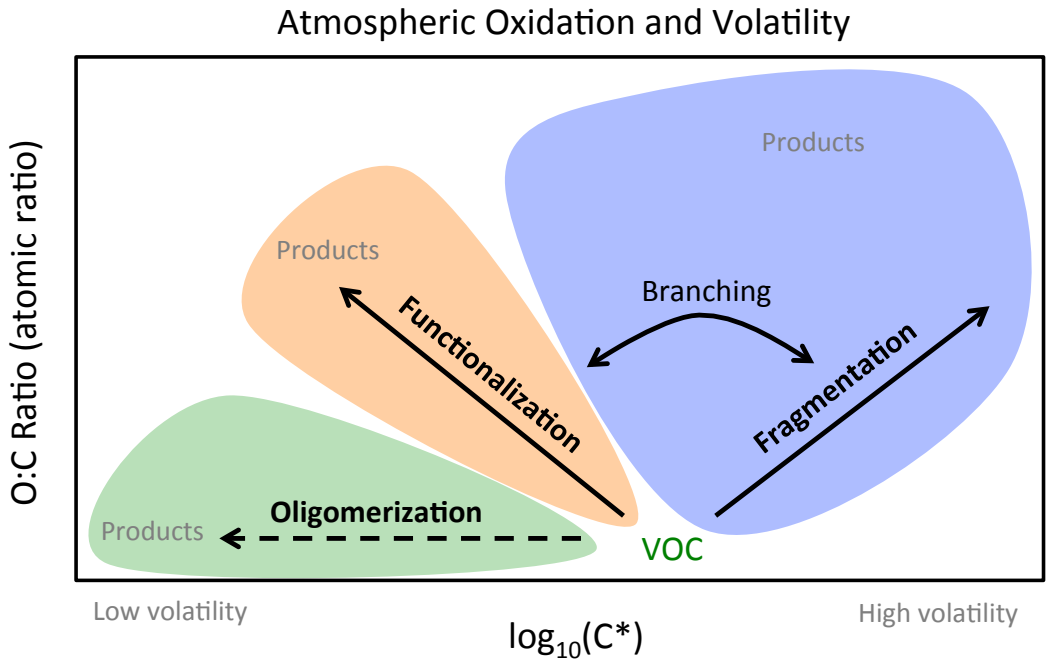

Figure 1.2 Schematic of atmospheric oxidation and changes in vapor pressure. Oxidation may take place in the gas or particle phase following reactions outlined in Figure 1.1 with the exception of oligomerization, which is specific to the condensed phase only. Reactions form three general categories: fragmentation, functionalization and oligomerization, based on whether the carbon number decreases, stays the same, or increases. The branching between functionalization and fragmentation is critical for determining the yield of SOA. Functionalization will reduce volatility, whereas fragmentation can generate more-volatile species, which are less likely to contribute to SOA mass. Figure adapted from (Jimenez et al., 2009).

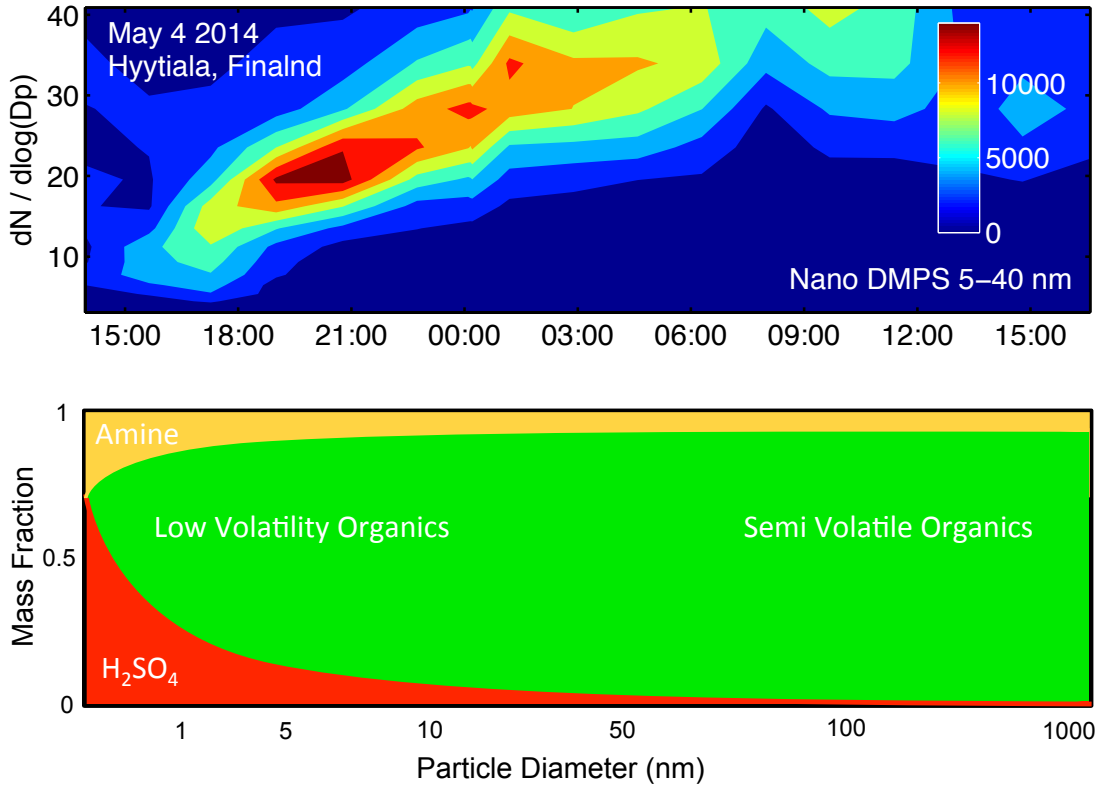

Figure 1.3 Nucleation in the Boreal Forest.

Top: A nucleation event during the spring in Hyytiälä, Finland from the top of a 35m tower. Bottom: A schematic of the relative importance of different chemical species during the initial steps of nucleation and subsequent particle growth. Sulfuric acid and acid base reactions are thought to be important during the initial cluster formation. Organics are believed to rapidly dominate the mass growth and therefore their composition and formation mechanisms are of critical importance in growing newly formed particles to CCN active sizes.

Chapter 2. AN IODIDE-ADDUCT HIGH-RESOLUTION TIME-OF-FLIGHT CHEMICAL-IONIZATION MASS SPECTROMETER: APPLICATION TO ATMOSPHERIC INORGANIC AND ORGANIC COMPOUNDS[*]

Abstract

A High-Resolution Time-of-Flight Chemical-Ionization Mass Spectrometer (HR-ToF-CIMS) using Iodide-adducts has been characterized and deployed in several laboratory and field studies to measure a suite of organic and inorganic atmospheric species. The large negative mass defect of Iodide, combined with soft ionization and the high mass-accuracy (< 20 ppm) and mass-resolving power (R > 5500) of the time-of-flight mass spectrometer, provides an additional degree of separation and allows for the determination of elemental compositions for the vast majority of detected ions. Laboratory characterization reveals Iodide-adduct ionization generally exhibits increasing sensitivity towards more polar or acidic volatile organic compounds. Simultaneous retrieval of a wide range of mass-to-charge ratios (m/Q from 25 to 625 Th) at a high frequency (> 1 Hz) provides a comprehensive view of atmospheric oxidative chemistry, particularly when sampling rapidly-evolving plumes from fast moving platforms like an aircraft. We present the sampling protocol, detection limits and observations from the first aircraft deployment for an instrument of this type, which took place aboard the NOAA WP-3D aircraft during the Southeast Nexus (SENEX) 2013 field campaign.

---

[*] Reprinted with permission from: Lee, B. H.*, Lopez-Hilfiker, F. D.*, Mohr, C., Kurtén, T., Worsnop, D. R. and Thornton, J. A.: An Iodide-Adduct High-Resolution Time-of-Flight Chemical-Ionization Mass Spectrometer: Application to Atmospheric Inorganic and Organic Compounds, Environ. Sci. Technol., 48(11), 6309–6317, doi:10.1021/es500362a, 2014.

*Equally Contributing Authors. Author contributions: B.H.L, F.D.L and J.A.T wrote the manuscript. F.D.L. and J.A.T. developed the ion chemistry for application to the HR-TOF-MS. F.D.L designed, built, and tested systems for and led the aircraft deployment.

2.1 INTRODUCTION

Observational capabilities for atmospheric gas-phase composition remain incomplete, with implications for the accurate simulation of air quality and climate change. Several aspects of oxidative processing and subsequent particle formation and growth remain to be tested or more fully explored with observations (Heard 2006, Finlayson-Pitts 2010, Pratt and Prather 2012). Broad classes of reactive trace gases such as radical intermediates, molecular halogens and oxygenated volatile organic compounds (oVOCs) remain analytical challenges (Finley and Saltzman 2006, Goldstein and Galbally 2007, Mao, Ren et al. 2012). Negative-ion chemical ionization mass spectrometry (CIMS) represents one general approach capable of quantifying various classes of oVOCs and inorganic radicals (Caldwell and Kebarle 1984, Caldwell, Masucci et al. 1989).

The general benefits of CIMS approaches include: 1) linearity and reproducibility, 2) minimal sample preparation and handling, allowing for the measurement of highly functionalized low-volatility or reactive compounds, 3) high sensitivity combined with selectivity, and 4) high time resolution. The drawbacks of CIMS for atmospheric measurements have generally been related to the stability of the resulting molecular analyte ions, that is, ionization-induced fragmentation, and an inability to resolve structural isomers or isobaric compounds at high time resolution. Protonated oVOC, for example, can undergo dehydration, decarboxylation, and/or denitrification among other pathways, with differing and often unknown efficiencies for a given instrument (e.g. de Gouw and Warneke 2007). While such fragmentation from chemical ionization is still relatively minimal compared to electron impact ionization, quantification and attribution quickly becomes subject to significant uncertainties when applied to a complex matrix such as ambient air. The use of tandem mass spectrometry (MS-MS) can help identify structures of the dominant ions at a nominal mass-to-charge ratio and therefore partly address the presence of isobaric contaminant ions, but signal-to-noise limitations can prevent continuous application (Spicer, Kenny et al. 1994, St Clair, McCabe et al. 2010).

Ion-molecule adduct formation is a chemical ionization pathway which provides the potential to achieve minimum fragmentation during ionization and thus preserve the parent molecule's

composition. Adducts with iodide and bromide ions have formed an important approach in recent years to measuring molecular halogens and halogen oxide radicals using quadrupole mass spectrometers (QMS) (Chu and Heron 1995, Osthoff, Roberts et al. 2008, Kercher, Riedel et al. 2009, Saltzman, De Bruyn et al. 2009, Thornton, Kercher et al. 2010, Liao, Sihler et al. 2011, Mielke, Furgeson et al. 2011, Riedel, Bertram et al. 2012). Ion adducts have also been applied to VOC measurements. Examples include the use of chloride (Cl^-) ions to detect carboxylic acids and aromatic chlorinated pesticides (Dougherty, Roberts et al. 1975, Tannenbaum, Roberts et al. 1975), and more recently CF_3O^- to detect hydroxy hydroperoxides, peroxy acids and hydroxynitrates (Crounse, McKinney et al. 2006, Paulot, Crounse et al. 2009, Beaver, St Clair et al. 2012). In laboratory settings, *McNeill et al*. (2007) applied Iodide-adducts to quantify carboxylic acids of atmospheric relevance with a QMS, although the propensity of Iodide to cluster with carboxylic acids had been known previously (Caldwell, Renneboog et al. 1989). The Iodide-adduct QMS technique was also used by *Le Breton et al.* (2012) to make airborne measurements of formic acid (CH_2O_2). And recently, adduct ionization utilizing $NO_3^-(HNO_3)_n$ and HSO_4^- ions was used to measure highly oxygenated organic molecules with a high-resolution time-of-flight chemical-ionization mass spectrometer (HR-ToF-CIMS) (Ehn, Kleist et al. 2012, Kulmala, Kontkanen et al. 2013). Each of these various ion adduct approaches has a different selectivity towards VOC or inorganics.

Iodide (I^-) is significantly electronegative and a very weak gas-phase base. Electron transfer and proton abstraction are essentially negligible except for a few atmospherically relevant compounds, such as nitrate (NO_3) radicals in the case of charge transfer, and sulfuric acid (H_2SO_4) in the case of proton abstraction. Adduct formation is typically only slightly exoergic, and thus fragmentation is minimal. I^- also has a large mass-to-charge ratio (m/Q = 126.905 Th) and one of the largest negative mass defects, δ_m (= m/Q − round(m/Q)), among abundant natural elements (δ_m = -0.096 Th). Combined with the mass resolving power and mass accuracy of current commercially available field-deployable HR-ToF-MS instruments (Tofwerk AG, Aerodyne Research Inc.), > 5000 and < 20 parts per million (ppm), respectively, (Junninen, Ehn et al. 2010, Yatavelli, Lopez-Hilfiker et al. 2012) the negative δ_m of Iodide provides an added degree of separation from other possible contaminant ions. This separation in turn provides

greater selectivity and lower detection limits *via* higher signal at an exact m/Q relative to possible background signals caused by non-isobaric compounds at that nominal m/Q.

In this paper, we demonstrate the capabilities of HR-ToF-CIMS using Iodide-adduct ionization for the detection of oVOCs, and select inorganic gases such as nitrogen oxides, and illustrate its in-field performance using measurements made aboard the NOAA WP-3D aircraft during the Southeast Nexus (SENEX) campaign in June-July of 2013.

2.2 Experimental Section

The instrument used herein is similar to that described previously, consisting of a reduced-pressure ion-molecule reaction (IMR) region (Yamdagni and Kebarle 1973, Bertram, Kimmel et al. 2011, Aljawhary, Lee et al. 2013), coupled to an atmospheric pressure interface HR-ToF-MS (Tofwerk AG, Thun, Switzerland) (Junninen, Ehn et al. 2010, Yatavelli, Lopez-Hilfiker et al. 2012, Mohr, Lopez-Hilfiker et al. 2013). A schematic is shown in the Supplemental Information (SI, Figure S1). As such, we briefly review updated components and focus on the Iodide-adduct HR-ToF-CIMS sensitivity to a suite of oVOCs and its deployment on an aircraft.

2.2.1 *Ionization, Ion transmission and Data Acquisition.*

A detailed schematic of the front-end interface between the aircraft sampling inlet and IMR is shown in the SI (Figure S2). Ambient air is drawn through a critical orifice at 2.0 standard liters per minute (slpm) into the IMR, which is held at 90 mbar by means of a scroll pump (Agilent IDP3) and a custom servo-controlled vacuum valve used to continuously regulate pumping speed. The pressure varies by < 1% even as ambient pressure changes by factors of 5. The IMR temperature is controlled to within 0.2°C at a setpoint between ambient and 40°C depending upon application. Up to two commercial radioactive ion sources (Po-210, 10 mCi, NRD) oriented 90° apart and orthogonal to the ion-molecule reaction mixture flow can be used for switching between positive and negative reagent ions (Mohr, Lopez-Hilfiker et al. 2013). The IMR also contains a diffusion cell to continuously deliver calibration compounds for converting measured ion flight times into m/Q. As demonstrated below, Iodide-adduct ionization typically

provides useful internal ions for calibrating the m/Q scale without the need for additional calibration compounds.

Iodide ions are generated by passing a 2 slpm flow of ultra-high purity (UHP) N_2 over a permeation tube filled with methyl iodide and then through the Po-210 ion source into the IMR. The ionizer and sample flows mix and interact for ~120 ms until a fraction is sampled through an orifice into a 4-stage differentially pumped chamber housing the HR-ToF-MS (Junninen, Ehn et al. 2010). The first stage is held at 2 mbar by a molecular drag pump (Alcatel MDP 5011), and the second stage is held at 0.01 mbar by a split-flow turbo molecular pump (Pfeiffer). Two quadrupole ion guides transmit the ions through these two stages while providing collisional cooling and thus energetic homogenization of the ions as they enter the third "extractor" region. In the third and final stages, additional optics further focus the ions prior to being orthogonally pulsed at 22.22 kHz into the drift region where their arrival time after a V-mode trajectory is detected with a pair of microchannel plate detectors (Photonis Inc., U.S.A.).

The axial electric field strengths (< 1 V/cm) in the first two stages are set to simultaneously optimize the total ion signal and the transmission of Iodide-adducts. Optimization is obtained by maximizing the ratio of $I(H_2O)^-/I^-$ at a constant water vapor pressure in the IMR. It is possible to "tune" the selectivity of the instrument towards adducts with binding energies greater than that of $I(H_2O)^-/I^-$. Using previously determined thermodynamic values for Iodide water monomer adducts (National Institute of Standards and Technology (U.S.) , Caldwell and Kebarle 1984, Caldwell, Masucci et al. 1989), it is clear that a significant fraction of these adducts are lost due to collision-induced declustering during transit from the IMR through the system (see SI).

The data acquisition procedures of this instrument have been described elsewhere in detail (Junninen, Ehn et al. 2010, Bertram, Kimmel et al. 2011). We have altered some aspects of this process for integration onto an aircraft. A standard laptop computer is used for instrument control and data acquisition, communicating with the acquisition and timing cards (AP240 and NI6320) via an external custom-built PCI box that allows data acquisition at ambient temperatures exceeding 40°C. Additionally, at a chosen time interval (typically hourly) the temperature-dependent baseline of the AP240 acquisition card is determined in order to avoid

unnecessarily rejecting small ion signals. The current version of the instrument, complete with pumps, draws < 900 W of power, fits entirely within a 42×60×81 cm rack, and weighs 140 kg; it has been operated unattended for hours to days at a time in aircraft, ground-based trailers and on sampling towers.

2.2.2 *In-flight sampling, calibration and background determinations.*

Minimizing sampling losses of low volatility species is a priority. Ambient air is drawn at 22 slpm through a 72 cm long 1.6 cm inner diameter polytetrafluoroethylene (PTFE) tubing by a dedicated scroll pump (Agilent IDP3). The first 25 cm of the inlet tube is housed in an aerodynamic winglet that extends outside of the boundary layer of the WP-3D aircraft (Figure S2). We estimate an inlet residence time of approximately 0.4 s at 1013 hPa while maintaining laminar flow (Re ~1900). A small fraction of the centerline flow (2 slpm) is sampled through a conical-shaped critical orifice into the IMR, while the remainder is exhausted through four radially symmetric ports located downstream and around the raised sampling orifice. The inlet is heated to 40°C to minimize condensation on the tubing surface and to maintain a constant sampling environment under rapidly evolving outside and cabin conditions. Additional details are provided in the SI.

The instrument background signal is established by routinely introducing dry UHP N_2 directly in front of the critical orifice to displace the incoming ambient air. This addition is achieved by a servo-controlled, 7 cm (2.8 inch) long 0.3 cm (1/8 inch) diameter stainless steel probe that when actuated, enters from the side of the inlet at a 45° angle and is positioned directly upstream of, but not in contact with, the sampling cone. Ambient air is rejected from the IMR by overblowing the sampling orifice with N_2 (~3 slpm). When not in use, the probe is retracted so that it resides outside of the sample streamline (Figure S2). Traditional methods of scrubbing ambient air with a heated catalyst and/or chemical scrubbers were tested in the laboratory but lacked sufficient reproducibility and/or selectivity across the full m/Q scale to merit incorporation into short flight measurements. The humidity dependent partitioning of semivolatiles to surfaces is a confounding factor in the chosen approach. Instrument sensitivity dependence on water vapor pressure (discussed below) is accounted for, but given that the sensitivity for most organic compounds is

higher in dry air, the measured background is more than likely an upper limit (Figure S3). UHP N_2 humidified to ambient levels will be used for background signal subtraction in future campaigns.

The stability of the instrument is determined by continuously delivering ^{13}C-labeled formic acid, $^{13}CH_2O_2$, through a 30 gauge 1.5 cm long needle bored through the PTFE inlet near the inlet entrance. The $^{13}CH_2O_2$ (Cambridge Isotopes) was contained in a custom-built PTFE permeation tube, held at constant temperature (40°C) and pressure. The permeation rate was determined gravimetrically and compared to independently verified $^{12}CH_2O_2$ permeation tubes (KIN-TEK). Any drift in the instrument sensitivity measured by the $I(^{13}CH_2O_2)^-$ ion signal, not due to ambient water vapor (see below), is similarly applied to all other species using relative sensitivities which have been determined in the laboratory.

2.3 Results and Discussion

General Spectrometer Performance and Mass Spectral Analysis. To introduce the ion chemistry and mass spectral analysis, an Iodide-adduct ionization spectrum observed during a SENEX flight is presented in Figure 1a. Iodide-adduct mass spectra contain several known single-ion peaks (*e.g.* I^-, IO^-, $I(H_2O)^-$, IO_2^-, $I(CH_2O_2)^-$, IO_3^-, $I(HNO_3)^-$, I_2^-, I_3^-), which are utilized to convert measured ion time-of-flight to mass-to-charge (m/Q, Th), and to determine the resolution and non-Gaussian ion peak shape using modified Toftools software from the University of Helsinki (Junninen, Ehn et al. 2010). During SENEX, the absolute in-flight deviation of the assigned m/Q from their corresponding fitted curve is typically ±5 ppm (2σ), well within the manufacturer's stated mass accuracy of ± 20 ppm.

The mass accuracy and resolving power can be used to separately quantify two compounds with the same nominal m/Q at high time-resolution. Figure 1b shows a time series and high-resolution mass spectra of ions with a nominal m/Q of 201 Th recorded during a nighttime flight over the Southeastern U.S. High resolution peak fitting requires two distinct ion compositions at that nominal m/Q: $I(C_2H_2O_3)^-$, the glyoxylic acid adduct, and $I(C_3H_6O_2)^-$, propionic acid or

hydroxyacetone adducts. These two ion signals display dramatically different behavior as the aircraft flies through biomass burning plumes, illustrating the enhanced capability for attribution and detection provided by the instrument's mass resolving power and mass accuracy.

The above capabilities coupled to Iodide adduct ionization allow for additional insights into composition. Figure 2a contains the mass defect (δ_m) plotted versus the nominal m/Q of an Iodide ionization spectrum obtained during an α-pinene ozonolysis experiment using a steady state 0.75 m^3 PTFE chamber at the University of Washington (UW chamber). Ions that contain Iodide (dark green with orange edge) generally have a negative or small positive δ_m, whereas those without (light green) have a positive δ_m, thereby creating an "Iodide Valley" separating compounds in m/Q space that cluster with Iodide from those that do not. Such additional information is not possible with charge transfer or proton transfer ionization schemes.

This space illustrates the multitude of byproducts observed during α-pinene ozonolysis. The δ_m of an ion increases with m/Q for each additional -CH_2 (Figure 2a, green line), whereas an additional oxygen atom yields a compound with a more negative δ_m (Figure 2a, red line). The row-like arrangement along the latter plane represents a loss of two hydrogen atoms for every oxygen atom added (gain of degree of unsaturation) for a given number of carbon atoms. Iodide-adduct ionization of a compound with a halogen atom will be shifted even further towards negative δ_m (Iodine more so than Bromine followed by Chlorine than Fluorine), a distinguishing feature of this class of compounds, suggesting that molecular halogen adducts with Iodide will be entirely separable in mass space from a range of possible interferences. This is evident in the δ_m versus m/Q plane associated with I^-, I_2^- and I_3^- (Figure 2a, orange line), the latter two of which are common but minor constituents of an Iodide-adduct ionization mass spectrum.

The compositions of organic anions lacking an Iodide (light green dots) typically involve an odd number of hydrogen atoms, at least 2 oxygen atoms and at least 1 degree of unsaturation, consistent with carboxylate anions. Additions of peroxyacetic acid (Sigma Aldrich) and peroxypropionic acid (synthesized according to *Phillips et al.* (1958)) yielded carboxylate signal levels that were comparable to that of the peroxyacid Iodide-adduct (Figure 2b). In contrast, additions of carboxylic acids, with a range of functionalities, never produced signal levels of the

carboxylate anion above 0.1% of the corresponding Iodide-adduct. Indeed, scanning the electric field strength within the instrument induces decomposition of the peroxyacid-Iodide adducts into the corresponding carboxylate anion (Figure 2b), providing a potential means of identifying these isomers by both the persistence of the cluster ion (see also Figure S5) and the correlated appearance, or lack thereof, of product ions. Thus, many of the organic anions lacking an Iodide are likely from a reaction between I^- and peroxy acids, RC(O)OOH, as shown by *Phillips et al.* (2013), or other peroxides. Secondary ion chemistry involving, *e.g.*, proton abstraction ionization by acetate ions (Veres, Roberts et al. 2008), also cannot be ruled out. Regardless, this type of complexity encourages use of a "labeling" reagent ion such as Iodide-adducts to allow separation and/or identification of such processes.

2.3.1 *Sensitivity to Oxygenated VOC.*

We have quantified the sensitivity of the Iodide-adduct HR-ToF-CIMS to several oVOCs and inorganic compounds. The response to a given compound is linear for atmospherically relevant concentrations (see Figures S6 and S7). In Table S1 (SI) and below we report sensitivities normalized to a million total reagent ion [$I^- + I(H_2O)^-$] counts per second (cps), which can vary from instrument to instrument and over time as the ion source degrades. These normalized sensitivity values depend on instrument parameters, including inlet and IMR temperature and pressures, and electric fields, which determine the m/Q transmission efficiency and declustering strength. Water vapor pressure can also affect sensitivities, as discussed in the next section. Consequently, the absolute values presented in Table S1 are specific to our instrument, which has been tuned to optimize the signal of $I(H_2O)^-$ (see SI), the thermodynamics of which are well understood (Figure S4) (Caldwell and Kebarle 1984, Caldwell, Masucci et al. 1989). The trends presented will likely be consistent between different instruments, assuming they are similarly optimized.

Calibrations are conducted using a range of methods. In one approach, a solution of the compounds is prepared at known concentrations in acetone (HPLC grade, Fischer Scientific). Between 1 and 20 μL of the solution is injected onto a PTFE filter using a microliter syringe (Hamilton). The filter sits within a PTFE manifold 0.25 cm upstream of the critical orifice to the

IMR. UHP N_2 gas that is continuously passed over the filter is slowly heated to 200°C until the signal returns to pre-injection levels. Integration of the signal and the mass injected allow a determination of the sensitivity. Injections are repeated several times to ensure repeatability, but may be biased low due to surface losses or degradation in solution. Calibration to very low volatility compounds is especially challenging given that thermal decomposition is possible prior to desorption from the filter (Lopez-Hilfiker, Mohr et al. 2013), and that Iodide-adducts are also subject to thermal decomposition at higher temperatures. The IMR on the current system is maintained at a constant temperature, so this latter effect is dampened, but both ultimately lead to lower limits to sensitivity values for compounds found predominantly in the condensed phase. A second approach uses calibrated permeation devices for formic, acetic, propionic, and nitric acids, the outputs of which were determined gravimetrically. The consistency between the solution injection and permeation device methods was confirmed by acetic, propionic and nitric acids for which both methods were possible. We also use a vapor pressure based delivery method, with catalytic conversion and subsequent optical measurement of carbon dioxide (CO_2) co-located at the inlet to the HR-ToF-CIMS (see SI).

The sensitivity of the Iodide-adduct HR-ToF-CIMS to a compound depends upon its polarity and hydrogen bonding capability, and is strongly influenced by molecular geometry and steric factors. The method is not sensitive to mono-alcohols, mono-ketones or mono-aldehydes, with sensitivity values falling below 0.1 cps $pptv^{-1}$, and is completely insensitive to non-oxygenated VOCs, due to their weak polarity and H-bonding, resulting in low binding energies with the I^- (Yamdagni and Kebarle 1973, Caldwell, Renneboog et al. 1989). For organic compounds, a single acid group can provide the necessary binding energy to sensitively detect such compounds in the atmosphere, but an acid group is not required for high sensitivity. Sensitivity generally increases with the addition of a polar functional group such as keto-, hydroxy- and acid groups, in that order.

An example of sensitivity dependence on functional group is shown in Figure 3a for C_3 compounds (blue). The sensitivity to the mono-acid (propionic acid, $C_3H_6O_2$), 6.6×10^{-2} counts s^{-1} ppt^{-1}, is less than that for the keto-mono-acid (pyrvuvic acid, $C_3H_4O_3$), which is less sensitively detected than the hydroxy-mono-acid (lactic acid, $C_3H_6O_3$) and di-acid (malonic acid, $C_3H_4O_4$),

3.5×10^{-1}, 1.6 and 19 counts s^{-1} ppt^{-1}, respectively. The presence of a C=C double bond, as in the case of acrylic acid ($C_3H_4O_2$), compared to propionic acid does not appear to significantly alter the sensitivity. Moreover, though hydroxyacetone ($C_3H_6O_2$) and propionic acid are structural isomers, the former is not sensitively detected, 9.9×10^{-3} counts s^{-1} ppt^{-1}, consistent with carboxylic acids being better H-bonding donors than alcohols. In addition to the dependence on functional group, the sensitivity increases with mass-to-charge ratio, as shown in Figure 3a for mono-acids (red) and keto-mono-acids (cyan). This trend is attributed to the stability gained by the added vibrational modes over which to distribute excess energy for a larger molecule clustered to Iodide (see SI).

The enhancement in sensitivity provided by a second functional group is dependent on its location relative to the first. For instance, the instrument is particularly sensitive to specific isomers of isoprene hydroxy nitrate ($C_5H_9O_4N$) (Lee, Teng et al. 2014), namely, the β-4-hydroxy-3-nitrate and the *cis*-δ-1-hydroxy-4-nitrate. In contrast, it is not at all sensitive to the *trans*-δ-1-hydroxy-4-nitrate. These findings indicate that compounds containing hydroxyl and nitrate ($-ONO_2$) functional groups but without an acid group can be sensitively detected as Iodide adducts, but that both functional groups need to be accessible by Iodide to provide the necessary adduct stability required for efficient transmission to the time-of-flight region. In a similar way, though the instrument is minimally sensitive to most di-hydroxy and di-keto compounds, *cis*-2-butene-1,4-diol is an exception (Table S1), presumably due to the 1,4 placement of the two hydroxy groups and the *cis*- structure, which make the functional groups readily available to I^-.

The sensitivity to di-acids (Figure 3a, green) is highest amongst all tested functional groups and is largely independent of m/Q. This feature is likely the result of the stability of the di-acid Iodide-adduct allowing it to be transmitted through the system with minimal declustering. The observed sensitivity range of di-acids is about 10 to 15% of the maximum allowable sensitivity, calculated assuming the adduct ions are formed at the kinetic limit with no subsequent losses. Not all di-acids, however, are sensitively detected as an Iodide-adduct, as steric hindrance and geometry can affect the Iodide-adduct reaction yield and/or the binding energy. Sensitivity to oxalic ($C_2H_2O_4$) and phthalic ($C_8H_6O_4$) acids is much lower than the other tested di-acids, presumably due to the rigid structure and close proximity of the two hydroxy groups leading to

H-bonding, thus limiting access to Iodide. Similarly, the sensitivity to methacrylic acid ($C_4H_6O_2$) is much lower than acrylic ($C_3H_4O_2$) and propionic ($C_3H_6O_2$) acids, due likely to steric hindrance imparted by the $-CH_2$ or $-CH_3$ group adjacent to the carbonyl carbon.

The limit of detection for a given compound is determined by the signal (S) rate relative to the instrument background (B) count rate. Assuming the background count rate is the ion signal measured when the IMR inlet is overflowed with UHP N_2, we define the detection limit as the concentration which yields a S/B ratio of 3 in a 15-second integration time (Bertram, Kimmel et al. 2011). Corresponding average detection limits for a range of compounds measured during SENEX are listed in Table S1. For species with sensitivities >1 cps ppt^{-1}, detection limits are better than 17 ppt, and several are < 1 ppt.

Determining the sensitivity to other functional groups and molecular structures is part of an ongoing effort. For example, Table S1 shows that the instrument is also highly sensitive to some inorganic acids and molecular halogen compounds, as expected from the previous work using QMS and Iodide adduct ionization (Wolfe, Thornton et al. 2009, Riedel, Bertram et al. 2012). Moreover, it is plausible that manipulation of the electric fields used to transmit ions to the time-of-flight region, either in real time or prior to a measurement, can further enhance the selectivity of the instrument by utilizing differences in adduct binding energies (*e.g.* Figures 2b and S5).

2.3.2 *The Effect of Ambient Water Vapor on Ionization Efficiency.*

The efficiency of Iodide-adduct ionization, and thus the inferred sensitivity, is affected by the presence of water vapor (Slusher, Huey et al. 2004, Kercher, Riedel et al. 2009). The sensitivity to a given compound will depend, in part, on whether water vapor competes with the Iodide ion, thereby lowering the sensitivity, or whether the presence of water vapor provides a third body to stabilize the Iodide-analyte cluster by carrying away excess energy from the collision, thereby increasing the sensitivity. Alternatively, if a compound forms a very stable complex with Iodide, and/or has enough internal vibrational modes to distribute excess energy from the collision complex, it may have an adduct formation efficiency that is independent of water vapor. While

all of these possible effects are observed, we find the dominant effect of water vapor across the vast majority of organic compounds studied is to lower the sensitivity.

The I^- ion clustered with formic acid (CH_2O_2) is a good example of an adduct for which the competing influences of H_2O are exhibited, shown in Figure 3b (black). At low water vapor pressures in the IMR (P_{H2O}), the sensitivity to formic acid increases with increasing P_{H2O}, reaches maximum sensitivity around 0.2 mbar, then decreases with further increase in P_{H2O}. Computational results discussed in the SI indicate that reaction of CH_2O_2 with $I(H_2O)^-$ is less favorable than reaction with I^-. Therefore, the observed enhancing effect of water vapor pressure is a kinetic rather than a thermodynamic effect. That is, water molecules provide a third body to stabilize the Iodide-analyte cluster by distributing the excess energy over a greater number of vibrational modes, and carrying away excess energy from the ion-molecule collision leading to increased sensitivity, at least at low P_{H2O}. At high P_{H2O}, it appears that the kinetic enhancement is not enough to compensate for the additional competition of water for the Iodide ions, and $I(CH_2O_2)^-$ formation decreases with further increases in P_{H2O}.

We can estimate the maximum size of molecules for which enhancement of adduct formation by $I(H_2O)^-$ is important assuming binding energies and mean frequencies roughly similar to those of $I(CH_2O_2)^-$. Using quantum Rice-Ramsberger-Kassel (QRRK) theory (Rice and Ramsperger 1927, Kassel 1928, Dean 1985) we estimate ion-molecule cluster dissociation rates, which are strongly dependent upon the number of accessible vibrational modes (*s*) within the cluster (see SI). The predicted cluster decay rate becomes equal to the ion-molecule collision rate (at 90 mbar total pressure) for *s* of 8 to 9. Using the rule of thumb that *s* corresponds to half the total number of modes (Laidler 1987), then molecules with 5 atoms or less will demonstrate an enhancement in Iodide adduct formation with increasing water vapor pressure, while molecules with > 8 atoms will not do so (at least not for kinetic reasons).

Figure 3b presents experimental data consistent with the above theoretical guidelines. Using a dual-port inlet to minimize the effects of humidity dependent gas-surface partitioning (see SI), we find most oVOCs exhibit either a negative or negligible dependence on water vapor pressure. Di-acids are the exception, the sensitivity to which tends to increase slightly with water vapor

pressure for reasons yet to be determined. Molecular chlorine (Cl_2) and bromine (Br_2) exhibit increasing sensitivities as a function of water vapor pressure (Figure S8), as expected from the above. Containing 3 total atoms as adducts, the third-body effect due to the presence of water vapor outweighs the competition of water vapor for I^- over the range of P_{H2O} studied. Similar effects of water vapor have been reported for Iodide detection of other halogens and the peroxyacetyl radical, which have < 8 atoms (Slusher, Huey et al. 2004, Kercher, Riedel et al. 2009). The water vapor pressure dependence for a range of other compounds detected as Iodide adducts is shown in Figures S9 and S10. The effect generally weakens as the atom number and oxygen and hydrogen content of the compound increases, consistent with an expected increase in the binding energy with Iodide for more polar compounds.

The HR-ToF-CIMS instrument has a continuous measure of water vapor in the ratio of $I(H_2O)^-/I^-$, see Figure S11, which can be used to account for changes in sensitivity when independent measures of water vapor are lacking (see SI). Moreover, continuous dilution with dry UHP N_2 or addition of water vapor to the ion source flow, can be used to suppress the actual vapor pressure of water in the IMR or the effects of atmospheric variability.

2.3.3 *Applications to studies of the ambient atmosphere.*

The I^- adduct HR-ToF-CIMS was deployed aboard the NOAA WP-3D aircraft as part of the Southeast Nexus (SENEX) campaign, based out of Smyrna, TN, during June and July of 2013. Boundary layer measurements in the Southeast U.S. were obtained over a span of nearly 125 flight hours under day and nighttime conditions, encountering a mixture of biogenic, urban, gas fields, power generation and biomass burning emissions. The HR-ToF-CIMS provided simultaneous high-time resolution observations of a suite of oVOCs as well as select inorganic compounds.

Figure 4a shows part of the flight path colored by the mixing ratio of $C_4H_7O_5NI^-$ near Atlanta, GA (33.755°N, 84.390°W) on June 12th. An urban influence is clearly evident as the aircraft repeatedly intersects the Atlanta plume over and downwind of the city. The signal for $C_4H_7O_5NI^-$ increases within the urban plume – while the signal for a few others, notably

$C_5H_{10}O_3I^-$, simultaneously decreases (Figure 4b). In the urban plume, which contains elevated levels of nitrogen oxides due to combustion, the dominant fate of organic peroxy radicals formed from the photo-oxidation of VOC such as isoprene will be reaction with nitric oxide (NO) to form organic nitrates and other products (Horowitz, Liang et al. 1998, Paulot, Crounse et al. 2009). Outside the plume, the dominant fate will likely be formation of organic hydroperoxides from reaction with the hydroperoxy radical (HO_2) (Crutzen, Williams et al. 2000, Paulot, Crounse et al. 2009). Based on our sensitivity to functionalities discussed above, the C_4 and C_5 compounds shown in Figure 4 likely correspond to a hydroxy nitrate and hydroxy hydroperoxide or the derivative epoxide of isoprene. In addition to $C_5H_{10}O_3I^-$, the signals for only a few others (highlighted in Figure 4c) decrease within urban plumes, while most others increase. We have tentatively assigned elemental formulae for each ion peak shown in this spectrum. Sensitive and simultaneous detection of a suite of compounds in these rapidly changing chemical environments provides a comprehensive set of constraints on the cascade of oxidation products of biogenic VOCs, and the influence of anthropogenic emissions, temperature and sunlight.

Figure 4d shows the full flight path for a nighttime flight on July 2-3, colored and sized by the dinitrogen pentoxide, N_2O_5, mixing ratio measured with the instrument. In contrast to plumes emitted from cities (Figures 4a-c), those intercepted on this night are much narrower given their localized sources and weaker turbulent dispersion during nighttime. Figure 4e shows a brief time-series in which distinct plumes co-located in space but of different origin are sampled. A biomass burning plume – characterized by high levels of a phenolic compound, major constituents of biomass burning (Mohr, Lopez-Hilfiker et al. 2013, Yee, Kautzman et al. 2013) – is sampled immediately before encountering a power plant plume – which due to its relatively high combustion efficiency is devoid of VOC but enriched in SO_x and NO_x. These conditions result in the production of N_2O_5 and subsequently nitryl chloride, $ClNO_2$, whereas in the VOC-rich biomass burning plumes the formation of N_2O_5 is presumably suppressed by the rapid reaction of its precursor, the nitrate radical, with VOCs. In addition to $C_7H_8O_2I^-$, the signal for numerous other C_6, C_7 and C_8 species are enhanced in these biomass burning plumes that have elemental formulae consistent with the presence of a phenyl group (Figure 4f).

The deployment on the NOAA WP-3D is the first for a HR-ToF-CIMS of its kind. These observations, though they represent only a subset of the data collected with this instrument during SENEX, illustrate the value of acquiring highly resolved mass spectra across a large m/Q range at high time-resolution when sampling a complex matrix such as ambient air where the type of compounds or locations that may be important are not necessarily known *a priori*. Using Iodide-adduct ionization we were able to detect a suite of aliphatic and aromatic oVOCs and alkyl nitrates derived from various directly-emitted biogenic VOC (*i.e.* isoprene, 2-methyl-3-buten-2-ol, monoterpenes, *etc.*), as well as select inorganic species, all at the same time resolution (1 Hz), allowing for the characterization of air masses on small spatial scales from a rapidly moving platform. These capabilities will help determine the air quality and climate impacts of urban and industrial emissions in this region dominated by forests. To fully realize the potential of this instrument requires continued characterization and optimization of the selectivity and sensitivity of the Iodide-adduction ionization technique, *e.g.*, by utilizing differences in binding and/or reaction energies to allow separation of isomers containing different functional groups (see SI).

2.4 SUPPLEMENTAL INFORMATION

2.4.1 *HR-ToF-CIMS optimization and Reagent Ion Water Cluster Distribution.*

The adduct-ion signals are optimized by using electric fields between the IMR and time-of-flight region that are as weak as possible to minimize collisional declustering without sacrificing total ion transmission. We optimize the HR-ToF-CIMS for transmission of Iodide adducts using $I(H_2O)^-$ as a metric. The thermodynamics of this adduct ion are reasonably well known and the signal for $I(H_2O)^-$ is usually abundant because water vapor is ubiquitous in the lower troposphere. Compared to predictions using published thermodynamic data (National Institute of Standards and Technology (U.S.)), the distribution of Iodide water clusters, $I(H_2O)_n^-$, measured by the HR-ToF-CIMS in humid ambient air is shifted more towards n = 0 and 1 clusters, with some n = 2 detected, while n = 3 is not detected even at the highest water vapor concentrations where the predicted distribution is dominated by the n = 2 and n = 3 clusters (Figure S4a). In addition to evaporation of water from $I(H_2O)^-$ and $I(H_2O)_2^-$ clusters during transmission to the time-of-flight region, the RF voltage on the first quadrupole ion guide, and residual electric fields

after the first quadrupole lead to active declustering. With the first quadrupole ion guide radiofrequency (RF) potential switched off (Figure S4b), there is better agreement with the model, indicating that the focusing effect of the RF field leads to declustering, and is a major cause of the discrepancy between modeled and measured I^- hydrates. However, when the RF potential is turned off the ion transmission decreases by approximately a factor of ten. Future versions will allow finer tuning of the peak-to-peak RF amplitude to maintain some focusing but with less declustering as we have done in previous QMS instruments (McNeill, Wolfe et al. 2007, Kercher, Riedel et al. 2009, Lopez-Hilfiker, Constantin et al. 2012). The remaining discrepancy between predicted and observed trends, with the RF off is presumably due to evaporative losses. Preservation of a significant fraction of the $I(H_2O)^-$ in the HR-ToF-CIMS suggests that I^- adducts having a binding energy greater than that of $I(H_2O)^-$, which includes molecular halogens, inorganic and carboxylic acids and presumably other organic compounds with H-bonding capability, will be detectable by this method.

2.4.2 *Quantum chemical calculations.*

We use quantum Rice-Ramsberger-Kassel (QRRK) theory (Rice and Ramsperger 1927, Kassel 1928, Dean 1985) to model the effect of water vapor pressure on sensitivity, discussed below. QRRK theory treats a molecule (or in this case a cluster) as a collection of *s* harmonic oscillators with an identical frequency ν (estimated as the geometric mean of the vibrational normal modes). All energies are expressed as integer quanta of hν, where h is the Planck constant. The required parameters are the total thermal energy of the system, *j*, and the energy required for the decay or dissociation reaction, *m*. For cluster dissociation reactions, *m* is simply the cluster binding energy (see *e.g.* (Kurten, Kuang et al. 2010) for an application to atmospheric clusters). The unimolecular decay rate coefficient is then:

$$k_{decay} = \nu \frac{j!(j-m+s-1)!}{(j-m)!(j+s-1)!} \quad \text{(E5)}$$

This decay rate can be compared to the collision rate of bath gas molecules with the cluster. If the decay rate is much larger than the collision rate, most of the nascently formed clusters will decompose before being collisionally stabilized. If the decay rate is much smaller than the

collision rate, the opposite applies: almost all clusters will be stabilized. Gas molecules (mainly N_2 and O_2) likely collide with I^- - analyte clusters such as $I(CH_2O_2)^-$ or $I(N_2O_5)^-$ with a typical ion-molecule collision rate coefficient on the order of 1×10^{-9} cm^3 $molecules^{-1}$ s^{-1}. At room temperature and an instrumental pressure of 90 mbar, this corresponds to a net collision rate of about 2×10^9 s^{-1}.

Two separate quantum chemical calculations were conducted to obtain reasonable values for the parameters in Equation 1 for $I(CH_2O_2)^-$. All calculations were performed using the Gaussian 09 program suite (Frisch, Trucks et al. 2009)with default convergence criteria and standard approximations (*e.g.* rigid rotor and harmonic oscillator). For calculations involving Iodine atoms, we employed the relativistic pseudopotentials developed by *Peterson et al.* (2003) for use with the aug-cc-pVDZ and aug-cc-pVTZ basis sets. Table S2 lists the computed reaction energetics.

At the CCSD(T)/aug-cc-pVTZ-PP//MP2/aug-cc-pVDZ-PP level, the binding enthalpy of the $I(CH_2O_2)^-$ cluster is 25.46 kcal/mol (or 8940.8 cm^{-1} if expressed in wavenumbers). The combined thermal energy of the isolated CH_2O_2 and I^- molecules (excluding the vibrational zero-point energy of CH_2O_2) at 298.15 K is 2.93 kcal/mol. The total thermal (translational, rotational and vibrational) energy of the newly formed $I(CH_2O_2)^-$ cluster before any thermalizing collisions have occurred is thus the sum of these two terms: 28.39 kcal/mol (9930.7 cm^{-1}). The geometric mean of the vibrational frequencies of the cluster is 2.34×10^{13} s^{-1} (780.6 cm^{-1}). We thus obtain:

$\nu = 2.34\times10^{13}$ s^{-1}
$m = 8940.8$ $cm^{-1}/780.6$ $cm^- \approx 11$
$j = 9930.7$ $cm^{-1}/780.6$ $cm^- \approx 12$

The remaining parameter in equation 1 is *s*, the number of accessible vibrational modes. The total number of vibrational modes of a polyatomic non-linear molecule or cluster with *N* atoms is 3*N*-6, or 12 for the case of $I(CH_2O_2)^-$. Inserting $s = 12$ into equation 1 yields a decay rate of 2×10^8 s^{-1}. However, all 12 modes are unlikely to be accessible for dissipation of excess energy.

A common rule of thumb in chemical kinetics (Laidler 1987) is that the value of *s* used in QRRK calculations should be roughly half of the total number of modes. With $s = 6$, the decay rate predicted by equation 1 is around 2×10^{10} s^{-1}. Since this is about an order of magnitude higher than the collision rate with bath gas molecules, we can conclude that under dry conditions energy non-accommodation significantly decreases the net formation rate of $I(CH_2O_2)^-$. In other words, the majority of newly formed clusters decay back to the reactants before being thermalized.

If the I^- ion is clustered with water when it collides with CH_2O_2, the probability that the resulting cluster is collisionally stabilized increases significantly. This enhancement occurs due to two reasons. First, the presence of the water molecule increases the total number of vibrational modes of the cluster from 12 to 21. In terms of the QRRK decay rate computed by assuming that *s* is half of the total number of modes, this effect outweighs the decrease in the $[I(H_2O)^- - CH_2O_2]$ binding energy compared to $[I^- - CH_2O_2]$. Second, and perhaps more importantly, the cluster with water vapor has a second dissociation route available: $I(CH_2O_2)(H_2O)^- \Leftrightarrow I(CH_2O_2)^- + H_2O$. At the MP2/aug-cc-pVDZ-PP level, the enthalpy of this reaction is 9.1 kcal/mol, implying that the reaction will occur very rapidly, and certainly much faster than dissociation back to $I^-(H_2O)$ and CH_2O_2, which requires 22.5 kcal/mol. We applied Equation 5 to the $I(CH_2O_2)(H_2O)^-$ cluster, assuming it forms from $I(H_2O)^- + CH_2O_2$, yielding a total thermal energy of about 25 kcal/mol, but requiring only 9 kcal/mol to dissociate into $I(CH_2O_2)^- + H_2O$. This resulted in a rate of about 10^{12} s^{-1} for H_2O evaporation, implying that it will occur much faster than collisional stabilization. After evaporating a water molecule, the remaining $I(CH_2O_2)^-$ cluster no longer has enough energy to dissociate, and is therefore effectively stabilized.

This effect explains why the CH_2O_2 detection efficiency increases with water vapor pressure at low humidity levels. However, since one water molecule is enough to ensure complete stabilization of $I(CH_2O_2)^-$ by the above mechanism, further hydration will not provide any additional enhancement. Instead, additional water molecules will slightly hinder $I^- - CH_2O_2$ adduct formation, as the clustering reaction becomes thermodynamically less favorable, consistent with the observed decrease in formic acid sensitivity at high water vapor pressure (Figure 3b).

2.4.3 *In-field sampling and Water Vapor Pressure Dependence Correction.*

The mass flowrate into the IMR depends on altitude. We use the measured ambient pressure and known size of the critical orifice to correct for the resulting changes in the relative dilution and residence time in the IMR. The total mass flowrate through the inlet also continuously decreases with altitude, from 22 slpm near the surface to 9 slpm at 6 km. With the simultaneous drop in ambient pressure, the residence time changes by < 20% to 0.5 seconds (Figure S13). Given the sampling conditions described here, we expect minimal contribution from the evaporation of aerosols. An explicit kinetic calculation of evaporation timescales has not yet been done for this specific setup. However, we have conducted such calculations for a warmer IMR in the study by *Lopez-Hilfiker et al.* (Lopez-Hilfiker, Mohr et al. 2014).

Because sensitivity is influenced by ambient water vapor pressure (Figure 3b, Figures S8-10), we individually correct the measured signal by the known P_{H2O} dependence for each species to obtain mixing ratios. For species whose P_{H2O} dependencies have not been directly measured, we use one that is inferred from observed trends of similar compounds. For most field and laboratory campaigns, we use measured water vapor pressure to correct for the sensitivity dependence on water vapor pressure. But the relationship between water vapor pressure and $I(H_2O)^-/I^-$ ratio has been well characterized and is reproducible. Figure S11 shows the average $I(H_2O)^-/I^-$ measured during of 12 SENEX flights (black) and in the laboratory (red), as a function of water vapor mixing ratio. Figure S14 shows a time series of ^{13}C formic acid signal during a typical flight during SENEX that is uncorrected (blue) and corrected (magenta) for water vapor pressure dependence.

2.4.4 *Calibration.*

One method by which the HR-ToF-CIMS is calibrated is VOC conversion by heated (350°C) palladium catalyst and subsequent measurement of CO_2 by a non-dispersive infrared analyzer (LI-COR, LI-820), similar to the method presented by *Veres et al.* (Veres, Gilman et al. 2010). The VOC source is generated in zero-air and split into two flows. One flow is directed to the heated catalyst to obtain the total carbon mixing ratio. The other flow is directed to the HR-ToF-

CIMS inlet, which allows dynamic dilution by about a factor of 20. For VOC sources that are liquid at room temperature, flowing zero-air over the headspace typically generates sufficient levels of vapor pressure. For sources that are solids at room temperature, a steady source of vapor pressure is generated by trapping the chemical solids between two particle filters housed in a PFA particle filter holder. Tubing – kept short to minimize response time and surface losses – were PTFE, all except for the portion that housed the heated palladium catalyst (stainless steel).

The permeation device method is typically preferred, given its portability and ease of use. However, its application is limited to the more volatile species (rules out any compound that is solid at room temperature). Whenever feasible, we attempt to test each compound with different methods to ensure accuracy in sensitivity.

2.4.5 *Sensitivity.*

We define the total reagent ion counts per second (cps) as the sum of the count rate for I^- and $I(H_2O)^-$, since the signal for these two typically dominate all the signals combined and are what directly determine the sensitivity of the HR-ToF-CIMS to a particular compound. As such, reported mixing ratios are normalized first by the ratio of the total available I^- cps to its mean value over the course of an experiment. Each compound is then corrected for its dependence on water vapor pressure, as described above.

References:

Aljawhary, D., A. K. Y. Lee and J. P. D. Abbatt (2013). "High-resolution chemical ionization mass spectrometry (ToF-CIMS): application to study SOA composition and processing." Atmospheric Measurement Techniques **6**(11): 3211-3224.

Beaver, M. R., J. M. St Clair, F. Paulot, K. M. Spencer, J. D. Crounse, B. W. LaFranchi, K. E. Min, S. E. Pusede, P. J. Wooldridge, G. W. Schade, C. Park, R. C. Cohen and P. O. Wennberg (2012). "Importance of biogenic precursors to the budget of organic nitrates: observations of multifunctional organic nitrates by CIMS and TD-LIF during BEARPEX 2009." Atmospheric Chemistry and Physics **12**(13): 5773-5785.

Bertram, T. H., J. R. Kimmel, T. A. Crisp, O. S. Ryder, R. L. N. Yatavelli, J. A. Thornton, M. J. Cubison, M. Gonin and D. R. Worsnop (2011). "A field-deployable, chemical ionization time-of-flight mass spectrometer." Atmospheric Measurement Techniques **4**(7): 1471-1479.

Caldwell, G. and P. Kebarle (1984). "Binding-Energies and Structural Effects in Halide Anion Roh and Rcooh Complexes from Gas-Phase Equilibria Measurements." Journal of the American Chemical Society **106**(4): 967-969.

Caldwell, G., R. Renneboog and P. Kebarle (1989). "Gas-Phase Acidities of Aliphatic Carboxylic-Acids, Based on Measurements of Proton-Transfer Equilibria." Canadian Journal of Chemistry-Revue Canadienne De Chimie **67**(4): 611-618.

Caldwell, G. W., J. A. Masucci and M. G. Ikonomou (1989). "Negative-Ion Chemical Ionization Mass-Spectrometry Binding of Molecules to Bromide and Iodide Anions." Organic Mass Spectrometry **24**(1): 8-14.

Chu, L. T. and J. W. Heron (1995). "Uptake of Hbr on Ice at Polar Atmospheric Conditions." Geophysical Research Letters **22**(23): 3211-3214.

Crounse, J. D., K. A. McKinney, A. J. Kwan and P. O. Wennberg (2006). "Measurement of gas-phase hydroperoxides by chemical ionization mass spectrometry." Analytical Chemistry **78**(19): 6726-6732.

Crutzen, P. J., J. Williams, U. Poschl, P. Hoor, H. Fischer, C. Warneke, R. Holzinger, A. Hansel, W. Lindinger, B. Scheeren and J. Lelieveld (2000). "High spatial and temporal resolution measurements of primary organics and their oxidation products over the tropical forests of Surinam." Atmospheric Environment **34**(8): 1161-1165.

de Gouw, J. and C. Warneke (2007). "Measurements of volatile organic compounds in the earths atmosphere using proton-transfer-reaction mass spectrometry." Mass Spectrometry Reviews **26**(2): 223-257.

Dean, A. M. (1985). "Predictions of Pressure and Temperature Effects Upon Radical-Addition and Recombination Reactions." Journal of Physical Chemistry **89**(21): 4600-4608.

Dougherty, R. C., J. D. Roberts and F. J. Biros (1975). "Positive and Negative Chemical Ionization Mass-Spectra of Some Aromatic Chlorinated Pesticides." Analytical Chemistry **47**(1): 54-59.

Ehn, M., E. Kleist, H. Junninen, T. Petaja, G. Lonn, S. Schobesberger, M. Dal Maso, A. Trimborn, M. Kulmala, D. R. Worsnop, A. Wahner, J. Wildt and T. F. Mentel (2012). "Gas phase formation of extremely oxidized pinene reaction products in chamber and ambient air." Atmospheric Chemistry and Physics **12**(11): 5113-5127.

Finlayson-Pitts, B. J. (2010). "Halogens in the Troposphere." Analytical Chemistry **82**(3): 770-776.

Finley, B. D. and E. S. Saltzman (2006). "Measurement of Cl-2 in coastal urban air." Geophysical Research Letters **33**(11).
Frisch, M. J., G. W. Trucks, H. B. Schlegel, G. E. Scuseria, M. A. Robb, J. R. Cheeseman, G. Scalmani, V. Barone, B. Mennucci, G. A. Petersson, H. Nakatsuji, M. Caricato, X. Li, H. P. Hratchian, A. F. Izmaylov, J. Bloino, G. Zheng, J. L. Sonnenberg, M. Hada, M. Ehara, K. Toyota, R. Fukuda, J. Hasegawa, M. Ishida, T. Nakajima, Y. Honda, O. Kitao, H. Nakai, T. Vreven, J. J. A. Montgomery, J. E. Peralta, F. Ogliaro, M. Bearpark, J. J. Heyd, E. Brothers, K. N. Kudin, V. N. Staroverov, R. Kobayashi, J. Normand, K. Raghavachari, A. Rendell, J. C. Burant, S. S. Iyengar, J. Tomasi, M. Cossi, N. Rega, J. M. Millam, M. Klene, J. E. Knox, J. B. Cross, V. Bakken, C. Adamo, J. Jaramillo, R. Gomperts, R. E. Stratmann, O. Yazyev, A. J. Austin, R. Cammi, C. Pomelli, J. W. Ochterski, R. L. Martin, K. Morokuma, V. G. Zakrzewski, G. A. Voth, P. Salvador, J. J. Dannenberg, S. Dapprich, A. D. Daniels, Ö. Farkas, J. B. Foresman, J. V. Ortiz, J. Cioslowski and D. J. Fox (2009). Gaussian 09, Revision D.01. Wallingford, CT, Gaussian, Inc.

Goldstein, A. H. and I. E. Galbally (2007). "Known and unexplored organic constituents in the earth's atmosphere." Environmental Science & Technology **41**(5): 1514-1521.

Heard, D. E. (2006). Analytical techniques for atmospheric measurement. Oxford ; Ames, Iowa, Blackwell Pub.

Horowitz, L. W., J. Y. Liang, G. M. Gardner and D. J. Jacob (1998). "Export of reactive nitrogen from North America during summertime: Sensitivity to hydrocarbon chemistry." Journal of Geophysical Research-Atmospheres **103**(D11): 13451-13476.

Junninen, H., M. Ehn, T. Petaja, L. Luosujarvi, T. Kotiaho, R. Kostiainen, U. Rohner, M. Gonin, K. Fuhrer, M. Kulmala and D. R. Worsnop (2010). "A high-resolution mass spectrometer to measure atmospheric ion composition." Atmospheric Measurement Techniques **3**(4): 1039-1053.

Kassel, L. S. (1928). "Studies in homogeneous gas reactions II Introduction of quantum theory." Journal of Physical Chemistry **32**: 1065-1079.

Kercher, J. P., T. P. Riedel and J. A. Thornton (2009). "Chlorine activation by N2O5: simultaneous, in situ detection of ClNO2 and N2O5 by chemical ionization mass spectrometry." Atmospheric Measurement Techniques **2**(1): 193-204.

Kulmala, M., J. Kontkanen, H. Junninen, K. Lehtipalo, H. E. Manninen, T. Nieminen, T. Petaja, M. Sipila, S. Schobesberger, P. Rantala, A. Franchin, T. Jokinen, E. Jarvinen, M. Aijala, J. Kangasluoma, J. Hakala, P. P. Aalto, P. Paasonen, J. Mikkila, J. Vanhanen, J. Aalto, H. Hakola, U. Makkonen, T. Ruuskanen, R. L. Mauldin, J. Duplissy, H. Vehkamaki, J. Back, A. Kortelainen, I. Riipinen, T. Kurten, M. V. Johnston, J. N. Smith, M. Ehn, T. F. Mentel, K. E. J. Lehtinen, A. Laaksonen, V. M. Kerminen and D. R. Worsnop (2013). "Direct Observations of Atmospheric Aerosol Nucleation." Science **339**(6122): 943-946.

Kurten, T., C. A. Kuang, P. Gomez, P. H. McMurry, H. Vehkamaki, I. Ortega, M. Noppel and M. Kulmala (2010). "The role of cluster energy nonaccommodation in atmospheric sulfuric acid nucleation." Journal of Chemical Physics **132**(2).

Kassel, L. S. (1928). "Studies in homogeneous gas reactions II Introduction of quantum theory." Journal of Physical Chemistry **32**: 1065-1079.

Laidler, K. J. (1987). Chemical kinetics. New York, Harper & Row.

Le Breton, M., M. R. McGillen, J. B. A. Muller, A. Bacak, D. E. Shallcross, P. Xiao, L. G. Huey, D. Tanner, H. Coe and C. J. Percival (2012). "Airborne observations of formic acid using a chemical ionization mass spectrometer." Atmospheric Measurement Techniques **5**(12): 3029-3039.

Lee, L., A. P. Teng, P. O. Wennberg, J. D. Crounse and R. C. Cohen (2014). "On Rates and Mechanisms of OH and O-3 Reactions with Isoprene-Derived Hydroxy Nitrates." Journal of Physical Chemistry A **118**(9): 1622-1637.

Lee, L., A. P. Teng, P. O. Wennberg, J. D. Crounse and R. C. Cohen (2014). "On Rates and Mechanisms of OH and O-3 Reactions with Isoprene-Derived Hydroxy Nitrates." Journal of Physical Chemistry A **118**(9): 1622-1637.

Lin, Y. H., Z. F. Zhang, K. S. Docherty, H. F. Zhang, S. H. Budisulistiorini, C. L. Rubitschun, S. L. Shaw, E. M. Knipping, E. S. Edgerton, T. E. Kleindienst, A. Gold and J. D. Surratt (2012). "Isoprene Epoxydiols as Precursors to Secondary Organic Aerosol Formation: Acid-Catalyzed Reactive Uptake Studies with Authentic Compounds." Environmental Science & Technology **46**(1): 250-258.

Liao, J., H. Sihler, L. G. Huey, J. A. Neuman, D. J. Tanner, U. Friess, U. Platt, F. M. Flocke, J. J. Orlando, P. B. Shepson, H. J. Beine, A. J. Weinheimer, S. J. Sjostedt, J. B. Nowak, D. J. Knapp, R. M. Staebler, W. Zheng, R. Sander, S. R. Hall and K. Ullmann (2011). "A comparison of Arctic BrO measurements by chemical ionization mass spectrometry and long path-differential optical absorption spectroscopy." Journal of Geophysical Research-Atmospheres **116**.

Lopez-Hilfiker, F. D., C. Mohr, M. Ehn, F. Rubach, E. Kleist, J. Wildt, T. F. Mentel, A. Lutz, M. Hallquist, D. Worsnop and J. A. Thornton (2013). "A novel method for on-line analysis of gas and particle composition: description and evaluation of a Filter Inlet for Gases and AEROsols (FIGAERO)." Atmos. Meas. Tech. Discuss. **6**(5): 9347-9395.

Lopez-Hilfiker, F. D., K. Constantin, J. P. Kercher and J. A. Thornton (2012). "Temperature dependent halogen activation by N2O5 reactions on halide-doped ice surfaces." Atmospheric Chemistry and Physics **12**(11): 5237-5247.

Mao, J., X. Ren, L. Zhang, D. M. Van Duin, R. C. Cohen, J. H. Park, A. H. Goldstein, F. Paulot, M. R. Beaver, J. D. Crounse, P. O. Wennberg, J. P. DiGangi, S. B. Henry, F. N. Keutsch, C. Park, G. W. Schade, G. M. Wolfe, J. A. Thornton and W. H. Brune (2012). "Insights into hydroxyl measurements and atmospheric oxidation in a California forest." Atmospheric Chemistry and Physics **12**(17): 8009-8020.

McNeill, V. F., G. M. Wolfe and J. A. Thornton (2007). "The oxidation of oleate in submicron aqueous salt aerosols: Evidence of a surface process." Journal of Physical Chemistry A **111**(6): 1073-1083.

Mielke, L. H., A. Furgeson and H. D. Osthoff (2011). "Observation of ClNO2 in a Mid-Continental Urban Environment." Environmental Science & Technology **45**(20): 8889-8896.

Mohr, C., F. D. Lopez-Hilfiker, P. Zotter, A. S. H. Prevot, L. Xu, N. L. Ng, S. C. Herndon, L. R. Williams, J. P. Franklin, M. S. Zahniser, D. R. Worsnop, W. B. Knighton, A. C. Aiken, K. J. Gorkowski, M. K. Dubey, J. D. Allan and J. A. Thornton (2013). "Contribution of Nitrated Phenols to Wood Burning Brown Carbon Light Absorption in Detling, United Kingdom during Winter Time." Environmental Science & Technology **47**(12): 6316-6324.

National Institute of Standards and Technology (U.S.) NIST chemistry webbook. NIST standard reference database 69. Washington, D.C., National Institute of Standards and Technology.

Osthoff, H. D., J. M. Roberts, A. R. Ravishankara, E. J. Williams, B. M. Lerner, R. Sommariva, T. S. Bates, D. Coffman, P. K. Quinn, J. E. Dibb, H. Stark, J. B. Burkholder, R. K. Talukdar, J. Meagher, F. C. Fehsenfeld and S. S. Brown (2008). "High levels of nitryl chloride in the polluted subtropical marine boundary layer." Nature Geoscience **1**(5): 324-328.

Paulot, F., J. D. Crounse, H. G. Kjaergaard, J. H. Kroll, J. H. Seinfeld and P. O. Wennberg (2009). "Isoprene photooxidation: new insights into the production of acids and organic nitrates." Atmospheric Chemistry and Physics **9**(4): 1479-1501.

Paulot, F., J. D. Crounse, H. G. Kjaergaard, A. Kurten, J. M. St Clair, J. H. Seinfeld and P. O. Wennberg (2009). "Unexpected Epoxide Formation in the Gas-Phase Photooxidation of Isoprene." Science **325**(5941): 730-733.

Peterson, K. A., D. Figgen, E. Goll, H. Stoll and M. Dolg (2003). "Systematically convergent basis sets with relativistic pseudopotentials. II. Small-core pseudopotentials and correlation consistent basis sets for the post-d group 16-18 elements." Journal of Chemical Physics **119**(21): 11113-11123.

Phillips, B., P. S. Starcher and B. D. Ash (1958). "Preparation of Aliphatic Peroxyacids." Journal of Organic Chemistry **23**(12): 1823-1826.

Phillips, G. J., N. Pouvesle, J. Thieser, G. Schuster, R. Axinte, H. Fischer, J. Williams, J. Lelieveld and J. N. Crowley (2013). "Peroxyacetyl nitrate (PAN) and peroxyacetic acid (PAA) measurements by iodide chemical ionisation mass spectrometry: first analysis of results in the boreal forest and implications for the measurement of PAN fluxes." Atmospheric Chemistry and Physics **13**(3): 1129-1139.

Pratt, K. A. and K. A. Prather (2012). "Mass spectrometry of atmospheric aerosolsuRecent developments and applications. Part II: On-line mass spectrometry techniques." Mass Spectrometry Reviews **31**(1): 17-48.

Rice, O. K. and H. C. Ramsperger (1927). "Theories of unimolecular gas reactions at low pressures." Journal of the American Chemical Society **49**: 1617-1629.

Riedel, T. P., T. H. Bertram, T. A. Crisp, E. J. Williams, B. M. Lerner, A. Vlasenko, S. M. Li, J. Gilman, J. de Gouw, D. M. Bon, N. L. Wagner, S. S. Brown and J. A. Thornton (2012). "Nitryl Chloride and Molecular Chlorine in the Coastal Marine Boundary Layer." Environmental Science & Technology **46**(19): 10463-10470.

Saltzman, E. S., W. J. De Bruyn, M. J. Lawler, C. A. Marandino and C. A. McCormick (2009). "A chemical ionization mass spectrometer for continuous underway shipboard analysis of dimethylsulfide in near-surface seawater." Ocean Science **5**(4): 537-546.

Slusher, D. L., L. G. Huey, D. J. Tanner, F. M. Flocke and J. M. Roberts (2004). "A thermal dissociation-chemical ionization mass spectrometry (TD-CIMS) technique for the simultaneous measurement of peroxyacyl nitrates and dinitrogen pentoxide." Journal of Geophysical Research-Atmospheres **109**(D19).

Spicer, C. W., D. V. Kenny, W. J. Shaw, K. M. Busness and E. G. Chapman (1994). "A Laboratory in the Sky - New Frontiers in Measurements Aloft." Environmental Science & Technology **28**(9): A412-A420.

St Clair, J. M., D. C. McCabe, J. D. Crounse, U. Steiner and P. O. Wennberg (2010). "Chemical ionization tandem mass spectrometer for the in situ measurement of methyl hydrogen peroxide." Review of Scientific Instruments **81**(9).

Tannenbaum, H. P., J. D. Roberts and R. C. Dougherty (1975). "Negative Chemical Ionization Mass-Spectrometry - Chloride Attachment Spectra." Analytical Chemistry **47**(1): 49-54.

Thornton, J. A., J. P. Kercher, T. P. Riedel, N. L. Wagner, J. Cozic, J. S. Holloway, W. P. Dube, G. M. Wolfe, P. K. Quinn, A. M. Middlebrook, B. Alexander and S. S. Brown (2010). "A large atomic chlorine source inferred from mid-continental reactive nitrogen chemistry." Nature **464**(7286): 271-274.

Veres, P., J. M. Roberts, C. Warneke, D. Welsh-Bon, M. Zahniser, S. Herndon, R. Fall and J. de Gouw (2008). "Development of negative-ion proton-transfer chemical-ionization mass spectrometry (NI-PT-CIMS) for the measurement of gas-phase organic acids in the atmosphere." International Journal of Mass Spectrometry **274**(1-3): 48-55.

Wolfe, G. M., J. A. Thornton, R. L. N. Yatavelli, M. Mckay, A. H. Goldstein, B. LaFranchi, K. E. Min and R. C. Cohen (2009). "Eddy covariance fluxes of acyl peroxy nitrates (PAN, PPN and MPAN) above a Ponderosa pine forest." Atmospheric Chemistry and Physics **9**(2): 615-634.

Yamdagni, R. and P. Kebarle (1973). "Intrinsic Acidities of Carboxylic-Acids from Gas-Phase Acid Equilibria." Journal of the American Chemical Society **95**(12): 4050-4052.

Yatavelli, R. L. N., F. Lopez-Hilfiker, J. D. Wargo, J. R. Kimmel, M. J. Cubison, T. H. Bertram, J. L. Jimenez, M. Gonin, D. R. Worsnop and J. A. Thornton (2012). "A Chemical Ionization High-Resolution Time-of-Flight Mass Spectrometer Coupled to a Micro Orifice Volatilization Impactor (MOVI-HRToF-CIMS) for Analysis of Gas and Particle-Phase Organic Species." Aerosol Science and Technology **46**(12): 1313-1327.

Yee, L. D., K. E. Kautzman, C. L. Loza, K. A. Schilling, M. M. Coggon, P. S. Chhabra, M. N. Chan, A. W. H. Chan, S. P. Hersey, J. D. Crounse, P. O. Wennberg, R. C. Flagan and J. H. Seinfeld (2013). "Secondary organic aerosol formation from biomass burning intermediates: phenol and methoxyphenols." Atmospheric Chemistry and Physics **13**(16): 8019-8043.

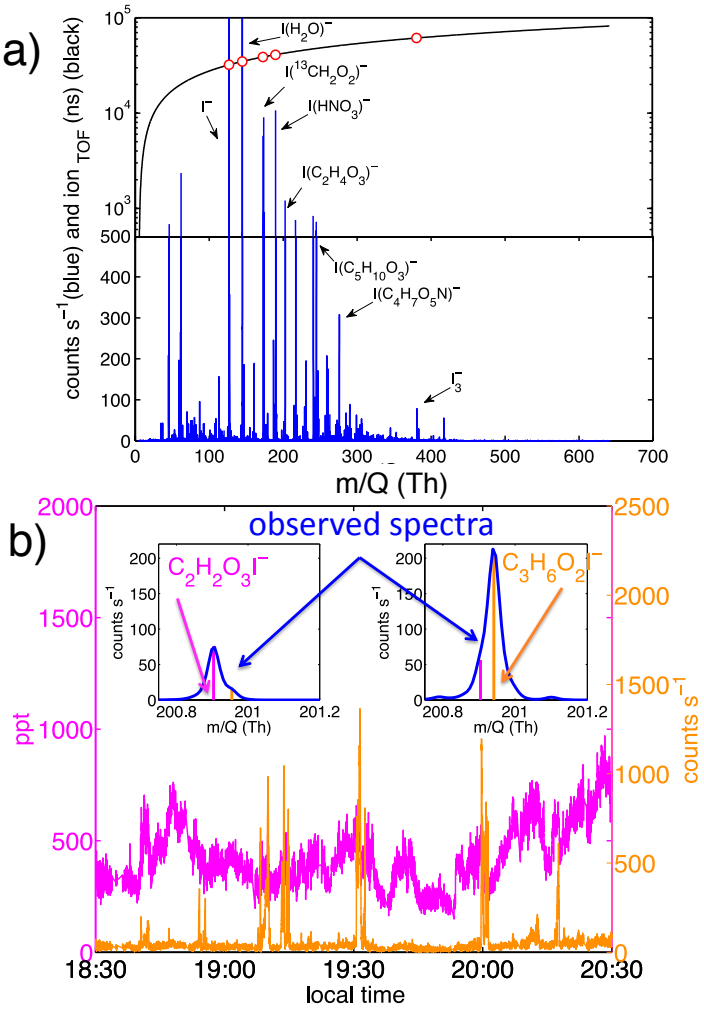

Figure 2.1 High-resolution mass spectra.

(a) A one-second averaged high-resolution mass spectrum (blue) observed in-flight during the SENEX 2013 campaign (lower portion), and the measured ion times of flight of known single ions (I^-, IH_2O^-, $^{13}CH_2O_2I^-$, $IHNO_3$) are plotted. The latter are used to determine the mass-to-charge (m/Q) for the rest of the spectrum (black). (b) Time series of $C_2H_2O_3I^-$ (magenta, left axis) and $C_3H_6O_2I^-$ (orange, right axis) observed on July 2 over Arkansas during SENEX. The high-resolution mass spectrum on the right inset is influenced by the presence of biomass burning tracers, while that on the left is not. At 1500 counts s^{-1}, the signal for $C_3H_6O_2I^-$ represents 340 ppt of propionic acid or 2.9 ppb of hydroxyacetone. Signal for $C_2H_2O_3I^-$ is attributed to glyoxylic acid.

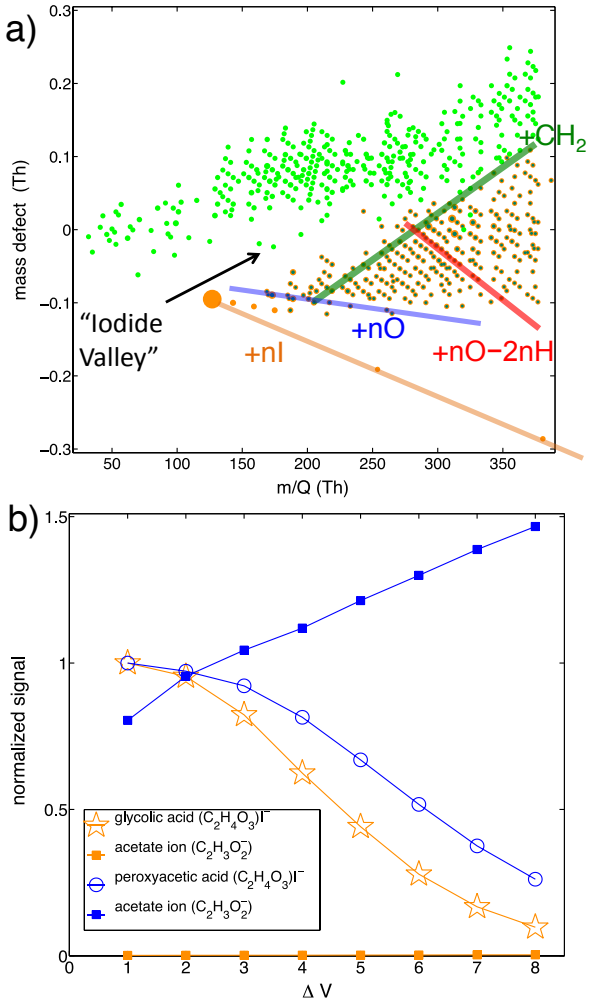

Figure 2.2 Voltage scanning and mass defect.

(a) High-resolution mass defect spectrum obtained during ozonolysis of α-pinene conducted in a 0.75 m^3 steady state PTFE chamber. The high mass-resolution and accuracy of the instrument allows ions containing Iodide (orange w/dark green) to be easily distinguished from those that do not (light green circles) due to the mass defect of Iodide. (b) Signals for the Iodide adducts, and the non- Iodide containing acetate ion, $C_2H_3O_2^-$, are plotted versus the voltage difference between the two quadrupoles regions (SI Figure S1) during additions of glycolic acid (gold stars and squares) and peroxyacetic acid (blue circles and squares). Raw signals are normalized to that of $(C_2H_4O_3)I^-$ at normal electric field settings ($\Delta V = 1$), and the voltage difference is referenced to that normally used. Note during peroxyacetic acid additions the presence of a large signal of the acetate ion, even at normal voltage settings. Both the rate at which the Iodide adduct ion is lost due to increasing the electric fields strengths, that is,

declustering, and also the appearance of a fragment ion are ways in which varying these voltages can allow selectivity toward certain functional groups.

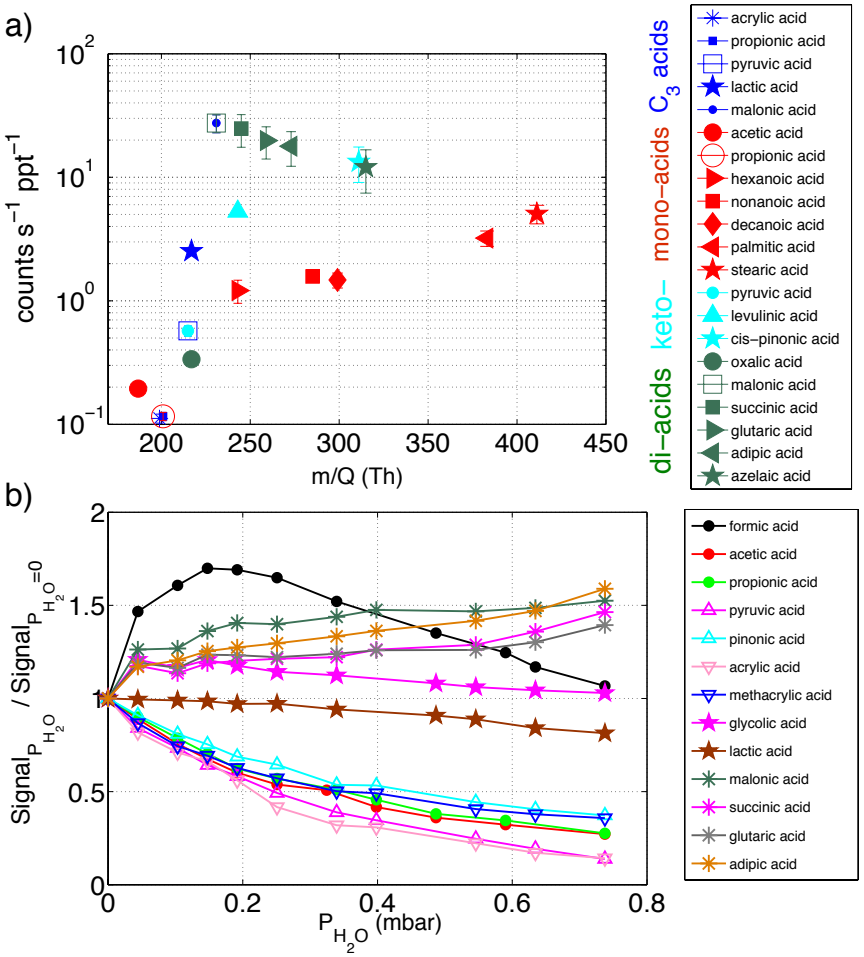

Figure 2.3 TOF-CIMS sensitivity.

(a) Sensitivity (cps ppt^{-1}) per million total reagent ion cps at 0.25 mbar water vapor pressure for C_3 compounds (blue), monoacids (red), keto-monoacids (cyan), and diacids (green), plotted as a function of their m/Q (Th). Pyruvic acid, malonic acid and propionic acid are plotted twice, as they fall into two categories listed above. (b) Sensitivities of various oVOCs normalized to their respective values under dry conditions ($P_{H2O} = 0$, UHP N_2) as a function of water vapor pressure in the IMR.

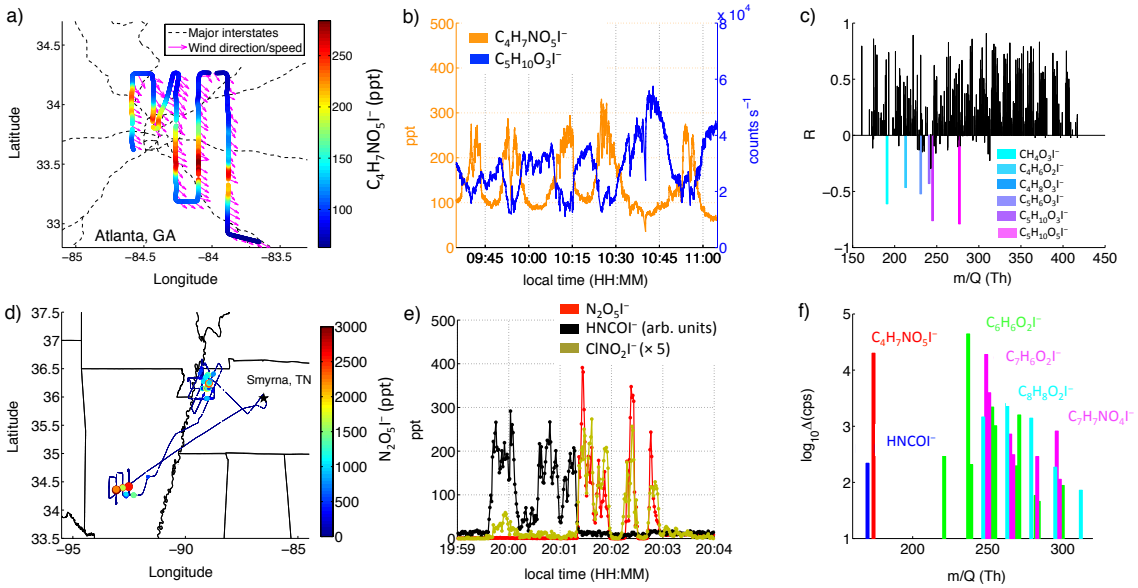

Figure 2.4 Example Flight Data during SENEX.

(a) Partial flight path over Atlanta, GA colored by $C_4H_7O_5NI^-$ mixing ratio obtained by applying the sensitivity of isoprene hydroxy nitrate, (b) time series of $C_4H_7O_5NI^-$ mixing ratio and $C_5H_{10}O_3I^-$ signals, and (c) the correlation spectrum with respect to $C_4H_7O_5NI^-$. Data presented in (a–c) correspond to observations made between 9:30 and 11:30 am local time on June 12 during the SENEX 2013 campaign. (d) Full flight path colored and sized by $N_2O_5I^-$ mixing ratio on the night of July 2–3 near the Tennessee, Arkansas and Missouri borders, (e) time series of $N_2O_5I^-$ and $ClNO_2I^-$ mixing ratios and the signal for $HNCOI^-$ (presumably isocyanic acid, a biomass burning tracer) on the same night, and (f) $\log_{10}$ of the median signal between 20:00 and 20:01 of select species enhanced with $HNCOI^-$. SI Figure S12 lists the full legend of the species in (f). The application of the isoprene hydroxy nitrate sensitivity to $C_4H_7O_5NI^-$ likely yields a low limit estimate on its mixing ratio.

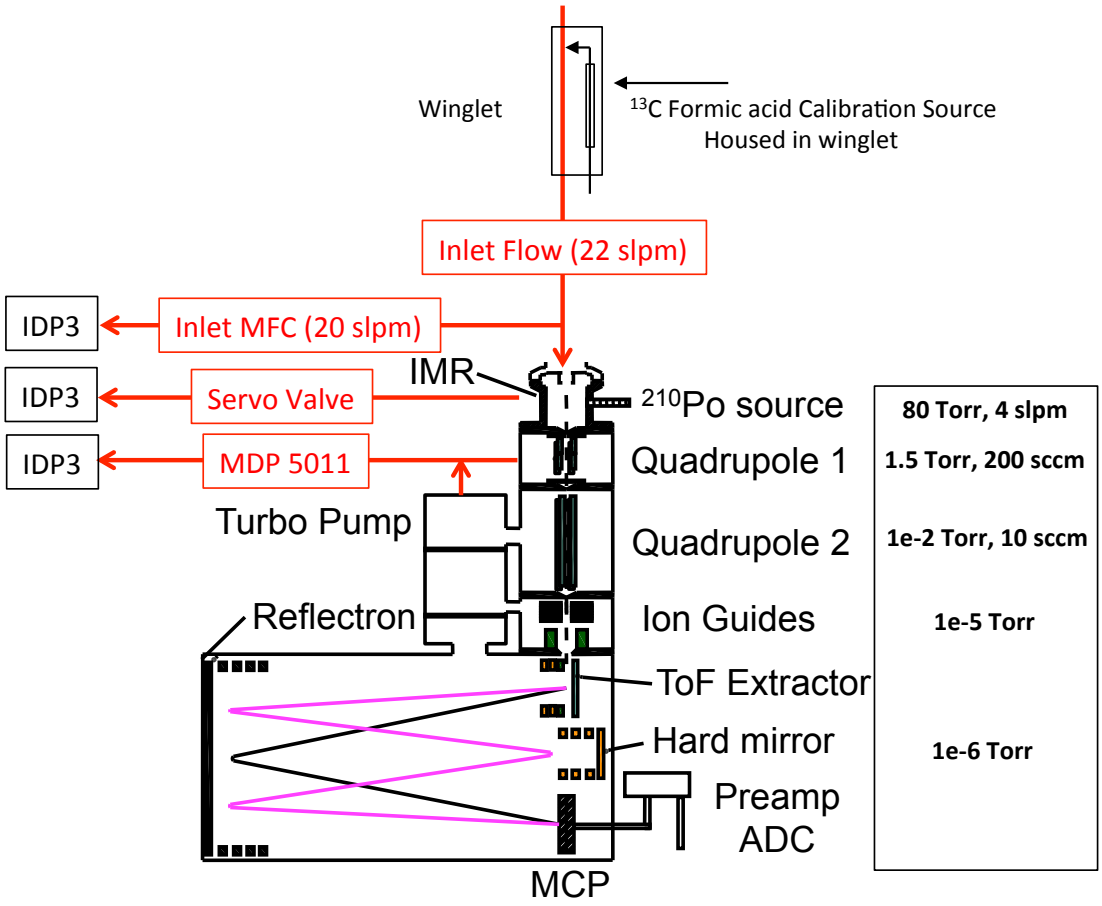

Figure S1. Basic schematic of the HR-ToF-CIMS.

Distribution of the pumps and approximate pressures and flowrates through each region. For the SENEX campaign, three IDP3 pumps (Agilent) were used to maintain flow through the inlet and to provide backing pressure support for the IMR and turbo molecular pump (Pfeiffer). The normal operation pressures and flowrates in each region is listed in the inset. Only the V-mode ion trajectories were used in the time-of-flight region, the W-mode trajectories (magenta lines) were not employed.

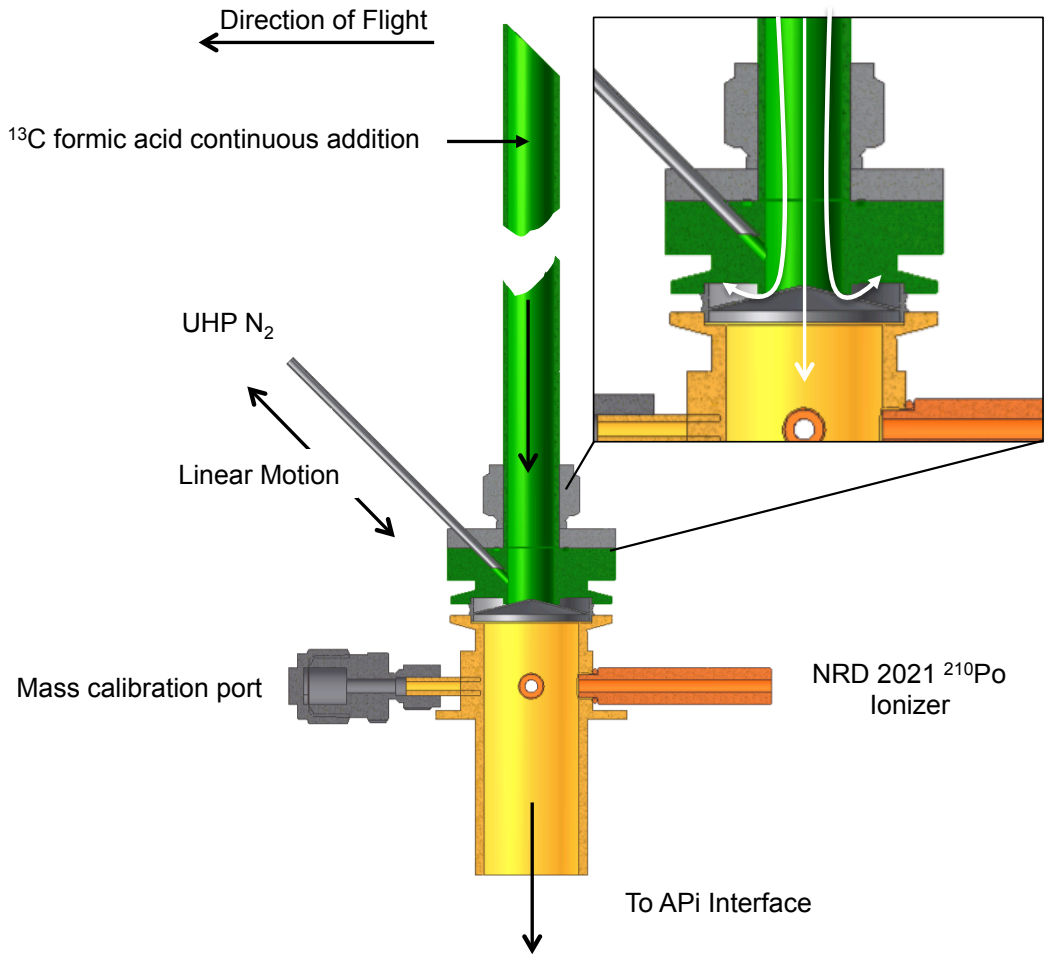

Figure S2. SENEX Inlet and Ionization Region

Schematic of the inlet and chemical ionization (CI) interface used during the SENEX campaign flights. The inset shows a close-up of the pinhole leading to the IMR. The pinhole is slightly raised above four radially symmetric ports through which 9 to 20 slpm (altitude dependent) is flowed to minimize inlet residence time, while approximately 2 slpm flows through to the IMR. A linear actuator introduces a stainless steel arm to deliver UHP N_2 close to the pinhole without having to perturb the main inlet flow, and retracts during ambient measurements. Ions are produced by flowing methyl iodide in UHP N_2 through a 10 mCi ^{210}Po source (NRD 2021 EOL Ionizer). The resulting ions mix with the sample gas flow exiting the first critical orifice before being transferred to the CI-APi interface of the ToF. Automated reagent ion switching is possible with various complimentary ions. The mass calibration port is able to deliver trace levels of select compounds to calibrate ion time of flight to m/Q.

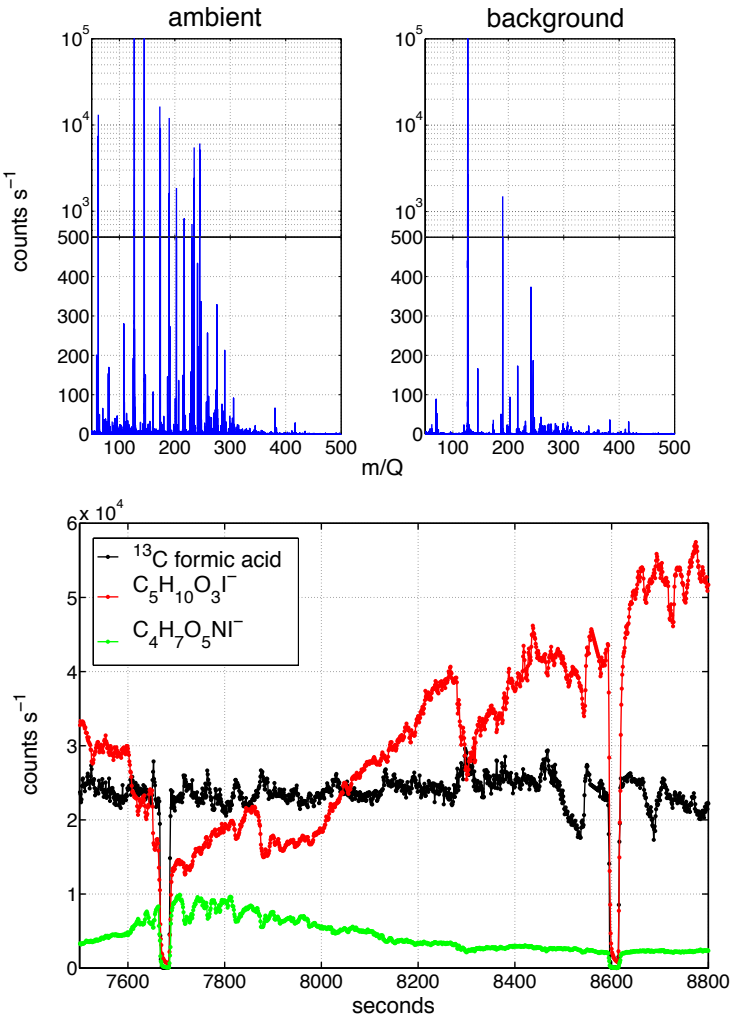

Figure S3. In flight calibration and mass spectra.

High-resolution mass spectra recorded during ambient measurement (top left) and UHP N_2 additions (top right) spaced a few minutes apart, during a SENEX 2013 campaign flight. Not all signals approach zero during the N_2 additions. This is characteristic of low-volatility compounds that take time to completely desorb from exposed instrument surfaces, longer than the time for allotted for each in-flight background cycle, and because there are persistent sources of some compounds within the instrument from the ion source (*e.g.* I_3^-) or Teflon (*e.g.* trifluoroacetic acid). Most organic species tested so far are more sensitive under dry conditions, such as during UHP N_2 addition which will bias the measured background signals high. If not taken into account the reported mixing ratios would be biased low. The bottom panel shows a time series

encompassing two background cycles during SENEX for the signals of ^{13}C formic acid, $C_5H_{10}O_3I^-$ and $C_4H_7O_5NI^-$, uncorrected for water vapor pressure changes.

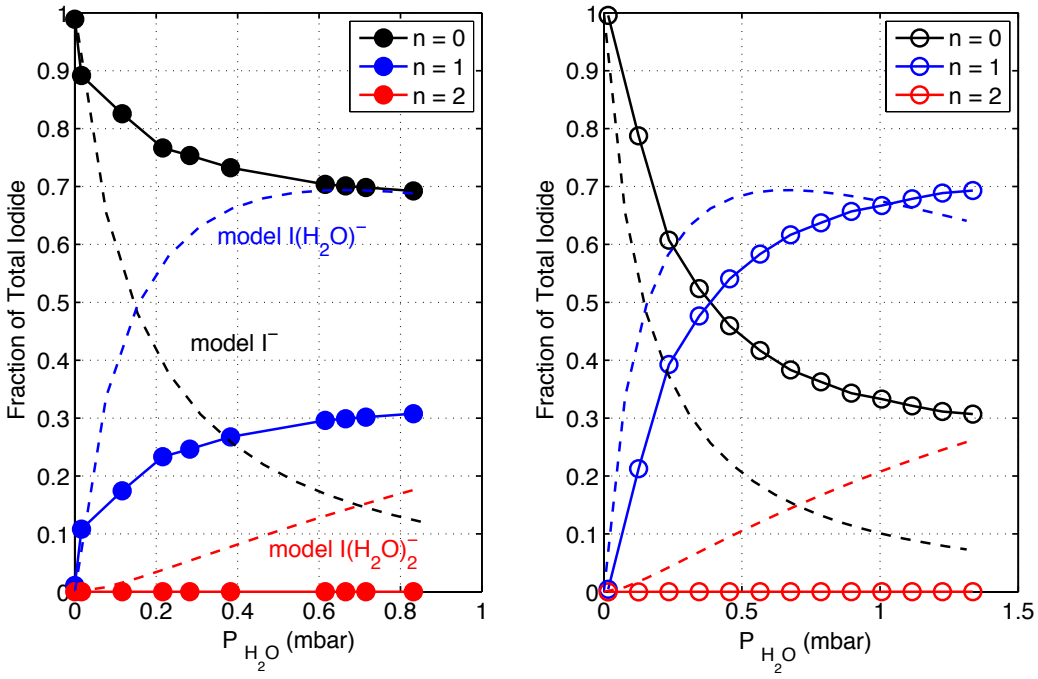

Figure S4. Iodide water distribution measurement and model

Fraction of I^-, $I(H_2O)^-$ and $I(H_2O)_2^-$ (n = 0, 1, 2) to total iodide (= I^- + $I(H_2O)^-$ + $I(H_2O)_2^-$) as predicted by the model (--) and measured (•) for a set IMR condition (T = 313 K; P = 75 torr) with the first quadrupole ion guide RF potential on (a) and off (b), plotted versus water vapor pressure (mbar) in the IMR. A description of the I^-, $I(H_2O)^-$ and $I(H_2O)_2^-$ distribution prediction is provided in the first part of the SI.

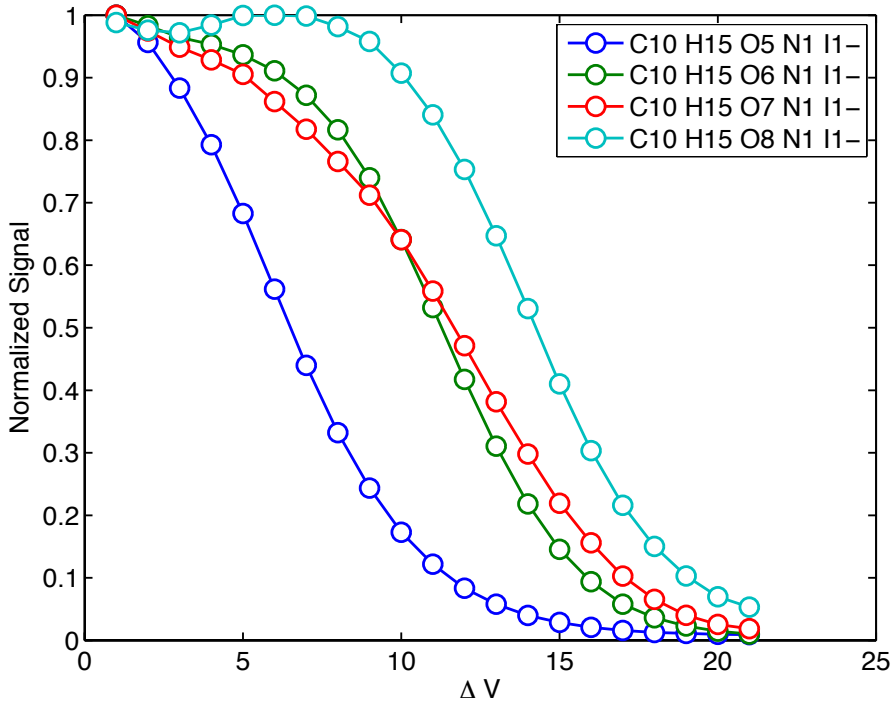

Figure S5. Organic Nitrate Declutering Scan Example.

The signals for four N-containing C_{10} species observed from the ozonolysis of α-pinene in a chamber containing NO_x, normalized to their respective signals at normal electric field settings ($\Delta V = 1$) are plotted versus the voltage difference between the two quadrupoles regions (Figure S1) relative to normal settings. We typically observe that Iodide adducts composed of species with greater functionalization persist at higher declustering field strengths.

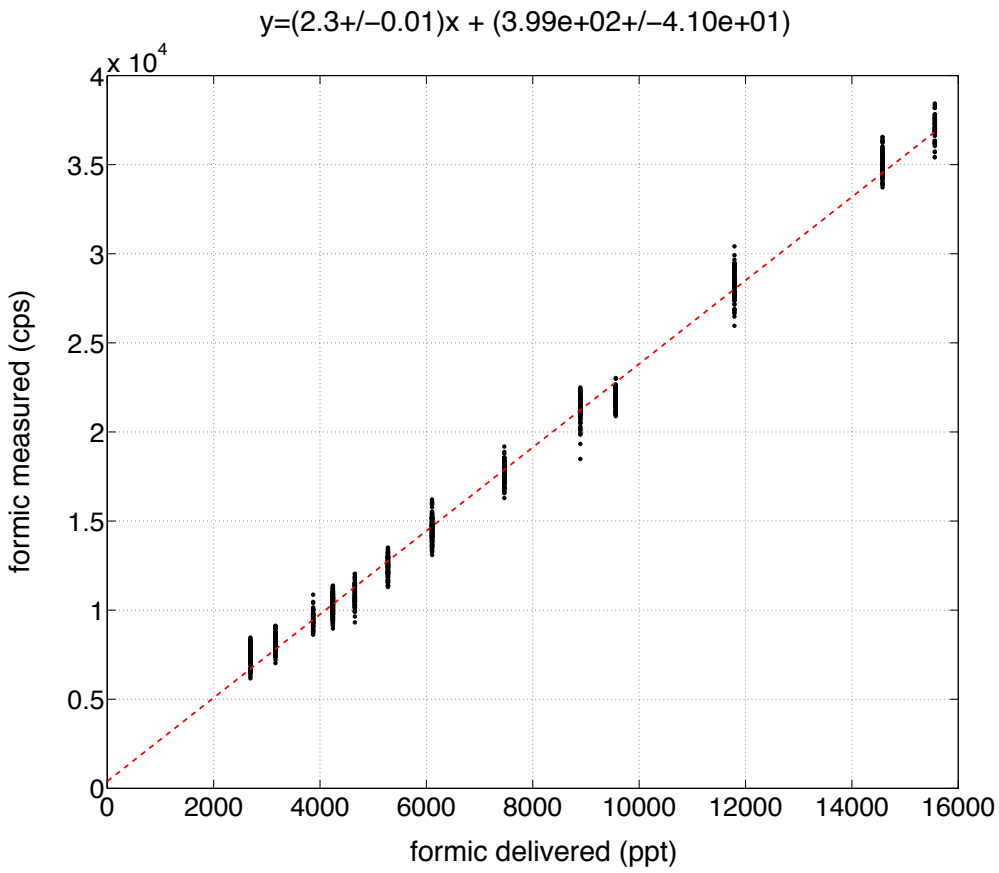

Figure S6. Formic acid linearity.

Detected $CH_2O_2I^-$ signal (cps) versus added formic acid (ppt). Formic acid from a permeation device (KIN-TEK) was added to a 1 m long 1.6 cm inner diameter PTFE tubing, similar to that used on the aircraft. Ambient (laboratory) air was drawn through the tube at different volumetric flow rates to create discrete dilutions of the formic acid. The slope of the signal versus formic acid delivered in log-log space is 0.96±0.003, consistent with a linear relationship. The corresponding sensitivity to formic acid per million total ion cps, is 2.3±0.01 cps ppt^{-1}, where the quoted error is the (random) uncertainty in the slope from the least squares fit. This linearity test was conducted under more humid conditions than described in Table S1 and is therefore slightly less sensitive than the value reported in Table S1. For compounds less sensitively detected compared to formic acid, such as acetic or propionic acids, the linearity extends up to higher concentrations. For compounds more sensitively detected than formic acid, titration of the reagent ions and thus non-linearity occurs at lower concentrations, *e.g.* HNO_3 (see Figure S7)

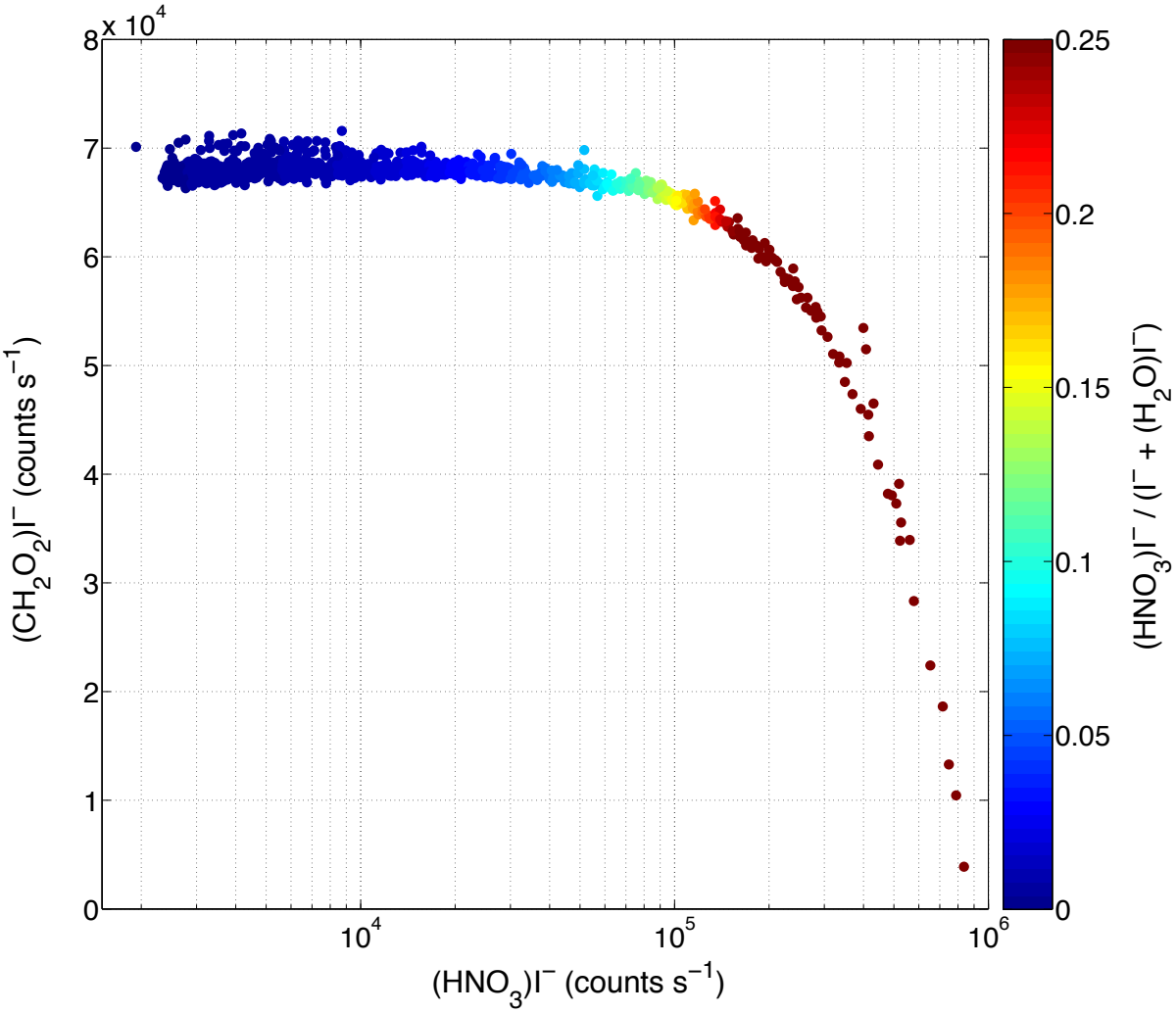

Figure S7. Titration of reagent ions by nitric acid.

Scatter plot of the signals for formic acid and nitric acid adducts to Iodide, colored by the ratio $(HNO_3)I^-$ / $[I^- + (H_2O)I^-]$. Large pulses of nitric acid (> 20 ppb) were introduced during a constant addition of approximately 26 ppbv of formic acid. The signal for formic acid – like that of all other species – is adjusted for the total available Iodide cps as described above. The formic acid signal starts to deviate from the expected count rate as $(HNO_3)I^-$ exceeds 10% of the reagent ion signal. The values here are normalized to per million total reagent ion cps.

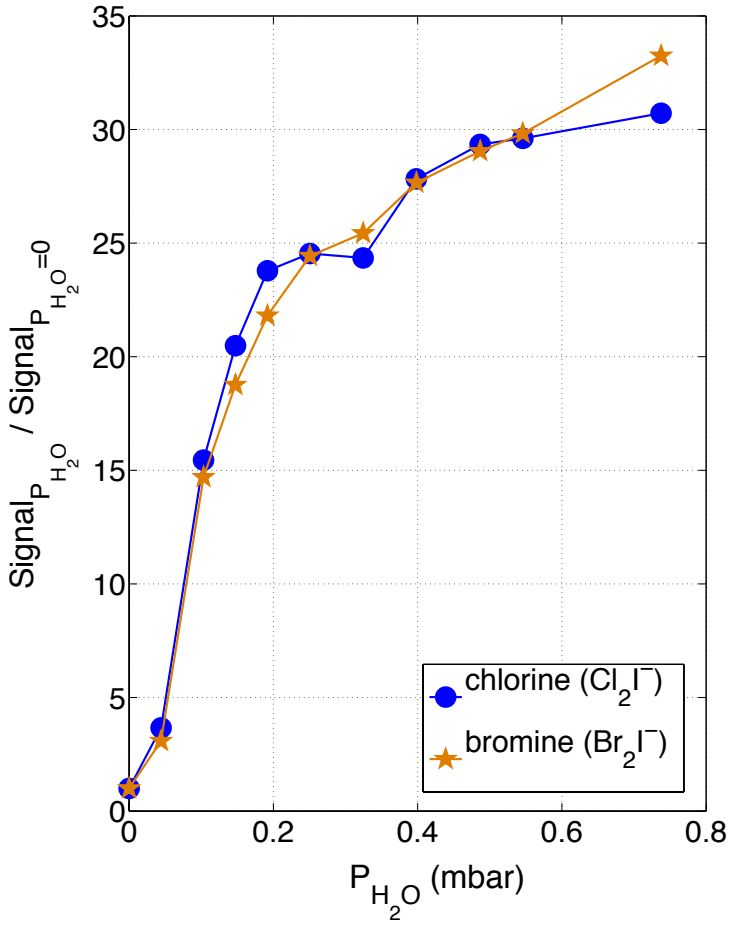

Figure S8. Sensitivity of molecular chlorine and bromine as a function of water vapor pressure (P_{H2O}) in the IMR. Sensitivities are normalized by their respective values observed under dry conditions (P_{H2O} = 0, UHP N_2).

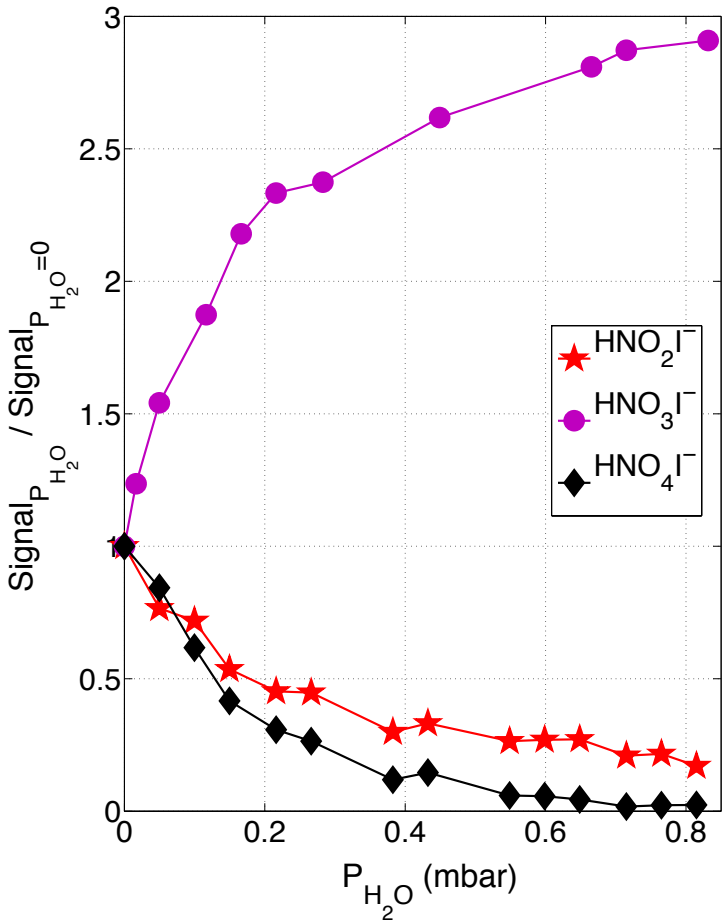

Figure S9. Sensitivity of nitrogen oxides to water vapor pressure.

Same as Figure S8 but for nitrogen oxides.

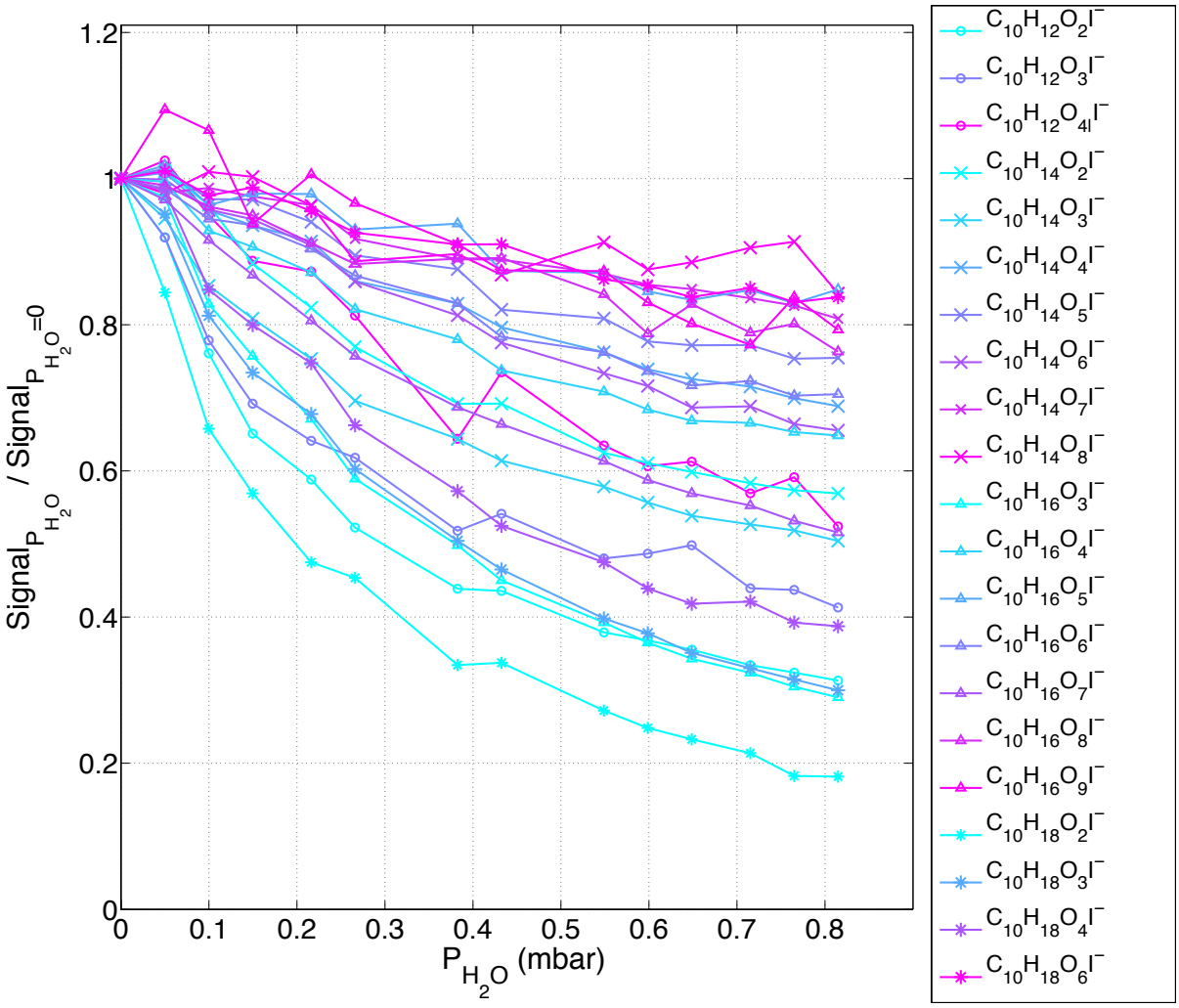

Figure S10. Water vapor dependence of a-pinene products.

Same as Figure S8 but for oxygenated VOCs containing 10 carbons resulting from α-pinene ozonolysis. The C_{10} compounds are grouped into 4 different categories; H_{12} (**O**), H_{14} (*), H_{16} (Δ) and H_{18} (★). Each category is colored from light blue to dark magenta as the number of oxygen atoms increases.

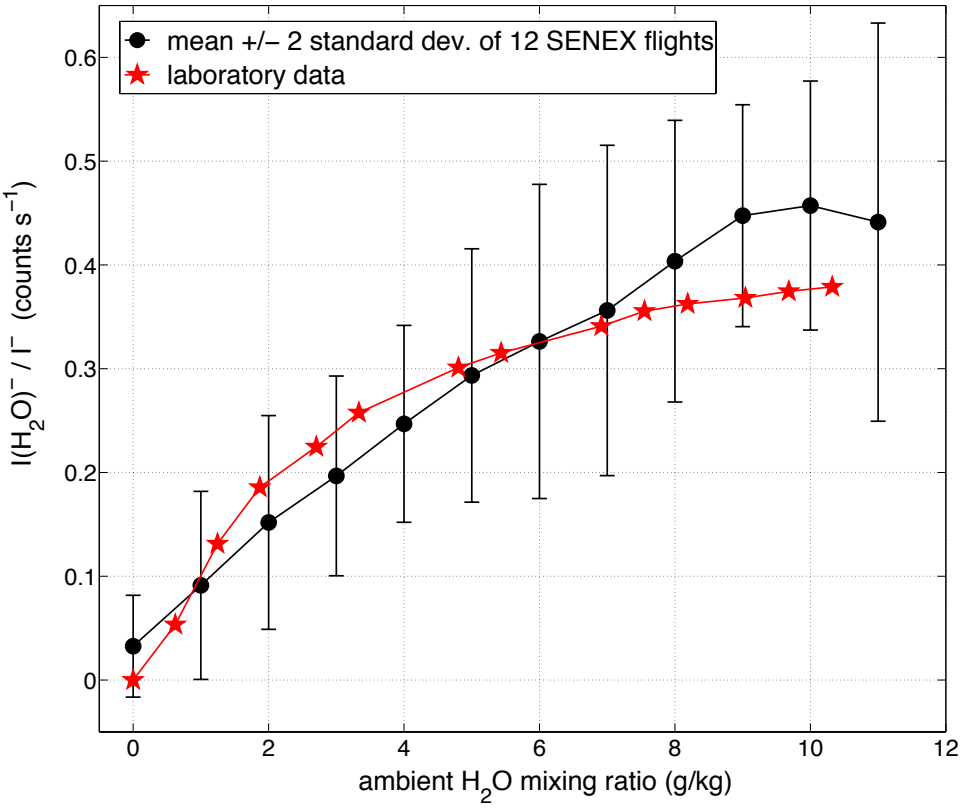

Figure S11. Water vapor reproducibility during SENEX.

The mean of $I(H_2O)^-/I^-$ for 12 SENEX flights (black) and as observed in the laboratory (red), plotted versus ambient water vapor mixing ratio.

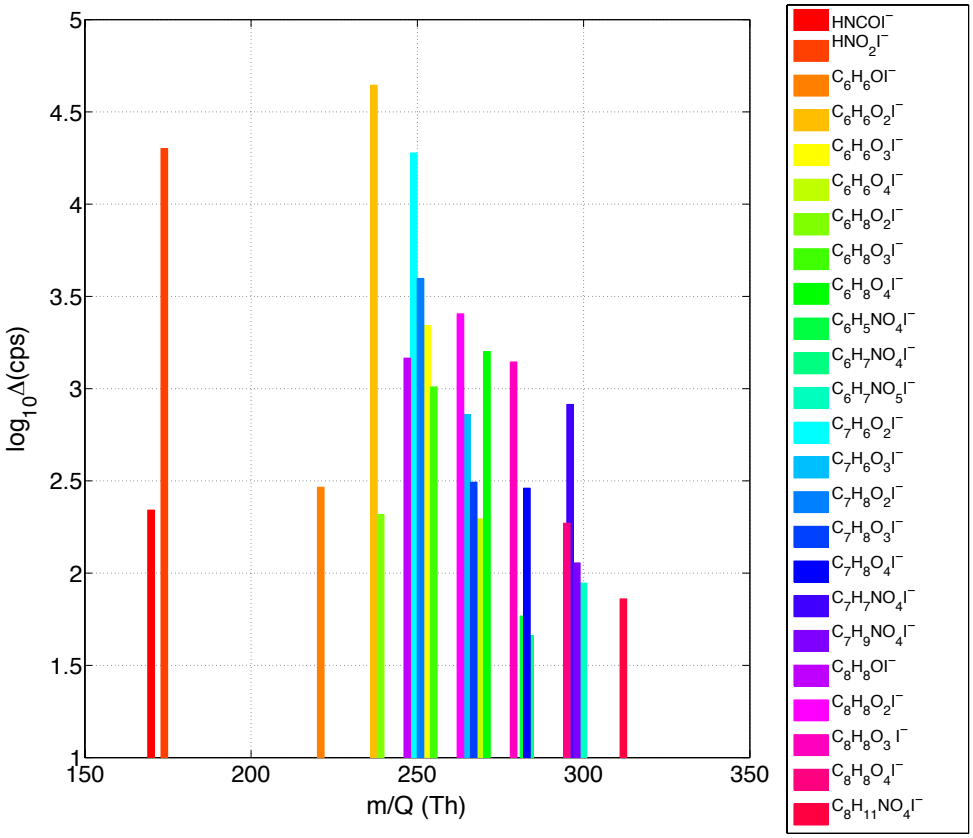

Figure S12. Biomass burning tracers during SENEX

Figure 4f with complete legend.

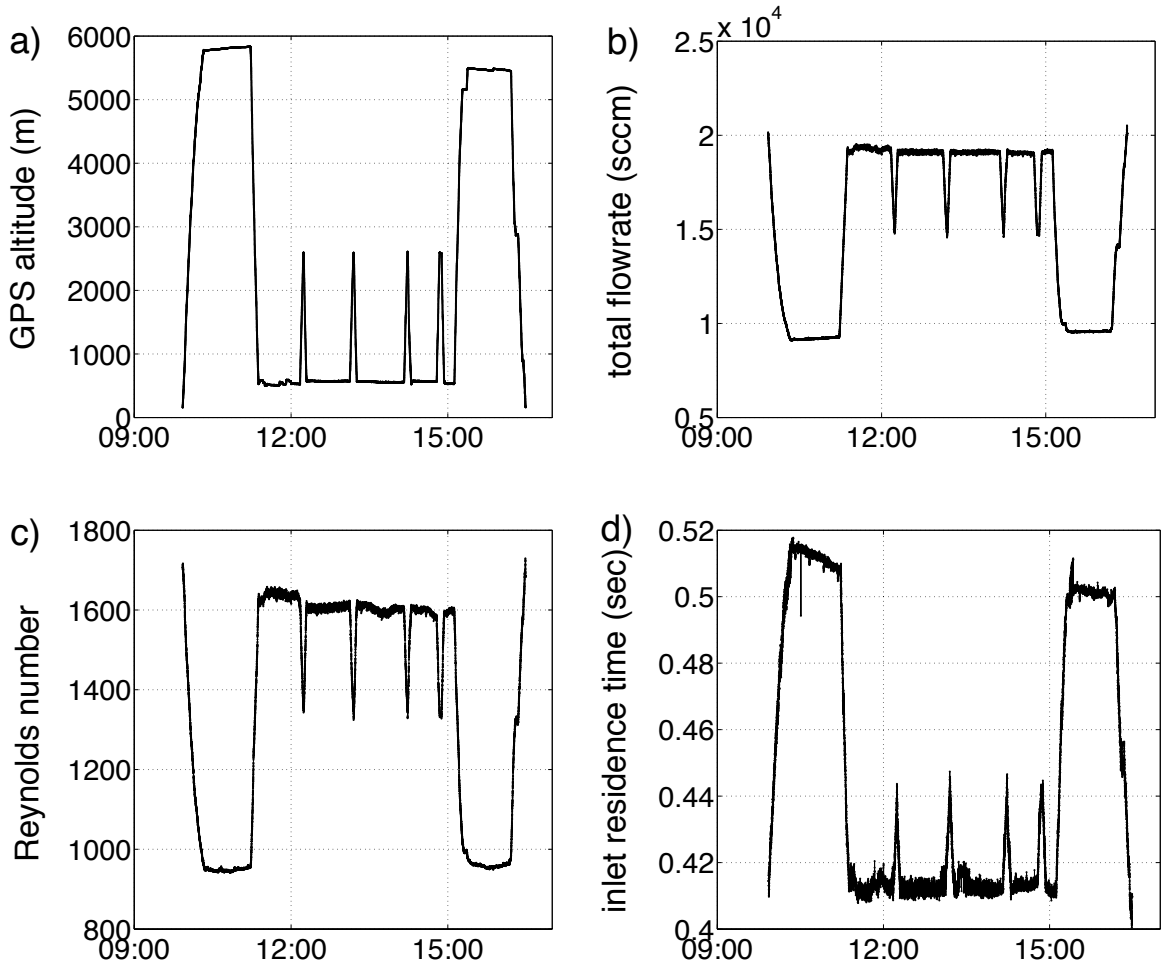

Figure S13. Inlet characteristics during SENEX.

Time series during the June 12, 2013 SENEX flight over Atlanta, GA of (a) altitude, (b) total mass flowrate through in the HR-ToF-CIMS inlet, (c) Reynold's number and (d) average inlet residence time. Due to the limitation on pumping speed, the mass throughput slows with altitude resulting in an increase in the inlet residence time from about 0.4 to 0.5 seconds. The Reynold's number decreases at high altitude given the lower ambient pressure, meaning turbulent flow (Re ~2300) is not attained.

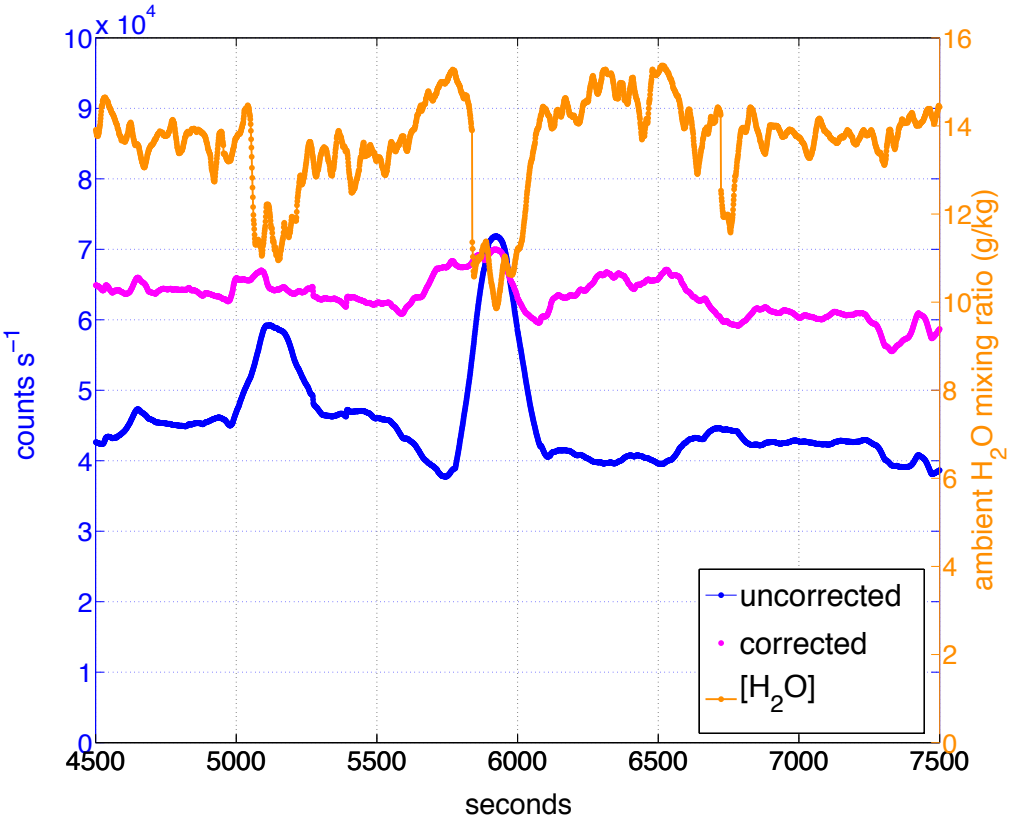

Figure S14. In flight calibration and water vapor correction.

Time series of ^{13}C formic acid calibration gas signal (left axis), uncorrected (blue) and corrected (magenta) for dependence on water vapor pressure for a flight during the SENEX campaign. The observed signal (blue) is clearly influenced by the decreasing ambient water vapor pressure (gold, right axis), as the WP-3 aircraft ascends from about 900 m to 2 km and back down. Both ^{13}C formic acid signals are smoothed here by a 120-second running average to clearly demonstrate the water vapor pressure correction.

Table 2.1. Sensitivity per million total reagent ion cps and detection limits.

Compound	Formula	Observed formula	Sensitivity[†] ± uncertainty (cps ppt^{-1})	Detection limit[‡] (ppt in 15-seconds, S/N=3)
formic acid	CH_2O_2	$CH_2O_2I^-$	2.9 ± 0.6	3.6
acrylic acid	$C_3H_4O_2$	$C_3H_4O_2I^-$	0.063 ± 0.01	32
propionic acid	$C_3H_6O_2$	$C_3H_6O_2I^-$	0.066 ± 0.01	3.6×10^{1}
pyruvic acid	$C_3H_4O_3$	$C_3H_4O_3I^-$	0.35 ± 0.06	19
lactic acid[*]	$C_3H_6O_3$	$C_3H_6O_3I^-$	1.6 ± 0.2	17
malonic acid	$C_3H_4O_4$	$C_3H_4O_4I^-$	19 ± 4.5	0.34
acetic acid	$C_2H_4O_2$	$C_2H_4O_2I^-$	0.1 ± 0.01	140
hexanoic acid	$C_6H_{12}O_2$	$C_6H_{12}O_2I^-$	0.89 ± 0.26	7.3
nonanoic acid	$C_9H_{18}O_2$	$C_9H_{18}O_2I^-$	1.4 ± 0.12	4.5
decanoic acid	$C_{10}H_{20}O_2$	$C_{10}H_{20}O_2I^-$	1.4 ± 0.2	7.6
palmitic acid	$C_{16}H_{32}O_2$	$C_{16}H_{32}O_2I^-$	2.2 ± 0.5	9.5
stearic acid	$C_{18}H_{36}O_2$	$C_{18}H_{36}O_2I^-$	2.9 ± 0.9	2.6
levulinic acid	$C_5H_8O_3$	$C_5H_8O_3I^-$	3.9 ± 0.3	2.6
cis-pinonic acid	$C_{10}H_{16}O_3$	$C_{10}H_{16}O_3I^-$	13 ± 4.2	0.41
oxalic acid	$C_2H_2O_4$	$C_2H_4O_2I^-$	0.21 ± 0.09	71
succinic acid	$C_4H_6O_4$	$C_4H_6O_4I^-$	18 ± 7.3	0.76
glutaric acid	$C_5H_8O_4$	$C_5H_8O_4I^-$	16 ± 5.8	0.56
adipic acid	$C_6H_{10}O_4$	$C_6H_{10}O_4I^-$	15 ± 5.6	0.44
azelaic acid	$C_9H_{16}O_4$	$C_9H_{16}O_4I^-$	12 ± 4.6	0.47
glycolic acid	$C_2H_4O_3$	$C_2H_4O_3I^-$	1.1 ± 0.52	13
methacrylic acid	$C_4H_6O_2$	$C_4H_6O_2I^-$	$(7.7 \pm 3.2)\times10^{-5}$	22
oleic acid	$C_{18}H_{34}O_2$	$C_{18}H_{34}O_2I^-$	1.1 ± 0.4	6.9
peroxyacetic acid	$C_2H_4O_3$	$C_2H_4O_3I^-$	0.04 ± 0.01	430
hydroxyacetone	$C_3H_6O_2$	$C_3H_6O_2I^-$	$(9.9 \pm 1.9)\times10^{-3}$	280
cis-2-butene-1,4-diol	$C_4H_8O_2$	$C_4H_8O_2I^-$	1.2 ± 0.1	3.3
1,2-butanediol	$C_4H_{10}O_2$	$C_4H_{10}O_2I^-$	0.21 ± 0.04	73
1,2-octanediol	$C_8H_{18}O_2$	$C_8H_{18}O_2I^-$	0.017 ± 0.004	221
1,12-dodecanediol	$C_{12}H_{26}O_2$	$C_{12}H_{26}O_2I^-$	0.22 ± 0.05	14
5-hydroxy-2-pentanone	$C_5H_{10}O_2$	$C_5H_{10}O_2I^-$	$(5.6 \pm 2.0)\times10^{-3}$	820
2,5-hexanedione	$C_6H_{10}O_2$	$C_6H_{10}O_2I^-$	$(7.9 \pm 0.8)\times10^{-5}$	1.4×10^{5}
glyoxylic acid	$C_2H_2O_3$	$C_2H_2O_3I^-$	0.78 ± 0.19	5.2
salicylic acid	$C_7H_6O_3$	$C_7H_6O_3I^-$	0.77 ± 0.09	5.1
phthalic acid	$C_8H_6O_4$	$C_8H_6O_4I^-$	4.5 ± 1.9	0.8
ISOPN[**] (β-4,3)	$C_5H_9O_4N$	$C_5H_9O_4NI^-$	6.1 ± 0.2	0.9
ISOPN[**] (*cis*-δ-1,4)	$C_5H_9O_4N$	$C_5H_9O_4NI^-$	5.7 ± 1.2	0.9
ISOPN[**] (*trans*-δ-1,4)	$C_5H_9O_4N$	$C_5H_9O_4NI^-$	0.37 ± 0.29	14.2

IEPOX*** (*trans*-beta)	$C_5H_{10}O_3$	$C_5H_{10}O_3I^-$	0.39 ± 0.07	86
chlorine	Cl_2	Cl_2I^-	20 ± 4	0.1
bromine	Br_2	Br_2I^-	9.4 ± 1.9	0.4
dinitrogen pentoxide	N_2O_5	$N_2O_2I^-$	7.9 ± 4.0	0.8
nitryl chloride	$ClNO_2$	$ClNO_2I^-$	0.7 ± 0.35	3.0
nitric acid	HNO_3	HNO_3I^-	4.0 ± 0.8	7.3

† Reported values represent sensitivities for when the water vapor pressure in the IMR (P_{H2O}) is ~ 0.25 mbar (equivalent to ~ 30% relative humidity at 25°C of ambient air). Uncertainty is determined as the standard deviation of at least six injections during calibrations. The uncertainty for formic acid, nitric acid, chlorine and bromine is the uncertainty associated with the permeation rate of the source. We assume 50% uncertainty for the sensitivities of N_2O_5 and $ClNO_2$, which were calibrated during the SENEX campaign using sources provided by P. Edwards, S. Brown, P. Veres and J. Roberts (NOAA ESRL).

‡ Detection limits are obtained using equation 2 of *Bertram et al*.(Bertram, Kimmel et al. 2011) for each compound, over a 15-second time period of each UHP N_2 addition, for a signal-to-noise ratio (S/N) of 3. The reported values represent the maximum observed over the course of the SENEX field campaign, assuming the species of interest is the dominant source of background noise.

* Lactic acid ($C_3H_6O_3$), a byproduct of human perspiration, exhibited a large and persistent background signal during SENEX, thus was excluded in the data presentation and analysis.

** The three isomers of isoprene hydroxy nitrate ($C_5H_9O_4N$) was synthesized by L. Lee of the Cohen Group at UC Berkeley(Lee, Teng et al. 2014).

*** Dihydroxy-trans-beta-isoprene-epoxide ($C_5H_{10}O_3$) was synthesized by Y.-H. Lin of the Surratt Group at UNC, Chapel Hill(Lin, Zhang et al. 2012).

Table 2.2. Computed energetics (electronic energies ΔE_{elec}, enthalpies ΔH and Gibbs free energies ΔG) for the clustering of formic acid (CH_2O_2) with unhydrated and hydrated I^-. All values in kcal/mol, at standard conditions (298.15 K and 1 atm reference pressure).

	MP2[a] ΔE_{elec}	MP2 [a] ΔH	MP2 [a] ΔG	CCSD(T)[b] ΔE_{elec}
$I^- + CH_2O_2 \Leftrightarrow I(CH_2O_2)^-$	–24.46	–24.31	–17.77	–25.62
$I(H_2O)^- + CH_2O_2 \Leftrightarrow I(CH_2O_2)(H_2O)^-$	–23.73	–22.52	–13.50	-
$I(CH_2O_2)(H_2O) \Leftrightarrow I(CH_2O_2) + H_2O$	+10.51	+9.10	+1.36	-

[a] MP2/aug-cc-pVDZ-PP
[b] CCSD(T)/aug-cc-pVTZ-PP energies at the MP2 geometries

Chapter 3. A NOVEL METHOD FOR ON-LINE ANALYSIS OF GAS AND PARTICLE COMPOSITION: DESCRIPTION AND EVALUATION OF A FILTER INLET FOR GASES AND AEROSOLS (FIGAERO)*

We describe a novel inlet that allows measurement of both gas and particle molecular composition when coupled to mass spectrometric, chromatographic, or optical sensors: the Filter Inlet for Gases and AEROsols (FIGAERO). The design goals for the FIGAERO are to allow unperturbed observation of ambient air while simultaneously analyzing gases and collecting particulate matter on a Teflon filter via an entirely separate sampling port. The filter is analyzed periodically by the same sensor on hourly or faster timescales using temperature-programmed thermal desorption. We assess the performance of the FIGAERO by coupling it to a high-resolution time-of-flight chemical-ionization mass spectrometer (HRToF-CIMS) in laboratory chamber studies of α-pinene oxidation and field measurements at a boreal forest location. Low instrument backgrounds give detection limits of ppt or lower for compounds in the gas-phase and in the picogram/m^3 range for particle phase compounds. The FIGAERO-HRToF-CIMS provides molecular information about both gases and particle composition on the 1 Hz and hourly timescales, respectively for hundreds of compounds. The FIGAERO thermal desorptions are highly reproducible (better than 10%), allowing a calibrated assessment of the effective volatility of desorbing compounds and the role of thermal decomposition during the desorption process. We show that the often multi-modal desorption thermograms arising from secondary organic aerosol (SOA) provide additional insights into molecular composition and/or particle morphology, and exhibit changes with changes in SOA formation or aging pathways.

* Reprinted with permission from: Lopez-Hilfiker, F. D., Mohr, C., Ehn, M., Rubach, F., Kleist, E., Wildt, J., Mentel, T. F., Lutz, A., Hallquist, M., Worsnop, D. and Thornton, J. A.: A novel method for online analysis of gas and particle composition: description and evaluation of a Filter Inlet for Gases and AEROsols (FIGAERO), Atmos. Meas. Tech., 7(4), 983–1001, doi:10.5194/amt-7-983-2014, 2014

3.1 INTRODUCTION

Aerosol particles scatter and absorb radiation, influence cloud formation processes and properties, provide surfaces to facilitate multiphase reactions, and affect trace gas concentrations by providing an adsorptive medium for semi-volatile gases. As a result, aerosol particles have a significant effect on the radiative balance of the atmosphere and thus on earth's climate (Hallquist et al., 2009). Atmospheric particles also have adverse effects on human health, impacting respiratory and cardiovascular systems (Davidson et al., 2005; Hallquist et al., 2009; Pope and Dockery, 2006).

Of specific importance to both air quality and climate are particles smaller than ~ 1 μm in diameter, a significant and ubiquitous portion of which is secondary organic aerosol (SOA) (Hallquist et al., 2009; Jimenez et al., 2009). The sources, aging, and chemical properties of SOA still remain highly uncertain, and these uncertainties can lead to large errors between modeled and measured aerosol loadings (Volkamer et al., 2006). These errors limit our ability to confidently predict future changes in aerosol particle composition and concentration under a warming climate (Hallquist et al., 2009). To develop adequate model parameterizations of organic aerosol (OA) and its formation, growth, and loss, there remains a need to improve source apportionment capabilities and to develop and test chemical mechanisms that involve conversion and partitioning of organic compounds between gas and condensed phase. Both of these needs are facilitated by a more detailed understanding of molecular composition in both phases at higher time resolution. Measurements of specific tracers on timescales similar to the typical variability in emissions, photochemical activity, and meteorology, arguably an hour or shorter in polluted regions, would improve source apportionment, testing of partitioning theory (Pankow, 2007), and characterization of molecular properties such as the distribution of average oxidation state across carbon number (Kroll et al., 2011) against mechanistic photochemical models.

A range of methods are available to measure trace gases online and *in situ*, however measurements of molecular composition of aerosol particles have so far mostly been conducted offline, using high-volume filter samplers, which typically integrate aerosol composition over 12 to 24 hours (Turpin et al., 2000). More recently, online techniques have been developed, but

while providing important constraints on elemental composition, the most common approaches are generally not suitable for molecular analysis of the organic aerosol fraction. The Aerosol Mass Spectrometer (AMS), which measures non-refractory particle composition in the 0.050-1 μm size range at high time resolution was a major breakthrough in quantifying organic aerosol time evolution and absolute mass concentrations (Canagaratna et al., 2007; DeCarlo et al., 2006; Jayne et al., 2000). Another example of a bulk particle composition measurement is the particle beam temperature-programmed desorption mass spectrometer which uses an aerodynamic lens for focusing aerosol to a desorption plate (Tobias et al., 2000). Single particle mass spectrometers (ex. SPLAT, PALMS, ATOFMS, Laser Desorption MS, and the RSMS III) provide a detailed picture of individual particles and thus particle mixing state (Gard et al., 1997; Lake et al., 2003; McKeown et al., 1991; Thomson et al., 2000; Zelenyuk and Imre, 2005). However, as with electron impact ionization employed in the AMS, laser desorption and ionization lead to highly fragmented organic ions, erasing the individual molecular identity of the OA components. Particle into Liquid Samplers (PILS) have been coupled to ion chromatography and mass spectrometer systems to measure aerosol composition (Saarnio et al., 2013; Weber et al., 2001) but are generally used to measure water soluble compounds only. Another separation technique using a pumped counter flow virtual impactor coupled to a vaporizer and atmospheric pressure chemical ionization ion trap mass spectrometer was developed for the detection of organic acids (Vogel et al., 2013). Moreover, instruments for atmospheric applications have typically been designed for either exclusive gas or particulate phase analysis.

Recently, to study the dynamic organic aerosol system in a molecular framework, online methods to analyze both gas and particle phase molecular composition on timescales much faster than typical hi-vol filter analyses have been developed. These include inline volatilization methods (Aljawhary et al., 2013; Hearn and Smith, 2004; McNeill et al., 2007) coupled to CIMS, as well as particle impaction based techniques, such as the TAG (Thermal Desorption Aerosol GC/MS-FID and HR-TD-PTR-MS) (Holzinger et al., 2010; Williams et al., 2006) and the MOVI (Micro Orifice Volatilization Impactor) (Yatavelli and Thornton, 2010). *Thornberry et. al. (2009)* also operated a similar impaction system with a single jet and cooled collection plate coupled to a Proton-Transfer-Ion-Trap mass spectrometer (PTR-IT-MS). Electrostatic precipitator based methods such as Thermal Desorption CIMS (TDCIMS) (Voisin et al., 2003)

are not subject to the same impaction limitations, discussed below, but are subject to variable charging efficiencies and can be limited to particles which are highly mobile. Common to these techniques is the use of thermal desorption (or laser desorption) of collected particles with subsequent analysis of the desorbed vapors via soft ionization and or chromatographic separation techniques such as GC/MS-FID and chemical ionization (CI).

Historically, the largest problems with impaction-based techniques are related to the particle collection efficiency, namely the loss of small particles to cut point diameter limitations, and particles that bounce after impacting the collection plate. Significant pressure drops are required to impact particles less than ~ 150 nm, which can then lead to loss of semi-volatiles, and thus most impaction approaches settle on collecting particles > 150 nm or use cooled collection stages (Thornberry et al., 2009; Williams et al., 2006; Yatavelli and Thornton, 2010). In many environmental chambers or often in the atmosphere, a significant fraction of organic aerosol mass can be below this cut-point. To reduce particle bounce, humidification of the sample stream to grow the aerosol into a liquid (or gel-like) phase have been used (Williams et al., 2006). However, the humidification process possibly changes the partitioning and composition of the collected aerosol. Alternatively, applying a thin film of low volatility grease to increase the sticking efficiency of aerosol has been used (Vasiliou et al., 1999), but grease leads to contamination or interferences during the thermal analysis and typically eliminates that option for mass spectrometry applications. Impactor methods that do not humidify the sample flow or grease the impaction surface ultimately suffer from more bounce, which is variable in an unpredictable way and therefore can result in potentially large systematic errors.

The need to thermally desorb collected particle material for subsequent analysis of the vapors, common to many approaches discussed above, puts design constraints on the type of material used in the particle collection and desorption region. Metals are a common choice, as they are easy to heat, either resistively or by conduction, and do not deform significantly at typical operating temperatures (200-300 °C). However, metals are known to provide significant adsorptive sites for semi-volatile gases, especially when held at atmospherically relevant temperatures (Neuman et al., 1999). This adsorption of gases then results in a positive artifact during the thermal desorption of collected particles as heat forces the adsorbed gases off the

surfaces just as it desorbs compounds from the particles. Inert coatings have been employed and developed in GC applications to make surfaces less reactive and therefore less likely to adsorb gases (Williams et al., 2006; Yatavelli et al., 2012), but these coatings tend to be most effective at elevated temperatures typical of GC operation and therefore can do little to change the transmission of semi-volatiles when kept at near ambient temperatures. Electrostatic precipitators can be designed to collect particles out of the ambient gas stream into an ultra-high purity buffer gas such as nitrogen, thereby avoiding the gas-contamination issue (Voisin et al., 2003). These designs potentially restrict the analyzable size range due to the added aerosol mobility requirement and can lead to loss of semi volatile components during collection given that the particles are no longer in equilibrium with the ambient gases and are confounded by the equilibrium or induced charge distribution on the particles of a given diameter. Moreover, materials that are best for transmitting gases are not necessarily the same as types which are best for transmitting particles. These issues suggest that the gas analysis should be separated from the particle collection and desorption analysis to minimize cross-talk between these measurements and to optimize the transmission and artifact determinations for a given phase.

We developed a novel approach that captures the evolution and molecular composition of both gas and particle components with separate optimized inlets utilizing a single chemical ionization mass spectrometer. The Filter Inlet for Gases and AEROsols (FIGAERO) provides a simple platform for ambient air analysis using three specialized ports; one port for particle collection on a Teflon filter, a second for thermal desorption of particles on the filter using a temperature-controlled ultra-high purity (UHP) N_2 stream, and a third for direct sampling of ambient air. The filter is moved between the collection and desorption ports automatically by means of a linear actuator. In this paper, we assess the capabilities of this inlet in terms of its particle collection efficiency, linearity, reproducibility, the magnitude of the instrumental background in the particle phase measurement and the associated minimum detectable concentration of an individual component. For this purpose, we coupled the FIGAERO to a high-resolution time of flight chemical ionization mass spectrometer (HRToF-CIMS) (Aljawhary et al., 2013; Mohr et al., 2013; Yatavelli et al., 2012) to study α-pinene oxidation in laboratory chambers and to measure ambient air in the boreal forest of Finland. We report a wide suite of carboxylic acid containing compounds having oxygen to carbon ratios (O/C) ranging from 0.2 to >1 and carbon numbers

from 1 to 30. These compounds were present to some degree both in the gas-phase and in the organic aerosol (OA) fraction of particles of size 0.01-1 μm. Particles in this size range were measured with unit collection efficiency (>99.997%) and were analyzed by thermal desorption HRToF-CIMS, approximately hourly, while gases were measured at 1 Hz or faster. We discuss opportunities to infer information on volatility, partitioning, and thermal decomposition using the combined gas and particle thermal desorption data.

3.2 INSTRUMENT DESCRIPTION.

The FIGAERO is essentially a multi-port inlet manifold that operates in two distinct modes: (1) ambient air sampling with trace gas analysis during simultaneous particle collection on a PTFE filter via separate dedicated ports, and (2) temperature-programmed thermal desorption of the collected particles in UHP N_2 with the detection of the desorbed vapors via a separate dedicated port. The two modes are fully automated and programmable allowing for continuous online sampling. In this section we describe the FIGAERO manifold in detail, its operation, and coupling to an HRToF-CIMS.

3.2.1 *FIGAERO Design.*

The FIGAERO was designed with the goal of measuring both gas and particle composition with minimal contamination to each phase from the other (cross-contamination). Towards this end, we designed a manifold with two separate inlet and exit ports. One exit port is used for sampling and analyzing gases, and the other for sampling and analyzing vapors arising from the thermal desorption of collected aerosol. A moveable tray holding a filter is used to select between these two states. Figure 1A shows a schematic section view of the FIGAERO which is comprised of four principle components: (1) the main manifold (green) which provides the platform for connecting to the analysis instrument as well as the sampling pump; (2) the inlet plate (grey) which provides the interface to the sampling inlets; (3) the moveable tray (red), which acts as a valve, and carries the primary FIGAERO particle collection filter; (4) a particle blanking manifold which is periodically used to block particles from reaching the primary collection filter in the FIGAERO to determine filter-related background signals. Also shown for reference is the

ion-molecule reaction region (IMR, grey) of the HRToF-CIMS which is below the main manifold.

The main FIGAERO manifold is made entirely of PTFE to minimize gas-surface interactions and is 105 x 55 x 35 mm in size. The Teflon manifold houses a series of dynamic o-ring seals, and the two selectable exit ports for chemical analysis, which in this case lead to the ionization region of the mass spectrometer, and three additional ports for connecting to sampling pumps. The selectable exit ports sit within the center of a NW40 clamp flange machined into the Teflon manifold that facilitates coupling to our mass spectrometer. A rectangular slot cut into the main manifold allows a linearly actuated tray to slide parallel to the inlet and outlet faces of the manifold and perpendicular to the flow direction. This tray is made of PTFE and houses a 24 mm Zefluor PTFE filter (Pall Corp.) with a built-in filter support to reduce filter deflection during sampling and heating. The tray is moved to engage different operation modes, and to couple a specific exit port on the manifold to be sampled by the mass spectrometer.

The moveable PTFE tray is compressed against the inlet face of the main manifold by a 6 mm thick stainless steel plate. This plate serves as the connection point to ambient air and UHP N_2 used for the temperature-programmed thermal desorption. Two Swagelok compression tube fittings for 19 and 25 mm (3/4" and 1") OD tubes are welded onto opposite ends of the plate to provide an interface between sampling inlets and the FIGAERO. The 19 mm OD fitting is used to sample ambient air directly through the manifold for detection of gases and is bored out so that a 19 mm OD PTFE inlet tube can slide through the inlet plate thereby avoiding contact of gases with the stainless steel walls. The other fitting is used to draw ambient air across the Teflon filter for particle collection. In the center of the top plate a 12.5 mm (1/2 ") OD thin walled (0.5 mm wall thickness) stainless steel tube is socket welded and wrapped with heat tape and insulation. This tube is used to deliver heated UHP nitrogen to the PTFE filter during a temperature-programmed thermal desorption. The exterior of the stainless steel tube is temperature controlled via a MICROmega PID temperature controller (Omega Engineering). The interior of the heating tube is filled with steel wool to facilitate heat transfer so that the exiting gas stream temperature is uniform before passing over the filter.

3.2.2 *HR-TOF Coupling.*

The FIGAERO collector was specifically designed for coupling to a HRToF-CIMS, however it could easily be adapted to other analytical instruments. The HRToF-CIMS employed here has been described previously (Aljawhary et al., 2013; Mohr et al., 2013; Yatavelli et al., 2012). Briefly, using a Tofwerk (Tofwerk AG, Thun, Switzerland) HToF-MS with an atmospheric pressure interface (APi), a collaboration between the University of Washington, Aerodyne Research Inc, University of California San Diego, and University of Colorado, led to the development of a reduced pressure selected-ion chemical ionization mass spectrometer (Bertram et al., 2011; Yatavelli et al., 2012). The high time resolution acquisition of the entire mass spectrum and the high mass resolving power (R>5000 V mode) allow for de-convolution of multiple ion compositions at a given nominal mass across the entire spectrum. The combination of mass resolving power and mass accuracy, which we find to be 10 ppm or better when assessing the location of known ions allows the elemental composition of dominant ions to be confidently assigned up to and often beyond 400 Th.

Chemical ionization provides a sensitive and selective method of detecting various volatile and semi-volatile organic compounds (VOC and SVOC) as well as inorganic compounds. Its selectivity is largely defined by the reagent ion chosen. Herein, we show results from acetate negative-ion proton transfer (Bertram et al., 2011; Veres et al., 2008; Yatavelli et al., 2012) for selective detection of organic acids, as well as Iodide adduct ionization (Aljawhary et al., 2013; Kercher et al., 2009; McNeill et al., 2007) which has been used to measure organic acids, more general oxygenated organic products as well as inorganics. Example mass spectra from α-pinene ozonolysis using acetate as the reagent ion are shown in Figure 2. The thermal desorption spectrum is shown in red and shifted 0.5 amu to the right for clarity; the adjacent gas phase signals are shown in black. Regions of the spectra containing well-known α-pinene ozonolysis carboxylic acid products and trace highly oxygenated acids are shown expanded in panels b and c. The excellent signal-to-noise (S/N), and low backgrounds at high mass-to-charge (m/Q) make ultra-trace gas phase components detectable and identifiable at concentrations well below 1 ppt as discussed later.

To couple the FIGAERO to our HRToF-CIMS we use two separate critical orifices, each of which allow 2 slpm to enter the mass spectrometer. The moveable tray that carries the filter and toggles orifices is designed such that each mode (gas or particle analysis) is mutually exclusive, that is, only one orifice at a time is open to the mass spectrometer. Because our ionization region is operated at a reduced pressure (~80 torr) the instrument is sensitive to pressure perturbations during the switch between modes when both orifices are briefly open as the movable tray is actuated. To avoid loss of vacuum conditions in the mass spectrometer, we actively pressure control (to within +/- 0.1 torr) the ionization region, i.e. the IMR, using a servo-controlled vacuum valve upstream of the vacuum pump. As the switch begins the servo-controlled vacuum valve is actuated to the fully open position dropping the ionization region pressure to a safe level for the switch. After the switch is complete, normal operation pressures are restored.

To improve the instrument response time we actively heat the IMR to 50-60 °C. This temperature range is chosen such that particles in the gas sample stream do not efficiently volatilize and the decomposition rate of large molecular weight compounds is slow during the ~100 ms transit through the IMR. To shield the IMR and FIGAERO from stray fields induced by heaters or other sources we electrically connect the IMR and the FIGAERO inlet plate together to provide a uniform field in the ionization region: this voltage is typically set to ground.

3.2.3 *FIGAERO Operation.*

The operation of the FIGAERO is fully automated using a LabVIEW program. A typical sampling and filter desorption time series for various ion elemental compositions from a steady state α-pinene ozonolysis mixture is shown in Figure 3 as a guide. The instrument is continuously cycled between gas (Figure 3, ‘S’) and particle analysis modes (Figure 3, ‘TD’) with periodic determinations of the desorption signal in the absence of particles, but in the presence of gases, which we refer to as the ‘filter blank’ and discuss in greater detail in the next sections. In Figure 3, these filter blanks are the thermal desorptions (‘TD’) that appear just following the sampling periods labeled ‘FB’.

During gas analysis (Figure 3, ‘S’), ambient air is sampled through a 19 mm OD PTFE tube at a flow rate of up to 22 slpm (limited by the turbulence transition region). While the flow is entirely adjustable, we use large flows to optimize transmission of low volatility or ‘sticky’ compounds, and to dilute the flux of compounds from the inlet tubing walls. The sample flow is drawn through 4 symmetrical 3.15 mm holes, radially arranged on the same plane as the selectable exit ports in the main PTFE manifold. The placement of these pumping holes reduces the dead volume within the manifold and allows for sampling from the centerline of the main flow. Flow through these holes is routed internally to two 6.25 mm ports on the external faces of the main manifold. A mass flow controller (MKS 1179a 20000 sccm) in line with the vacuum pump maintains the inlet flow to within 2% of the desired value and a three-way solenoid valve provides a by-pass so that the inlet tube used for detection of gases is continuously flushed when not sampled by the mass spectrometer, such as, during the particle analysis mode.

During gas analysis, ambient air is simultaneously drawn by a vacuum pump via the separate 25 mm OD port into the manifold and through the PTFE filter to collect aerosol particles. Upstream of the entrance port an optional 2 μm impactor or cyclone is used to remove large particles prior to sampling. The large diameter conductive stainless steel tubing allows for laminar flow to be maintained up to 30 slpm (Reynolds number Re=1930). A large laminar particle sample flow rate shortens both inlet residence time for optimal transmission of smaller particles and the time necessary to collect sufficient mass for subsequent desorption analysis. The particle sample flow is monitored by a mass flow meter (MKS 1179a) to track the total volume sampled over the collection period.

After a predetermined time for gas phase analysis and particle collection, the switch from gas analysis to particle analysis by thermal desorption from the filter (Figure 3, ‘TD’) is initiated. The switching is achieved by actuating a mini linear actuator (Firgelli Technologies, L16) which slides the central tray until the filter is moved from the collection stage to the desorption stage. This process blocks the exit port used for gas phase analysis and simultaneously opens the exit port used exclusively to analyze vapor arising from the thermal desorption of material collected on the filter. By physically changing stages and exit ports we minimize contamination of the particle-phase analysis by semi-volatiles present from the gas phase analysis that may have

adsorbed to the surrounding surfaces of the manifold. That is, without moving the filter to a clean desorption region there would be a much higher non-particle background during desorptions, degrading detection limits and adding greater ambiguity to the primary phase (gas or particle) of the detected compounds.

As the switch to particle phase analysis begins, a mass flow controller delivers 2 slpm of UHP N_2 across the filter. The flow rate across the filter is set in our application primarily by the mass spectrometer requirements. The N_2 is delivered through the central 'heating' tube on the manifold (see Figure 1) which is ramped from ambient temperature up to 200 °C at a specified ramp rate. This ramp rate sets the resolution in temperature space and amplitude of the signals detected during desorption. For example, for a given particle mass on the filter, a faster ramp rate would amplify the S/N (signal to noise ratio), allowing for improved detection of trace components, whereas a slower ramp rate allows for better separation of desorbing compounds in a volatility sense as the evaporation rate is proportional to the vapor pressure at a given temperature. We have empirically determined that a ramp rate between 10-50 °C/min provides a good balance between these two thermogram properties (S/N and resolution).

After the temperature ramp is complete, the N_2 stream is kept at 200 °C for approximately 20 minutes as part of a 'soak', such that signals return to near their pre-heating levels. The aim of the soak is to provide sufficient time at an elevated temperature so that all the organic material is driven from the filter and that there is not residue remaining, which could accumulate and contribute to the blank signals. The 'soak' time is set by the typical mass loading on the filter and the volatility of the aerosol mass. Typical desorption times, including the soak period, have been on the order of 30-45 min at a ramp rate of 10-20 °C/min for both ambient and chamber studies, and can be shortened by ~ 10 min using a faster ramp rate. The return to gas analysis mode follows the same procedure as the switch to particle phase analysis mode, but in reverse. The full switch takes approximately 10 seconds.

3.2.4 *Chamber and Field Site Descriptions*

The FIGAERO has been deployed to a variety of locations for use both on laboratory chambers as well as in the field. The first application of the collector was to study α-pinene ozonolysis at the Univeristy of Washington, followed by α-pinene ozonolysis and photochemical OH oxidation at the Jülich Plant Atmosphere Chamber (JPAC, Jülich Forschungszentrum, Germany). A subsequent deployment to Hyytiälä, Finland, a monoterpene-dominated boreal forest site provides ambient data to compare to the chamber experiments as well as evaluation of the method under field conditions. A description of each location follows below.

3.2.4.1 The University of Washington Chamber.

The University of Washington (UW) chamber was used for optimization and initial testing of the FIGAERO. The chamber consists of a 0.7 m^3 Teflon bag with multiple sampling or fill ports. The chamber is pressure controlled by a servo-controlled valve which regulates the draw of air out of the chamber which is held slightly above atmospheric pressure. The chamber is continuously filled with zero air, generated by a Teledyne zero air generator (Model 701) and set by a 20000 sccm MFC (MKS 1179a). α-Pinene is delivered by a perforated Teflon diffusion tube held at room temperature and mixes with the incoming zero air which contains ozone (O_3) generated by passing 100 sccm of UHP N_2 with 10% O_2 through a UV photolysis cell. The α-pinene mass loading in the chamber is set by the flow through the diffusion tube.

3.2.4.2 Jülich Plant Atmosphere Chamber.

The Jülich Plant Atmosphere Chamber (JPAC) (Mentel et al., 2009) consists of a series of glass chambers housed in separate temperature controlled rooms. We used a 1450 L borosilicate glass chamber housed in a temperature-controlled room held at 15 °C and relative humidity (RH) of 65%. The chamber is operated under steady state conditions and is continuously stirred by a mixer mounted at the top of the chamber. The residence time is on average 45 minutes at a flush rate of ~30 slpm. The chamber is also equipped with different types of UV lamps, one set can be used for photolysis of NO_2 to NO and the other set of lamps for OH production from O_3 photolysis in the presence of H_2O. The OH lamps can be shielded such that the actinic UV flux

and therefore the OH production rate can be varied. We oxidized α-pinene with varying concentrations of O_3 and UV intensity and in the presence and absence of effloresced ammonium sulfate seed particles during a week that was part of a more extensive measurement campaign.

3.2.4.3 Boreal Forest Site.

The FIGAERO was deployed during spring 2013 (April 16 – May 17) at the Station for Measuring Ecosystem-Atmosphere Relations II (SMEAR II) site of the University of Helsinki situated in the Hyytiälä Forestry Field Station in Hyytiälä, Finland (61° 50' 51" N; 24° 17' 42" E). The instrument was housed in a standard mobile office trailer located at the edge of a clearing of a managed 50-year-old stand dominated by Scots Pine (*Pinus sylvestris*). The FIGAERO inlets went straight out of the container through the roof. The FIGAERO was run continuously in the following sampling cycle: ~23.5 slpm of outside air were drawn through the 25 mm (1") OD stainless steel particle phase inlet (length 315 cm, residence time ~3 s, Reynolds number R = 1600) and particles were deposited on the Teflon filter (Zefluor 25 mm, pore size 1 μm, Pall Corp.), while also sampling ambient air through the gas analysis inlet (19 mm (3/4") OD Teflon (PTFE), length 320 cm, R = 2200) at 22 slpm. After each desorption we allowed the N_2 gas stream passing over the filter to cool for 10 min to obtain a measure of instrument backgrounds. After 3 consecutive ambient samples, a filter blank cycle was conducted by putting another filter (Teflo 24 mm, 1 μm pore size, Pall) just upstream (~ 30 cm) of the FIGAERO particle filter.

3.3 FIGAERO PERFORMANCE.

The metrics we used to assess the performance of the FIGAERO design described here are, (1) gas transmission, (2) the particle collection efficiency, (3) the extent to which gas adsorption to the filter contaminates the desorption signal, (4) the reproducibility of the filter and thermal desorption process, (5) detection limits and reliability of the inlet system.

To evaluate the FIGAERO in terms of these metrics we used data obtained from the UW chamber where α-pinene was reacted with excess ozone in the dark to produce semi-volatile oxygenated products and SOA. A portion of this data is shown in Figure 3. The UW chamber

was run in steady-state for extended periods of time (days-weeks) so that multiple samples of a given aerosol population could be measured to determine the FIGAERO reproducibility, response to changing instrument parameters, such as thermal desorption temperature ramp rates and different manifold designs.

3.3.1 *Particle Collection Efficiency and Linearity.*

The FIGAERO collection efficiency was measured with the standard 24 mm Zefluor 1 μm pore size PTFE filters in the moveable tray of the FIGAERO collector. The FIGAERO collector, because it relies on a Teflon filter, has essentially unit collection efficiency (>99.997% of number), independent of particle morphology down to at least 10 nm, the lower limit of detection for our SMPS system (TSI Model: 3080). A 2 μm pore size PTFE filter of the same type had a similar collection efficiency. Thus, virtually all particles are collected by the FIGAERO without requiring perturbations to the sample flow, such as humidification to reduce bounce or for neutralizing surface charges.

An acetate quadrupole (Q-CIMS) was coupled to the FIGAERO to examine the linearity of desorption signals in response to changes in particle mass deposited on the filter. The area under a given thermogram is presumably linearly related to the mass collected and desorbed. While examining the output from the steady-state α-pinene ozonolysis chamber, the particle collection time before each desorption was varied to change the mass loadings on the filter. The absolute mass loadings present on the filter were determined by integrating the aerosol mass concentrations measured by the SMPS over the time particles were collected on the filter. Particle-free filter blanks were done periodically during this process, employing the same collection time of the preceding sample. The filter blank desorption signals were then subtracted from the particle desorptions to obtain blank corrected particle desorption signals. The blank corrected desorption signals, shown in Figure 4, exhibit excellent linearity with mass collected. Linear fits to the data are shown, with a median R^2 of .995 (mean R^2 = .980). Thus, the FIGAERO responds linearly to changes in mass on the filter across a wide spectrum of compounds.

3.3.2 *Instrument Backgrounds, Artifact Determinations, and Detection Limits.*

Instrument backgrounds arise from off-gassing of semi volatiles adsorbed to the walls of the inlet tube or IMR or from impurities in the reagent ion precursor and carrier gas. Periodically delivering UHP N_2 or zero air into the ionization region provides one measure of instrumental backgrounds from that specific region. These backgrounds are subtracted from the ambient gas phase signals. Additionally the gas phase inlet can be periodically overflowed with zero air or a subset of the flow can be drawn through a chemical scrubber to measure the inlet or isomeric or isobaric contributions to the measured ion signals. When using a long inlet line, wall collisions or evaporation from the walls will become an important sink or source, respectively of trace gases and can thus cause slower time-response or higher detection limits for low volatility compounds. For an analogous aircraft inlet system with the same flows and internal geometry as we use with the FIGAERO, response times of seconds or less are attainable for intermediate volatility compounds. Memory inside the ionization region contributes to a multi-exponential response over longer timescales (minutes), the timescale of which can be adjusted by the IMR temperature. We estimate that for our ionization region temperature and residence time (T_{IMR} 50-60 C and τ_{IMR}~100 ms) evaporation of particle phase compounds is a relatively minor contribution to the observed gas-phase concentrations [see e.g., Yatavelli and Thornton, 2010]. The coupling of the FIGAERO to detectors or ionization regions that operate at higher temperatures or longer residence times would likely result in a contamination of the gas phase signals by vaporized particles and would require different quality controls to evaluate the effect of volatilizing particles inside the instrument.

Similarly, the desorption signal is composed of that from particle-bound compounds and a non-particulate background which likely arises from gases that had adsorbed on the PTFE filter and other surfaces in the apparatus during sampling. To routinely measure this non-particulate background ("filter blank") we developed a filter blanking manifold identical to that in the FIGAERO collector, to automatically put another PTFE filter just upstream of the FIGAERO (see Figure 1). During a filter blank determination, ambient air is then drawn through both the "front" filter, which removes >99.97% of entering particles but largely leaves semi-volatile gases unperturbed, as well as the FIGAERO filter for the same duration as a normal particle sample collection. The corresponding signal from the "particle-free" desorption that immediately

follows is then integrated and subtracted from the ambient particle samples to obtain a desorption signal from particles only. When not in use, a small purge flow (~100 sccm) of 150 °C N_2 is passed across the front filter to desorb organic aerosol collected during the zeroing process.

The magnitude of these filter blanks depends on the sampling environment (chambers or polluted air *versus* clean remote air). They can range from nearly undetectable signals, to being equivalent to 100's of nanograms depending on the specific compound and sampling circumstances (see, e.g. Figure 3 for relative differences). We have found that the filter blank for a given desorbing compound is generally correlated with the gas phase concentration of that compound (R^2 typically ~0.6-0.7), suggesting that gases which had adsorbed to the filter and subsequently desorb during the filter heating contribute significantly to the variability in the filter blank. We attribute the peak in signal during a filter blank desorption (see, e.g., Figure 5) to gases that had adsorbed to the filter and the baseline that the peak appears on to off-gassing from the ionization region of the mass spectrometer. The contribution of the ionization region to the total blank signal is likely to change as a function of gas loading, but with a slower timescale than the filter.

The instrument background and the ability to adequately capture its variability, whether in the gas or particle mode, ultimately set the detection limit for a given compound. We have coupled the FIGAERO to a HRToF-CIMS, which will have unique sensitivity, electronic noise, detector stability, etc. This discussion is therefore not general to all potential applications of the FIGAERO, but instead provides a guide for what likely controls the detection limits when using the FIGAERO. In terms of gas-phase compounds the factors affecting detection limits of our instrument are largely similar to any CIMS instrument as we designed the FIGAERO to be nearly indistinguishable from a standard CIMS inlet assembly. Thus, for a typical sensitivity of 30 counts s^{-1} ppt^{-1}, electronic noise < 0.1 counts s^{-1}, a background typical of both formic acid (~400 counts s^{-1}) or a C_9 pinene acid (~4 counts s^{-1}), and Poisson counting statistics, a detection limit of 2 and 0.3 ppt or less can be achieved, respectively, defined as the concentration that yields a S/N ratio of 2 in 1 second, assuming minimal interferences or inlet memory effects.

The detection limit for particle phase compounds is largely set by variability in the filter blank. To assess this variability, multiple samples were taken from the steady state ozonolysis chamber

(see Figure 5) to measure the reproducibility at constant loadings of gases and aerosol. The variability (1σ) in the blank measured by the adjacent difference between over 15 determinations was approximately 2.5% of the signal for the majority of ions. We therefore take 5% to be the uncertainty in any single blank measurement. Typically, atmospheric samples are collected between filter blank determinations, and thus two blank measurements are averaged or interpolated before subtracting from the atmospheric sample. The uncertainty in the blank applied to the data is then found by adding in quadrature. We define the detection limit for a particle component as 3x this uncertainty in the blank, examples of which are shown in Table 1 for compounds detected as the following ions $C_8H_{11}O_6^-$, $C_5H_5O_6^-$, $C_9H_{13}O_4^-$, $C_{10}H_{15}O_7^-$, $C_{10}H_{13}O_8^-$, and $C_{10}H_{15}O_3^-$. These are representative compounds spanning a wide range in both volatilities and the typical magnitude of signal relative to blank. Table 1 shows typical detection limits obtained while sampling on chambers and in a remote forest environment. For this purpose, ions signals were converted to mass using a formic acid sensitivity, typically of order 10 counts per second (cps) per ppt. The detection limits in the field are significantly larger than those on the steady state chambers because larger atmospheric variability in gas-phase abundance, temperature, relative humidity, etc., induces a larger variability in the blank measurements. By tracking the blank regularly, the variability is accurately captured, and thus the detection limits are kept within a workable range.

Despite the incorporation of these quality control checks into the FIGAERO operation, care must still be used when interpreting the implied phase partitioning that results from the measurement of a compound in the gas and particle phase. For example a very “sticky” low volatility gas that is nearly entirely lost to a Teflon surface with near unit efficiency per collision will be measured as a particle component as it will contribute to the particle desorption signal but will have a negligible contribution to the filter blank because the front filter will scrub it. Similarly semi-volatile and volatile compounds that would normally be entirely in the gas phase can through adsorption and absorption adhere to Teflon surfaces (Matsunaga and Ziemann, 2010). We cannot distinguish between adsorption or absorption, but routinely measure the sum of them using the blanking filter. This issue is not entirely problematic because a vapor that is entirely removed by a Teflon surface is likely to partition to the particle phase. Semi-volatiles that evaporate from the filter during collection, due to a change in the ambient air concentration represent a negative bias

to the particle signal. However, the continuous exposure of the collected particles to a high flow of ambient air for relatively short particle collection times (~30 min) makes this issue less of a problem compared to high-vol samples collected over 12 to 24 hrs (Turpin et al., 2000), or for particles collected at reduced pressure or in UHP N_2.

3.3.3 *Thermal Desorption Reproducibility and Volatility Separation.*

To examine the reproducibility of the thermal desorption signals, we coupled the FIGAERO to a HRToF-CIMS, operating in acetate mode, and sampled continuously from the UW steady state α-pinene ozonolysis system for approximately two days. In Figure 5 (top panel) the particle desorption signals (lines) and corresponding particle-free filter blank signals (open symbols) are shown on a log scale for several ion compositions obtained during this two-day period. In the bottom panel of Figure 5, the particle desorptions are reproduced on a linear scale for greater clarity. The integrated areas and the shapes of the desorption profiles are highly reproducible for both particle desorptions and filter blanks. With a constant collection time, ramp rate, and particle concentration, not only is the integrated desorption area the same within 5-10 % but also that the location of the maximum signal in temperature space is the same within ~2 °C showing reproducibility in both absolute mass recovered and thermal behavior. This reproducibility is essential for volatility estimation and separation of desorbed aerosol components and gives confidence that the Teflon filter is robust to repeated exposure to temperatures > 200 °C.

The reproducibility of the desorption profiles suggests a fundamental connection between characteristics of the desorption profile and the chemical and physical properties of the compounds in the particle phase. To examine this connection, and to facilitate the development of a representative volatility axis we deposited mixtures of known carboxylic acid compounds on the Teflon filter, and subsequently conducted thermal desorptions with detection by Iodide adduct HRToF-CIMS. In Figure 6a, we show the corresponding desorptions for a few representative compounds that bracket the full range of behavior from the mixture. The separation in temperature space follows the expected pattern where higher volatility compounds desorb at lower temperatures and lower volatility compounds desorb at higher temperatures. Temperature programmed thermal desorption profiles, which for pure compounds are effectively

a measure of the evaporation rate and thus the temperature-dependent equilibrium vapor pressure, have been used to extract the enthalpy and entropy of vaporization of various organic aerosol surrogates (Bilde and Pandis, 2001; Cappa et al., 2008; Salo et al., 2010; Yatavelli and Thornton, 2010). In this experiment all ions show a clear and smooth monotonic peak during the desorption, signifying little contamination at those masses from other interferences (discussed later). In Figure 6b we scatter the temperature of maximum desorption signal (T_{max}) with ΔH_{sub} in an effort to calibrate the desorption temperature axis. Letters correspond to the identifier (ID) listed in Table 2 along with the source for the literature ΔH_{sub} used in the correlation. In Figure 6c we correlate T_{max} with published vapor pressures; the correlation with enthalpy of sublimation is much stronger presumably because of the smaller relative error in enthalpy determinations than for vapor pressure measurements (see Table 2).

We find an approximately linear relationship ($R^2 = 0.82$) between the temperature at which the desorption signal for a given compound reaches a maximum (T_{max}) and the enthalpy of sublimation, ΔH_{sub}, a physical parameter useful in further developing partitioning models (Donahue et al., 2006; Epstein et al., 2010). Using the T_{max} provides an estimate of volatility that is independent of the absolute evaporation rate, which would require knowing the instrument's detection sensitivity to every compound detected.

By using known compounds with well-defined ΔH_{sub} values, and the inherent reproducibility of the desorption profiles, the volatility scale based on T_{max} can be calibrated. An effective enthalpy of "desorption" ΔH_{eff} can then be estimated for hundreds of compounds detected in the atmosphere or laboratory chamber studies. We stress that the ΔH_{eff} we obtain from mixtures of unknown contents is intrinsic to the FIGAERO process and properties of the aerosol which may or may not be knowable by this method, and therefore is not necessarily a measure of the actual ΔH_{sub}. For example formic acid is often detected in the particle-phase desorptions. The corresponding desorption profile maximizes at high temperatures more consistent with a much lower volatility compound. This behavior suggests that its source is likely not actual formic acid which has physically partitioned to the aerosol, but rather a decomposition fragment of larger thermally unstable compounds that have a lower volatility. Nonetheless, this approach provides a physically relevant scale with which to compare compounds within a sample, or across different

samples. Applying the calibrated relationship between the observed T_{max} and ΔH_{sub} we find carboxylic acids that desorb from α-pinene SOA separate into two broad volatility bins. These two bulk bins each explain approximately half of the total desorption signal, and correspond to an ΔH_{eff} of ~140 kJ/mol and ~240 kJ/mol, respectively.

Our method of determining ΔH_{eff} is significantly different than previous measures of the evaporation rates and volatility estimations, such as those using thermal denuder tandem differential mobility analyzers (DMAs) (Bilde and Pandis, 2001; Salo et al., 2010), making direct comparisons difficult. In our approach, the gas phase concentration of a desorbing compound arises only from that desorbed from the filter, and is continuously diluted away into the sample flow, whereas other methods can initially have high gas loadings, in addition to those generated from volatilizing the particles before being denuded (Bilde and Pandis, 2001; Salo et al., 2010). Moreover, we have a relatively slow temperature ramp, and exposure to hot nitrogen for 15 minutes or longer, whereas thermal denuders typically have residence times of less than a few tens of seconds. Finally, chemical ionization methods such as those that we use, have an inherent selectivity, e.g. to carboxylic acids. The effective enthalpies of evaporation are then only relevant to compounds that are efficiently ionized and detected. That said, the two effective enthalpies of evaporation for carboxylic acids in α-pinene ozonolysis SOA reported above imply that a significant fraction have much lower volatilities than consistent with common ozonolysis products such as pinonic and pinic acids or the bulk mass as inferred from thermal denuder studies (Bilde and Pandis, 2001; Salo et al., 2010). We show that, consistent with previous studies of the molecular composition of SOA, these lower volatility components are likely larger molecular weight dimers, trimers, or other oligomeric or extremely low volatility compounds which thermally decompose during desorption.

3.3.4 *Thermogram Fitting and the Role of Decomposition.*

The thermogram (desorption signal *versus* temperature) for a single compound should have a single mode, as evidenced by the profiles shown in Figure 6 which were produced from the deposition of a mixture of known compounds to the filter. However, thermograms for individual ions in more complex SOA mixtures reveal multiple features, e.g. shoulders or multiple peaks,

throughout the thermal evolution of the collected samples; examples are shown in Figures 5 and 7. To investigate the source of and thus information carried by the secondary desorption features we applied a custom non-linear least squares peak fitting routine. First, single-mode thermogram peaks are identified and standardized on a normalized width scale. The resulting normalized peaks are averaged to obtain a typical thermogram peak shape that presumably represents the desorption of a single component. An iterative fitting routine using the Levenberg-Marquardt algorithm for nonlinear least squares problems fits the multimodal thermograms by applying a variable number of thermogram peaks having the average desorption peak shape. The number, location and amplitude of each additional desorption peak within a thermogram are optimized to explain the total thermogram of a given ion. To allow for individual compounds having slightly different desorption profiles, the width of the typical desorption peak shape is allowed to vary by up to 30% based on fitting a range of thermograms from pure component desorptions.

Example fits of the $C_8H_{11}O_4^-$ thermogram are shown in Figure 7. Under α-pinene ozonolysis conditions, this ion displayed a bi-modal thermogram, with significant high temperature tailing compared to the typical thermogram peak shape (Figure 7, bottom left). However, the signals within these three regimes (see Figure 7) systematically changed in a relative sense, when α-pinene oxidation was dominated by OH instead of O_3 (Figure 7, bottom right). The top panel of Figure 7 shows a time series of the corresponding thermogram fits in each of the three integration regions. During ozonolysis, the primary and secondary thermogram peaks grow proportionally in the aerosol phase when inorganic seed concentrations are increased during steady-state α-pinene ozonolysis conditions. However, when the UV lights are turned on, generating significant OH ($10^7 – 10^8$ cm^{-3}), the first peak in the thermogram grows significantly relative to the second. Similar and, at times, more dramatic changes in the distribution of signal during thermograms are observed for many other ions measured in this experiment.

The multi-modal thermograms for an ion with the same elemental composition likely arise from either isomers having different volatilities or from thermal decomposition of larger molecular weight components prior to or during desorption from the condensed phase. For the specific example of $C_8H_{11}O_4^-$, the former case seems unreasonable given that there are a limited number of configurations that lead to two isomers having vapor pressures that are different by several

orders of magnitude. The secondary thermogram maxima occur at higher temperature than consistent with the relationship between effective enthalpy of evaporation and composition (e.g. Figure 6). The change in the relative contribution of the primary and secondary thermogram peaks to the total desorption signal at $C_8H_{11}O_4^-$ suggests that, compared to intense oxidation by OH, ozonolysis favors the formation of a larger molecular weight compound, such as a more highly oxidized monomer, dimer, trimer, or other oligomeric compound, that can decompose into the C_8 molecule. Similar multi-modal thermograms are often observed for a large number of different ion compositions spanning a large m/Q range and average oxidation state.

Such issues are likely important for testing gas-particle partitioning theories, but they are not unique to the FIGAERO. Instead, most methods employing thermal desorption will be impacted by thermal decomposition. We find that thermal decomposition can be a significant contribution to the total desorption signal of an ion consistent with previous work (e.g. (Docherty et al., 2005)). In the example shown in Figure 7 (top), the secondary maximum can be ~50% of the total signal and even higher for other ions. Decomposition can therefore lead to incorrect inferences into partitioning of semi-volatile acids if not properly addressed. With the FIGAERO we appear to be able to separate, to a first approximation, the effect of thermal decomposition by utilizing the reproducibility of the thermal desorptions and by fitting the thermograms as demonstrated above. This ability allows us to more accurately estimate partitioning, quantitatively track a contribution to particle mass that stems from compounds that do not survive thermal desorption, and develop spectral fingerprints that likely represent thermal "cracking" of these compounds. One feature that likely aids in this separation is that the FIGAERO is made entirely of Teflon (manifold and collection surface) resulting in components only loosely bound to the surface (if interacting with the surfaces at all), and thus a better separation of compounds physically adsorbed to the aerosol undergoing volatilization from those derived from decomposition is made possible.

3.4 Application to Chamber and Field Studies and Instrument Comparisons.

3.4.1 *Jülich Plant Chamber Experiments.*

The experiments at JPAC were designed to investigate the formation of α-pinene derived aerosol and new particle formation events. A prototype of the FIGAERO was deployed to measure aerosol composition across a wide variety of chamber conditions, including the addition of inorganic seed aerosol to α-pinene ozonolysis products as well as varying levels of ozone, α-pinene, and OH. α-Pinene was added using pure diffusion sources and reacted with ozone, which was held at roughly 85 ppb. The precursor VOC concentrations were measured by a proton transfer mass spectrometer (PTRMS) (Lindinger et al., 1998) at the inlet and outlet of the chamber tracking α-pinene reacted which was typically ~20 ppb. The chamber was run at steady-state with slow changes so that the FIGAERO could take multiple samples while chamber conditions evolved and reached steady-state as determined by the concentrations of aerosol mass and a wide-suite of semi-volatile gas-phase products. Aerosol loadings were measured with an HRToF-AMS (DeCarlo et al., 2006) as well as SMPS (TSI Model 3080) and PSM (Particle Size Magnifier Airmodus). The FIGAERO-HRToF-CIMS was configured for detection of carboxylic acids using acetate ionization. Iodide adduct ionization was employed towards the end of the measurement campaign. A time series of AMS organic mass concentration, and the FIGAERO-HRToF-CIMS measurement of total carboxylic acid (C_8-C_{10} green circles) and sulfur-containing compounds (red squares) in the particle phase are shown in Figure 8 (top panel). The lower panels show individual ions measured in both the gas and particle phase, and highlight the changes in aerosol composition and loading with changes in seed addition as well as the presence of UV radiation (OH oxidation) towards the end of the week long measurements. These individual ions show different responses from each other, in both the gas and particle phases, to the various conditions employed on the chamber. As hundreds of ions were tracked, there is a continuum of responses that is likely best analyzed using various statistical factorization approaches (Ulbrich et al., 2009). At all times the FIGAERO provides detailed information on the specific composition of the aerosol and is highly correlated with the organics and sulfate measured by the AMS. A more quantitative comparison that incorporates the full range of typical HRToF-CIMS sensitivities to various acids is forthcoming, but will allow direct assessment of

the fraction of SOA mass that contains a carboxylic acid functionality or that develops such a functionality upon desorption.

After refinements to the prototype deployed at Jülich and further optimization of the instrument tuning, samples were taken from the UW steady-state chamber to gain sampling statistics for further evaluation of the FIGAERO manifold. Experiments were carried out at similar precursor conditions as Jülich but with no addition of seed or UV. In Figure 9 we show the O/C ratio *versus* carbon number for each ion detected, colored blue for gas phase compounds (top), by maximum desorption temperature (middle), and fraction in the particle phase (bottom), and sized by the relative contribution to particle mass based on the desorption signal and molecular weight. A large range of acidic compounds spanning C_1-C_{30} is produced during α-pinene ozonolysis as detected by the FIGAERO. The fraction of a given compound measured in the particle phase (Figure 9 (bottom)) generally follows expected trends with elemental composition, i.e. larger and more highly oxygenated compounds are more strongly partitioned to the particle phase and desorb at higher temperatures. Some compounds at low carbon number stand out for desorbing only at high temperatures (Figure 9 (middle)), and not following the overall trend of increasing temperature required for desorption with increasing carbon number and oxygen content. These compounds are likely decomposition fragments, which would need to be reconciled before testing against partitioning theories, as discussed in section 3.3. If we assume most carboxylic acid compounds are detected with a similar sensitivity in acetate ionization, which is reasonable for more highly oxygenated compounds that tend to be present in SOA, these data imply an average O/C of ~0.6 for α-pinene ozonolysis SOA. This O/C is slightly larger than most published values from AMS data, which range from 0.4 – 0.5 (Ng et al., 2010), though is likely consistent to within the uncertainty of both methods especially given a weighting of our approach towards carboxylic acid compounds.

3.4.2 *Ambient Data at Hyytiälä.*

The remote field site at Hyytiälä located in a boreal forest allows the study of new particle formation events and provides a strong test case for ambient measurements with the FIGAERO-

HRToF-CIMS given the typically low organic aerosol loadings and photochemical activity of spring time in this region.

The instrument operated nearly continuously for 3.5 weeks, with most interruptions related to power outages. Acetate ionization was employed for most of the deployment; with a short time at the end of the period spent using Iodide adduct ionization. Figure 10 summarizes some performance metrics and initial results from this deployment. In the upper left panel, we show two days of both ambient air signals and background determinations for CHO_2^- and $C_{10}H_{15}O_3^-$, which we attribute to formic acid and a monoterpene derived acid, most likely pinonic acid. Both the C_1 and the C_{10} compound continually exhibit significant signal above background. In the upper right panel, we show one day of raw filter desorption data for $C_8H_{11}O_4^-$ and $C_9H_{13}O_4^-$, which represent two of the more abundant ion compositions measured in the particle phase. Three ambient desorptions were followed by a filter blank desorption (described above). Even though particle mass loadings were generally low, the integrated ambient desorption signals are higher than the variability in the integrated blank desorption signals. In the middle panel we show the time series of ionic compositions consistent with formic acid and pinonic acid (or a similar monoterpene derived acid) as measured in the gas-phase. Ion count rates were converted to mixing ratios using the sensitivity to formic acid determined continuously on site with a C-13 labeled formic acid permeation tube. Pre and post-campaign laboratory calibrations confirmed a similar sensitivity to pinonic acid. These two compounds represent the single largest concentration organic acid (formic), often reaching ~1 ppbv at this site, and a typical monoterpene ozonolysis derived acid which reaches maxima of only a few pptv. Other monoterpene acid tracers were typically of similar or lower concentrations in the gas-phase. The CHO_2^- and $C_{10}H_{15}O_3^-$ both exhibited a strong diurnal profile with afternoon maxima which is consistent with a source driven by daytime oxidants and biogenic emissions. In the bottom panel, we show the time series of two ionic compositions, $C_8H_{11}O_4^-$ and $C_9H_{13}O_4^-$, measured in the particle phase. These two compositions are consistent with either norpinic or terpenyllic acids and pinic acid, respectively, and typically comprised a significant fraction (>10%) of the signal detected during desorptions. The particle-phase components have a relatively more muted diurnal cycle than the gas-phase compounds discussed above, likely representing more regionally unified sources, sinks, and distribution of organic aerosol. Minima in the time series often

correspond to strong rain events, and the single maximum shown corresponds to a brief period when the site received air influenced by a nearby sawmill – a well documented point source for monoterpene derived aerosol at this site (Liao et al., 2011).

3.5 CONCLUSIONS.

We present a novel inlet for measuring both gas and particle composition at a molecular level. While by no means free of artifacts, it provides a platform, which directly measures the dominant artifacts contributing to aerosol desorptions by gases. By coupling the FIGAERO to a HRToF-CIMS we are able to report molecular formulas for detected compounds as well as partitioning related volatility measurements. Further work determining the remaining sources of blank signals will remain an important step towards lowering detection limits and improving measurement reproducibility, however in its current state the FIGAERO is well suited for both chamber measurements as well as measurements in remote locations where organic aerosol and gas loadings are low. The FIGAERO thermograms provide additional insight into the role of thermal decomposition and add an additional degree of separation to the aerosol composition data, which until now has remained unexplored with negative-ion HRTOF-CIMS. Further application of the FIGAERO to chambers as well as ambient measurement campaigns will help improve models by increasing our understanding of OA composition as well as volatility and partitioning.

References:

Aljawhary, D., Lee, A. K. Y. and Abbatt, J. P. D.: Application of high resolution Chemical Ionization Mass Spectrometry (CI-ToFMS) to study SOA composition: focus on formation of oxygenated species via aqueous phase processing, Atmos. Meas. Tech. Discuss., 6(4), 6147–6186, doi:10.5194/amtd-6-6147-2013, 2013.

Bertram, T. H., Kimmel, J. R., Crisp, T. A., Ryder, O. S., Yatavelli, R. L. N., Thornton, J. A., Cubison, M. J., Gonin, M. and Worsnop, D. R.: A field-deployable, chemical ionization time-of-flight mass spectrometer, Atmos. Meas. Tech., 4(7), 1471–1479, doi:10.5194/amt-4-1471-2011, 2011.

Bilde, M. and Pandis, S. N.: Evaporation Rates and Vapor Pressures of Individual Aerosol Species Formed in the Atmospheric Oxidation of α- and β-Pinene, Environ. Sci. Technol., 35(16), 3344–3349, doi:10.1021/es001946b, 2001.

Bilde, M., Svenningsson, B., Mønster, J. and Rosenørn, T.: Even−Odd Alternation of Evaporation Rates and Vapor Pressures of C3−C9 Dicarboxylic Acid Aerosols, Environ. Sci. Technol., 37(7), 1371–1378, doi:10.1021/es0201810, 2003.

Canagaratna, M. R., Jayne, J. T., Jimenez, J. L., Allan, J. D., Alfarra, M. R., Zhang, Q., Onasch, T. B., Drewnick, F., Coe, H., Middlebrook, A., Delia, A., Williams, L. R., Trimborn, A. M., Northway, M. J., DeCarlo, P. F., Kolb, C. E., Davidovits, P. and Worsnop, D. R.: Chemical and microphysical characterization of ambient aerosols with the aerodyne aerosol mass spectrometer, Mass Spectrom. Rev., 26(2), 185–222, doi:10.1002/mas.20115, 2007.

Capouet, M. and Müller, J. F.: A group contribution method for estimating the vapour pressures of α-pinene oxidation products, Atmos. Chem. Phys., 6(6), 1455–1467, doi:10.5194/acp-6-1455-2006, 2006.

Cappa, C. D., Lovejoy, E. R. and Ravishankara, A. R.: Evaporation Rates and Vapor Pressures of the Even-Numbered C 8−C 18Monocarboxylic Acids, J. Phys. Chem. A, 112(17), 3959–3964, doi:10.1021/jp710586m, 2008.

Chattopadhyay, S. and Ziemann, P. J.: Vapor Pressures of Substituted and Unsubstituted Monocarboxylic and Dicarboxylic Acids Measured Using an Improved Thermal Desorption Particle Beam Mass Spectrometry Method, Aerosol Science and Technology, 39(11), 1085–1100, doi:10.1080/02786820500421547, 2005.

Chickos, J.S. “Heat of Sublimation Data” in NIST Chemistry WebBook, NIST Standard Reference Database Number 69, Eds. P.J. Linstrom and W.G. Mallard, National Institute of Standards and Technology, Gaithersburg MD, 20899, http://webbook.nist.gov, (retrieved September 26, 2013).

Davidson, C. I., Phalen, R. F. and Solomon, P. A.: Airborne Particulate Matter and Human Health: A Review, Aerosol Science and Technology, 39(8), 737–749, doi:10.1080/02786820500191348, 2005.

DeCarlo, P. F., Kimmel, J. R., Trimborn, A., Northway, M. J., Jayne, J. T., Aiken, A. C., Gonin, M., Fuhrer, K., Horvath, T., Docherty, K. S., Worsnop, D. R. and Jimenez, J. L.: Field-Deployable, High-Resolution, Time-of-Flight Aerosol Mass Spectrometer, Anal. Chem., 78(24), 8281–8289, doi:10.1021/ac061249n, 2006.

Docherty, K. S., Wu, W., Lim, Y. B. and Ziemann, P. J.: Contributions of Organic Peroxides to Secondary Aerosol Formed from Reactions of Monoterpenes with O 3, Environ. Sci. Technol., 39(11), 4049–4059, doi:10.1021/es050228s, 2005.

Donahue, N. M., Robinson, A. L., Stanier, C. O. and Pandis, S. N.: Coupled Partitioning, Dilution, and Chemical Aging of Semivolatile Organics, Environ. Sci. Technol., 40(8), 2635–2643, doi:10.1021/es052297c, 2006.

Epstein, S. A., Riipinen, I. and Donahue, N. M.: A Semiempirical Correlation between Enthalpy of Vaporization and Saturation Concentration for Organic Aerosol, Environ. Sci. Technol., 44(2), 743–748, doi:10.1021/es902497z, 2010.

Gard, E., Mayer, J. E., Morrical, B. D., Dienes, T., Fergenson, D. P. and Prather, K. A.: Real-Time Analysis of Individual Atmospheric Aerosol Particles: Design and Performance of a Portable ATOFMS, Anal. Chem., 69(20), 4083–4091, doi:10.1021/ac970540n, 1997.

Hallquist, M., Wenger, J. C., Baltensperger, U., Rudich, Y., Simpson, D., Claeys, M., Dommen, J., Donahue, N. M., George, C., Goldstein, A. H., Hamilton, J. F., Herrmann, H., Hoffmann, T., Iinuma, Y., Jang, M., Jenkin, M. E., Jimenez, J. L., Kiendler-Scharr, A., Maenhaut, W., McFiggans, G., Mentel, T. F., Monod, A., Prevot, A. S. H., Seinfeld, J. H., Surratt, J. D., Szmigielski, R. and Wildt, J.: The formation, properties and impact of secondary organic aerosol: current and emerging issues, Atmos. Chem. Phys., 9(14), 5155–5236, doi:10.5194/acp-9-5155-2009, 2009.

Hearn, J. D. and Smith, G. D.: A Chemical Ionization Mass Spectrometry Method for the Online Analysis of Organic Aerosols, Anal. Chem., 76(10), 2820–2826, doi:10.1021/ac049948s, 2004.

Holzinger, R., Kasper-Giebl, A., Staudinger, M., Schauer, G. and Röckmann, T.: Analysis of the chemical composition of organic aerosol at the Mt. Sonnblick observatory using a novel high mass resolution thermal-desorption proton-transfer-reaction mass-spectrometer (hr-TD-PTR-MS), Atmos. Chem. Phys., 10(20), 10111–10128, doi:10.5194/acp-10-10111-2010, 2010.

Jayne, J. T., Leard, D. C., Zhang, X., Davidovits, P., Smith, K. A., Kolb, C. E. and Worsnop, D. R.: Development of an Aerosol Mass Spectrometer for Size and Composition Analysis of Submicron Particles, Aerosol Science and Technology, 33(1-2), 49–70, doi:10.1080/027868200410840, 2000.

Jimenez, J. L., Canagaratna, M. R., Donahue, N. M., Prevot, A. S. H., Zhang, Q., Kroll, J. H., DeCarlo, P. F., Allan, J. D., Coe, H., Ng, N. L., Aiken, A. C., Docherty, K. S., Ulbrich, I. M., Grieshop, A. P., Robinson, A. L., Duplissy, J., Smith, J. D., Wilson, K. R., Lanz, V. A., Hueglin, C., Sun, Y. L., Tian, J., Laaksonen, A., Raatikainen, T., Rautiainen, J., Vaattovaara, P., Ehn, M., Kulmala, M., Tomlinson, J. M., Collins, D. R., Cubison, M. J., E., Dunlea, J., Huffman, J. A., Onasch, T. B., Alfarra, M. R., Williams, P. I., Bower, K., Kondo, Y., Schneider, J., Drewnick, F.,

Borrmann, S., Weimer, S., Demerjian, K., Salcedo, D., Cottrell, L., Griffin, R., Takami, A., Miyoshi, T., Hatakeyama, S., Shimono, A., Sun, J. Y., Zhang, Y. M., Dzepina, K., Kimmel, J. R., Sueper, D., Jayne, J. T., Herndon, S. C., Trimborn, A. M., Williams, L. R., Wood, E. C., Middlebrook, A. M., Kolb, C. E., Baltensperger, U. and Worsnop, D. R.: Evolution of Organic Aerosols in the Atmosphere, Science, 326(5959), 1525–1529, doi:10.1126/science.1180353, 2009.

Kercher, J. P., Riedel, T. P. and Thornton, J. A.: Chlorine activation by N_2O_5: simultaneous, in situ detection of $ClNO_2$ and N_2O_5 by chemical ionization mass spectrometry, Atmos. Meas. Tech., 2(1), 193–204, doi:10.5194/amt-2-193-2009, 2009.

Kroll, J. H., Donahue, N. M., Jimenez, J. L., Kessler, S. H., Canagaratna, M. R., Wilson, K. R., Altieri, K. E., Mazzoleni, L. R., Wozniak, A. S., Bluhm, H., Mysak, E. R., Smith, J. D., Kolb, C. E. and Worsnop, D. R.: Carbon oxidation state as a metric for describing the chemistry of atmospheric organic aerosol, Nature Chemistry, 3(2), 133–139, doi:10.1038/nchem.948, 2011.

Lake, D. A., Tolocka, M. P., Johnston, M. V. and Wexler, A. S.: Mass Spectrometry of Individual Particles between 50 and 750 nm in Diameter at the Baltimore Supersite, Environ. Sci. Technol., 37(15), 3268–3274, doi:10.1021/es026270u, 2003.

Liao, L., Dal Maso, M., Taipale, R., Rinne, J., Ehn, M., Junninen, H., ÄIJÄLÄ, M., Nieminen, T., Alekseychik, P. and Hulkkonen, M.: Monoterpene pollution episodes in a forest environment: indication of anthropogenic origin and association with aerosol particles, Boreal environment research, 16(4), 288–303, 2011.

Lindinger, W., Hansel, A. and Jordan, A.: On-line monitoring of volatile organic compounds at pptv levels by means of proton-transfer-reaction mass spectrometry (PTR-MS) medical applications, food control and environmental research, International Journal of Mass Spectrometry and Ion Processes, 173(3), 191–241, doi:10.1016/S0168-1176(97)00281-4, 1998.

Matsunaga, A. and Ziemann, P. J.: Gas-Wall Partitioning of Organic Compounds in a Teflon Film Chamber and Potential Effects on Reaction Product and Aerosol Yield Measurements, Aerosol Science and Technology, 44(10), 881–892, doi:10.1080/02786826.2010.501044, 2010.

May, A. A., Saleh, R., Hennigan, C. J., Donahue, N. M. and Robinson, A. L.: Volatility of organic molecular markers used for source apportionment analysis: measurements and implications for atmospheric lifetime, Environ. Sci. Technol., 46(22), 12435–12444, doi:10.1021/es302276t, 2012.

McKeown, P. J., Johnston, M. V. and Murphy, D. M.: On-line single-particle analysis by laser desorption mass spectrometry, Anal. Chem., 63(18), 2069–2073, 1991.

McNeill, V. F., Wolfe, G. M. and Thornton, J. A.: The Oxidation of Oleate in Submicron Aqueous Salt Aerosols: Evidence of a Surface Process, J. Phys. Chem. A, 111(6), 1073–1083, doi:10.1021/jp066233f, 2007.

Mentel, T. F., Wildt, J., Kiendler-Scharr, A., Kleist, E., Tillmann, R., Dal Maso, M., Fisseha, R., Hohaus, T., Spahn, H., Uerlings, R., Wegener, R., Griffiths, P. T., Dinar, E., Rudich, Y. and

Wahner, A.: Photochemical production of aerosols from real plant emissions, Atmos. Chem. Phys., 9(13), 4387–4406, doi:10.5194/acp-9-4387-2009, 2009.

Mohr, C., Lopez-Hilfiker, F. D., Zotter, P., Prévôt, A. S. H., Xu, L., Ng, N. L., Herndon, S. C., Williams, L. R., Franklin, J. P., Zahniser, M. S., Worsnop, D. R., Knighton, W. B., Aiken, A. C., Gorkowski, K. J., Dubey, M. K., Allan, J. D. and Thornton, J. A.: Contribution of Nitrated Phenols to Wood Burning Brown Carbon Light Absorption in Detling, United Kingdom during Winter Time, Environ. Sci. Technol., 130610071812007, doi:10.1021/es400683v, 2013.

Neuman, J. A., Huey, L. G., Ryerson, T. B. and Fahey, D. W.: Study of Inlet Materials for Sampling Atmospheric Nitric Acid, Environ. Sci. Technol., 33(7), 1133–1136, doi:10.1021/es980767f, 1999.

Ng, N. L., Canagaratna, M. R., Zhang, Q., Jimenez, J. L., Tian, J., Ulbrich, I. M., Kroll, J. H., Docherty, K. S., Chhabra, P. S., Bahreini, R., Murphy, S. M., Seinfeld, J. H., Hildebrandt, L., Donahue, N. M., DeCarlo, P. F., Lanz, V. A., Prevot, A. S. H., Dinar, E., Rudich, Y. and Worsnop, D. R.: Organic aerosol components observed in Northern Hemispheric datasets from Aerosol Mass Spectrometry, Atmos. Chem. Phys., 10(10), 4625–4641, doi:10.5194/acp-10-4625-2010, 2010.

Oja, V. and Suuberg, E. M.: Vapor Pressures and Enthalpies of Sublimation of d-Glucose, d-Xylose, Cellobiose, and Levoglucosan, J. Chem. Eng. Data, 44(1), 26–29, doi:10.1021/je980119b, 1999.

Pankow, J. F.: An absorption model of the gas/aerosol partitioning involved in the formation of secondary organic aerosol, Atmospheric Environment, 41, 75–79, doi:10.1016/j.atmosenv.2007.10.060, 2007.

Pope, C. A., III and Dockery, D. W.: Health Effects of Fine Particulate Air Pollution: Lines that Connect, Journal of the Air & Waste Management Association, 56(6), 709–742, doi:10.1080/10473289.2006.10464485, 2006.

Saarnio, K., Teinilä, K., Saarikoski, S., Carbone, S., Gilardoni, S., Timonen, H., Aurela, M. and Hillamo, R.: Online determination of levoglucosan in ambient aerosols with Particle-into-Liquid Sampler - High-Performance Anion-Exchange Chromatography -Mass Spectrometry (PILS-HPAEC-MS), Atmos. Meas. Tech. Discuss., 6(3), 5495–5527, doi:10.5194/amtd-6-5495-2013, 2013.

Salo, K., Jonsson, Å. M., Andersson, P. U. and Hallquist, M.: Aerosol Volatility and Enthalpy of Sublimation of Carboxylic Acids, J. Phys. Chem. A, 114(13), 4586–4594, doi:10.1021/jp910105h, 2010.

Thomson, D. S., Schein, M. E. and Murphy, D. M.: Particle Analysis by Laser Mass Spectrometry WB-57F Instrument Overview, Aerosol Science and Technology, 33(1-2), 153–169, doi:10.1080/027868200410903, 2000.

Thornberry, T., Murphy, D. M., Thomson, D. S., de Gouw, J., Warneke, C., Bates, T. S., Quinn, P. K. and Coffman, D.: Measurement of Aerosol Organic Compounds Using a Novel

Collection/Thermal-Desorption PTR-ITMS Instrument, Aerosol Science and Technology, 43(5), 486–501, doi:10.1080/02786820902763132, 2009.

Tobias, H. J., Kooiman, P. M., Docherty, K. S. and Ziemann, P. J.: Real-Time Chemical Analysis of Organic Aerosols Using a Thermal Desorption Particle Beam Mass Spectrometer, Aerosol Science and Technology, 33(1-2), 170–190, doi:10.1080/027868200410912, 2000.

Turpin, B. J., Saxena, P. and Andrews, E.: Measuring and simulating particulate organics in the atmosphere: problems and prospects, Atmospheric Environment, 34(18), 2983–3013, 2000.

Ulbrich, I. M., Canagaratna, M. R., Zhang, Q., Worsnop, D. R. and Jimenez, J. L.: Interpretation of organic components from Positive Matrix Factorization of aerosol mass spectrometric data, Atmos. Chem. Phys., 9(9), 2891–2918, doi:10.5194/acp-9-2891-2009, 2009.

Vasiliou, J. G., Sorensen, D. and McMurry, P. H.: Sampling at controlled relative humidity with a cascade impactor, Atmospheric Environment, 33(7), 1049–1056, doi:10.1016/S1352-2310(98)00323-9, 1999.

Veres, P., Roberts, J. M., Warneke, C., Welsh-Bon, D., Zahniser, M., Herndon, S., Fall, R. and de Gouw, J.: Development of negative-ion proton-transfer chemical-ionization mass spectrometry (NI-PT-CIMS) for the measurement of gas-phase organic acids in the atmosphere, International Journal of Mass Spectrometry, 274(1-3), 48–55, doi:10.1016/j.ijms.2008.04.032, 2008.

Vogel, A. L., Äijälä, M., Brüggemann, M., Ehn, M., Junninen, H., Petäjä, T., Worsnop, D. R., Kulmala, M., Williams, J. and Hoffmann, T.: Online atmospheric pressure chemical ionization ion trap mass spectrometry (APCI-IT-MS^n) for measuring organic acids in concentrated bulk aerosol – a laboratory and field study, Atmos. Meas. Tech., 6(2), 431–443, doi:10.5194/amt-6-431-2013, 2013.

Voisin, D., Smith, J. N., Sakurai, H., McMurry, P. H. and Eisele, F. L.: Thermal Desorption Chemical Ionization Mass Spectrometer for Ultrafine Particle Chemical Composition, Aerosol Science and Technology, 37(6), 471–475, doi:10.1080/02786820300959, 2003.

Volkamer, R., Jimenez, J. L., San Martini, F., Dzepina, K., Zhang, Q., Salcedo, D., Molina, L. T., Worsnop, D. R. and Molina, M. J.: Secondary organic aerosol formation from anthropogenic air pollution: Rapid and higher than expected, Geophys. Res. Lett., 33(17), L17811, doi:10.1029/2006GL026899, 2006.

Weber, R. J., Orsini, D., Daun, Y., Lee, Y. N., Klotz, P. J. and Brechtel, F.: A Particle-into-Liquid Collector for Rapid Measurement of Aerosol Bulk Chemical Composition, Aerosol Science and Technology, 35(3), 718–727, doi:10.1080/02786820152546761, 2001.

Williams, B. J., Goldstein, A. H., Kreisberg, N. M. and Hering, S. V.: An In-Situ Instrument for Speciated Organic Composition of Atmospheric Aerosols: Thermal Desorption Aerosol GC/MS-FID (TAG), Aerosol Science and Technology, 40(8), 627–638, doi:10.1080/02786820600754631, 2006.

Yatavelli, R. L. N. and Thornton, J. A.: Particulate Organic Matter Detection Using a Micro-Orifice Volatilization Impactor Coupled to a Chemical Ionization Mass Spectrometer (MOVI-CIMS), Aerosol Science and Technology, 44(1), 61–74, doi:10.1080/02786820903380233, 2010.

Yatavelli, R. L. N., Lopez-Hilfiker, F., Wargo, J. D., Kimmel, J. R., Cubison, M. J., Bertram, T. H., Jimenez, J. L., Gonin, M., Worsnop, D. R. and Thornton, J. A.: A Chemical Ionization High-Resolution Time-of-Flight Mass Spectrometer Coupled to a Micro Orifice Volatilization Impactor (MOVI-HRToF-CIMS) for Analysis of Gas and Particle-Phase Organic Species, Aerosol Science and Technology, 46(12), 1313–1327, doi:10.1080/02786826.2012.712236, 2012.

Zelenyuk, A. and Imre, D.: Single Particle Laser Ablation Time-of-Flight Mass Spectrometer: An Introduction to SPLAT, Aerosol Science and Technology, 39(6), 554–568, doi:10.1080/027868291009242, 2005.

	$C_8H_{12}O_6$	$C_5H_6O_6$	$C_9H_{14}O_4$	$C_{10}H_{16}O_7$	$C_{10}H_{14}O_8$	$C_{10}H_{16}O_3$
UW Chamber (pg)	3 ±1	1±1	170± 61	3±2	1±1	86±50
pg/m^3	35±16	11±5	1690±610	25±15	5±8	860±475
Hyytiälä, Finland (pg)	125±210	130±150	630±690	55±90	40±90	160±180
pg/m^3	180±300	180±210	900±980	80±130	60±125	230±255

Table 3.1 Detection limits for two different sampling conditions: first, from the UW-Chamber (see text for operation details), second, for a 2-week ambient dataset from Hyytiälä, Finland. All species reported were detected at the deprotonated ion. Detection limits represent 3σ confidence levels, where ion signals were converted to mass using the instrument's formic acid sensitivity. All detection limits are calculated for each blank pair and the average is reported here, with ±1 standard deviation. For the chamber conditions there is little temporal change, but high gas phase concentrations. In Hyytiälä, gas phase concentrations are significantly lower, however temperatures are much colder and there is more temporal atmospheric change, resulting in higher detection limits on average. For Hyytiälä, there is also an increase in the variability of the blank, represented by the standard deviation, relative to the steady-state chamber because atmospheric variability drives relatively larger changes in the field blanks. Because of frequent determinations, we are able to capture much of that variability on the timescales of hours and are therefore able to remove the changing artifact from the data. Detection limits are also reported in pg/m^3 by taking into account the volume of air sampled across the filter during particle collection which was different between the chamber and the field deployment.

ID	Comp.	Chemical Name	ΔH_{sub} kJ/mol	T_{max} (°C)	p(298 K) 10^{-5} Pa	Source
a	$C_4H_{10}O_4$	Erythritol	135± 2	52.9	--	NIST
b	$C_7H_{12}O_4$	Pimelic Acid	127± 20	37.6	9-17	(Salo et al., 2010)
c	$C_6H_{10}O_5$	Levoglucosan	125 ± 10	61.5	20	(May et al., 2012; Oja and Suuberg, 1999)
d	$C_{10}H_{20}O_2$	Decanoic Acid	119± 2	<32.4	5400	NIST (Cappa et al., 2008)
e	$C_{10}H_{16}O_3$	Pinonic Acid	90± 7	<32.4	.4-7	(Salo et al., 2010)
f	$C_9H_{14}O_4$	Pinic Acid	109±21	61.5	4-10	(Salo et al., 2010)
g	$C_9H_{16}O_4$	Azelaic Acid	178±10	71.4	.6	(Bilde et al., 2003)
h	$C_{10}H_{18}O_4$	Sebacic Acid	161 ± 4	72.9	.147	NIST (Chattopadhyay and Ziemann, 2005)
i	$C_{13}H_{26}O_2$	Tridecylic Acid	141 ± 10	39.2	140	NIST(Chattopadhyay and Ziemann, 2005)
j	$C_{12}H_{22}O_4$	Dodecanedioic Acid	153 ± 4	71.9	.006-.242	NIST, (Chattopadhyay and Ziemann, 2005)
k	$C_{16}H_{32}O_2$	Hexadecanoic Acid	154 ± 4	65.3	.39-29	NIST (Cappa et al., 2008)
l	$C_{14}H_{26}O_4$	Decanedioic Acid	161 ± 4	70.0	.1-1	NIST, (Yatavelli and Thornton, 2010)
m	$C_{16}H_{32}O_3$	Hydroxy-Hexadecanoic Acid	149 ± 10	81.5	.653	(Chattopadhyay and Ziemann, 2005)
n	$C_{18}H_{32}O_2$	Oleic Acid	136 ± 8	71.9	.066-2.66	(Cappa et al., 2008) (Chattopadhyay and Ziemann, 2005)
o	$C_{18}H_{36}O_2$	Octadecanoic Acid	167 ± 4	79.5	.056-.19	NIST (Cappa et al., 2008)
p	$C_{18}H_{36}O_3$	Hydroxy-Stearic Acid	172 ± 10	89.7	.0865	Calc (Chattopadhyay and Ziemann, 2005)
q	$C_{22}H_{44}O_2$	Docosanoic Acid	193 ± 8	92.7	7e-4	NIST,(Chattopadhyay and Ziemann, 2005)
r	$C_{23}H_{46}O_2$	Tricosanoic Acid	197 ± 8	99.8	--	Calc
s	$C_{22}H_{42}O_3$	Hydroxy-Docosanoic Acid	250 ± 15	96.8	--	Calc

Table 3.2 Compounds used to determine the relationship between ΔH_{sub} and maximum desorption temperature. The letters correspond to the labeled points in Figure 6. Compounds

were manually deposited on the FIGAERO primary filter and subsequently desorbed. Calculated values follow (Capouet and Müller, 2006) for evaluating the group contribution change in vapor pressure and therefore ΔH_{sub} from known compounds. For hydroxy-acids the hydroxy group was added to calculate ΔH_{sub}.

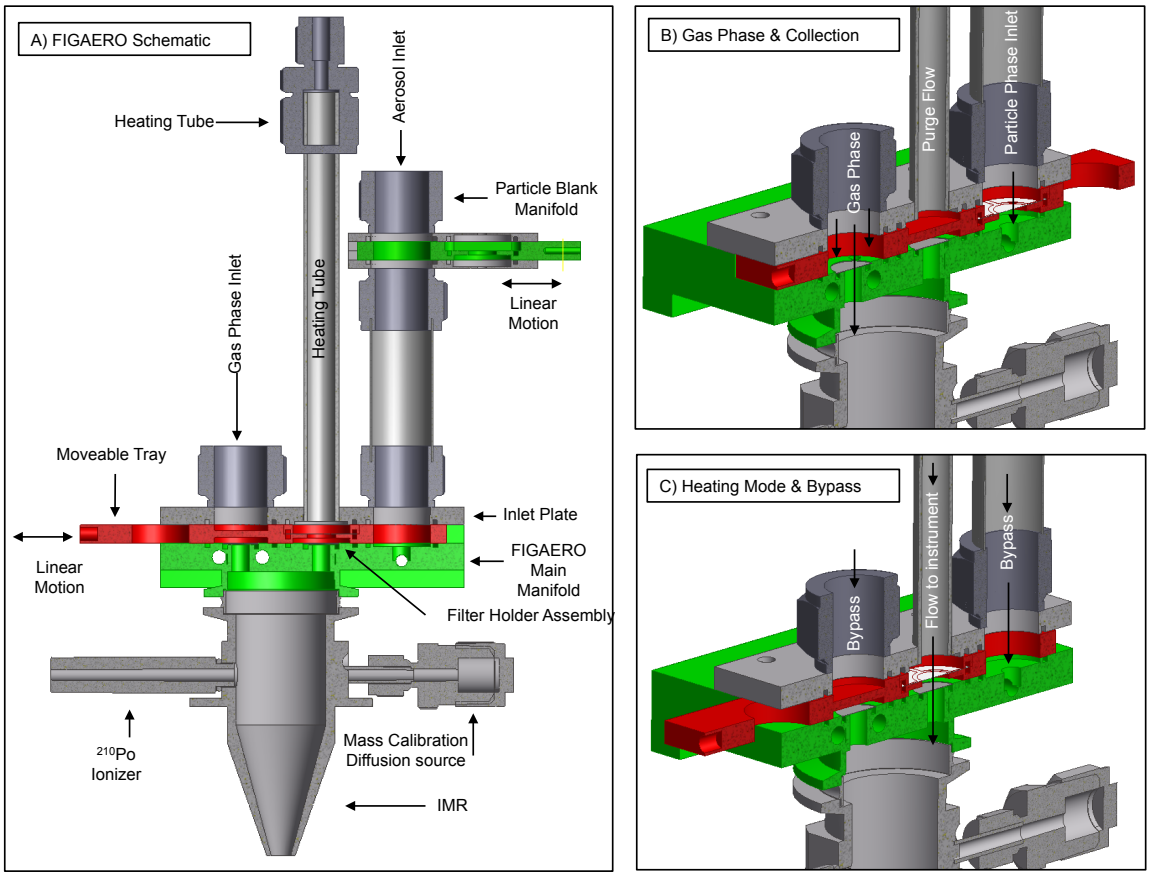

Figure 3.1. FIGAERO Schematics.

(A) FIGAERO section view. The main FIGAERO manifold (green), made entirely from Teflon, provides inlet and outlet connections for sampling pumps and delivery of gases to the CIMS. The HRTOF-CIMS ionization region is shown for reference below the green manifold. The moveable tray (red), also Teflon, acts as the main FIGAERO valve, and carries the PTFE filter between collection and desorption stages. The moveable tray simultaneously switches the sample flow entering the instrument between the two dedicated exit ports, one exclusively for gases, one exclusively for thermal desorptions. The inlet plate assembly (grey on top of red section) provides the interface between the FIGAERO manifold and the ambient sampling inlets. The gas analysis port is a 19 mm Swagelok compression fitting; the particle collection port is a 25 mm compression fitting. (B) A perspective section view of the FIGAERO in gas measurement and particle collection mode. The desorption orifice is blocked by the moveable tray. Black arrows show the flow paths, both into the instrument and across the filter. The gas

phase flow rate is ~22 slpm, only 2 slpm of which enter the instrument. The particle collection inlet has a flow rate of up to 30 slpm. (C) A perspective section view of the FIGAERO in particle analysis mode. The gas sampling orifice is blocked by the moveable tray, and the filter has been moved to the thermal desorption region of the manifold where 2 slpm of UHP N_2 are delivered across the filter. This N_2 stream is programmatically heated to desorb the components from the filter. The resulting vapors are sampled through a dedicated orifice into the mass spectrometer.

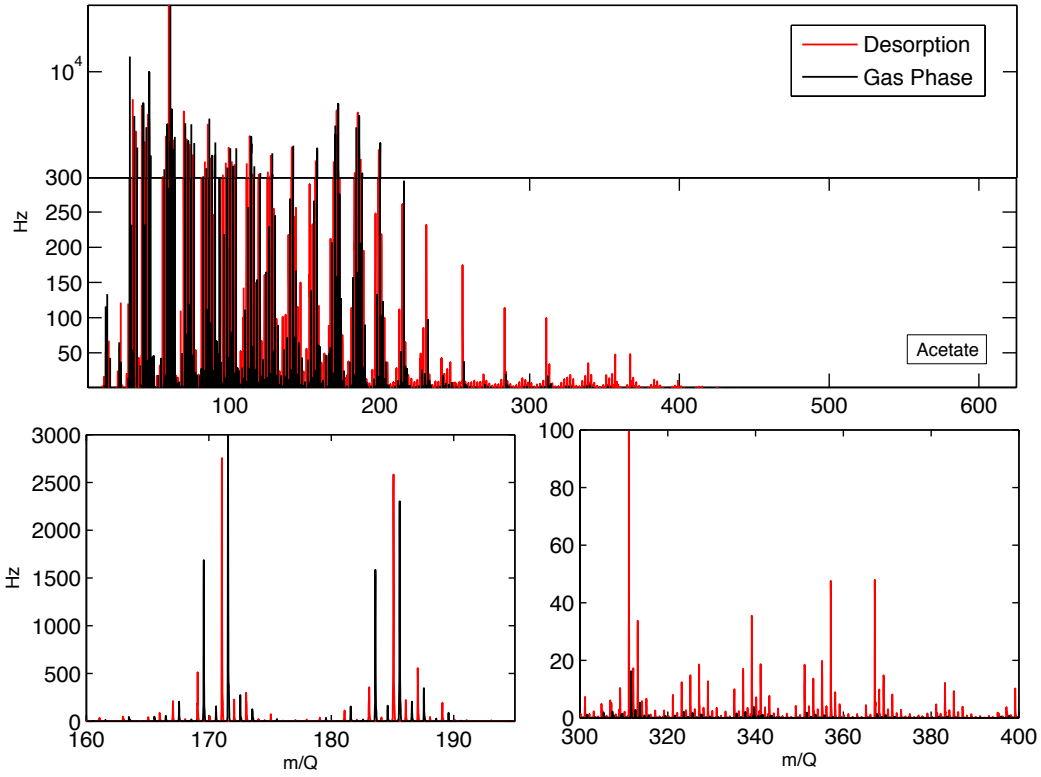

Figure 3.2. Example spectra from ozonolysis of α-pinene from the UW-Seattle chamber. Thermal desorption data are shown in red, using the average desorption signal for one collection. The gas signal is shown in black shifted to the right by .5 amu for clarity. The lower panels show zoomed in regions of the spectra: common major acid products from the α-pinene + ozone reaction (left) and highly oxygenated, large molecular weight compounds which are predominantly found in the particle phase (right).

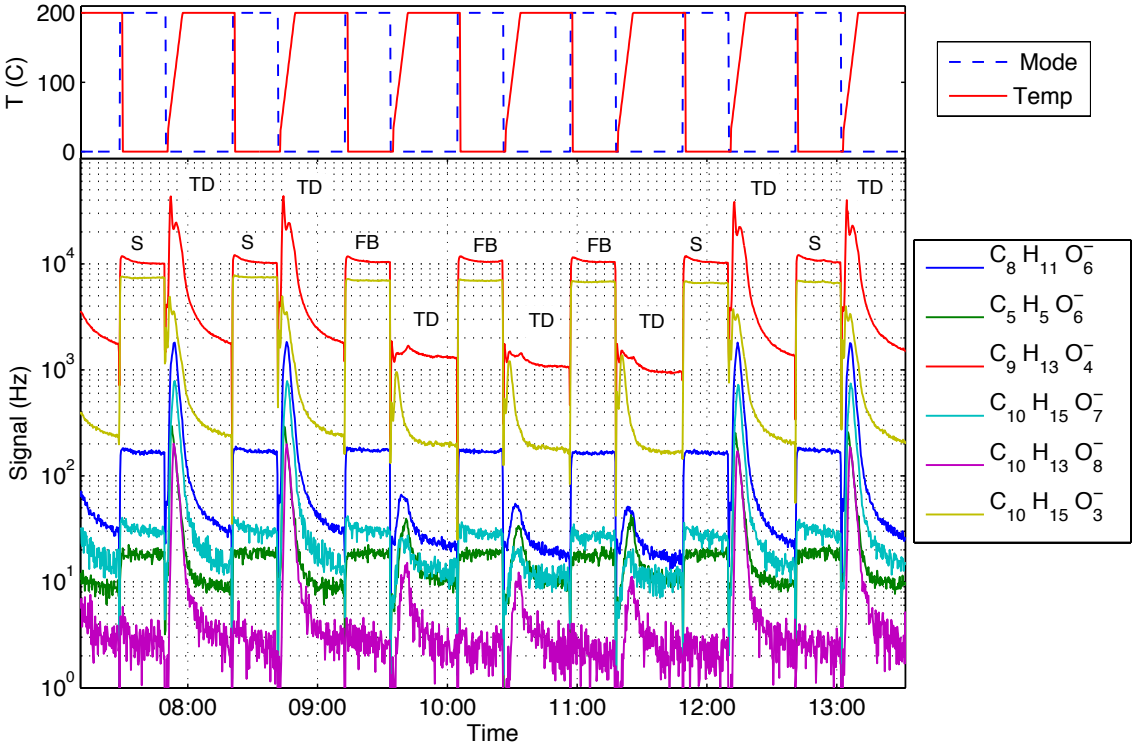

Figure 3.3. The FIGAERO sampling from a steady-state chamber .

Top: FIGAERO manifold operational mode (blue dashed line), high during gas phase sampling and particle collection, low during thermal desorption, and UHP N_2 temperature (red solid line) during thermal desorption of the collected particle samples. The temperature was ramped at 20 °C/min from room temperature to 200 °C where it was held for ~20 additional minutes ('soak') to ensure all detectable organic material was removed from the filter. Bottom: Time series of selected ion signals which span a large range in signals and m/Q, and which have different filter blank behaviors are shown during the various operational modes of the FIGAERO. Modes are denoted by text: (S) gas analysis and particle collection, (TD) thermal desorption, (FB) filter blank sampling (see text for details). The signals during TD that immediately follow the FB sampling periods represent the magnitude of the FB for a given ion composition.

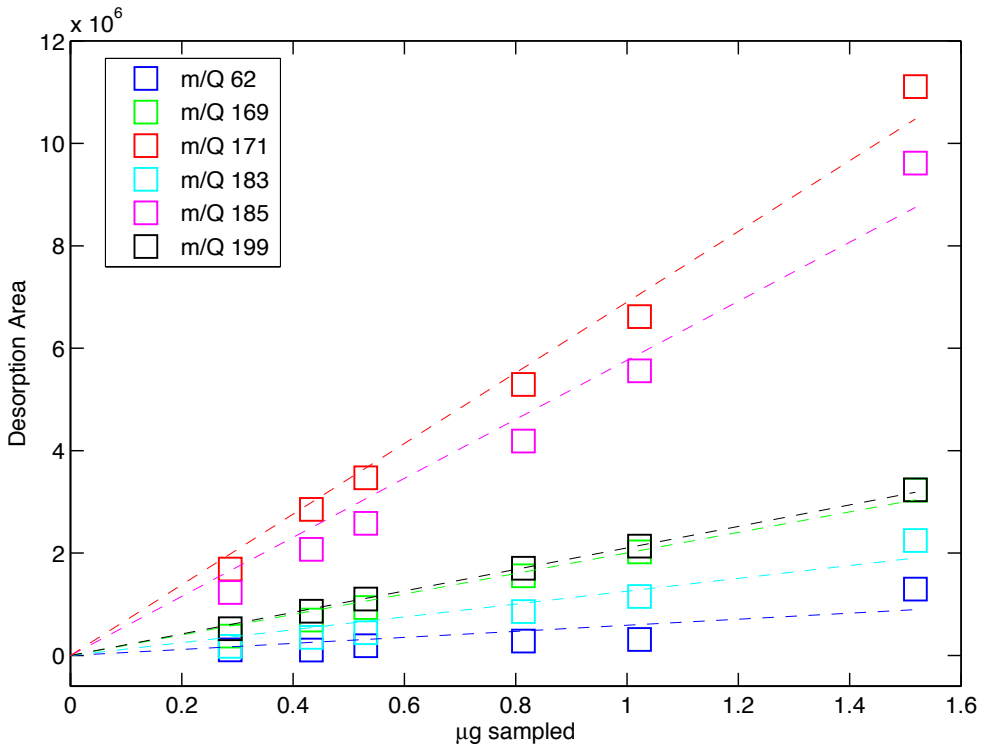

Figure 3.4. FIGAERO Linearity.

Blank-corrected integrated signals measured during thermal desorption for various ion compositions plotted *versus* the total particle mass collected on the filter. Desorbed compounds were detected with a quadrupole CIMS employing acetate ionization coupled to the FIGAERO. To change the mass loading on the filter, particle collection times were varied while sampling from the UW steady-state α-pinene ozonolysis chamber output. Particle mass concentrations were measured by an SMPS. Linear fits to the data forced through the origin are shown with the mean R^2= 0.98.

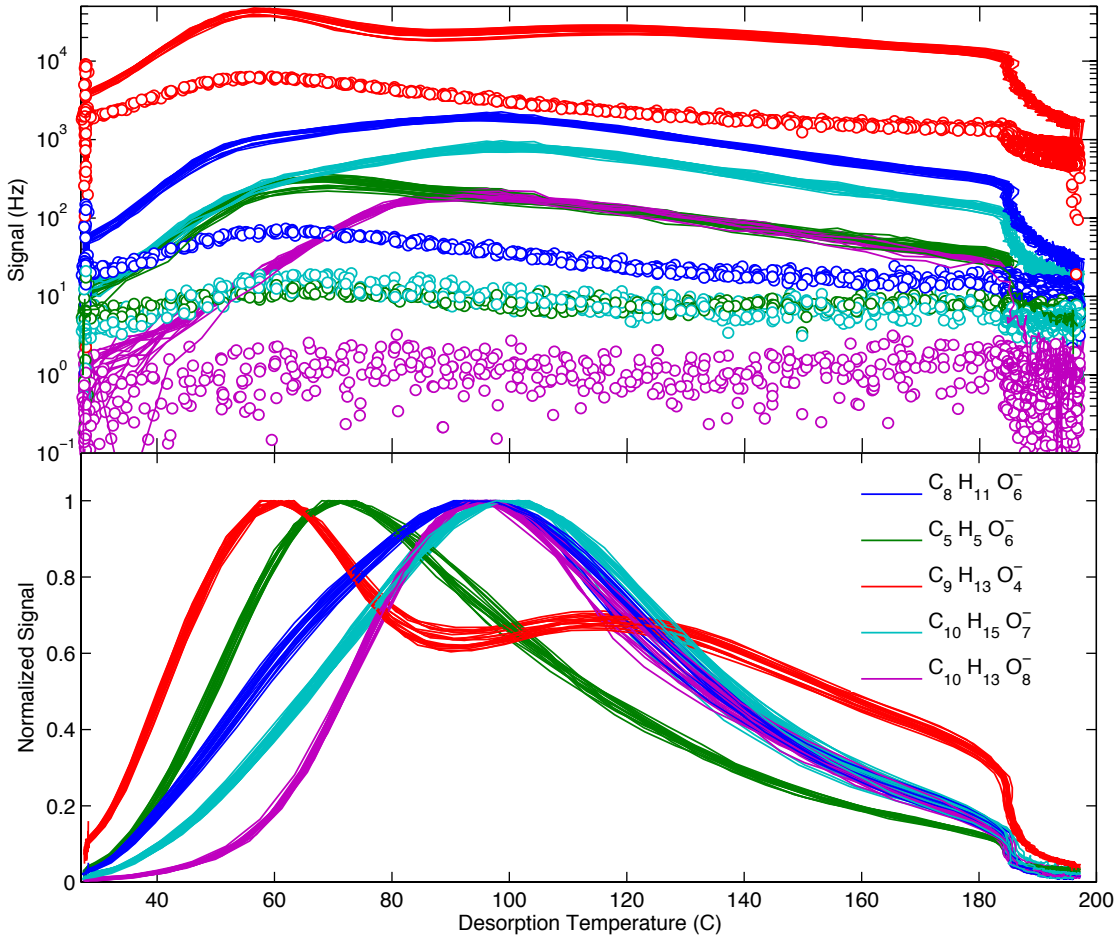

Figure 3.5. Thermogram reproducibility.

Top: Selected ion signals (counts per second) are plotted on a log-scale *versus* N_2 carrier gas temperature during thermal desorptions of α-pinene ozonolysis derived organic aerosol particles (solid lines) and of corresponding filter blanks (open circles). Repeated equal duration particle collection and desorptions are shown from a two-day period sampling from constant chamber conditions. The filter blank is factors of 10 to 100 lower than the particle-laden chamber sample depending on the specific composition of the compound. Bottom: The same particle desorption signals are shown normalized to the maximum signal on a linear scale for clarity. As temperatures near 200 °C signals drop smoothly towards background levels during the soak period of the heating cycle. The structure of the desorptions is highly reproducible both in

amplitude and temperature space. The details of the bimodal features are discussed further in the text.

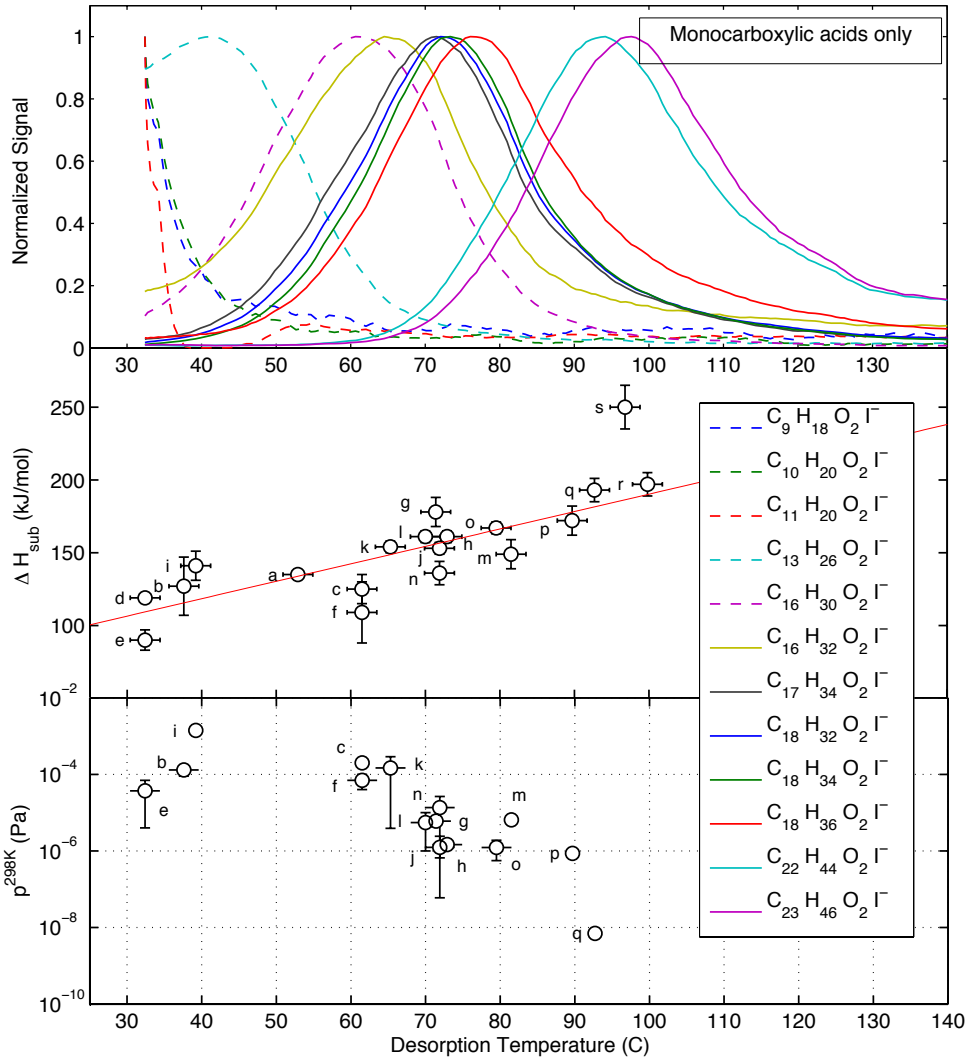

Figure 3.7. Thermogram calibration and relation to vapor pressure.

Top. Thermograms from a series of mono carboxylic acids are shown as detected by a FIGAERO-HRToF-CIMS operating in the field employing Iodide adduct ionization. The acids were part of a single mixture of several organic compounds that was deposited manually *via* a micro-syringe onto the FIGAERO filter, and then the filter was subjected to a standard thermal desorption. The series of acids each desorb with a single signal maximum (mode), signifying little contamination from other ions (see text). Middle. ΔH_{sub} values for compounds in the deposited mixture from the literature (open symbols) or estimated here using group contribution methods (dots) are plotted *versus* the temperature at which the compound's signal reached a

maximum in the desorption (T_{max}, see text). Letters correspond to the identifier (ID) listed in Table 2. Bottom. Literature vapor pressures over the solid scattered with maximum desorption temperature. The relationship is less clear than enthalpy of sublimation likely resulting from the larger relative uncertainties in the measured vapor pressures.

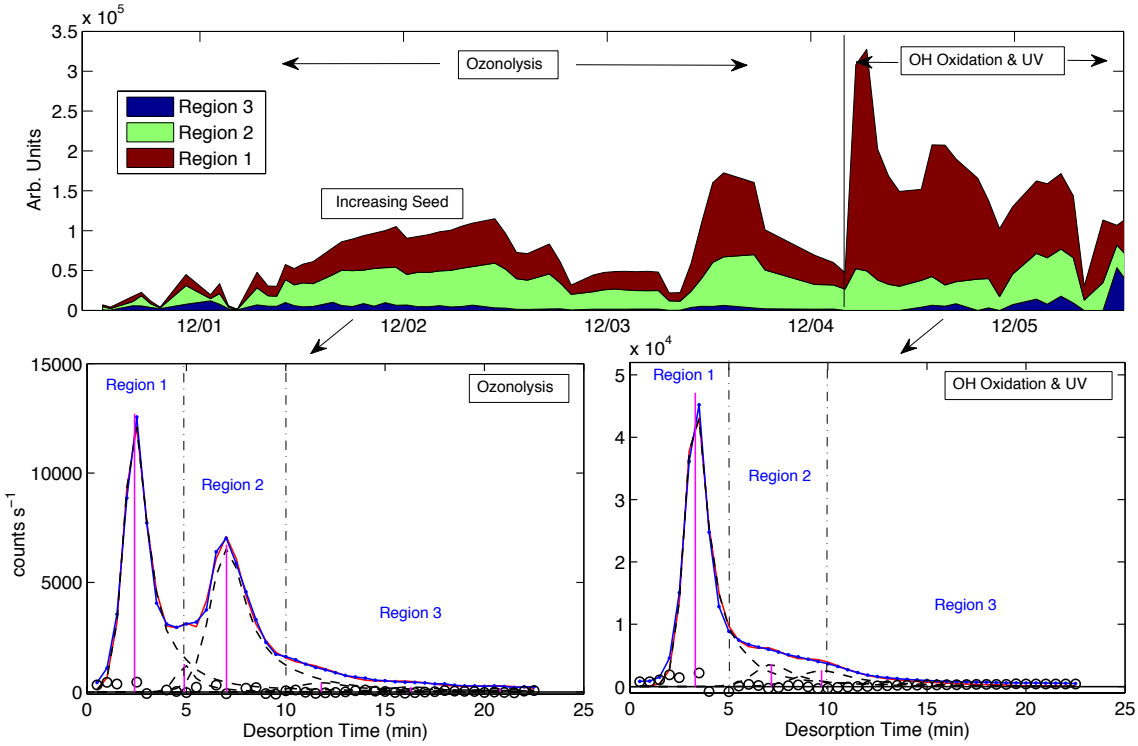

Figure 3.7. Thermogram Fitting.

An example of thermogram fitting using the $C_8H_{11}O_4$- desorption signal from particles collected at JPAC. Bottom Left: A thermogram from α-pinene ozonolysis is shown. The total raw signal is shown as a blue line with dots. Individual desorption peaks used to fit the total signal are shown as dashed lines with locations of the maxima indicated by vertical magenta lines. The sum of the fitted desorption peaks is shown as a red line and the residual between the signal and fitted thermogram is shown as open circles. Bottom Right: A thermogram from α-pinene oxidation by OH and the corresponding fits are shown – colors and symbols are the same as at the left. Although the location (in time or temperature) of the fitted desorption peaks are mostly similar for the two periods, for simplicity the fitted thermograms are divided into three regions for comparing the relative signal in the different portions of the thermogram. Top: The

time series constructed from the thermogram fits using the three integration regions shown in the lower panels. Evident is the difference in absolute magnitude of the ratio of signal in Region 1 and Region 2, between ozonolysis with variable seed and OH oxidation, suggesting the thermograms track changes in the chemical or physical properties of the aerosol given changes in formation and processing pathways.

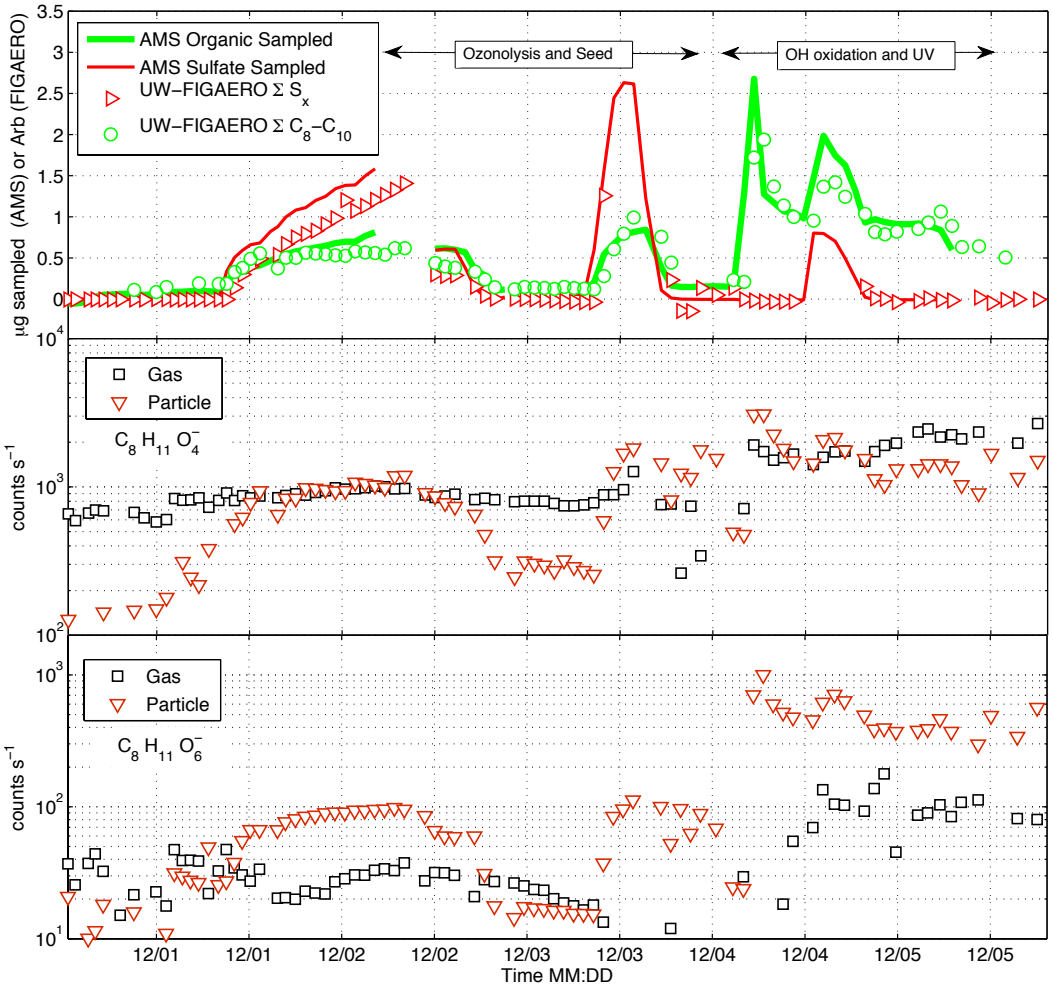

Figure 3.8. A time series of the α-pinene oxidation experiments at JPAC. Top. Aerosol composition as measured by a HRToF-AMS for bulk organics as well as sulfate (thick green and thin red lines, respectively). FIGAERO data are shown as circles for both the sum of C_8-C_{10} acids and of sulfur containing compounds. During the addition of ammonium sulfate seed the FIGAERO and AMS measure changes in organic aerosol loading and composition. In the lower panels, ion signals for two compounds, $C_8H_{11}O_4^-$ (top) and

$C_8H_{11}O_6^-$ (bottom) are shown as measured for both gas and particle phases. The $C_8H_{11}O_6^-$ ion signal changes substantially during the switch from ozonolysis to OH oxidation. For the $C_8H_{11}O_4^-$ compound, the addition of seed significantly increases its detection in the particle phase, while oxidation by OH dampens the effect of seed on its abundance.

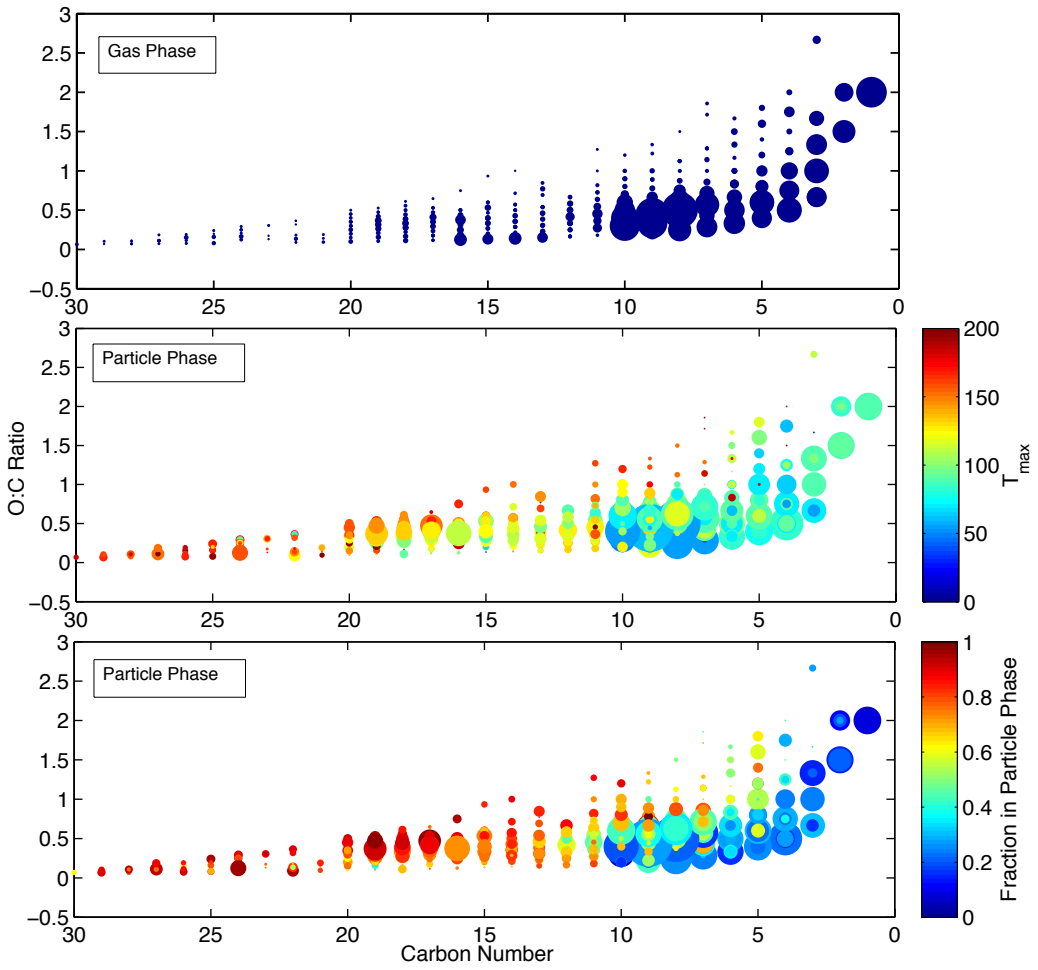

Figure 3.9. Detected compounds in oxidation space.

The oxygen to carbon ratio (O/C) plotted *versus* carbon number for ions detected in the gas and particle phases when sampling from the UW Chamber under α-pinene ozonolysis conditions. In each panel the points are sized by the square root of the mass concentration. Top: Compositions for a suite of compounds measured in the gas-phase. Maximum mass concentrations are measured at compounds with less than 10 carbons. Middle: Composition measured during thermal desorptions of collected particles, colored by the temperature at which the desorption signal reaches a maximum. Compounds with increasing carbon number and oxygen content generally require higher temperature to desorb. However, thermal decomposition is evident at low carbon numbers where compounds desorb at relatively higher temperatures. Bottom: As in the middle panel, except colored by the fraction of mass measured in the particle phase. Generally, increasing carbon number and oxygen content in a detected compound is associated with a greater partitioning to the particle phase.

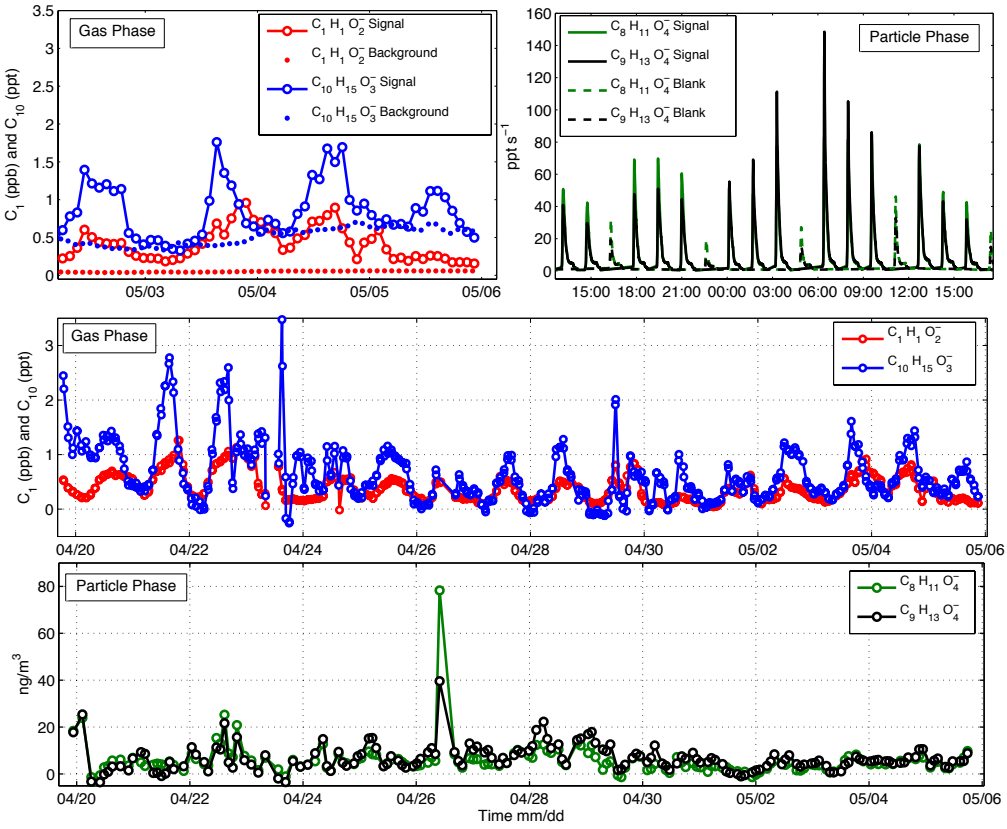

Figure 3.10. Field Performance.

An overview of the FIGAERO performance during a field campaign at Hyytiälä, Finland, a boreal forest site. Top (left): Example time series of both the total signal (open circles) and measured background (dots), in mixing ratio equivalent units, for the deprotonated ions of two compounds detected in the gas phase, HCOOH (formic acid) and C10H16O3 (pinonic acid or other monoterpene derived acid). Significant signal above the background is measured, allowing routine measurement of sub ppt concentrations. Top (right): Raw thermal desorption signals (solid lines) and filter blank determinations (dashed lines) for two major particle components in the FIGAERO HRToF-CIMS spectra during measurements at the Hyytiälä field site. Filter blank desorptions are significantly lower than those containing ambient particles, allowing measurement of individual components present in particles at 1 ng/m3 concentrations. Middle: A time series of the background corrected C1 and C10 compounds displayed in the upper left panel, exhibiting a semi-regular diurnal pattern. Bottom: A time series of filter blank corrected particle composition. Evident is the spike in concentrations on the 26th when a sawmill plume was intercepted at the field site, otherwise the time series shows the influence of regional transport, rain events, and other meteorological influences.

Chapter 4. PHASE PARTITIONING AND VOLATILITY OF SECONDARY ORGANIC AEROSOL COMPONENTS FORMED FROM α-PINENE OZONOLYSIS AND OH OXIDATION: THE IMPORTANCE OF ACCRETION PRODUCTS AND OTHER LOW VOLATILITY COMPOUNDS[*]

We measured a large suite of gas and particle phase multi-functional organic compounds with a Filter Inlet for Gases and AEROsols (FIGAERO) coupled to a high-resolution time-of-flight chemical ionization mass spectrometer (HR-ToF-CIMS) developed at the University of Washington. The instrument was deployed on environmental simulation chambers to study monoterpene oxidation as a secondary organic aerosol (SOA) source. We focus here on results from experiments utilizing an ionization method most selective towards acids (acetate negative ion proton transfer), but our conclusions are based on more general physical and chemical properties of the SOA. Hundreds of compounds were observed in both gas and particle phases, the latter being detected upon temperature programmed thermal desorption of collected particles. Particulate organic compounds detected by the FIGAERO HR-ToF-CIMS are highly correlated with, and explain at least 25 – 50% of, the organic aerosol mass measured by an Aerodyne Aerosol Mass Spectrometer (AMS). Reproducible multi-modal structures in the thermograms for individual compounds of a given elemental composition reveal a significant SOA mass contribution from high molecular weight organics and/or oligomers (i.e. multi-phase accretion reaction products). Approximately 50% of the HR-ToF-CIMS particle phase mass is associated with compounds having effective vapor pressures 4 or more orders of magnitude lower than commonly measured monoterpene oxidation products. The relative importance of these accretion-type and other extremely low volatility products appears to vary with photochemical

[*] Reprinted with permission from: Lopez-Hilfiker, F. D., Mohr, C., Ehn, M., Rubach, F., Kleist, E., Wildt, J., Mentel, Th. F., Carrasquillo, A. J., Daumit, K. E., Hunter, J. F., Kroll, J. H., Worsnop, D. R., and Thornton, J. A.: Phase partitioning and volatility of secondary organic aerosol components formed from α-pinene ozonolysis and OH oxidation: the importance of accretion products and other low volatility compounds, Atmos. Chem. Phys., 15, 7765-7776, doi:10.5194/acp-15-7765-2015, 2015.

conditions. We present a desorption temperature based framework for apportionment of thermogram signals into volatility bins. The volatility-based apportionment greatly improves agreement between measured and modeled gas-particle partitioning for select major and minor components of the SOA, consistent with thermal decomposition during desorption causing the conversion of lower volatility components into the detected higher volatility compounds.

4.1 INTRODUCTION

The sources, oxidation pathways and chemical properties of secondary organic aerosol (SOA) remain highly uncertain on a molecular basis. These uncertainties can lead to large errors between modeled and measured aerosol loadings (Heald et al., 2010; Volkamer et al., 2006), and ultimately limit our ability to confidently predict changes in aerosol properties under a warming climate (Hallquist et al., 2009) or in response to other anthropogenic perturbations such as emissions of nitrogen oxides and sulfur dioxide. To develop adequate model parameterizations of organic aerosol (OA) formation, growth, and loss, there remains a need to improve and evaluate chemical mechanisms that involve conversion and partitioning of organic compounds between gas and condensed phases (Roldin et al., 2014). These needs are likely to be at least partially addressed by a more detailed understanding of molecular composition in both phases at higher time resolution from which mechanistic insights are more easily discerned.

While SOA is ubiquitous in the lower atmosphere, our understanding of its composition and properties, from nucleation and growth of freshly formed particles to background ambient particles, is still lacking (Donahue et al., 2011; Ehn et al., 2014; Riccobono et al., 2014; Riipinen et al., 2012; Ziemann, 2002). Identifying the sources and functional groups of organic molecules within SOA remains a difficult analytical challenge, given that their inherent low volatility makes routine online analysis by mass spectrometry impossible without perturbation (thermal desorption, dissolution, derivatization, etc.) and that the actual source molecules initially condensing into the particle phase may have been transformed *via* condensed phase chemistry, such as acid-base reactions or various organic accretion processes (Smith et al., 2010; Ziemann and Atkinson, 2012).

Recently, *in situ* measurement methods have been developed which can address the volatility distribution or molecular composition of organic aerosol. Volatility Tandem Differential Mobility Analyzers (VTDMA) allow the measurement of kinetic evaporation in a series of ovens, which can be used to constrain the bulk volatility of compounds present in the aerosol (Cappa, 2010). Similarly, thermal denuders have been coupled to aerosol mass spectrometers to examine the loss organic aerosol mass during transit through a programmatically heated oven with some molecular information derived from factor analysis (Cappa and Jimenez, 2010). Other chemically speciated measurements, for example the TAG (Thermal Desorption Aerosol Gas Chromatograph) (Williams et al., 2006) measure the molecular composition of thermally desorbed compounds but lack a direct measure of the aerosol volatility and rather use functional group dependencies to infer the volatility distribution based on detected compositions. Holzinger et al. coupled an analogous collection-thermal-desorption (CTD) inlet to a PTR-MS (Proton Transfer Reaction Mass Spectrometer) to detect organic and inorganic compounds while also providing thermogram information, but this type of chemical ionization often leads to fragmentation and dehydration (Holzinger et al., 2010). We recently developed the FIGAERO (Filter Inlet for Gases and Aerosol), which allows both the separation of components in a volatility space, via a temperature programmed thermal desorption, and determination of the corresponding molecular composition on an hourly timescale (Lopez-Hilfiker et al., 2014).

We present measurements of compounds produced from α-pinene oxidation by OH and ozone in an environmental simulation chamber using the FIGAERO coupled to a HRToF-CIMS (Lopez-Hilfiker et al., 2014). Carboxylic acids are thought to be important components of monoterpene-derived SOA, in part because the acid functionality represents an approximate end point in carbon oxidation state and its incorporation leads to a significant reduction (1000-fold) in vapor pressure relative to the parent compound (Capouet and Müller, 2006; Russell et al., 2011). We therefore chose acetate negative proton transfer ionization, which is most sensitive to carboxylic acid groups (Veres et al., 2010; 2008), though also detects other functionalities as we have previously demonstrated and extend herein (Mohr et al., 2013). Our main goal is not so much a functional group characterization but to examine the extent to which compounds containing acid functionalities contribute to the SOA and the distribution of these compounds in a volatility/abundance space. We find that a significant fraction of the SOA mass characterized by

the HR-ToF-CIMS is of extremely low volatility, 4 or more orders of magnitude lower than typical monoterpene oxidation products. We discuss the implications of these compounds with respect to partitioning models and the lifetime of atmospheric aerosol.

4.2 Experimental Methods

A prototype FIGAERO-HRToF-CIMS was coupled to both the Jülich Plant Atmosphere Chamber (JPAC, Jülich Forschungszentrum, Germany (Mentel et al., 2009) and a smaller chamber with similar conditions at the University of Washington (UW). Below we provide detailed descriptions of the coupling of the FIGAERO-HRToF-CIMS to the JPAC and UW chambers.

4.2.1 *Simulation Chambers.*

Most data presented here was obtained at the Jülich Plant Atmosphere Chamber (JPAC) (Mentel et al., 2009), which consists of a series of glass chambers housed in separate temperature controlled rooms. We used a 1450 L borosilicate glass chamber housed in a temperature-controlled room held at 15 °C and relative humidity (RH) of 35 to 65%. The chamber is operated under steady-state conditions and is continuously stirred by a mixer mounted at the top of the chamber. The residence time is on average 50 minutes at a flush rate of ~30 slpm. The chamber is equipped with different types of UV lamps, one set can be used for photolysis of NO_2 to NO and the other set of lamps for OH production from O_3 photolysis in the presence of H_2O. The OH lamps can be shielded such that the actinic UV flux, and therefore the OH production rate, can be varied. We oxidized α-pinene with varying concentrations of O_3 and UV intensity, and in the presence and absence of effloresced ammonium sulfate seed particles, as part of a more extensive measurement campaign (PANDA - Probing Aerosol Nucleation During Alpha-pinene oxidation).

Here we present measurements at the end of the PANDA campaign when we utilized the FIGAERO inlet system. Concurrent measurements were made of gas-phase ELVOC (Ehn et al., 2014) using a nitrate-CIMS (Jokinen et al., 2012), 1 – 3 nm sized particles with a Particle Size

Magnifier (PSM, Airmodus, Finland), the number size distribution from 3 – 600 nm using a Scanning Mobility Particle Sizer (SMPS TSI model 3071), monoterpene concentrations using a quadrupole PTR-MS (Ionicon, Austria), and non-refractory particle composition with a High-Resolution Aerosol Mass Spectrometer (HR-AMS, Aerodyne, USA) (DeCarlo et al., 2006). We used the composition measured from the AMS and total particle volume from a SMPS to calculate particle mass of sulfate and SOA present in the chamber. The chamber was run in steady state mode with constant addition of 30 ppb α-pinene and 80 ppb ozone. We began with α-pinene ozonolysis in the dark followed by OH oxidation, where the OH was produced by shielded UV lamps (Mentel et al., 2009). For both conditions, we added seed particles to increase the particle/chamber wall surface ratio in order to better compete with condensation and partitioning of low and semi-volatile gases to the chamber walls (Matsunaga and Ziemann, 2010). We added effloresced (solid) ammonium sulfate particles with concentrations spanning from 0 to 70 μg m^{-3}. Except for the period at ~ 25 μg m^{-3} of sulfate, most seed particle concentrations were a momentary state, i.e. steady-state was not assessed, nor likely achieved for most components.

A University of Washington chamber was also used for optimization and initial testing of the FIGAERO in steady-state conditions as well as batch mode experiments to explore the time dependence of oxidation products. The chamber consists of a 0.7 m^3 Teflon bag with multiple sampling or fill ports. The chamber is pressure controlled by a servo-controlled valve that regulates the draw of air out of the chamber held slightly above atmospheric pressure (~+1 mb). The chamber is continuously filled with zero air, generated by a Teledyne zero air generator (Model 701) and flow is set by a 20000 sccm mass flow controller (MKS 1179a). α-Pinene is delivered by a perforated Teflon diffusion tube held at room temperature, or a vial of pure α-Pinene in an ice bath, the output from which mixes with the incoming zero air containing O_3 generated by passing 100 sccm of UHP N_2 with 10% O_2 through a UV photolysis cell. The α-pinene mass loading in the chamber is set by the ratio of flows through the diffusion source and the main chamber air. For the data discussed here, the RH of the UW chamber was < 5%.

4.2.2 *FIGAERO-HRToF-CIMS.*

The FIGAERO and its HR-ToF-CIMS coupling has been described in detail elsewhere (Lopez-Hilfiker et al., 2014), therefore only a review of its general operation and differences from the standard operation are described here. The FIGAERO is essentially a multi-port inlet assembly that allows sampling of either gas phase components or thermally desorbed particulate compounds into a high-resolution time of flight mass spectrometer (HR-ToF-CIMS) with selective detection by chemical ionization. Here we present results using acetate negative-ion proton transfer ionization (Veres et al., 2008). The instrument is continuously cycled between gas and particle analysis modes with periodic determinations of the particle and gas-phase background signals using a secondary filter (Lopez-Hilfiker et al., 2014).

A prototype of the FIGAERO-HRToF-CIMS was deployed at JPAC and installed directly under the chamber in the temperature controlled chamber room. As the FIGAERO was primarily designed for ambient sampling at high flows, for faster particle concentration onto the filter, we reduced the flow rate across each of the inlets and changed the inlet tube diameters to be more appropriate for the low flow conditions required on the chamber, which has a finite fill rate. At JPAC, chamber air was drawn at 10 slpm from the base of the chamber through a 1.5 m long 10 mm OD stainless steel tube. About 1 m of the tube extended into the center of the chamber, and the other 0.5 m spanned from the chamber edge to a manifold located at the instrument. Approximately 2 slpm was drawn from this manifold to sample the gas-phase composition via a 6.5 mm OD PTFE inlet with a length of approximately 12 cm to the HRToF-CIMS. Another 5 slpm was drawn from the manifold via a 20 cm length of 6.5 mm OD copper tube across the primary FIGAERO filter to collect particles. We collected particles for 30 minutes at 5 slpm and thermally desorbed the particles for 40 minutes at a ramp rate of 20 °C/min from ambient to 200 °C at which point the temperature was held constant to ensure that particle phase signals returned to their pre-heating levels. The particle sample flow is monitored by a mass flow meter (MKS 1179a) to track the total volume sampled over the collection period and relates the integrated particle desorption signal area to a mass loading in the chamber.

To assess the particle background due to adsorption and/or absorption of gases onto the Teflon filter, we manually placed an identical filter in a Teflon filter holder immediately upstream of the

FIGAERO filter. Particle backgrounds were conducted at each photochemical condition in the chamber, usually multiple times, to obtain representative backgrounds at each stage. Gas-phase backgrounds were assessed at the point prior to desorption when the instrument is sampling UHP N_2, and also when the pre-filter was in place which allows for assessing whether particle components volatilized in the heated portions of the IMR and transfer tubing between the prototype FIGAERO filter and the IMR.

4.2.3 *Acetate Chemical Ionization.*

The measurements reported here were obtained using acetate ionization, employed as described previously (Mohr et al., 2013; Veres et al., 2008; Yatavelli et al., 2012). The dominant ionization mechanism is expected to be proton abstraction governed by the gas-phase pK_a of a compound relative to acetic acid.

$$HA + CH_3C(O)O^-(CH_3C(O)OH)_n \rightarrow A^-(CH_3C(O)OH)_n + CH_3C(O)OH$$

The reagent ion cluster distribution is unknown for our conditions, but tests changing the collisional declustering after the ionization region indicate n=1 with some minor contribution from n=2 or higher. The collisional declustering strength is set such that ~99% of the reagent ion is detected as n=0, and <1% as n=1 or higher. Thus, ion-neutral clusters are likely to be minor components of the ion signal. The sensitivity of the instrument was periodically calibrated during the JPAC campaign by adding the output of a formic acid permeation device to the inlet. The permeation device output was calibrated gravimetrically before and after the measurements.

The acetate chemical ionization scheme is still relatively novel, and as such, its selectivity and sensitivity towards a large range of compounds and functional groups remains to be characterized. For this reason, we performed a series of calibrations after the measurement campaign to investigate the sensitivity of acetate ionization to a series of carboxylic acids, RC(O)OH, and related functional groups, such as peroxy acids, RC(O)O-OH, and a diacyl peroxide (benzoyl peroxide), see Figure 1. In all cases, compounds were calibrated as described previously (Mohr et al., 2013). For these tests, the walls of the ion-molecule reaction (IMR)

region were heated to 60 °C – though it is unlikely the gas equilibrates to that temperature for the ~ 100 ms of transit through the region. While limited in number and type, the compounds tested to date suggest that acetate ionization, as employed in our instrument, converts peroxy acids to the corresponding carboxylate anion with nearly the same efficiency as the corresponding carboxylic acids. In addition, benzoyl peroxide is detected at the benzoate anion more efficiently than is benzoic acid. Other functional groups, e.g. polyols and esters, were not detected nearly as efficiently, nor were clusters of the tested components with acetate ions detected at significant signals. Thus, we conclude, perhaps conservatively, that acetate ionization is a measure of functionalities that can easily produce carboxylate anions, such as peroxy acids and di-acyl peroxides in addition to carboxylic acids under the operating conditions used here.

For compounds with a carboxyl-related group, there appears to be a convergence of sensitivity towards a maximum value similar to that for formic acid (see Figure 1). Given the available evidence, using this maximum sensitivity value for the entire spectrum would presumably lead to a lower-limit estimate of the mass concentrations of such compounds in the chamber. Clearly, further investigation and optimization of acetate ionization selectivity is needed, as is care attributing any signal to a specific functionality measured with acetate ionization. That said, our main conclusions are not dependent upon the exact functional groups acetate detects.

4.3 RESULTS

4.3.1 *Contribution of Acyl containing compounds to α-Pinene SOA*

Figure 2 shows an overview of the key aerosol measurements during the time when the FIGAERO was installed at JPAC. As the surface area concentration of the seed particles increased, the detected AMS organic aerosol mass increased while the amount of monoterpene reacted remained constant. Consequently, during ozonolysis conditions, the inferred SOA mass yield increased from 1% to 10% even though the α-pinene reacted remained constant. Similarly, the inferred SOA mass yield nearly doubled during OH oxidation of constant Δ(α-pinene) just by adding seed particles. The absolute abundance of detected compounds in the particle-phase, measured by the FIGAERO, also increases with the addition of seed, and is highly correlated

with the total SOA measured by the AMS at all times. However, the fractional contribution of "acyl-containing" compounds to SOA changes little over the varying SOA mass concentration and oxidant conditions (inset Figure 2).

To make the comparison between the FIGAERO-HRToF-CIMS and AMS quantitative, we used the sensitivity of the instrument to formic acid (ions/sec per mole/m^3) as a measure of the average sensitivity to all detected compounds. Based on the data shown in Figure 1, this assumption is reasonable to within a factor of 1.5 as governed by the spread of calibration factors to individual compounds, especially in the m/Q range where much of the particle phase mass is detected. We include in the analysis only ions having a molecular formula ($C_xH_yO_z$) that contain at least one degree of unsaturation, an odd number of H atoms and at least two O atoms. This selection represents the vast majority of signal measured during these experiments (>85%). We convert the integrated thermograms of each ion to μg m^{-3} using the formic acid sensitivity, the molecular mass of the ion plus the mass of one H, and the volume of air sampled prior to the thermogram measurement (see *Lopez-Hilfiker, et al.* (2014) for more details). The resulting total signal accounts for 25 – 50% of the organic aerosol measured by the AMS. We discuss the volatility distribution and phase partitioning of this significant fraction of OA below.

4.3.2 *Gas-Particle Partitioning: Measurement, theory, and the role of thermal decomposition.*

As the FIGAERO allows measurement of compounds in both gas and particle phase, we are able to assess the phase partitioning directly of individual molecular compositions, after accounting for the volumetric concentration in the particle phase inlet relative to the instantaneous gas phase measurement. To calculate the phase partitioning, we follow a similar procedure to that of *Yatavelli et al. 2014*, defining fraction in the particle phase (F_p) as the concentration in the particle phase divided by the sum of gas and particle phases (Equation 1) for a given ion elemental composition. Because the HR-ToF-CIMS does not resolve structural isomers, this approach implicitly assumes that all isomers with the same elemental composition have the same saturation vapor pressures and activity coefficients. Before evaluating phase-partitioning, we first

assess this assumption by performing an analysis of the thermal desorption profiles, i.e. "thermograms", for specific ion compositions.

In Figure 3 (top panels), we show the thermal desorption profiles for two molecular compositions, $C_8H_{12}O_4$ (left) and $C_9H_{14}O_4$ (right) consistently measured as major components of the detected monoterpene SOA. For the purposes of comparing to a phase partitioning model below, we assume these compositions represent common pinene derived acids – pinic and norpinic acid, though terpenylic acid (Yasmeen et al., 2010) is also a possibility for the latter. As shown in our previous work (Lopez-Hilfiker et al., 2014), thermograms of compounds desorbing from synthetic mixtures deposited on the filter exhibit fairly uniform, single-mode desorption profiles, with signal maxima occurring at distinct desorption temperatures which correlate with a compound's enthalpy of sublimation. In contrast, the multi-modal form of the thermograms of individual α-pinene SOA components suggest these thermograms contain added chemical information, either about the presence of isomers with vastly different heats of vaporization (vapor pressures) or higher molecular mass and lower volatility compounds that thermally decompose into the compositions which are measured by the HR-ToF-CIMS.

To further investigate the sources of, and thus information carried by, the more complex desorption features observed in the α-pinene SOA (shoulders, multiple modes, enhanced tailing, etc), we applied a custom non-linear least squares peak-fitting routine to the thermograms. First, single-mode thermogram peaks are identified and standardized on a normalized width scale. The resulting normalized peaks are averaged to obtain a typical thermogram peak shape that represents the desorption profile of a single component. An iterative routine using the Levenberg-Marquardt algorithm for nonlinear least squares problems fits the multimodal thermograms by applying a variable number of thermogram peaks having the average desorption peak shape. The number, location and amplitude of each additional desorption peak within a thermogram are optimized to explain the total thermogram of a given ion. To allow for individual compounds having slightly different desorption profiles, the width of the typical desorption peak shape is allowed to vary by up to 30% based on fitting a range of thermograms from pure component desorptions.

Typical results from this thermogram fitting routine are shown in the top panels of Figure 3. Two or three separate particle phase components are desorbing as $C_8H_{12}O_4$ ("norpinic") and $C_9H_{14}O_4$ ("pinic") at distinctly different temperatures. Blue areas represent the fraction of the detected mass desorbing at lower temperatures and which would be consistent with desorption temperatures expected for norpinic or pinic acid volatilities based on our relationship between enthalpy of sublimation (vapor pressure) and desorption temperature (Lopez-Hilfiker et al., 2014). In red, we show the contribution of secondary modes to the overall thermogram that occur at much higher temperatures than expected for these compounds. There is a third possible intermediate bin, but its presence is always much smaller and not statistically significant across the full time series, and so it is not included in the time series discussed below. Based on our calibrated desorption temperature axis, the two major portions of the thermograms correspond to order-of-magnitude effective 298 K saturation vapor pressures of ~10^{-4}, and ~10^{-10} Pa (or C* of ~10 and ~10^{-6} ug/m^3). As it is highly unlikely that there would be two structural isomers (one for norpinic and one for pinic acid) both with 6 orders of magnitude lower vapor pressures than the other isomers, we conclude that the secondary desorption events are caused by larger molecular weight compounds, e.g. oligomeric accretion reaction products, thermally decomposing to compounds with the same compositions as norpinic and pinic acid that subsequently desorb and are detected by the HR-ToF-CIMS. Large macromolecules are of sufficiently low volatility that the enthalpy of vaporization is very likely larger than the dissociation energies of their weakest bonds, leading to preferential decomposition into smaller components (e.g., oligomeric building blocks) instead of evaporation. For example, we note here that a typical O-O bond energy (one of the weaker organic covalent bonds) is ~140 kJ/mol (Blanksby and Ellison, 2003; Epstein et al., 2010), which corresponds to a desorption temperature of ~ 80 °C based on our calibration of sublimation enthalpy, though other thermal decomposition processes are of course possible. This idea is consistent with previous work using a TPTD which also investigated the multimodal nature of thermally desorbed SOA from the reaction of a-pinene and ozone (Docherty et al., 2005) which concluded a large fraction of the SOA formed consisted of organic peroxides.

In the bottom panels of Figure 3 we show the time series of the fractional contribution each of the fitted desorption peaks makes to the overall thermogram area. Interestingly, the lower volatility secondary modes in the thermal desorption of norpinic and pinic acids are more

prominent during ozonolysis than OH dominated oxidation of α-pinene. Despite increased overall production (mass loading) of pinic and norpinic acids during OH dominated oxidation, the secondary modes are much less important, especially in the pinic acid case. Aside from providing a potential mechanistic insight into the chemical origins of these lower volatility compounds, their varying importance due to a change only in the chamber photochemical conditions suggests that these secondary modes are likely not an artifact of the desorption process but rather are evidence for lower volatility components that decompose into the C_8 and C_9 acids.

With the above insights into the thermal desorption process, we can more accurately assess gas-particle partitioning. We use equilibrium partitioning theory first described by *Pankow* (Pankow, 1994) to model the phase partitioning of three monoterpene derived acids: pinic, norpinic, and pinonic acids. Equation 2 shows the transformation of equilibrium partitioning theory to a formulation of fraction in the particle phase (F_p) that we use to evaluate the quality of agreement between modeled and measured partitioning.

$$F_p = \frac{Particle}{Gas+Particle} \quad \text{(Eq. 1)}$$

$$F_p = \left(1 + \frac{\frac{M10^6\zeta P}{760RT}}{C_{OA}}\right)^{-1} \quad \text{(Eq. 2)}$$

In Equation 2, C_{OA} (μg m^{-3}) is the organic aerosol mass concentration, M (g mol^{-1}) is the molar mass of the compound of interest, ζ is the activity coefficient, which we assume is unity (and discuss later in detail), P (torr) is the vapor pressure of compound the over the pure component, R (8.2 x 10^{-5} m^3 atm K^{-1} mol^{-1}) is the gas constant, T (K) is the environmental temperature and 760 (torr atm^{-1}) and 10^6 (μg g^{-1}) are unit conversion factors. As the JPAC chamber is held at fixed temperature (15 °C), the free variables in Equation 2 become the total organic mass concentration, which was measured by the AMS and SMPS, and the pure compound saturation vapor pressure. Using literature values to constrain saturation vapor pressures, specifically those predicted by the structure activity relationship of Capouet et al, we then evaluate whether or not

equilibrium adsorptive partitioning explains the observed phase partitioning for our chamber conditions (Capouet and Müller, 2006).

Based on the thermogram analysis presented above, it is highly unlikely that norpinic and pinic acid partitioning would be well described by an equilibrium partitioning model that assumed all of the measured particle mass (thermogram area) carried in those two acids was in equilibrium with the corresponding gas-phase acids. We demonstrate this issue in Figure 4. In the top panels of Figure 4, we show the thermal desorption profiles for the three molecular compositions, $C_9H_{14}O_4$, $C_{10}H_{16}O_3$, and $C_8H_{12}O_4$, from particles collected under each set of conditions (O_3 + seed and OH). Ozonolysis conditions are shown in black, while OH oxidation conditions are shown in red. As above, we assume these compositions correspond to pinic, pinonic acid, and norpinic acids, respectively. Pinonic acid provides a useful contrast to the other two in that it does not show evidence for secondary desorption peaks under either set of conditions.

Previous comparisons to adsorptive partitioning models have used the full integrated thermogram arising from thermal desorption to compare with the model prediction and found varying levels of agreement (Yatavelli et al., 2014; Zhao et al., 2013). In the middle panels of Figure 4, we plot the measured F_p, calculated from the full integral of the thermogram, *versus* the F_p predicted by the adsorptive partitioning model. The points are colored by experiment time, with reddish points corresponding to OH oxidation towards the end of the experiment and all other colors (blueish) corresponding to ozonolysis conditions. Generally poor agreement is observed, highlighted by non-linearity, and by points falling far from the 1:1 line. There is one exception: pinic acid during OH oxidation (red points). This condition is also when the thermogram for the composition corresponding to pinic acid is largely a single mode (see Figure 4 top), suggesting that if the thermograms are deconvolved into contributions representing the different modes, the agreement between measured and predicted F_p would improve.

In the lower panels of Figure 4 we show the results of deconvolving the thermograms into the different modes using the above fitting approach for a more direct test of the actual partitioning of these three acids into the particle phase. Based on our previous work, compounds with compositions similar to those under consideration here, C_8-C_{10} keto and diacids, would have

thermogram signals that maximize at a desorption temperature (T_{max}) of 80 °C, or below, if they were non-interacting components of a solution (Lopez-Hilfiker et al., 2014). Therefore, in our revised partitioning analysis, we assume that in order to be in dynamic equilibrium with the gas-phase, a compound should desorb from the particle-phase at a temperature consistent with its expected enthalpy of sublimation. Thus, we use only a portion of the area under the thermogram to calculate the particle-phase concentration of each acid in equilibrium with that in the gas-phase. In this case, that area corresponds to the desorption mode at the lowest temperature in the thermogram analysis. The other peaks and shoulders in the thermograms that arise at significantly higher temperatures are presumably from processes related to thermal decomposition and/or high temperature formation of acid functionalities which produce the molecular "fragments" detected by the CIMS. The abundance of these molecular "fragments" from lower volatility components would have no direct impact on the equilibrium partitioning of the actual C_8 – C_{10} acids. Accounting for these structures in the thermograms leads to much better agreement (pinic acid: R^2 = 0.8, slope = 0.99, intercept -0.07, norpinic acid: R^2 = 0.92, slope = 0.78, intercept -0.04) between the partitioning model and measured F_p for pinic and norpinic acids across all chamber conditions, suggesting that *i*) literature estimates of their saturation vapor pressures used herein are reasonable, that *ii*) Raoult's Law based partitioning is applicable under the chamber conditions, and therefore that *iii*) particle viscosities can't be so high as to disrupt the equilibration process on the ~ hour timescale of the chamber measurements.

The revised partitioning calculation, using the thermogram fitting approach, does not improve the measurement-model agreement for pinonic acid. Pinonic acid desorbs as a single peak under all conditions, therefore providing no basis for selecting a smaller portion of the thermogram area. Yet, pinonic acid clearly desorbs from the α-pinene SOA at a temperature (T_{max} ~ 40 °C) that is significantly higher than if placed on the filter in pure form (or part of a synthetic mixture), where it desorbs at T_{max} << 32 °C (Lopez-Hilfiker et al., 2014). Our measurements therefore suggest that the effective vapor pressure of pinonic acid is lowered over the SOA ($F_p^{measured} >> F_p^{predicted}$) relative to over the pure substance or an ideal solution. As the temperature of maximum desorption for pinonic acid from the α-pinene SOA is less than that required to break the weakest of covalent bonds, and because the thermogram is a single mode, it

is unlikely that the pinonic acid desorption arises from the same processes that we hypothesize give rise to the secondary peaks in the thermograms of pinic and norpinic acids. We note that there are potentially lower energy pathways to decomposition than a typical bond strength analysis might suggest, and therefore decomposition can't easily be ruled out. However, the measurement-model agreement is highly linear, suggesting a single adjustment in the pinonic acid vapor pressure, i.e. an activity coefficient different from unity (~ .25), would bring agreement under most conditions (see Figure 4 bottom). Enhanced H-bonding of pinonic acid in the multi-functional SOA environment relative to the pure substance could explain these behaviors.

We conclude this section by noting that thermal decomposition of particulate organic material likely occurs in any technique that utilizes heat to drive compounds into the gas phase for analysis. But, by utilizing a calibrated relationship between molecular composition and desorption temperature, together with a slow desorption temperature ramp rate, the effects of thermal decomposition on inferred vapor pressure driven partitioning can be addressed and even utilized to arrive at a more complete view of SOA composition and volatility as we demonstrate below.

4.3.3 *Bulk Aerosol Volatility*

Above we provided specific examples of how a consistent framework can be used to relate SOA molecular composition and vapor pressure driven partitioning to thermal desorption measurements. However, as shown in Figure 5a, we observe many (hundreds) of compounds which desorb at much higher temperatures from α-pinene ozonolysis SOA than consistent with their composition. These particular data were obtained from analyzing α-pinene ozonolysis SOA generated in the UW chamber under steady-state continuous-flow conditions. The points are sized by the *square-root* (for dynamic range) of the particle mass concentration for each molecular composition detected and colored by its thermogram T_{max}. A swath of compounds containing 1 to 5 carbon atoms all desorb at temperatures between 50 - 90 °C, similar to much lower volatility compounds such as C_8-C_{10} diacids, and certainly inconsistent with expected heats of vaporization for those small compounds. We hypothesize that this whole group of compounds

(light blue) results from decomposition of larger molecules or from weakly bound complexes that effectively lower the vapor pressures of these smaller compounds.

The simplest way to organize and reduce the information in Figure 5a is by summing the calibration adjusted signal across all detected compounds. We show an example of the resulting sum thermogram in Figure 5b. Using the thermogram fitting approach discussed above, and our previously determined volatility axis based on desorption temperature, we can examine the bulk volatility of the α-pinene ozonolysis SOA detected by the FIGAERO HR-ToF-CIMS from the sum thermogram. We find that three volatility modes are required to explain the sum thermogram. The first mode is centered at ~ 60 °C, consistent with volatilities of C_8-C_{10} diacids ($C^* \sim 1$ - 10 ug/m^3). This mode represents ~ 50% of the measured desorption signal. Two other modes are apparent at higher desorption temperatures, one maximizing at ~110 °C and the other at ~ 150 °C. Clearly, a large fraction of the total mass of detected compounds desorbing from the α-pinene SOA are from very low volatility components. In the upper panel of Figure 5, these higher temperature modes correspond to the appearance of $C_{15} - C_{20}$ compounds, lending support to the conclusion that large molecular weight accretion products are a source of the smaller molecular components that also maximize at higher temperatures. Roughly 50% of the signal measured during a desorption occurs at temperatures greater than 100 °C, corresponding to effective $C^* < 10^{-5}$ ug m^{-3}.

The above estimates of C^* values and carbon mass associated with them are probably upper and lower limits, respectively, because extremely low volatility compounds likely decompose before desorbing, which biases the measured volatility higher, and the acetate ionization scheme may not be sensitive to all of the decomposition fragments, which biases the detected mass lower.

4.4 DISCUSSION

From an analysis of molecular thermograms of α-pinene SOA generated in chambers, we find that a large fraction of the characterized SOA is of very low volatility, with compositions having >10 C, and > 4 O. Moreover, we find that acetate ionization can explain at least 25 – 50% of the total SOA. We conclude that large molecular weight compounds must be present in the aerosol.

Indeed, we directly observe compounds with up to as many as 30 carbon atoms and up to 10 oxygen atoms desorbing from the α-pinene SOA. Additional indirect evidence is that commonly reported oxidation products of α-pinene, such as pinic, norpinic, and other carboxylic acids desorb at temperatures far too high to be consistent with their expected enthalpies of vaporization. Treating all of the mass that desorbs from the particles in the form of these common and smaller products as being in vapor pressure driven equilibrium with the corresponding gas-phase compounds leads to large errors between modeled and measured gas-particle partitioning that cannot be explained by a simple adjustment of the saturation vapor concentration nor its temperature dependence. Moreover, that some 50% or more of the CIMS-detected SOA mass is effectively non-volatile, having $C^* < 10^{-5}$ ug/m^3, conflicts with previous conclusions that α-pinene ozonolysis SOA is predominantly semi-volatile (An et al., 2007; Hallquist et al., 2009) but could be consistent with recent evidence that α-pinene SOA might be semisolid (Renbaum-Wolff et al., 2013).

Our findings are broadly similar with other online and offline molecular characterizations of α-pinene SOA, which have found evidence for oligomeric compounds (DePalma et al., 2013; Gao et al., 2004; Hall and Johnston, 2011; 2012). Our approach combines slow temperature ramps and molecular characterization without chromatography and thus provides a compliment to methods that have observed oligomeric material using liquid extraction followed by chromatography and electrospray ionization, or particle beam thermal desorption coupled to electron impact ionization (Ziemann, 2002). We provide an additional constraint on the fraction of SOA that is contained in these oligomeric compounds and how that fraction varies in response to different photochemical regimes.

The addition of OH and UV light suppresses the secondary low volatility modes in the thermograms of pinic and norpinic acids, which suggests that the products formed via accretion chemistry may be susceptible to photolysis and reaction with OH, or involve a precursor formed only during ozonolysis. The presence of peroxides as macromolecule linkages is certainly consistent with our results, given that the secondary modes in thermograms of many compounds arise at temperatures above the O-O bond strength, the weakest covalent bond. That there might be a significant source of low volatility peroxide compounds in α-pinene SOA was shown

recently by Ehn et al. 2014. Whether the oligomeric compounds we observe are from $RO_2 + RO_2$ reactions in the gas-phase or from particle-phase accretion reactions such as peroxy hemiacetal formation, or some combination thereof, is beyond the scope of this paper, but should be addressed in future studies in order to more accurately represent their contribution to SOA in models (Docherty et al., 2005; Ziemann and Atkinson, 2012).

We use an estimate of the O-O bond strength to put desorption temperature into a chemical bond context, but the O-O bond strength will depend upon molecular structure, and thus there is likely a distribution across the desorption temperature space of molecular fragments desorbing at higher temperatures than their composition would suggest due to O-O bond cleavage. Additionally, there may be other bond scission pathways beyond the O-O functionality which we have not yet identified. The pinonic acid thermogram is a possible example, desorbing from the α-pinene SOA at temperatures well below the O-O bond strength equivalent but well above that expected from its known enthalpy of vaporization. Non-covalent H-bonding within the SOA matrix that is stronger or more ubiquitous than in pure single component samples or simple ideal mixtures is another mechanism to explain lower than expected volatility. Three persistent H-bonds would be equivalent to about half the bond strength of an O-O bond (Dougherty, 1998). Oligomeric material may also be in thermodynamic equilibrium with semi volatile material such that losses of semi-volatile compounds even at lower temperatures than the weakest covalent or hydrogen bond could lead to decomposition of oligomeric material to re-achieve equilibrium. Processes like these need not occur at high temperatures but also may occur at near ambient temperatures. The FIGAERO approach would potentially be able to capture this process if the evaporation rate of monomers was large enough to produce detectable signal prior to ramping the temperature of the desorption N_2. That said, a majority of detected SOA mass desorbed at temperatures well above covalent bond strengths.

Previous studies to characterize the molecular composition and partitioning of atmospheric aerosol have observed small-oxygenated organics that were present in larger than expected concentrations based on ideal partitioning. We show thermal decomposition of large molecules can be a significant bias in thermal desorption techniques resulting in smaller stable fragments that are then detected. The process of thermal decomposition is likely common to any instrument

which uses heat to drive aerosol components into the gas phase for analysis (Holzinger et al., 2010; Smith et al., 2010; Williams et al., 2006; Yatavelli et al., 2012; Zhao et al., 2013). Our measurements utilizing the FIGAERO indicate that "small acids" present in higher than expected concentrations in SOA are likely entirely due to thermal decomposition of much lower volatility components of the aerosol.

4.5 CONCLUSIONS

We have explored the contribution, composition and volatility of acyl containing organic compounds present in α-pinene derived secondary organic aerosol under atmospherically relevant conditions using the FIGAERO HR-ToF-CIMS. The distribution of detected compounds spanned $C_{1\text{-}30}$ and $O_{2\text{-}10}$ with many of the compounds that were detected in the gas phase also present in the particle phase. The distribution of acyl containing compounds in the particle phase explains at least 25% of the total SOA mass produced under both OH oxidation and ozonolysis conditions and shows evidence for a significant contribution from oligomers and other large macromolecules, especially during ozonolysis. The volatility of the detected mass reflects this contribution, with a large fraction of the organic mass having vapor pressures 4 orders of magnitude lower than commonly detected diacid products from ozonolysis of α-pinene. In the particle analysis we highlight the role of thermal decomposition, and show that, when it is accounted for using the thermogram desorption profiles, equilibrium absorptive partitioning explains well the observed phase partitioning of pinic and norpinic acids though a non-ideal activity coefficient is required for pinonic acid under all conditions.

That we infer a significant fraction of the SOA is comprised of oligomeric compounds given the relatively short residence times of the JPAC and UW chambers (45 – 60 min) and the relatively small amount of α-pinene reacted in each case (~10 ppb), suggests these types of compounds can play an important role in ambient monoterpene derived SOA. If that is the case, it would imply that a significant fraction (~25% or perhaps more) of monoterpene ozonolysis SOA should be treated as effectively non-volatile in atmospheric models. Future work utilizing the FIGAERO in the field will allow analysis of ambient aerosol for comparison thereby providing a consistent view of SOA volatility and composition that will provide a direct test of these conclusions.

References:

An, W. J., Pathak, R. K., Lee, B.-H. and Pandis, S. N.: Aerosol volatility measurement using an improved thermodenuder: Application to secondary organic aerosol, Journal of Aerosol Science, 38(3), 305–314, doi:10.1016/j.jaerosci.2006.12.002, 2007.

Blanksby, S. J. and Ellison, G. B.: Bond Dissociation Energies of Organic Molecules, Acc. Chem. Res., 36(4), 255–263, doi:10.1021/ar020230d, 2003.

Capouet, M. and Müller, J. F.: A group contribution method for estimating the vapour pressures of α-pinene oxidation products, Atmos. Chem. Phys., 6(6), 1455–1467, doi:10.5194/acp-6-1455-2006, 2006.

Cappa, C. D.: A model of aerosol evaporation kinetics in a thermodenuder, Atmos. Meas. Tech., 3(3), 579–592, doi:10.5194/amt-3-579-2010-supplement, 2010.

Cappa, C. D. and Jimenez, J. L.: Quantitative estimates of the volatility of ambient organic aerosol, Atmos. Chem. Phys., 10(12), 5409–5424, doi:10.5194/acp-10-5409-2010, 2010.

DeCarlo, P. F., Kimmel, J. R., Trimborn, A., Northway, M. J., Jayne, J. T., Aiken, A. C., Gonin, M., Fuhrer, K., Horvath, T., Docherty, K. S., Worsnop, D. R. and Jimenez, J. L.: Field-Deployable, High-Resolution, Time-of-Flight Aerosol Mass Spectrometer, Anal. Chem., 78(24), 8281–8289, doi:10.1021/ac061249n, 2006.

DePalma, J. W., Horan, A. J., Hall, W. A., IV and Johnston, M. V.: Thermodynamics of oligomer formation: implications for secondary organic aerosol formation and reactivity, Phys. Chem. Chem. Phys., 15(18), 6935, doi:10.1039/c3cp44586k, 2013.

Docherty, K. S., Wu, W., Lim, Y. B. and Ziemann, P. J.: Contributions of Organic Peroxides to Secondary Aerosol Formed from Reactions of Monoterpenes with O 3, Environ. Sci. Technol., 39(11), 4049–4059, doi:10.1021/es050228s, 2005.

Donahue, N. M., Epstein, S. A., Pandis, S. N. and Robinson, A. L.: A two-dimensional volatility basis set: 1. organic-aerosol mixing thermodynamics, Atmos. Chem. Phys., 11(7), 3303–3318, doi:10.5194/acp-11-3303-2011, 2011.

Dougherty, R. C.: Temperature and pressure dependence of hydrogen bond strength: A perturbation molecular orbital approach, J. Chem. Phys., 109(17), 7372, doi:10.1063/1.477343, 1998.

Ehn, M., Thornton, J. A., Kleist, E., Sipilä, M., Junninen, H., Pullinen, I., Springer, M., Rubach, F., Tillmann, R., Lee, B., Lopez-Hilfiker, F., Andres, S., Acir, I.-H., Rissanen, M., Jokinen, T., Schobesberger, S., Kangasluoma, J., Kontkanen, J., Nieminen, T., Kurtén, T., Nielsen, L. B., Jørgensen, S., Kjaergaard, H. G., Canagaratna, M., Maso, M. D., Berndt, T., Petäjä, T., Wahner, A., Kerminen, V.-M., Kulmala, M., Worsnop, D. R., Wildt, J. and Mentel, T. F.: A large source of low-volatility secondary organic aerosol, Nature, 506(7489), 476–479,

doi:10.1038/nature13032, 2014.

Epstein, S. A., Riipinen, I. and Donahue, N. M.: A Semiempirical Correlation between Enthalpy of Vaporization and Saturation Concentration for Organic Aerosol, Environ. Sci. Technol., 44(2), 743–748, doi:10.1021/es902497z, 2010.

Gao, S., Keywood, M., Ng, N. L., Surratt, J., Varutbangkul, V., Bahreini, R., Flagan, R. C. and Seinfeld, J. H.: Low-Molecular-Weight and Oligomeric Components in Secondary Organic Aerosol from the Ozonolysis of Cycloalkenes and α-Pinene, The Journal of Physical Chemistry A, 108(46), 10147–10164, doi:10.1021/jp047466e, 2004.

Hall, W. A., IV and Johnston, M. V.: Oligomer Content of α-Pinene Secondary Organic Aerosol, Aerosol Science and Technology, 45(1), 37–45, doi:10.1080/02786826.2010.517580, 2011.

Hall, W. A., IV and Johnston, M. V.: The Thermal-Stability of Oligomers in Alpha-Pinene Secondary Organic Aerosol, Aerosol Science and Technology, 46(9), 983–989, doi:10.1080/02786826.2012.685114, 2012.

Hallquist, M., Wenger, J. C., Baltensperger, U., Rudich, Y., Simpson, D., Claeys, M., Dommen, J., Donahue, N. M., George, C., Goldstein, A. H., Hamilton, J. F., Herrmann, H., Hoffmann, T., Iinuma, Y., Jang, M., Jenkin, M. E., Jimenez, J. L., Kiendler-Scharr, A., Maenhaut, W., McFiggans, G., Mentel, T. F., Monod, A., Prevot, A. S. H., Seinfeld, J. H., Surratt, J. D., Szmigielski, R. and Wildt, J.: The formation, properties and impact of secondary organic aerosol: current and emerging issues, Atmos. Chem. Phys., 9(14), 5155–5236, doi:10.5194/acp-9-5155-2009, 2009.

Heald, C. L., Kroll, J. H., Jimenez, J. L., Docherty, K. S., DeCarlo, P. F., Aiken, A. C., Chen, Q., Martin, S. T., Farmer, D. K. and Artaxo, P.: A simplified description of the evolution of organic aerosol composition in the atmosphere, Geophys. Res. Lett., 37(8), L08803, doi:10.1029/2010GL042737, 2010.

Holzinger, R., Kasper-Giebl, A., Staudinger, M., Schauer, G. and Röckmann, T.: Analysis of the chemical composition of organic aerosol at the Mt. Sonnblick observatory using a novel high mass resolution thermal-desorption proton-transfer-reaction mass-spectrometer (hr-TD-PTR-MS), Atmos. Chem. Phys., 10(20), 10111–10128, doi:10.5194/acp-10-10111-2010, 2010.

Jokinen, T., Sipilä, M., Junninen, H., Ehn, M., Lönn, G., Hakala, J., Petäjä, T., Mauldin, R. L., III, Kulmala, M. and Worsnop, D. R.: Atmospheric sulphuric acid and neutral cluster measurements using CI-APi-TOF, Atmos. Chem. Phys., 12(9), 4117–4125, doi:10.5194/acp-12-4117-2012, 2012.

Lopez-Hilfiker, F. D., Mohr, C., Ehn, M., Rubach, F., Kleist, E., Wildt, J., Mentel, T. F., Lutz, A., Hallquist, M., Worsnop, D. and Thornton, J. A.: A novel method for online analysis of gas and particle composition: description and evaluation of a Filter Inlet for Gases and AEROsols (FIGAERO), Atmos. Meas. Tech., 7(4), 983–1001, doi:10.5194/amt-7-983-2014, 2014.

Matsunaga, A. and Ziemann, P. J.: Gas-Wall Partitioning of Organic Compounds in a Teflon Film Chamber and Potential Effects on Reaction Product and Aerosol Yield Measurements,

Aerosol Science and Technology, 44(10), 881–892, doi:10.1080/02786826.2010.501044, 2010.

Mentel, T. F., Wildt, J., Kiendler-Scharr, A., Kleist, E., Tillmann, R., Dal Maso, M., Fisseha, R., Hohaus, T., Spahn, H., Uerlings, R., Wegener, R., Griffiths, P. T., Dinar, E., Rudich, Y. and Wahner, A.: Photochemical production of aerosols from real plant emissions, Atmos. Chem. Phys., 9(13), 4387–4406, doi:10.5194/acp-9-4387-2009, 2009.

Mohr, C., Lopez-Hilfiker, F. D., Zotter, P., Prévôt, A. S. H., Xu, L., Ng, N. L., Herndon, S. C., Williams, L. R., Franklin, J. P., Zahniser, M. S., Worsnop, D. R., Knighton, W. B., Aiken, A. C., Gorkowski, K. J., Dubey, M. K., Allan, J. D. and Thornton, J. A.: Contribution of Nitrated Phenols to Wood Burning Brown Carbon Light Absorption in Detling, United Kingdom during Winter Time, Environ. Sci. Technol., 130610071812007, doi:10.1021/es400683v, 2013.

Pankow, J. F.: An absorption model of gas/particle partitioning of organic compounds in the atmosphere, Atmospheric Environment, 28(2), 185–188, doi:10.1016/1352-2310(94)90093-0, 1994.

Renbaum-Wolff, L., Grayson, J. W., Bateman, A. P., Kuwata, M., Sellier, M., Murray, B. J., Shilling, J. E., Martin, S. T. and Bertram, A. K.: Viscosity of α-pinene secondary organic material and implications for particle growth and reactivity, Proceedings of the …, 2013.

Riccobono, F., Schobesberger, S., Scott, C. E., Dommen, J., Ortega, I. K., Rondo, L., Almeida, J., Amorim, A., Bianchi, F., Breitenlechner, M., David, A., Downard, A., Dunne, E. M., Duplissy, J., Ehrhart, S., Flagan, R. C., Franchin, A., Hansel, A., Junninen, H., Kajos, M., Keskinen, H., Kupc, A., Kürten, A., Kvashin, A. N., Laaksonen, A., Lehtipalo, K., Makhmutov, V., Mathot, S., Nieminen, T., Onnela, A., Petäjä, T., Praplan, A. P., Santos, F. D., Schallhart, S., Seinfeld, J. H., Sipilä, M., Spracklen, D. V., Stozhkov, Y., Stratmann, F., Tomé, A., Tsagkogeorgas, G., Vaattovaara, P., Viisanen, Y., Vrtala, A., Wagner, P. E., Weingartner, E., Wex, H., Wimmer, D., Carslaw, K. S., Curtius, J., Donahue, N. M., Kirkby, J., Kulmala, M., Worsnop, D. R. and Baltensperger, U.: Oxidation products of biogenic emissions contribute to nucleation of atmospheric particles, Science, 344(6185), 717–721, doi:10.1126/science.1243527, 2014.

Riipinen, I., Yli-Juuti, T., Pierce, J. R., Petäjä, T., Worsnop, D. R., Kulmala, M. and Donahue, N. M.: The contribution of organics to atmospheric nanoparticle growth, Nature Geosci, 5(7), 453–458, doi:10.1038/ngeo1499, 2012.

Roldin, P., Eriksson, A. C., Nordin, E. Z., Hermansson, E., Mogensen, D., Rusanen, A., Boy, M., Swietlicki, E., Svenningsson, B., Zelenyuk, A. and Pagels, J.: Modelling non-equilibrium secondary organic aerosol formation and evaporation with the aerosol dynamics, gas- and particle-phase chemistry kinetic multilayer model ADCHAM, Atmos. Chem. Phys., 14(15), 7953–7993, doi:10.5194/acp-14-7953-2014-supplement, 2014.

Russell, L. M., Bahadur, R. and Ziemann, P. J.: Identifying organic aerosol sources by comparing functional group composition in chamber and atmospheric particles, Proceedings of the National Academy of Sciences, 108(9), 3516–3521, doi:10.1073/pnas.1006461108, 2011.

Smith, J. N., Barsanti, K. C., Friedli, H. R., Ehn, M., Kulmala, M., Collins, D. R., Scheckman, J. H., Williams, B. J. and McMurry, P. H.: Observations of aminium salts in atmospheric nanoparticles and possible climatic implications, Proceedings of the National Academy of Sciences, 107(15), 6634–6639, doi:10.1073/pnas.0912127107, 2010.

Veres, P., Roberts, J. M., Burling, I. R., Warneke, C., de Gouw, J. and Yokelson, R. J.: Measurements of gas-phase inorganic and organic acids from biomass fires by negative-ion proton-transfer chemical-ionization mass spectrometry, J. Geophys. Res., 115(D23), doi:10.1029/2010JD014033, 2010.

Veres, P., Roberts, J. M., Warneke, C., Welsh-Bon, D., Zahniser, M., Herndon, S., Fall, R. and de Gouw, J.: Development of negative-ion proton-transfer chemical-ionization mass spectrometry (NI-PT-CIMS) for the measurement of gas-phase organic acids in the atmosphere, International Journal of Mass Spectrometry, 274(1-3), 48–55, doi:10.1016/j.ijms.2008.04.032, 2008.

Volkamer, R., Jimenez, J. L., San Martini, F., Dzepina, K., Zhang, Q., Salcedo, D., Molina, L. T., Worsnop, D. R. and Molina, M. J.: Secondary organic aerosol formation from anthropogenic air pollution: Rapid and higher than expected, Geophys. Res. Lett., 33(17), L17811, doi:10.1029/2006GL026899, 2006.

Williams, B. J., Goldstein, A. H., Kreisberg, N. M. and Hering, S. V.: An In-Situ Instrument for Speciated Organic Composition of Atmospheric Aerosols: Thermal Desorption Aerosol GC/MS-FID (TAG), Aerosol Science and Technology, 40(8), 627–638, doi:10.1080/02786820600754631, 2006.

Yasmeen, F., Vermeylen, R., Szmigielski, R., Iinuma, Y., Böge, O., Herrmann, H., Maenhaut, W. and Claeys, M.: Terpenylic acid and related compounds: precursors for dimers in secondary organic aerosol from the ozonolysis of α- and β-pinene, Atmos. Chem. Phys., 10(19), 9383–9392, doi:10.5194/acp-10-9383-2010-supplement, 2010.

Yatavelli, R. L. N., Lopez-Hilfiker, F., Wargo, J. D., Kimmel, J. R., Cubison, M. J., Bertram, T. H., Jimenez, J. L., Gonin, M., Worsnop, D. R. and Thornton, J. A.: A Chemical Ionization High-Resolution Time-of-Flight Mass Spectrometer Coupled to a Micro Orifice Volatilization Impactor (MOVI-HRToF-CIMS) for Analysis of Gas and Particle-Phase Organic Species, Aerosol Science and Technology, 46(12), 1313–1327, doi:10.1080/02786826.2012.712236, 2012.

Yatavelli, R., Stark, H. and Thompson, S. L.: Semicontinuous measurements of gas–particle partitioning of organic acids in a ponderosa pine forest using a MOVI-HRToF-CIMS, Atmospheric …, 2014.

Zhao, Y., Kreisberg, N. M., Worton, D. R., Isaacman, G., Weber, R. J., Liu, S., Day, D. A., Russell, L. M., Markovic, M. Z., VandenBoer, T. C., Murphy, J. G., Hering, S. V. and Goldstein, A. H.: Insights into Secondary Organic Aerosol Formation Mechanisms from Measured Gas/Particle Partitioning of Specific Organic Tracer Compounds, Environ. Sci. Technol., 47(8), 3781–3787, doi:10.1021/es304587x, 2013.

Ziemann, P. J.: Evidence for Low-Volatility Diacyl Peroxides as a Nucleating Agent and Major Component of Aerosol Formed from Reactions of O 3with Cyclohexene and Homologous Compounds, The Journal of Physical Chemistry A, 106(17), 4390–4402, doi:10.1021/jp012925m, 2002.

Ziemann, P. J. and Atkinson, R.: Kinetics, products, and mechanisms of secondary organic aerosol formation, Chem. Soc. Rev., 41(19), 6582, doi:10.1039/c2cs35122f, 2012.

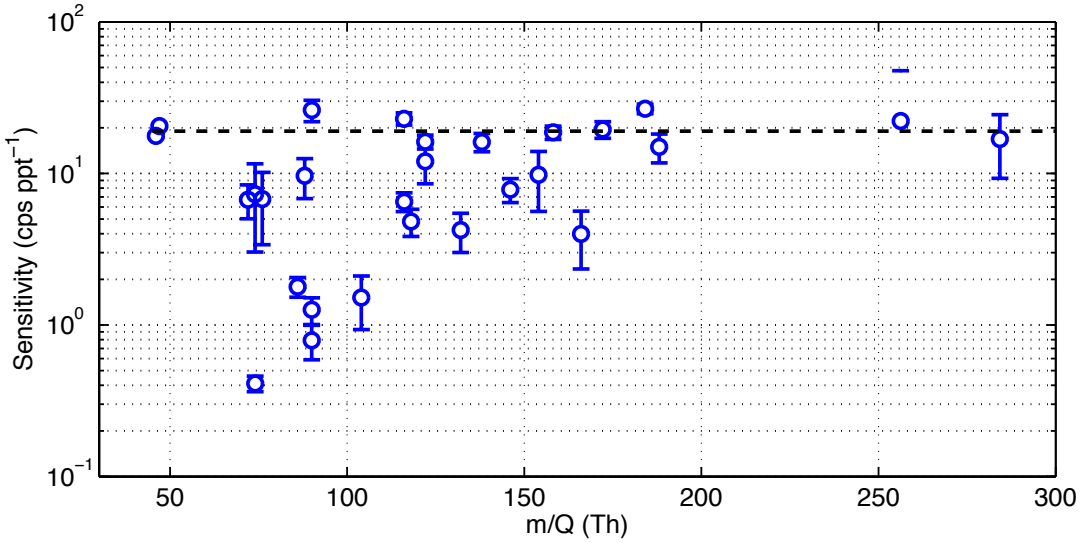

Figure 4.1 Acetate Sensitivity.

The distribution of observed sensitivites to carboxylic acids using acetate reagent ions. Error bars are 1σ based on multiple injections of solutions following *Mohr et al. 2013*. The black dashed line shows the sensitivity value used for bulk analysis.

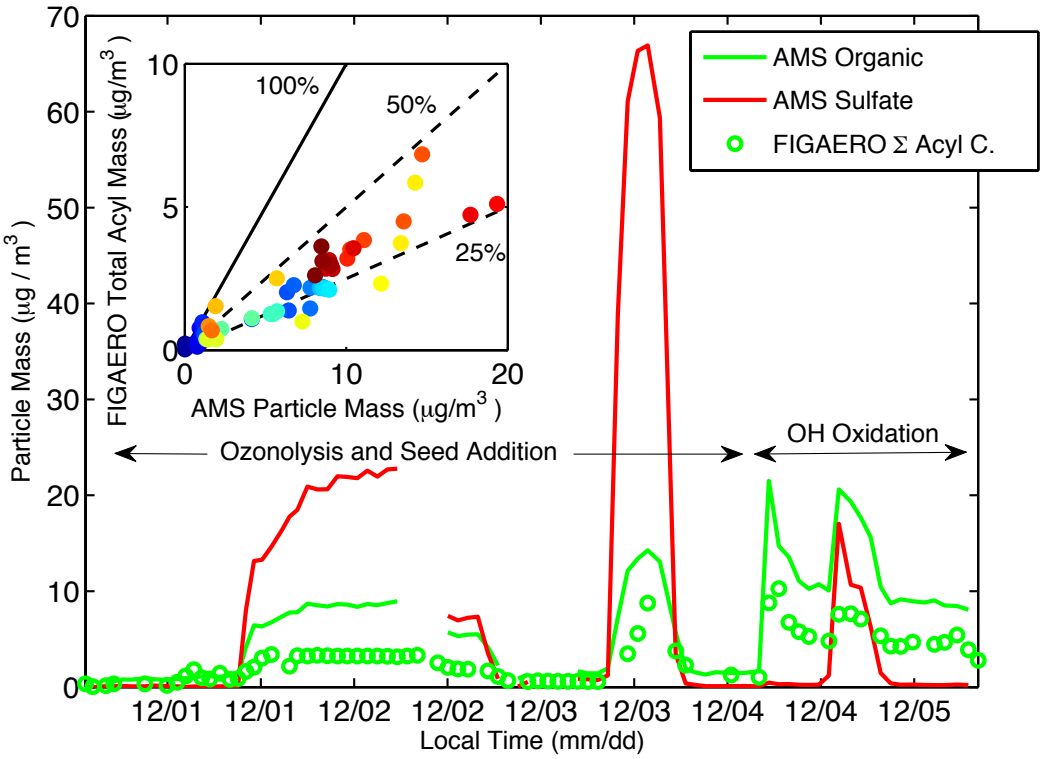

Figure 4.2 An overview of the experiments conducted in the JPAC chamber. Green and red lines are total organic and sulfate mass concentrations measured by an HR-AMS. The total organic aerosol mass detected by the AMS responded to changes in seed concentrations, increasing the inferred SOA yield. Size selected ammonium sulfate additions were performed to increase the particle surface area relative to chamber walls. The sum FIGAERO-HRTOF-CIMS particulate mass using acetate reagent ions is shown in green circles using the formic acid sensitivity for all detected compositions (see text for details). Inset: Correlation between the HR-AMS derived total organic aerosol mass concentrations and the FIGAERO HR-ToF-CIMS derived total "acyl" containing compound mass concentrations shows that across all chamber conditions the FIGAERO measurements explain 25-50% of the total organic aerosol mass.

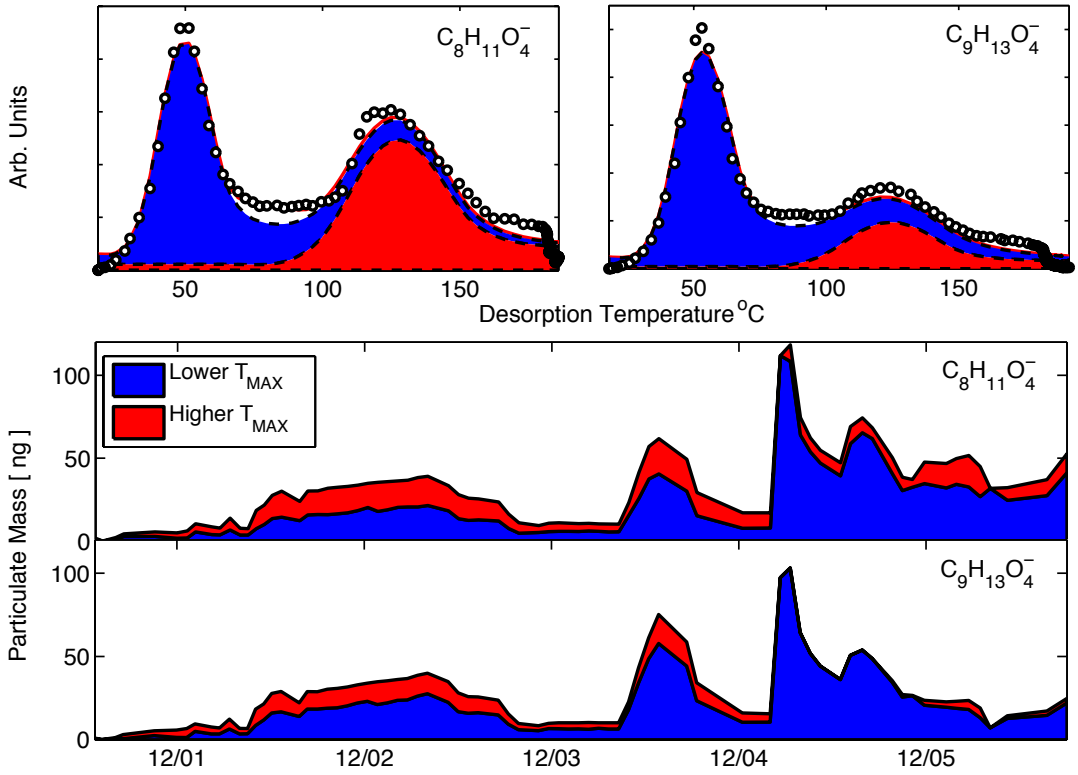

Figure 4.3 Thermograms of select compounds.

Top panels: Thermograms for two ion compositions, each showing two distinct modes in the thermogram, are plotted showing the results of fitting desorption profiles characteristic of an individual compound with a specific enthalpy of sublimation. The first, lower temperature, modes are consistent with the corresponding carboxylic acid desorbing as a non-interacting component of the collected organic aerosol. We attribute the second, higher temperature modes, to thermal decomposition of lower volatility compounds (such as oligomers or highly functionalized monomers) which are thermally unstable and which presumably do not affect the partitioning of the primary acids between the gas and particle phase. Lower Panels: The time series of the individual peak integrations within a fitted thermogram for the two different ion compositions across all chamber conditions. A significant fraction of the total detected signal arises from thermal decomposition (red) during desorption. Evident is the nearly complete disappearance of the second mode in $C_9H_{13}O_4^-$ (pinic acid) during OH oxidation suggesting that it is derived from a precursor that is only present during ozonolysis or which is reacted away in the presence of OH.

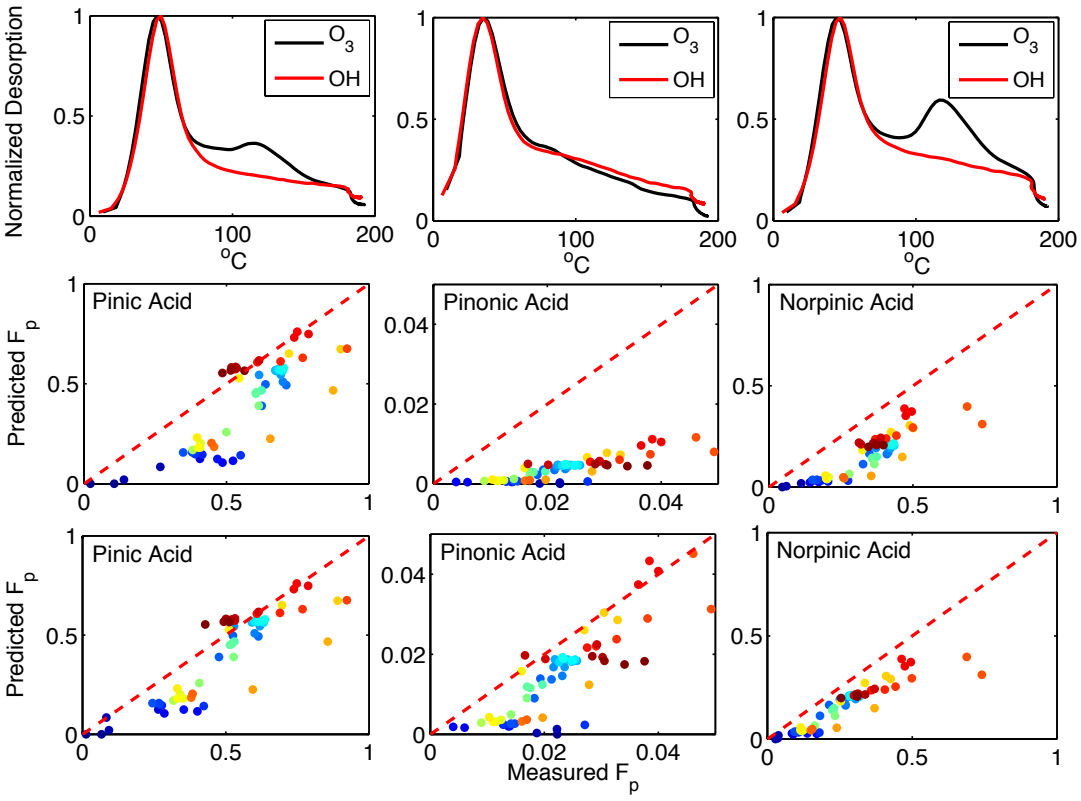

Figure 4.4 Partitioning of common monoterpene tracers.

Top panels: Thermogram shapes for ozonolysis conditions (black) and OH oxidation (red) for the ion compositions corresponding to those of pinic, pinonic, and norpinic acids (left to right). Middle panels: Comparison between modeled and measured gas-particle partitioning (F_p). Generally poor agreement is found with non-linearity and points far from the 1:1 line (red dashed). Bottom: The same partitioning comparison but with the thermogram fitting routine (Figure 3) applied to remove the secondary modes in the desorption profile which are likely a result of thermal decomposition (see text for details). For pinonic acid a single desorption mode is observed under all conditions. To achieve model measurement agreement an activity coefficient of 0.25 is required, or the pure compound vapor pressure used is too high by a factor of ~ 4.

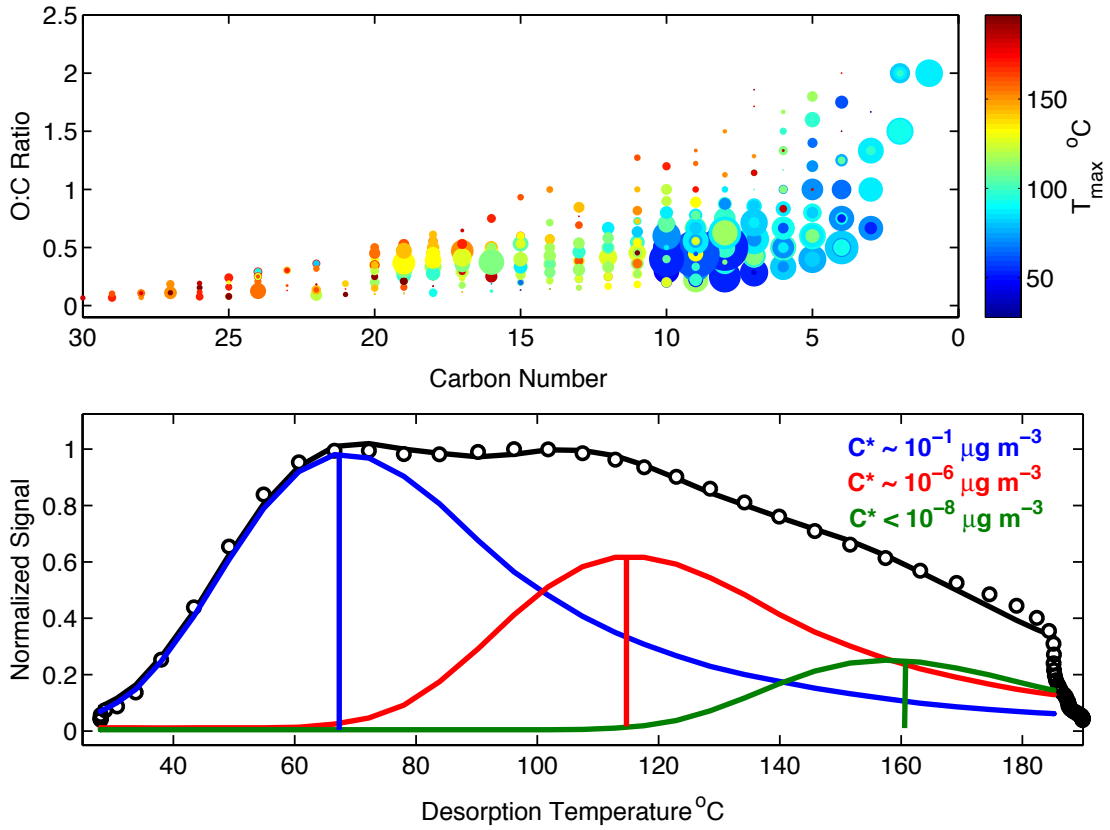

Figure 4.5 Volatility Distribution of monoterpene OA.

Top: Points are plotted sized by the square root of their particle phase desorption signal. Evident is a secondary mode in abundance space between #C 15-20. Each compound is colored by the temperature of maximum desorption signal, which is related to a compound's enthalpy of sublimation (saturation vapor pressure) as shown previously (Lopez-Hilfiker, et al 2014). Bottom: A sum thermogram, i.e. the entire mass spectral signal at each measurement time (using selection criteria detailed in the text), is summed and plotted versus desorption temperature. Clearly SOA from α-pinene ozonolysis exhibits multiple modes. The first mode is consistent with monoterpene derived diacids, where as the secondary modes which arise at temperatures >100 °C have effective vapor pressures at least 4 orders of magnitude lower than common monoterpene oxidation products.

Chapter 5. VOLATILITY AND ROLE OF ACCRETION PRODUCTS IN SOA FROM POLLUTED ISOPRENE REGIONS

5.1 INTRODUCTION.

Secondary organic aerosol (SOA), and specifically that derived from biogenic sources, makes up a dominant fraction of ambient submicron aerosol with important impacts on Earth's radiative balance and air quality (Hallquist et al., 2009; Heald et al., 2010; Ziemann and Atkinson, 2012). Isoprene dominates the emissions of biogenic volatile organic compounds (BVOC) into the atmosphere, with roughly 500 Tg C emitted per year. Therefore, isoprene derived oxidation products have the potential to be a significant source of SOA globally, particularly in temperate and tropical continental regions where isoprene emissions often dominate total BVOC emissions (Guenther et al., 1995). The ability for isoprene, and more generally BVOC to act as an SOA source depends on whether its oxidation products are (1) highly reactive towards existing aerosol and can therefore be incorporated into the particle phase via reactive uptake mechanisms (Surratt et al., 2010), or (2) of sufficiently low vapor pressure in the gas phase that they partition strongly into the condensed phase (Ehn et al., 2014; Pankow, 1994).

The photochemical oxidation of isoprene in the atmosphere leads to the formation of organic peroxy radicals (RO_2) intermediates, the fates of which ultimately determine the stable products which might influence SOA. The reaction of RO_2 with HO_2 generally leads to the formation of hydroperoxides (or peroxy acids), which have lower volatility than the precursor, while the reaction of RO_2 with nitrogen oxides leads primarily to the formation of alkoxy radicals (RO) which often undergo carbon-carbon bond scission resulting in higher volatility fragments. Similarly, self-reactions of RO_2 have a significant branching to RO, while also making somewhat lower volatility products such as alcohols or carbonyls. Therefore, higher SOA yields are often found under conditions where reactions of RO_2 with HO_2 dominate over those with NO or other RO_2 (Surratt et al., 2010). Moreover, a chemical pathway proposed to be an important source of particle mass from isoprene is the formation of second-generation isoprene epoxydiols (IEPOX) (Lin et al., 2012; Surratt et al., 2010) from reaction of isoprene hydroxy hydroperoxides

(ISOPOOH), which are the main first-generation products under HO_2 dominant conditions, with the hydroxyl radical (OH). Subsequent reactive uptake of IEPOX on aqueous aerosol particles has been shown to be an efficient means of generating SOA (Surratt et al., 2010). Aerosol growth by IEPOX reactive uptake is facilitated by acid catalyzed ring-opening reactions in the condensed phase, followed by nucleophilic substitution reactions involving water, sulfate, or nitrate, to form significantly lower volatility products such as methyl tetrols, organosulfates and dihyroxy nitrates. The saturation vapor pressures of such products are lower than the precursor molecule by more than two orders of magnitude per functional group addition (Capouet and Müller, 2006; Ziemann and Atkinson, 2012). In addition, another possible nucleophile are these products, resulting in the formation of dimers or mixed accretion products. However do to their inherent low volatility, quantifying their abundance has remained an analytical challenge.

The extent to which the IEPOX mechanism and more generally isoprene oxidation contributes to total organic aerosol mass remains poorly constrained under atmospherically relevant conditions. Chamber measurements suggest aerosol mass yields of up to ~28% in the presence of aqueous acidic seed, however, the actual yield under ambient conditions depends on a variety of factors, such as aerosol acidity and phase state, which are difficult to measure accurately in the atmosphere (Gaston et al., 2014; Surratt et al., 2010), as well as the branching reactions of the RO_2 radicals and the deposition or further reaction of semi-volatile products which contribute to SOA. Much of the inferred importance of IEPOX derived SOA has arisen from offline filter analysis and by positive matrix factorization (PMF) analysis of Aerosol Mass Spectrometer (AMS - Aerodyne Research Inc.) mass spectra. Analysis of the electron impact ionization mass spectra have identified elevated signals at mass-to-charge ratio 82 Th (f_{82} = 82 Th / total organic aerosol) in regions of isoprene oxidation (Robinson et al., 2011). High-resolution analysis showed that the major ion at 82 Th is $C_5H_6O^+$, consistent with a methyl furan fragment. This finding was later confirmed by additions of authentic standards to the AMS which showed that methyltetrahydrofuran-3,4-diols (3-MeTHF-3,4-diols) and other isomers associated with IEPOX-SOA result in enhanced f_{82} in AMS spectra (Lin et al., 2012).

Using this factor-based method, IEPOX-SOA was inferred to account for 33% of ambient organic aerosol in summertime Atlanta (Budisulistiorini et al., 2013). The source apportionment

was supported by the characteristic 82 Th peak in a PMF factor and reasonable temporal correlation of the factor with online sulfate mass concentrations and offline measurements of 2-methyltetrols, which have been identified from chamber based experiments (Budisulistiorini et al., 2013; Lin et al., 2012; Surratt et al., 2010). No studies have yet systematically examined whether enhanced f_{82} is solely unique to IEPOX chemistry or exactly what types of compounds comprise it. Higher time resolution *in situ* measurements of ambient aerosol molecular composition, which until recently were unavailable, can better elucidate chemical and physical variables which control the appearance of key oxidation products that contribute to SOA by allowing investigation of the covariance of molecular tracers with precursor concentrations, photochemical conditions, and meteorological parameters such as temperature and relative humidity. Knowledge of such controlling variables is required to model the evolution of SOA in the atmosphere.

In this chapter, I present measurements made during the Southeast Atmosphere Study (SAS) during which submicron aerosol was comprehensively characterized by a variety of *insitu* mass spectrometric techniques. The measurement site was situated in Centerville, Alabama a polluted region with emissions of both monoterpenes and isoprene. I focus on measurements of organic aerosol molecular composition and volatility utilizing a FIGAERO (Filter Inlet for Gas and Aerosol) (Lopez-Hilfiker et al., 2014) coupled to a high resolution chemical ionization mass spectrometer (HR-TOF-CIMS) using iodide ions. These measurements provide direct evidence that a large fraction of organic aerosol derived from isoprene, and in particular from IEPOX multiphase chemistry, is in oligomer or low volatility form, and should therefore be treated as effectively non-volatile under most atmospheric conditions. Furthermore, our measurements conflict with inferences about the volatility distribution of isoprene SOA based on common molecular isoprene aerosol tracers (e.g. methyl-tetrols, alkene-triols, furan diols), which would suggest that isoprene SOA is predominantly semi-volatile (Lin et al., 2012). This conflict is reconciled by noting that the majority of such tracer measurements involve thermal desorption which can result in thermal decomposition of lower volatility, larger molecular weight, compounds producing the detected tracer compounds.

5.2 METHODS AND CALIBRATION.

5.2.1 *UW-FIGAERO.*

We deployed the UW-FIGAERO coupled to a high-resolution time-of-flight mass spectrometer (FIGAERO-HR-TOF-CIMS) during the SOAS field project to measure oxidized organics in submicron aerosol as well as the gas phase (Lopez-Hilfiker et al., 2014). We utilize iodide adduct chemical ionization which is most sensitive towards multifunctional oxygenated organic compounds. We restrict our analysis to molecular ions containing an Iodide adduct, essentially guarantees detection of the parent organic compound without ionization induced fragmentation (Lee et al., 2014; Lopez-Hilfiker et al., 2014). Gas phase species are measured in real time at 1 Hz for approximately 30 minutes while particles are collected simultaneously in a separate stage of the FIGAERO on a Teflon filter (2 micron Zefluor, Pall Corp. 25 mm) via a ~2 um impactor for removing large particles. After particle collection, particles undergo temperature programmed thermal desorption at a rate of 10 °C/min by programmatically heating a flow of UHP nitrogen and passing it across the filter and directly into the ionization region of the mass spectrometer. The temperature ramp takes roughly 20 minutes to reach 200 °C and then is held at 200 °C for an additional 20 minutes to ensure all organic matter has desorbed from the filter. The vapors that arise from the thermal desorption process are detected by the HR-TOF-CIMS producing a thermogram (desorption signal *vs*. temperature) which can be integrated to quantify the mass of individual compounds in the aerosol.

We have shown previously that individual compounds desorb from a synthetic multi-component mixture with a characteristic desorption profile. The location of the maximum desorption signal in temperature space (T_{max}) is also highly correlated with enthalpy of sublimation and vapor pressure (Lopez-Hilfiker et al., 2014). This 'calibrated' desorption axis can be used to relate compounds with unknown chemical properties to effective vapor pressures for each molecular composition detected, or to confirm the molecular identification by using the desorption axis in a similar fashion to a gas-chromatograph. We have recently extended our desorption axis calibration to vapor pressures as low as 10^{-12} Pa ($C_{10}H_{22}O_7$ dipentaerythritol, T_{max}~160 °C) near the lower limit of volatility measured by this instrument which is approximately 10^{-18} Pa.

5.2.2 *Iodide ToF-CIMS Sensitivity to Organics*

Iodide chemical ionization mass spectrometry (I-CIMS) has been described in detail previously (Huey et al., 1995; Kercher et al., 2009; Lee et al., 2014). We have calibrated to many organic and inorganic molecules including hydroxy-hydroperoxides, multifunctional acids, diols, triols, tetrols, nitrated aromatics and other oxidized organic molecules in an effort to constrain the instrument response to a variety of different functionalities. As expected, given constraints imposed by ion-molecule collision frequencies, we find that there is a "maximum sensitivity", which for iodide-organic clusters is ~ 22 cps $pptv^{-1}$ (per million cps of reagent ion). In part, this limit is empirical, i.e., we have not yet measured a higher sensitivity to organic compounds. As discussed below, this limit is also consistent with the experimental ion-molecule collision limit of our instrument determined by calibrating to N_2O_5, which is known to react with iodide ions at the collision limit (Huey et al., 1995).

5.2.3 *Collision Limit Determination of the UW-TOF-CIMS*

To determine the collision limit of our instrument we generate isotopically labeled $^{15}N_2O_5$ by reacting excess $^{15}NO_2$ with ozone leading to the formation of $^{15}NO_3$ and $^{15}N_2O_5$ during transit down a Teflon reaction cell held at 30 psig by a glass capillary. The output can be modeled (Bertram et al., 2009) and has been independently verified by other techniques (e.g. TD-LiF or NOAA-CARDS) (Brown et al., 2001; Day et al., 2002). N_2O_5 reacts with iodide ions at the collision limit via two channels. One channel is the formation of an ion-molecule adduct between N_2O_5 and iodide $[IN_2O_5]$-. This cluster may simply be a stable intermediate on the way to the lowest energy reaction products NO_3^- and INO_2, but is detected as a major product under weak electric field settings (weak declustering) in the ion optics used to transmit ions through the vacuum chamber to the extraction region (Kercher, et al 2009). The other channel results in NO_3- + INO_2, presumably from the dissociation of the iodide adduct, and its contribution can be enhanced by increasing strength of the electric fields in the atmospheric pressure interface (APi) of the mass spectrometer (Kercher et al., 2009). Huey et al. 1995 showed that the reaction between N_2O_5 and iodide ions proceeds at the collision limit, even at low pressure, such that for every collision between iodide and N_2O_5, a product ion is always produced, which in their case was the dissociation product (NO_3-) due presumably to strong electric field settings (Huey et al.,

1995). Therefore, by adding the product ion signals from the two detection channels for N_2O_5, and dividing by the total N_2O_5 concentration (pptv) sampled, we arrive at the collision-limited sensitivity for our instrument of 22-26 cps ppt^{-1} per million reagent ions. An example time-series of this type of experiment is shown in Figure 5.1.

As each of our N_2O_5 detection channels are detected at very different mass to charge ratios (63 *vs*. 237 Th) our collision limit determination could be influenced by mass dependent transmission of the instrument. To account for this we measured the mass dependent transmission of our instrument by adding large quantities of known compounds with varying molecular mass to the ionization region. This method assumes that the total number of charges (ions) in the ionization region remains unchanged over short time periods (controlled by the activity of the ^{210}Po) and therefore any changes to the total number of ions measured at the detector is due to the varying efficiency with which ions having different masses are transmitted through the mass spectrometer. By measuring the relative change in total ions detected as a function of mass-to-charge (m/Q), a linear system of equations can be solved to derive the transmission efficiency as a function of mass-to-charge, known as the mass transmission function of the instrument. The transmission function depends on ion optic settings, primarily the two quadrupole ion guides which act as band-pass filters. The lower mass cutoff is most important for our collision limit determination as $^{15}NO_3$ (63 Th) is near the low end of the mass scale. We tune the transmission function to be as flat as possible by adjusting the RF frequency, amplitude and axial voltage gradient along the quadrupole ion guides. In the mass range of interest for developing the collision limit (63 – 237 Th) the mass transmission is approximately constant Figure 5.1 (top panel).

The collision limit developed above provides a useful constraint on sensitivity for compounds for which no calibration standard exists. To date, our calibrations to many organic compounds with varying functional groups suggest that more polar functional groups a molecule has increases its ability to bind with iodide (e.g. binding energy) and also increases the probability that a ion molecule collision will result in adduct formation resulting in a high overall sensitivity. Some organic compounds we have calibrated to are near this “maximum” or collision-limited

sensitivity. These include: the 2-methyl tetrols from isoprene (19 cps ppt^{-1}), dipentaerythritol (22 cps ppt^{-1}), malonic acid (19 cps ppt^{-1}) and levoglucosan (20 cps ppt^{-1}).

5.2.4 *Distribution of Binding Energies of Iodide Adducts*

Organic molecules are nearly exclusively detected as molecular clusters with iodide. A neutral molecule that forms a strongly bound cluster with iodide should result in a high sensitivity for that compound assuming it is formed at or near the collision limit given that it will then survive transmission through the ion optics. Thus, knowledge of a cluster's binding energy could provide a means to further constrain the instrument's sensitivity to a broader range of compounds it detects even if standards do not exist. However, very few binding energies with iodide are known, and while binding energies calculated using quantum chemical methods provides valuable information, carrying out the computationally expensive calculations for the 100's of molecular ions typically identified in our spectra is not feasible. Therefore, to constrain the effective binding energies of multifunctional organics we scanned the electric field strength while measuring a steady-state distribution of organic compounds to experimentally determine the energy required to break apart the iodide ion adducts. In concert with quantum chemical calculations, the experimentally and theoretically determined binding energies provide insights into the instrument sensitivity to a broad range of organic compounds.

We used a steady-state atmospheric simulation chamber at the University of Washington to oxidize a-pinene in the presence of ozone and NO_x to generate a wide range of oxidized organics (Lopez-Hilfiker et al., 2015). We scan the voltages in the APi region of the mass spectrometer to systematically add collisional energy to the iodide-organic adducts until they dissociate back to I- and a neutral organic molecule. We call these declustering scans. An example of this type of experiment is shown in Figure 5.2a, where ion count rates are plotted as a function of voltage difference (dV) between the skimmer and the entrance to the second quadrupole of the mass spectrometer. During a declustering scan, all potentials upstream of the second quadrupole of the mass spectrometer are moved together towards more negative voltages such that the electric field and therefore the declustering strength is incrementally changed while maintaining a constant voltage gradient across all other optics (see Figure 5.3 TOF schematic). Specifically, we

maintain a constant gradient across the quadrupoles to avoid simultaneous changes in the mass transmission function, which depends upon the axial voltage gradient along the quadrupole rods. We detect the survival of the molecular clusters as a function of electric field strength (Figure 5.2a), which is relatable to the ion-molecule binding energy. Molecules that are tightly bound to iodide require a larger dV (stronger electric field) to dissociate, whereas smaller, less functionalized organics that are weakly bound (e.g. simple acids, diols, triols) are rapidly dissociated during the first few voltage steps. We find that larger multifunctional organics are generally bound more strongly to iodide and survive to higher potentials during the scan (e.g. multifunctional organic nitrates in Figure 5.2a). That the larger, multifunctional molecules (e.g. $C_{10}H_{15}O_8N$) are initially detected with the same efficiency during the first few voltage steps implies that they are bound to iodide with sufficient binding energy to be efficiently transmitted by the normal operation of the ion optics in the mass spectrometer and are therefore likely to be detected at a sensitivity that depends only on their formation rate, which for lack of a better constraint we assume to be at the collision limit (Figure 5.2b). Compounds that are less tightly bound with iodide are to some degree dissociated (back to I- and a neutral organic) during transit through the APi of the mass spectrometer and are detected with a lower overall sensitivity than a measured or predicted formation rate would imply.

For compounds which are partially declustered even at our weakest declustering settings, and thus for which the true sigmoidal curve is not observed, we calculate an effective maximum sensitivity by using a custom non-linear least squares fitting algorithm to determine the extent to which the ion adduct has been declustered during transit. The algorithm uses a characteristic scan shape and width, but variable amplitude to extend the scan to weaker declustering conditions than is present during normal operation (dV = 1V). The fitted curve allows determination of the maximum possible sensitivity for a compound if a weaker declustering setting than is normally used on our instrument could be achieved (see Figure 5.2c for an example fit of $C_{10}H_{16}O_3I$-).

In the analysis that follows we utilize a combination of the measured collision limit and the results of declustering scanning to constrain the sensitivity to compounds for which there is no calibration standard available. We apply the experimentally determined collision limit to all

organics that we have not explicitly calibrated to, which results in a lower limit to mass concentrations reported below. We note that the values of the collision limit or other calibration derived sensitivity values reported herein are likely unique to the electric fields, IMR geometry and flows of our instrument. While useful as a relative guide, these values should not be applied to data from other instruments without similar experiments.

5.3 RESULTS

5.3.1 *Isoprene Derived Secondary Organic Aerosol.*

A major fraction of the total detected signal during SOAS in the particle phase was from molecular tracers traditionally used to quantify IEPOX SOA offline. In Figure 5.4 we present a time series of the contribution of IEPOX to total submicron organic aerosol as measured by an aerosol mass spectrometer (AMS). This factor, derived from positive matrix factorization (PMF) explains approximately 15-30% of total submicron organic aerosol during the SOAS field campaign and therefore represents a significant source of particle mass. Also shown is a sum of compositions detected in ambient aerosols by the FIGAERO-TOF-CIMS, which are highly correlated ($R > 0.8$) with $C_5H_{10}O_3$ and $C_5H_{12}O_4$, common semi-volatile molecular tracers from IEPOX derived aerosol (black). This CIMS IEPOX factor is comprised of predominantly C_5 molecules with 3-6 oxygen atoms and to a large degree explains the time evolution and mass loading of the AMS factor (for complete list of compositions see legend in Figure 5.8).

Our uncertainty in mass concentration (grey shading) is due to the inability of our instrument to resolve structural isomers (e.g. alkene triols vs furan diols), and to a lesser degree inferring calibration factors for compounds for which no direct standards are available. Different isomers, in the case of $C_5H_{10}O_3$, which is the single largest signal in this factor, can have varying sensitivities depending on molecular geometry and functional groups present. In Figure 5.4 the upper limit in concentration (grey shading) assumes detection by the CIMS as a diol (e.g. a 3-MeTHF-3,4-diols), the lower limit in concentration assumes detection as a triol. The central points (black) are calculated using the instrument sensitivity to IEPOX, which falls between a straight chain diol and triol. The second largest signal in the factor is $C_5H_{12}O_4$, presumably the C_5

methyl tetrol ($C_5H_{12}O_4$) as very few structural isomers are possible given the likely influence of isoprene chemistry at this site. We calibrated to 2-methyl tetrols using an authentic standard (synthesized by the Surratt Group, UNC) by direct injection of known concentrations onto the primary FIGAERO filter followed by temperature-programmed thermal desorption. For the remainder of the compounds included in the sum, no calibration standard is readily available so we apply the collision limit described above. Inset in Figure 5.4, a scatter plot of the AMS PMF factor for IEPOX *vs*. the CIMS IEPOX factor for the whole campaign shows that the FIGAERO-CIMS detects compounds which behave in a similar fashion as the AMS IEPOX factor, and within calibration uncertainty we explain 50-100% of the OA mass represented by the AMS IEPOX factor. Importantly, the FIGAERO data contains additional molecular composition and volatility information, which is lost by the electron impact ionization used in the AMS, and which we exploit for insights into the nature of IEPOX SOA.

The bottom panel of Figure 5.4 shows thermal desorption profiles of $C_5H_{12}O_4$ and $C_5H_{10}O_3$ from ambient aerosol particles measured by the FIGAERO during SOAS, the two largest signals in the FIGAERO factor. The thermal desorption profile of $C_5H_{12}O_4$ exhibits two distinct modes at the same high-resolution ion composition (blue). The first mode maximizes near a desorption temperature characteristic of a tetrol standard deposited during the campaign (T_{max} ~55 °C grey). The second mode maximizes at a much higher temperature (T_{max} ~90 °C). This desorption temperature is not consistent with a C_5 tetrol (or any possible isomer), but rather with a compound having a saturation vapor pressure 3 orders of magnitude lower than would be inferred from the molecular composition. Also shown is the thermogram for $C_5H_{10}O_3$ (green), presumably an alkene triol or furan diol, which would be expected to maximize at a lower desorption temperature than that of the tetrol standard based on structure-activity relationship estimates of saturation vapor pressures. Instead, $C_5H_{10}O_3$ maximizes at the same unexpectedly high temperature as the secondary mode of the tetrol. A scatter plot (inset) of the tetrol *vs* $C_5H_{10}O_3$ measured by the FIGAERO across the entire SOAS campaign, shows these two thermal desorption products are highly correlated (R = 0.873) across a wide range of atmospheric conditions. That both the tetrol and $C_5H_{10}O_3$ are highly correlated in time, and reach a maximum at nearly the same unexpectedly high temperature, suggests that they are co-sourced, presumably

via thermal decomposition of dimer compounds or higher order oligomers. We have shown similar behavior for products in the a-pinene system (Lopez-Hilfiker et al., 2015).

5.3.2 *Bulk Organic Aerosol Volatility.*

In Figure 5.5 we present a similar analysis to that of IEPOX derived organic aerosol but no longer constrained to only isoprene oxidation products. In the top panel, mass concentrations measured by the AMS are compared to the sum of all organic compounds measured by the FIGAERO as iodide adducts having the general formula $(C_xH_yO_z)I^-$. For compounds which we do not have a direct calibration, we assign the collision limit sensitivity, which likely results in a lower limit to measured organic aerosol mass. The results presented in Figure 5.5 show that the FIGAERO explains a minimum of 50% of the total organic aerosol mass detected by the AMS. A correlation plot between AMS total organic and the FIGAERO-CIMS sum is also shown (inset). In the lower panel of Figure 5.5 the average total thermogram from SOAS measured by the FIGAERO HR-ToF-CIMS is shown on a normalized axis. Evident are multiple desorption modes, though no significant mode is present at temperatures where commonly measured isoprene oxidation products (e.g. IEPOX, ISOPOOH, tetrols, triols, furans) would be expected to desorb if they were partitioning to the aerosol according to Raoult's or Henry's Laws.

A custom thermogram fitting routine described in detail elsewhere (Lopez-Hilfiker et al., 2014), suggest three distinct volatility modes explain the sum thermogram. Briefly, a characteristic desorption shape and width are constrained using single mode thermograms of individual ions, and then these general shapes are used as the basis function to fit the sum thermogram with a non-linear least squares fitting routine having freely varying height in signal space, and signal maximum location in temperature space. The resulting temperature at which each mode reaches a maximum, T_{max} (vertical lines), is then used to assign an effective saturation vapor pressure to the mode and thus to the compounds desorbing within it (Lopez-Hilfiker et al., 2014). The effective saturation vapor pressures can then be used to compare with expected volatility distributions either from laboratory chamber measurements or structure-activity relationship derived predictions based on molecular composition that might for example be used in the SOA parameterizations of regional or global chemical transport models.

In Figure 5.6 we present a volatility basis set approach to examining the volatility of organic aerosol during SOAS based on the thermogram modes derived above and shown in Figures 5.4 and 5.5. One way to estimate the volatility distribution is to use the FIGAERO-CIMS measured abundance of commonly reported tracers of IEPOX derived SOA, which are thought to be dominated by tetrols, triols, furan diols, with some small contribution from dimers, and then calculate the saturation vapor pressures for each of these components using a structure activity relationship. This distribution, potentially similar to what a mechanism-based model might estimate, is represented with white bars in Figure 5.6. In contrast, the volatility distribution of IEPOX derived aerosol components obtained directly from the measured thermograms (black bars in Figure 5.6), reveal effective saturation vapor pressures more than 3 orders of magnitude lower than those predicted based on molecular tracer composition (i.e. white bars). The thermogram-derived effective vapor pressures imply that a significant fraction of the measured IEPOX derived SOA mass is effectively non-volatile (i.e. evaporation timescales of 100+ hours) under most atmospheric conditions, and importantly, that representing this SOA in models as a sum of the individual tracers would drastically over-estimate IEPOX SOA volatility and thus its potential loss by dilution, gas-phase oxidation, or vapor deposition which would be expected to equilibrate on the hourly timescale based on its saturation vapor concentration (C*). In addition, the effective volatility of the bulk organic aerosol ($C_xH_yO_z$) as measured by the FIGAERO is shown in Figure 5.6 for comparison (green bars). This representation demonstrates that the IEPOX SOA is actually the highest volatility component measured by the FIGAERO, and that the vast majority of OA is effectively non-volatile. Given that most of this OA mass has molecular compositions associated with BVOC (isoprene, monoterpenes, or biomass burning), these data suggest that SOA derived from BVOC should be modeled as non-volatile. The mechanisms by which this SOA arrives at such a low volatility remain uncertain, but some combination of auto-oxidation, multi-generational photochemical aging, and multiphase accretion chemistry is required.

5.3.3 *Volatility Implications for Gas-Particle Partitioning Esitmates.*

That the overall volatility distribution detected by the FIGAERO does not contain a significant mode where commonly measured semi-volatile isoprene oxidation products (e.g. tetrols, triols, furans) would be expected to evaporate, suggests that direct partitioning of these types of compounds likely does not comprise a large source organic aerosol mass. However, observations of methyl tetrols and alkene triols are often reported to be a significant fraction of total organic aerosol mass in isoprene rich regions (e.g. Lin et al., 2012). Such a finding suggests either a problem with partitioning theory or with the observations.

In Figure 5.7a we present a time series of two measurements of C_5 methyl tetrols measured by different techniques during the SOAS campaign. In shaded colors (blue and green) particle and gas phase methyl tetrols are shown as measured by the FIGAERO-TOF-CIMS. In black dots the total tetrol measured by the SV-TAG is shown (Isaacman et al., 2014). The two measurements using fundamentally different techniques agree remarkably well across a range of atmospheric conditions. In the middle panels of Figure 5.7 we again show thermal desorption profiles of $C_5H_{12}O_4$ from ambient aerosol particles measured by the FIGAERO-CIMS for two different conditions during the campaign (black). As noted above, a desorption temperature of 90 ºC is not consistent with a C_5 tetrol (or any possible isomer), but rather with a compound having a saturation vapor pressure 3 orders of magnitude lower than expected. Assuming that this secondary mode is derived from thermal decomposition during the desorption process of larger thermally unstable molecules, such a compound would not be expected to be in gas-particle equilibrium with a gas-phase tetrol. Thus, a measurement technique that takes the entirety of tetrol mass that thermally desorbs would overestimate the particle-phase fraction of tetrol in equilibrium with the gas-phase.

In the lower panels we compare the fraction of tetrol mass that is found in the gas and particle phase to an absorptive partitioning model, by calculating F_p from the model as well as the ambient FIGAERO data (fraction in the particle phase – see Chapters 1 and 4). The FIGAERO uncorrected partitioning measurement is shown in black in the lower panel and is on average higher than the Raoult's law based partitioning model, which is driven by total organic aerosol

mass, temperature and the tetrol sub-cooled liquid vapor pressure (blue line) (Couvidat and Seigneur, 2011). The uncorrected measurement includes the entirety of the tetrol mass measured during desorption (i.e. both the blue and red desorption modes in Figure 5.7). In an attempt to reconcile the measured and modeled partitioning discrepancy we separate the measured tetrol mass into high and low volatility components utilizing a thermogram fitting routine (described in detail elsewhere (Lopez-Hilfiker et al., 2014)). We hypothesize that the fraction of tetrol mass represented by the area of the lower temperature desorption mode (higher volatility component) is in equilibrium with the gas-phase tetrol because that component desorbs at a temperature similar to the pure substance (T_{max} ~60 °C, Figure 6, blue). Applying this combined thermogram-composition approach to partitioning (Lopez-Hilfiker et al., 2015), improves the measurement model agreement significantly. The partitioning model does not account for secondary sources of tetrol detected due to thermal decomposition of other compounds which presumably have very different effective saturation vapor pressures and thus partitioning than would a tetrol. The improved agreement supports the idea that the tetrol partitions to the aerosol according to its saturation vapor pressure and that so long as an apples and apples comparison is made, partitioning theory adequately describes the IEPOX SOA.

The partitioning model used for comparison in Figure 5.7 based only on Raoult's law suggests that for SOAS conditions only a small fraction (maximum 20%) of the total tetrol mass should be observed in the particle phase. This is generally consistent with the measured contribution of a high volatility thermogram component, partitioning, literature vapor pressures for the tetrol (Couvidat and Seigneur, 2011) and the effective vapor pressure determined by the FIGAERO relationship between vapor pressure and desorption temperature (T_{max}). The measurement-model agreement observed with the FIGAERO is not consistent with measurements of tetrol partitioning during SOAS by the SV-TAG which suggests that 60-100% of total tetrol mass is found in the particle phase.

One possible explanation of this discrepancy is that the tetrol partitions rapidly into particle-phase liquid-water according to Henry's Law and during the last part of the FIGAERO switch to thermal desorption mode (<10 seconds) all particle liquid water is lost, and along with it the tetrol that had partitioned to the liquid water. Figure 5.8 shows an example switch from gas

phase sampling to particle phase sampling and shows no evidence that the FIGAERO is missing mass at the early parts of the thermal desorption. Even if all the water was immediately lost, the tetrol which was partitioned into the particle liquid water would still need to evaporate, which at ambient temperatures is slow (~hour), given the tetrol has a T_{max} of ~60 C and that evaporation rates increase exponentially with temperature. To further rule this potential FIGAERO bias out we have deposited authentic methyl tetrol on the FIGAERO filter and find that while evaporation at room temperature is slow, it is readily detectable by the CIMS.

That our measurements of the total tetrol agree well with the SV-TAG also suggests that the two measurements are capturing approximately the same amount of total mass. A more likely explanation for the discrepancy between the TAG and FIGAERO measurements of the tetrol partitioning is related to thermal decomposition, the derivatization process of the TAG, or incomplete removal of the gas phase by the TAG denuder, leading to a convolution of the two phases. This is an area of ongoing investigation.

5.4 DISCUSSION

Previous composition measurements of the oxidation products derived from isoprene reported dimer concentrations that were 3 orders of magnitude lower than monomer concentrations (e.g triol, tetrol) (Lin et al., 2012). Our measurements utilizing the composition as well as the volatility distribution reveal that dimers or higher order oligomers and accretion products likely represent the majority of IEPOX derived SOA (~80%) which in turn accounts for 15-30% of total OA during SOAS. That the overall volatility distribution of IEPOX SOA is much lower than would be inferred from the dominant tracers has important impacts for the treatment of these types of compounds in regional and global chemical models; particularly models utilizing a volatility basis set approach or inferring vapor pressures and therefore gas to particle partitioning from chemical tracer or factor based measurements. The identity of the SOA components which produce IEPOX tracers upon thermal desorption remain unidentified from our measurements alone, but we hypothesize they are polyols, esters or ether accretion products. Detection of the fragments in high desorption temperature modes allows us to estimate an upper limit of the

volatility of the parent compound(s), which is at least 3 orders of magnitude lower than expected for some of the most abundant products identified from chamber experiments of the isoprene system.

Our findings, which highlight the extent of thermal decomposition during thermal aerosol analysis is not limited to our instrument. Thermal decomposition also likely explains why other thermal desorption based techniques often report small molecules present in larger than predicted abundance in atmospheric aerosol (e.g. Zhao et al., 2013). These measurements, which lack a direct means to separate the volatility of the detected components has led to the assumption that unexplained mechanisms or physical properties effectively tie semi-volatile material in atmospheric aerosol (e.g. Zhao et al., 2013). Implied in this argument is that partitioning theory should not accurately explain the gas-particle partitioning in the atmosphere (Pankow, 1994). With our SOAS dataset, and our measurement of $C_5H_{12}O_4$ and $C_5H_{10}O_3$ we show that this is not necessarily the case, but rather that the measurement of small molecules is primarily a thermal decomposition artifact, which was not adequately resolved in previous measurements.

Our measurements of the tetrol also show it is heavily partitioned into the gas phase and that the particle phase fraction can be explained largely by Raoult's Law based partitioning. We are able to use this information to put an important constraint on the Henry's Law constant for the tetrol. Our measurements suggest that it is likely not larger than 10^8 M atm^{-1} as we never observe F_p in the range of 0.8 to 1 which would be consistent with a literature estimates of the Henry's Law constant (~10^{10} M atm^{-1}) and typical particle liquid water concentrations during SOAS (Couvidat and Seigneur, 2011). Additionally, that the measured partitioning of methyl tetrols is relatively well explained by a simple absorptive partitioning model implies that diffusion, viscosity, or other mass transfer limitations do not significantly impede the tetrol reaching equilibrium with the gas phase following atmospheric changes on approximately hour long timescales.

The measured total organic aerosol volatility distribution measured by the FIGAERO suggests the organic aerosol is most likely comprised of isoprene related dimers, organo-sulfates, or other oligomers (T_{max}>70), as well as monoterpene related oxidation products (T_{max}>70). That the overall volatility distribution, representing all detected organic components, is shifted to high

desorption temperatures suggests that generally SOA in the SE United States should be treated as effectively non-volatile and that mechanisms much exist which form low volatility products in high yield.

5.5 Conclusions

Through advances in measurement techniques we have provided a number of new constraints on the composition and volatility of ambient organic aerosol during the SOAS field project which took place in an isoprene dominated region. We show that the mass concentration of the IEPOX factor derived from AMS spectra can be described at the molecular level using a sum of molecular ions detected using a FIGAERO-CIMS allowing additional mechanistic insight and relating directly the AMS factor to chemically ionized molecules. By utilizing the online volatility measurement in combination with molecular composition we show that commonly reported molecular tracers from isoprene oxidation are nearly entirely derived from thermal decomposition of accretion products or other low volatility organics. That IEPOX SOA is effectively non-volatile material has important implications for modeling SOA derived from isoprene.

In a similar analysis applied to the total measured organic aerosol, we find that the FIGAERO-CIMS explains a large fraction of submicron organic aerosol mass measured by the AMS when utilizing an upper limit to the instrument sensitivity. That we explain such a large fraction of the total AMS organic aerosol mass with chemical speciation is an important step towards identifying the key mechanisms responsible for producing aerosol mass. The measured volatility distribution of total organic aerosol was remarkably low volatility with important implications for the lifetime and partitioning of organic aerosol components. In spite of the very low volatility of the bulk organic aerosol, we show that an assumption of equilibrium partitioning of individual tracers such as the methyl tetrol is reasonably valid if the role of thermal decomposition is taken into account. These advances in the understanding of the chemical and physical properties of organic aerosol, the importance of accretion chemistry, and a consistent framework for interpreting SOA molecular composition measurements within a volatility framework will help

develop new mechanistic insights which can be distilled and implemented into global chemical models.

References:

Bertram, T. H., Thornton, J. A. and Riedel, T. P.: An experimental technique for the direct measurement of N_2O_5 reactivity on ambient particles, Atmos. Meas. Tech., 2(1), 231–242, doi:10.5194/amt-2-231-2009, 2009.

Brown, S. S., Stark, H. and Ciciora, S. J.: In-situ measurement of atmospheric NO3 and N2O5 via cavity ring-down spectroscopy, Geophysical research …, 2001.

Budisulistiorini, S. H., Canagaratna, M. R., Croteau, P. L., Marth, W. J., Baumann, K., Edgerton, E. S., Shaw, S. L., Knipping, E. M., Worsnop, D. R., Jayne, J. T., Gold, A., et al.: Real-Time Continuous Characterization of Secondary Organic Aerosol Derived from Isoprene Epoxydiols in Downtown Atlanta, Georgia, Using the Aerodyne Aerosol Chemical Speciation Monitor, Environ. Sci. Technol., 47(11), 5686–5694, doi:10.1021/es400023n, 2013.

Capouet, M. and Müller, J. F.: A group contribution method for estimating the vapour pressures of α-pinene oxidation products, Atmos. Chem. Phys., 6(6), 1455–1467, doi:10.5194/acp-6-1455-2006, 2006.

Couvidat, F. and Seigneur, C.: Modeling secondary organic aerosol formation from isoprene oxidation under dry and humid conditions, Atmos. Chem. Phys., 11(2), 893–909, doi:10.5194/acp-11-893-2011, 2011.

Day, D. A., Wooldridge, P. J. and Dillon, M. B.: A thermal dissociation laser-induced fluorescence instrument for in situ detection of NO2, peroxy nitrates, alkyl nitrates, and HNO3, Journal of …, 2002.

Ehn, M., Thornton, J. A., Kleist, E., Sipilä, M., Junninen, H., Pullinen, I., Springer, M., Rubach, F., Tillmann, R., Lee, B., Lopez-Hilfiker, F., et al.: A large source of low-volatility secondary organic aerosol, Nature, 506(7489), 476–479, doi:10.1038/nature13032, 2014.

Gaston, C. J., Riedel, T. P., Zhang, Z., Gold, A., Surratt, J. D. and Thornton, J. A.: Reactive Uptake of an Isoprene-Derived Epoxydiol to Submicron Aerosol Particles, Environ. Sci. Technol., 48(19), 11178–11186, doi:10.1021/es5034266, 2014.

Guenther, A., Hewitt, C. N. and Erickson, D.: A global model of natural volatile organic compound emissions, Journal of …, 1995.

Hallquist, M., Wenger, J. C., Baltensperger, U., Rudich, Y., Simpson, D., Claeys, M., Dommen, J., Donahue, N. M., George, C., Goldstein, A. H., Hamilton, J. F., et al.: The formation, properties and impact of secondary organic aerosol: current and emerging issues, Atmos. Chem. Phys., 9(14), 5155–5236, doi:10.5194/acp-9-5155-2009, 2009.

Heald, C. L., Kroll, J. H., Jimenez, J. L., Docherty, K. S., DeCarlo, P. F., Aiken, A. C., Chen, Q., Martin, S. T., Farmer, D. K. and Artaxo, P.: A simplified description of the evolution of organic aerosol composition in the atmosphere, Geophys. Res. Lett., 37(8), L08803,

doi:10.1029/2010GL042737 [online] Available from: http://dx.doi.org/10.1029/2010GL042737, 2010.

Huey, L. G., Hanson, D. R. and Howard, C. J.: Reactions of SF6- and I- with Atmospheric Trace Gases, J. Phys. Chem., 99(14), 5001–5008, doi:10.1021/j100014a021, 1995.

Isaacman, G., Kreisberg, N. M., Yee, L. D., Worton, D. R., Chan, A. W. H., Moss, J. A., Hering, S. V. and Goldstein, A. H.: Online derivatization for hourly measurements of gas- and particle-phase semi-volatile oxygenated organic compounds by thermal desorption aerosol gas chromatography (SV-TAG), Atmos. Meas. Tech., 7(12), 4417–4429, doi:10.5194/amt-7-4417-2014-supplement, 2014.

Kercher, J. P., Riedel, T. P. and Thornton, J. A.: Chlorine activation by N_2O_5: simultaneous, in situ detection of $ClNO_2$ and N_2O_5 by chemical ionization mass spectrometry, Atmos. Meas. Tech., 2(1), 193–204, doi:10.5194/amt-2-193-2009, 2009.

Lee, B. H., Lopez-Hilfiker, F. D., Mohr, C., Kurtén, T., Worsnop, D. R. and Thornton, J. A.: An Iodide-Adduct High-Resolution Time-of-Flight Chemical-Ionization Mass Spectrometer: Application to Atmospheric Inorganic and Organic Compounds, Environ. Sci. Technol., 48(11), 6309–6317, doi:10.1021/es500362a, 2014.

Lin, Y.-H., Zhang, Z., Docherty, K. S., Zhang, H., Budisulistiorini, S. H., Rubitschun, C. L., Shaw, S. L., Knipping, E. M., Edgerton, E. S., Kleindienst, T. E., Gold, A., et al.: Isoprene Epoxydiols as Precursors to Secondary Organic Aerosol Formation: Acid-Catalyzed Reactive Uptake Studies with Authentic Compounds, Environ. Sci. Technol., 46(1), 250–258, doi:10.1021/es202554c, 2012.

Lopez-Hilfiker, F. D., Mohr, C., Ehn, M., Rubach, F., Kleist, E., Wildt, J., Mentel, T. F., Lutz, A., Hallquist, M., Worsnop, D. and Thornton, J. A.: A novel method for online analysis of gas and particle composition: description and evaluation of a Filter Inlet for Gases and AEROsols (FIGAERO), Atmos. Meas. Tech., 7(4), 983–1001, doi:10.5194/amt-7-983-2014, 2014.

Lopez-Hilfiker, F., Mohr, C., Ehn, M., Rubach, F., Kleist, E., Wildt, J., Mentel, T. F., Carrasquillo, A., Daumit, K., Hunter, J.others: Phase partitioning and volatility of secondary organic aerosol components formed from α-pinene ozonolysis and OH oxidation: the importance of accretion products and other low volatility compounds, Atmos. Chem. Phys. Discuss., 15(4), 4463–4494, 2015.

Pankow, J. F.: An absorption model of gas/particle partitioning of organic compounds in the atmosphere, Atmospheric Environment, 28(2), 185–188, doi:10.1016/1352-2310(94)90093-0, 1994.

Robinson, N. H., Hamilton, J. F., Allan, J. D., Langford, B., Oram, D. E., Chen, Q., Docherty, K., Farmer, D. K., Jimenez, J. L., Ward, M. W., Hewitt, C. N., et al.: Evidence for a significant proportion of Secondary Organic Aerosol from isoprene above a maritime tropical forest, Atmos. Chem. Phys., 11(3), 1039–1050, doi:10.5194/acp-11-1039-2011-supplement, 2011.

Surratt, J. D., Chan, A. W. H., Eddingsaas, N. C., Chan, M., Loza, C. L., Kwan, A. J., Hersey, S. P., Flagan, R. C., Wennberg, P. O. and Seinfeld, J. H.: Reactive intermediates revealed in secondary organic aerosol formation from isoprene., Proceedings of the National Academy of Sciences, 107(15), 6640–6645, doi:10.1073/pnas.0911114107, 2010.

Zhao, Y., Kreisberg, N. M., Worton, D. R., Isaacman, G., Weber, R. J., Liu, S., Day, D. A., Russell, L. M., Markovic, M. Z., VandenBoer, T. C., Murphy, J. G., et al.: Insights into Secondary Organic Aerosol Formation Mechanisms from Measured Gas/Particle Partitioning of Specific Organic Tracer Compounds, Environ. Sci. Technol., 47(8), 3781–3787, doi:10.1021/es304587x, 2013.

Ziemann, P. J. and Atkinson, R.: Kinetics, products, and mechanisms of secondary organic aerosol formation, Chem. Soc. Rev., 41(19), 6582, doi:10.1039/c2cs35122f, 2012.

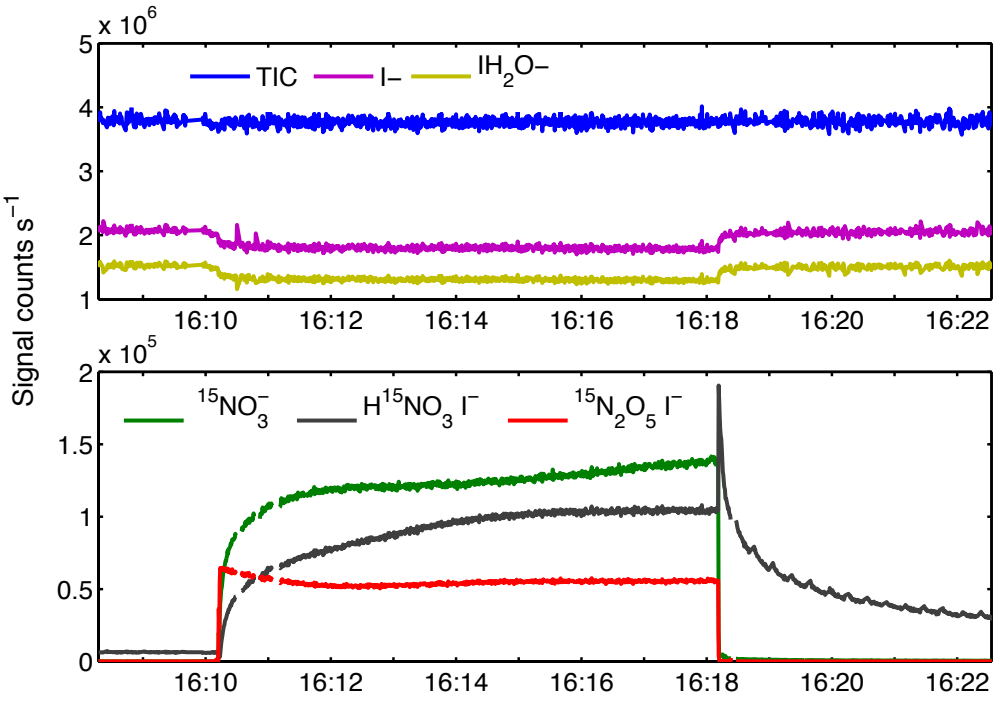

Figure 5.1 An example kinetic limit determination of the TOF-CIMS. Top: The reagent ions and sum of total ions during the addition of high concentrations of $^{15}N_2O_5$ to the inlet of the TOF-CIMS. Also evident is $H^{15}NO_3$ from trace water vapor in the reaction cell. By calibrating in this case to the independent TD-LiF we are able to derive the kinetic limit of the instrument by adding the two detection channels described in the text (Day et al., 2002; Huey et al., 1995).

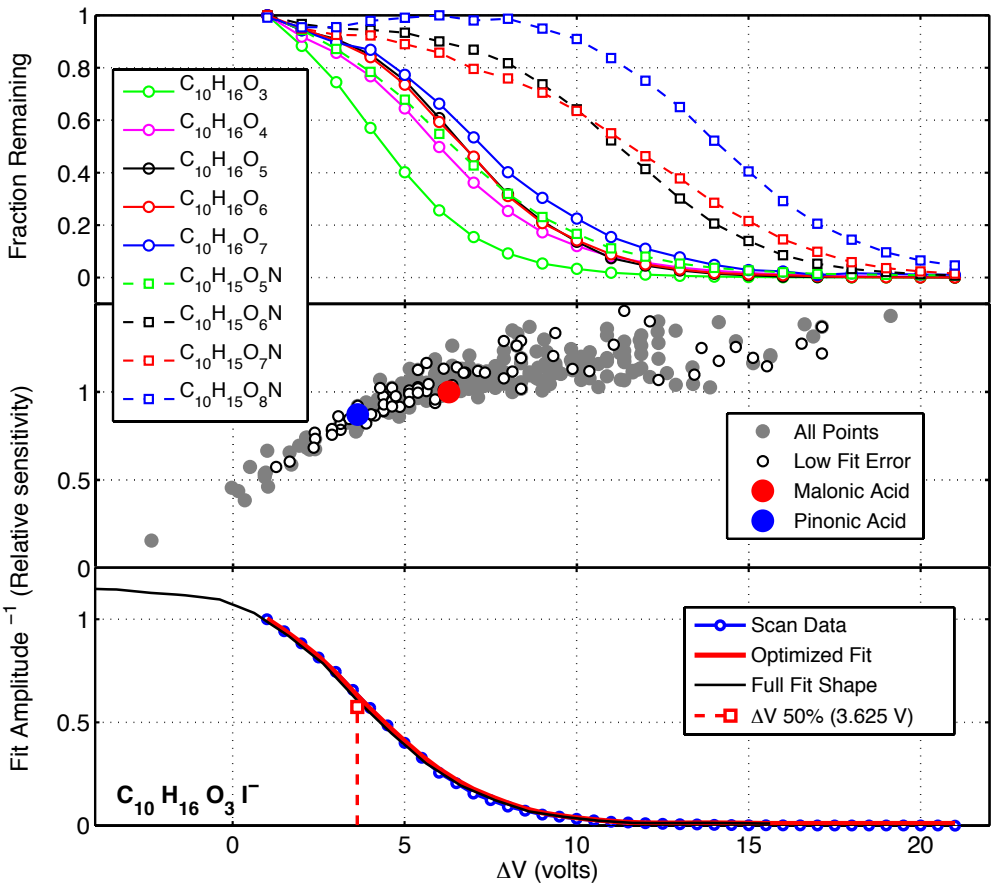

Figure 5.2 Effective sensitivity and binding energy.

Top: Declustering scans from the reaction of a-pinene and ozone in the presence of NO_x Some molecules dissociate rapidly during the first few voltage steps. Some multifunctional nitrates and highly oxidized C_{10} molecules show no dependence to the initial voltage steps before dissociating. These compounds we infer are strongly bound to I-, and therefore should be detected at a high sensitivity. Middle: The results of fitting declustering scans shows a plateauing effect as a function of dV. This suggests that compounds, which survive to high potentials, should be detected with a similar sensitivity as determined by the fit amplitude. Bottom: A example of a declustering scan fit is shown for $C_{10}H_{16}O_3I$-. The raw scan data is shown in blue circles, the region of optimization for the fit is shown in red, and the extrapolated scan curve is shown in black. We use dV (50%) as a measure of the relative binding energy between compounds.

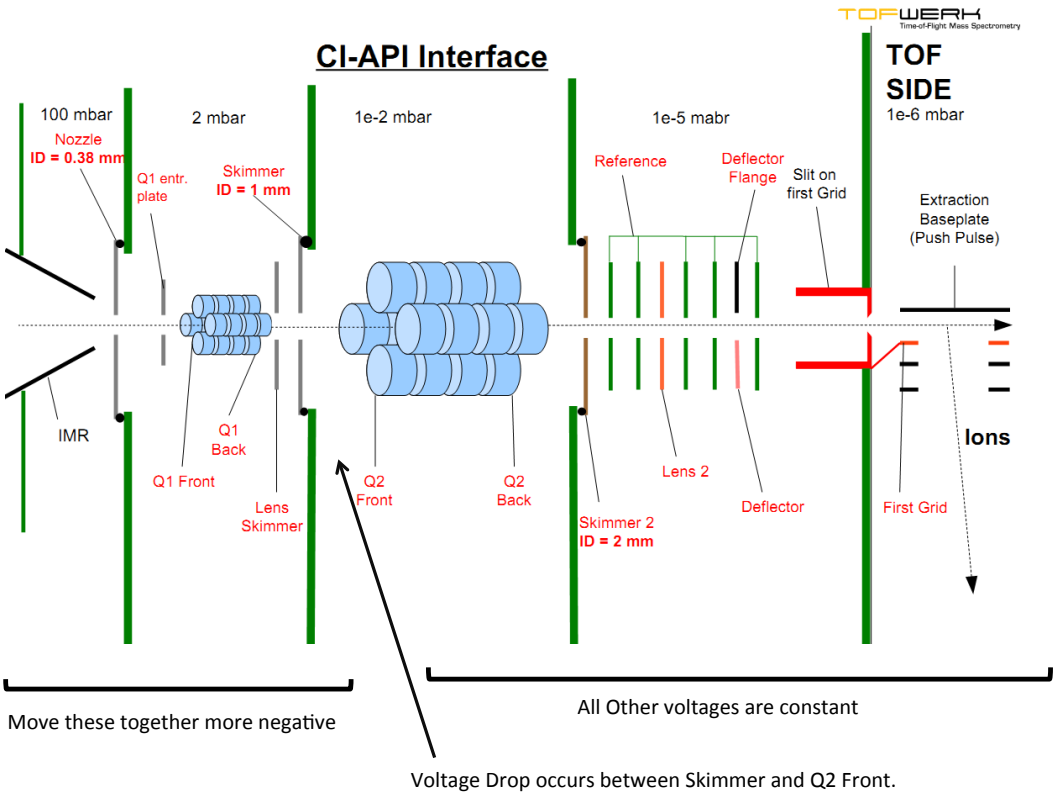

Figure 5.3. A Schematic of the voltages in the APi region of the TOF-MS. Highlighted by a black arrow is the region of the mass spectrometer where we collisionally decluster iodide adducts in an effort to constrain sensitivity and binding energy. Schematic from Tofwerk AG, Thun Switzerland.

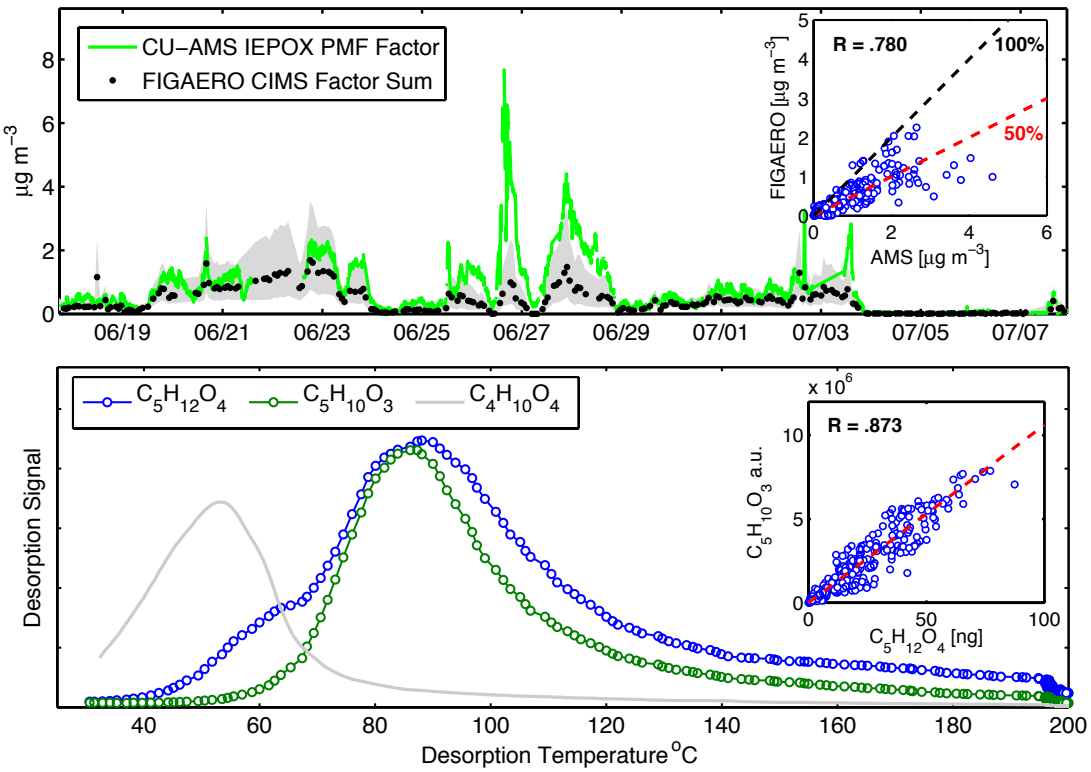

Figure 5.4. AMS and FIGAERO IEPOX Factor Comparison.

Top Panel: The IEPOX organic aerosol factor from an AMS during the SOAS campaign (green). The sum of compositions highly correlated in time with C5H10O3 and C5H12O4 traditional markers for IEPOX organic aerosol measured by the FIGAERO-TOF-CIMS (black). Uncertainty bars are dominated by uncertainty in the instrument sensitivity to the molecular composition of C5H10O3 due to differing sensitivity to different isomers (for example furan-diols and alkene triols). The sum of the CIMS based tracers explain within uncertainty the time evolution and mass concentration of the AMS IEPOX factor. Inset: A point by point correlation between the AMS IEPOX factor and the FIGAERO CIMS tracer sum which explain to a large degree the mass and time evolution of the AMS factor. Bottom Panel: Thermal desorption profiles of $C_5H_{12}O_4$ (blue), $C_5H_{10}O_3$ (green) from ambient aerosols measured during the SOAS campaign are shown. The tetrol, clearly shows two modes while the $C_5H_{10}O_3$ (presumably a furan diol or an alkene triol), which is expected to maximize before the tetrol, instead maximizes at the same temperature as the secondary mode of the tetrol. Inset: A scatter plot of the $C_5H_{12}O_4$ *vs* the $C_5H_{10}O_3$ mass concentration measured by the FIGAERO across the entire SOAS campaign, showing these two compounds are highly correlated. See text for details.

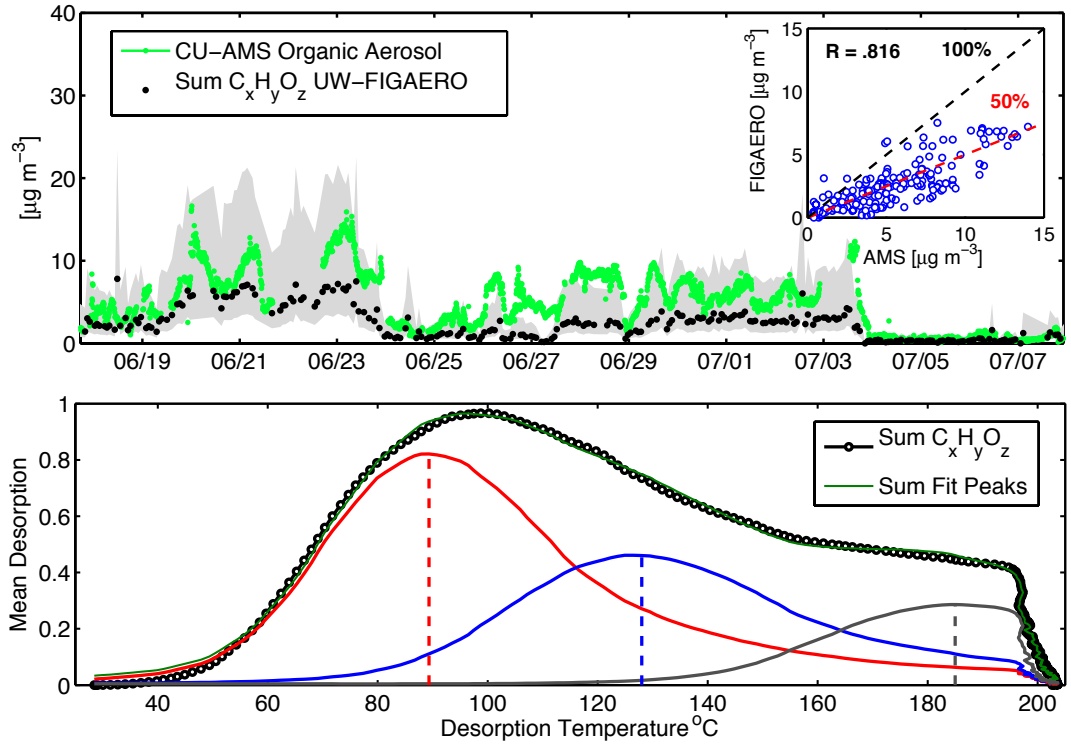

Figure 5.5. AMS and FIGAERO Organic Comparison.

Top Panel: Mass concentrations during the SOAS campaign reported by the CU-AMS and the UW-FIGAERO. The FIGAERO is a sum of all compounds, which formed, adducts with iodide (generic formula: $C_xH_yO_zI$-). For the majority of compounds we have no direct calibration and therefore apply the experimentally determined collision limit, in approximate agreement with the highest observed sensitivity of our instrument. Bottom Panel: The average total thermogram from SOAS measured by the FIGAERO HR-ToF-CIMS. Evident are multiple desorption modes, though no significant mode is present at temperatures where commonly measured isoprene oxidation products (e.g. tetrols, triols) would be expected to desorb if they were partitioning to the aerosol according to Raoult's or Henry's Laws. The measured FIGAERO volatility distribution instead suggests the organic aerosol is more likely comprised of isoprene related dimers, organo-sulfates, or other oligomers (T_{MAX}>70), as well as monoterpene related oxidation products (T_{MAX}>70). That the overall volatility distribution, representing all detected organic components, is shifted to higher than expected desorption temperatures suggest that SOA in the SE United States should be treated as effectively non volatile.

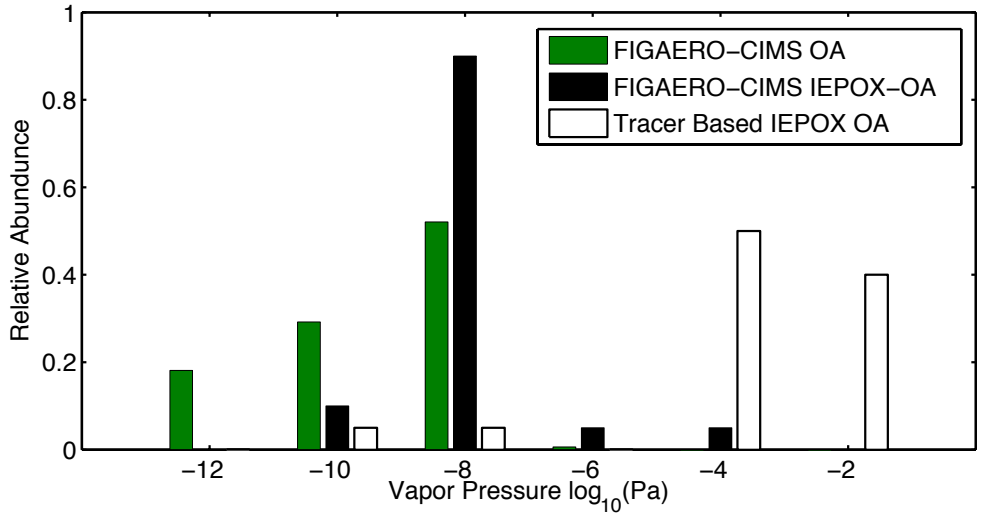

Figure 5.6. Volatility Distribution of Oxidized OA.

A volatility basis set approach to examining the volatility of organic aerosol in the SE United States. Estimated volatility based on the abundance of commonly reported components of isoprene epoxy diol derived organic aerosol, which are thought to be dominated by tetrols and triols with some contribution from dimers and organic sulfates (white bars). The volatility distribution of such aerosol components as measured by the FIGAERO reveal effective vapor pressures more than 3 orders of magnitude lower than predicted, implying that a significant fraction of the measured organic aerosol mass is effectively non-volatile. That higher volatility products (tetrols, triols, etc) are detected in organic aerosol is likely the result of thermal decomposition of the much lower volatility material during the thermal desorption process.

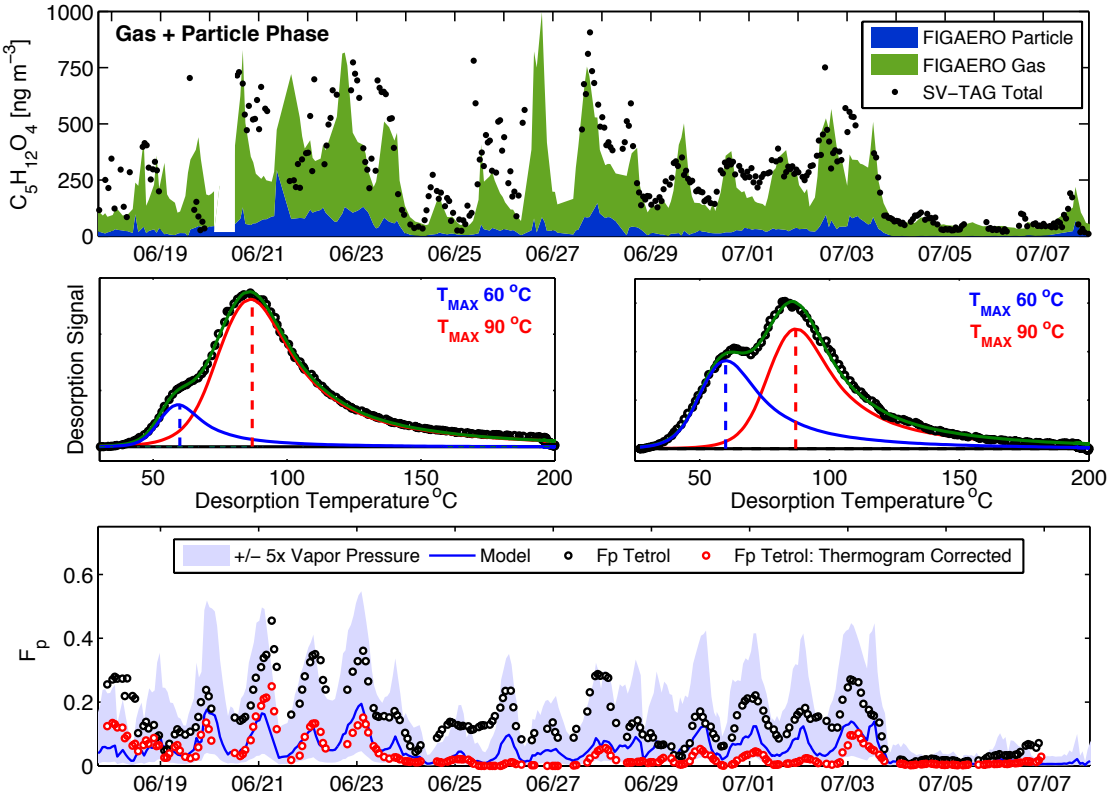

Figure 5.7 SV-TAG and FIGAERO Comparison.

Top: Mass concentrations measured by the FIGAERO TOF-CIMS (shaded) in the gas and particle phases along with the SV-TAG total tetrol. Both methods using very different approaches agree remarkably well in time and concentration, suggesting that the FIGAERO is indeed measuring methyl tetrols at $C_5H_{12}O_4I$-. Middle: Thermograms representing two different relative loadings at the semi-volatile and low volatility peak in methyl tetrols. Bottom: Predicted and measured partitioning for the tetrol during the SOAS campaign. The blue line represents the partitioning model based absorptive partition theory, forced by temperature, organic aerosol loading, and the tetrol pure vapor pressure. In black the uncorrected thermogram partitioning data is shown. Reconciling the thermogram profile improves the partitioning agreement. See text for discussion.

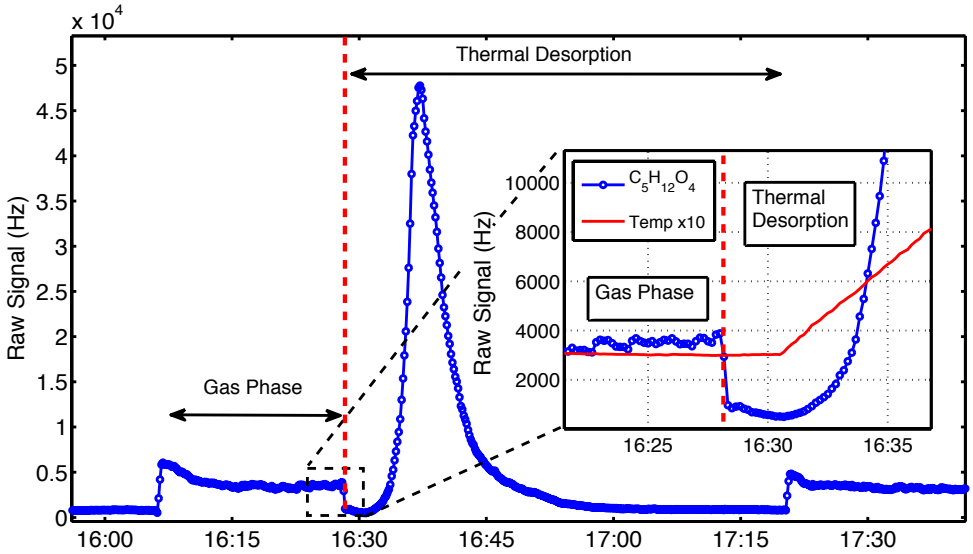

Figure 5.8 Example measurement cycles of C_5 Tetrols.

In blue, raw data acquired during SOAS showing the transition between gas and particle phases in the FIGAERO sequence. No evidence for a large fraction of mass out of the particles is evident during the initial parts of the heating when water is lost from the particles. This in addition to the model – measurement agreement using adsorptive partitioning suggests that water based partitioning is limited for the tetrol during SOAS.

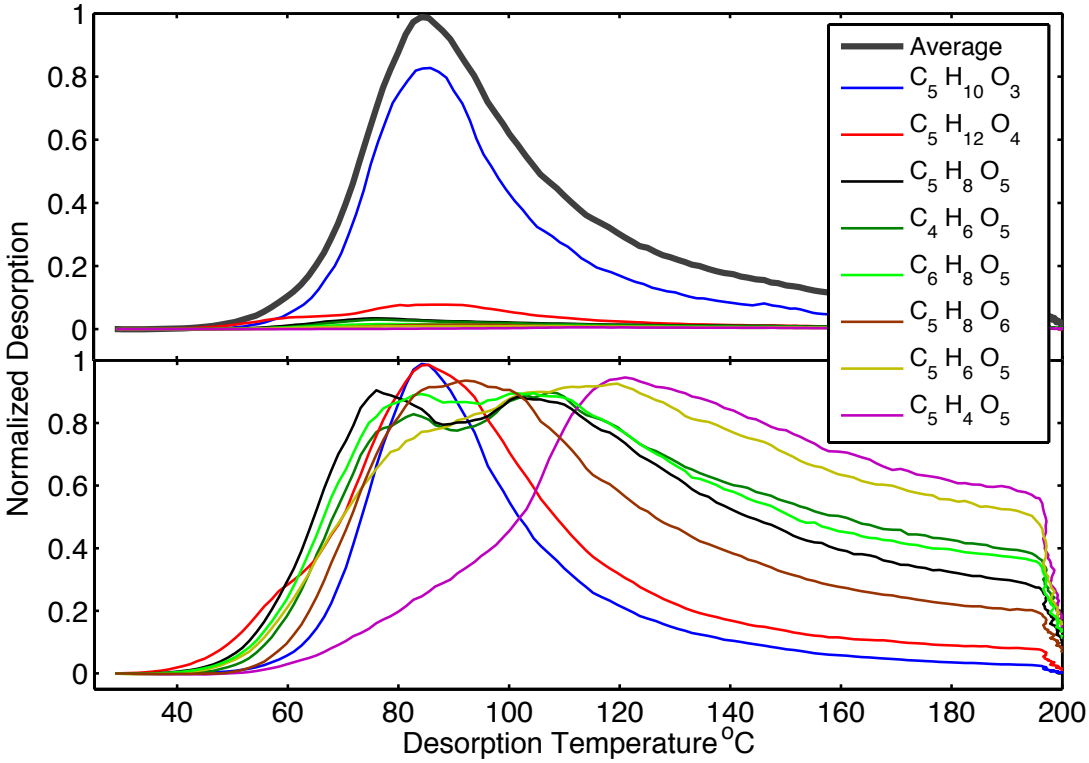

Figure 5.9 Thermograms of the CIMS IEPOX factor.

Top: relative average mass contributions to the sum thermogram of the CIMS IEPOX factor. Bottom: relative volatility of each products on a normalized axis. No significant evidence for semi-volatile mass is observed (e.g. T_{max} 40-60 C).

Chapter 6. CONCLUSIONS AND FUTURE DIRECTIONS

Understanding the evolution of organic aerosol and specifically that of secondary origin is critical for assessing the impact of aerosol particles on visibility, cloud formation processes and health. The advancement of our understanding of the processes leading to OA and specifically SOA is facilitated by advances in measurement techniques which have advanced rapidly over the last decade. A major part of my research was the development and optimization of a high-resolution chemical ionization time of flight mass spectrometer. I developed a variety of inlets for the instrument both for ground and aircraft based work. Chapter 2 describes the detailed development of the first airborne deployment of the HRTOF-CIMS and associated ion chemistry, which was extensively characterized both by quantum calculations and a series of targeted calibrations for the detection of inorganic and organic molecules.

Of specific relevance to SOA formation and properties is the coupling of this newly developed mass spectrometer with a recently developed inlet, the Filter Inlet for Gases and AEROsols (FIGAERO). The FIGAERO allows measurement of semi- and low volatility compounds in both the gas phase and the particle phase to elucidate the chemical compounds responsible for SOA formation by vapor uptake and multiphase chemistry. Experimental and measurement based atmospheric chemistry has traditionally been two separate communities, one focusing on aerosol research and composition while another community focuses on gas phase oxidation and mechanism development. Recently it has become evident that the evolution of SOA is part of dynamically changing equilibrium between the gas and particle phase. Therefore measurement technologies, which can quantitatively detect organic matter in both phases, are of critical need to further our understanding of SOA evolution and its response to atmospheric changes. The FIGAERO when coupled to the HR-TOF-CIMS fills this measurement gap by providing semi-continuous, speciated measurements *insitu* in both the gas and particle phases on approximately hourly timescales. When coupled with chemical ionization, which is selective and sensitive towards multifunctional organic molecules, we attain detection limits in the pg m^{-3} without ionization induced fragmentation, which allows us to test and develop new chemical mechanisms to explain the observations of new molecular compositions that this measurement technique provides.

The FIGAERO also provides critical volatility information, which allows vapor pressures of compounds to be estimated or molecular identification be confirmed. We present a linear relationship in terms of enthalpy of sublimation, or log-linear in terms of vapor pressure between the temperature of maximum desorption signal (T_{max}) and these physical parameters which are critical to modeling SOA either by volatility basis set methods or by absorptive partitioning. This method is robust and reproducible and requires no knowledge of the instrument sensitivity to derive an effective vapor pressure. A detailed description of the performance characteristics of the FIGAERO is presented in Chapter 3.

In Chapter 4 we present the first online measurements with the FIGAERO inlet on an atmospheric simulation chamber in Germany. We use the FIGAERO to explore the contribution, composition and volatility of acyl containing organic compounds present in α-pinene derived secondary organic aerosol. We detect a suite of compounds spanning $C_{1\text{-}30}$ and $O_{2\text{-}10}$ with many of the compounds that were detected in the gas phase also present in the particle phase. The distribution of detected compounds in the particle phase explains at least 25% of the total SOA mass produced under both OH oxidation and ozonolysis conditions and shows evidence for a significant contribution from oligomers, most notably during ozonolysis. We find that the effective volatility of the detected mass reflects this contribution, with a large fraction of the organic mass having vapor pressures 4 orders of magnitude lower than commonly detected diacid products from ozonolysis of α-pinene. In the particle analysis we highlight the role of thermal decomposition, and show that, when it is accounted for using the thermogram desorption profiles, equilibrium absorptive partitioning explains well the observed phase partitioning of a few acids across the range of chamber conditions. We infer a significant fraction of the SOA is comprised of oligomeric compounds given the relatively short residence times of the JPAC and UW chambers suggests these types of compounds can play an important role in ambient monoterpene derived SOA.

In Chapter 5 we present the first ambient analysis using the FIGAERO during the SOAS campaign in the SE United States. We show that the mass concentration of the IEPOX factor derived from AMS spectra can be described at the molecular level using a sum of molecular ions

detected using a FIGAERO-CIMS allowing mechanistic insight, previously unavailable. By utilizing the online volatility measurement in combination with molecular composition we are able to quantitatively show that commonly reported molecular tracers from isoprene oxidation are nearly entirely derived from thermal decomposition of accretion products or other low volatility organics. Similarly, we find that the FIGAERO-CIMS explains a large fraction of the total submicron organic aerosol measured by the AMS. That we explain such a large fraction of the total AMS organic aerosol mass with chemically speciated measurements is an important step towards identifying the key mechanisms responsible for forming and growing aerosol to climate relevant sizes. The measured volatility distribution of total organic aerosol was remarkably low volatility with important implications for the lifetime and partitioning of organic aerosol components. We compared measurements of common tracer compounds to an equilibrium partitioning model and find that the model reasonably well describes the partitioning.

The FIGAERO inlet is still in its infancy with the first prototype built in late 2012. There are still many important scientific questions that remain unanswered or untested but which will ultimately improve our understanding of secondary organic aerosol and are readily addressed by the FIGAERO-CIMS technique. Instrument improvements and additional experiments are outlined in the following sections and can be used as a guide for future developments and scientific research activities.

6.1 Instrument Improvements.

The time of flight mass spectrometer is largely optimized though newer models will likely accomplish higher sensitivity and resolution that will aid in data analysis and interpretation. However based on the work accomplished over the past 5 years, it has become clear that the region where the largest gains are likely to be made are in the optimization of the chemical ionization region of the mass spectrometer and further ion chemistry developments. Suggestions for these types of developments are outlined below.

(1) A refined ion molecule reaction region (IMR), which addresses the main issues with the current version, is desperately needed. These issues involve (a) memory on the interior walls of the IMR (e.g. offgassing, equilibration timescales), (b) the potential of radial chemistry to occur inside the IMR from radicals produced inside the polonium ionizer and (c) providing little control over the ionization conditions with respect to cluster distributions. While the current version is functional and provides a simple, sensitive and robust system a new design of the IMR should incorporate these controls. Until then, the addition of propane to the IMR would also allow determination of the extent of radical chemistry and should be periodically checked. The cluster distribution has already been modulated by water vapor addition, but the addition of more strongly bound molecules would perhaps be able to suppress any water vapor dependence, by for example changing the reagent ions from $I(H_2O)$- to I(organic)-. The addition of perflouroheptanoic acid or other molecules may also address some memory concerns by occupying surface sites in the IMR and inlet lines thereby improving time response, reducing offgassing and equilibration timescales.

(2) Iodide ion chemistry has been shown to be a powerful ion for the exploration of organic molecules which make up a significant fraction of the organic aerosol mass, however calibration remains a challenge even for compounds which are readily available. A automated calibration system either by syringe pump, atomized solution via a heated tube or conversion of organics to carbon dioxide by a catalyst is needed to further develop calibrations and functional group dependencies in a robust, reproducible and efficent way.

(3) Additional experiments and quantum calculations should be conducted to further develop the relationship between binding energy, sensitivity and cluster transmission through the APi of the mass spectrometer. There is significant promise to being able to scan voltages and therefore derive sensitivities but further work comparing known calibrations to quantum calculations is needed to demonstrate that the method is robust and reliable. Also the ability to separate isomers is presumably possible but has thus far not been

thoroughly investigated, beyond the separation of peroxy-acids, i.e. between iodide adducts and reactive charge transfer.

(4) Future field deployments will demand shorter inlets in an effort to transmit low volatility organics to the instrument without perturbation. In the field deployment to Hyytiälä in 2014 the instrument was deployed on the top of a tower, outside in a weatherproof box. This allowed sampling with 1 m high flow inlets but performance was hampered by DAQ temperature control problems that we subsequently addressed. Future work deploying the instrument in the field should focus on deploying the instrument in a way that perturbs incoming air as little as possible.

6.2 Experimental Possibilities with TOF-CIMS and FIGAERO

The FIGAERO while initially and predominantly used for volatility and composition analysis has the potential for a variety of other applications. Some experiments, which should be pursued, are outlined in this section.

(1) The measurement of the semi-volatile component of organic aerosol can be determined by holding the FIGAERO filter after collection but before heating in a steam of clean air. This has been done in UHP nitrogen streams to determine the fraction of mass lost during a so-called “wait experiment”, which is user specified to the range of minutes to hours. Preliminary work for the monoterpene system has shown that little mass was lost over a period of 45 minutes in a dry nitrogen stream. Future work should explore this measurement method by using humidified nitrogen and attempt to measure the gases, which evaporate during the wait period as well as examine the volatility distribution as a function of photochemical age. This type of experiment could answer remaining questions about the phase state; viscosity and mass transfer limitations in the aerosol.

(2) The addition of labeled compounds during a wait experiment as described above should also be done to try to characterize the number of exchangeable hydrogens and therefore help to identify functional groups. For example if D_2O was used as the humidification

source for every exchangeable hydrogen you would observe a shift in the mass spectrum of +1 Th which would be apparent by a mass spectral difference. This would help identify functional groups that are not directly resolvable under the normal operation of the TOF-CIMS and would be possible, for example, during a steady state chamber experiment.

(3) Utilizing declustering scanning and the observed collision limit (see Chapter 5) we presumably have a unique measurement of organic peroxyacid functionalities by observing the deprotonated carboxylic acid anion after reaction with iodide to form neutral HOI. Compounds containing these functionalities make up a large fraction of the total observed signal during a-pinene ozonolysis (see Chapter 2) and could be a potentially important source of low volatility acylperoxyhemiacetals. These acylperoxyhemiacetals may thermally decompose upon heating to explain the secondary modes in our thermal desorptions from a-pinene systems and therefore warrant further investigation both by investigation of their gas phase precursors (e.g. peroxy acids) and particle phase decomposition pathways.

(4) The instrument during the 2014 Hyytiälä deployment used the FIGAERO inlet to measure gas phase fluxes of oxygenated organic compounds as well as semi-continuous particle measurements. This was accomplished successfully for semi-volatile compounds however for the lowest volatility compounds (e.g. $C_{10}H_{16}O_9$ and other ELVOC) there was not enough signal to calculate significant flux. Future improvements utilizing a redesigned atmospheric pressure ionization IMR should facilitate lower detection limits and higher sensitivity towards these types of compounds and should therefore be pursued. The TOF-MS is ideal for eddy covariance fluxes as hundreds of compounds fluxes can be captured at high time resolution with a single instrument. Currently the limiting factor to acquiring this type of data is the IMR as the instrument has already been deployed inside a weatherproof box with a short inlet (i.e. < 1 meter).

(5) Aircraft based measurements have been very successful in producing high quality data using the TOF-CIMS and should continue to be a priority for deployments of this type of

instrument. The FIGAERO because of its relatively long desorption time is not suitable for aircraft work unless the duty cycle can be improved to 15 min or better. Other mass spectrometric techniques should therefore be developed utilizing the TOF as the mass analyzer to measure molecularly resolved aerosol composition on a regional basis.

To date there are now over 15 FIGAERO-TOF CIMS in use around the world working on questions ranging from SOA formation by VOC oxidation in chambers to chemically characterizing primary and secondary aerosol sources in China. The data that has already been collected and that which will be collected by groups around the world in the coming years will prove to be invaluable in developing our chemical understanding of aerosol evolution and therefore allow improvements in SOA modeling efforts, and the development of new chemical mechanisms.

VITA

Felipe D. Lopez-Hilfiker grew up in the San Juan Islands, Washington. Sports, primarily soccer and sailing were primary focuses from a young age as well as LEGOs. Designing new systems for his sailboat during high school satisfied his desire to make things work better. During high school Felipe began to develop interest in science and technology and applied to and accepted an internship at Luxel Corporation, in Friday Harbor, WA. Here he was introduced to the intricacies of laboratory work and high vacuum technology, and built his first vacuum system for deposition of precious metals for band pass filters. Soon after arriving to the University of Washington as an engineering student, he took an environmental chemistry course taught by his future undergraduate advisor Joel Thornton. After beginning work in the Thornton research group designing components for calibration sources, Felipe soon became involved in atmospheric chemistry research involving reactive halogens using custom mass spectrometers and changed to an atmospheric science major. At the completion of his undergraduate degree, graduate school seemed like the best avenue to continue doing research. He stayed at the Univeristy Of Washington and continued to work developing new technologies for atmospheric applications using state of the art mass spectrometers. Felipe graduated in 2015 with a Ph.D. in Atmospheric Chemistry.